YEARBOOK
2021

INSTITUTE OF TECHNICAL PHYSICS AND MATERIALS SCIENCE
CENTRE FOR ENERGY RESEARCH
PART OF EÖTVÖS LORÁND RESEARCH NETWORK

http://www.mfa.kfki.hu/

Published by
Institute of Technical Physics and Materials Science
Centre for Energy Research
Part of Eötvös Loránd Research Network

EK MFA Yearbook 2021

Director: Prof. Béla Pécz, D.Sc.

Address: Konkoly-Thege Miklós út 29-33, H-1121 Budapest, Hungary
Postal: P.O.Box 49, H-1525 Budapest, Hungary
Phone: +36-1-392 2224
E-mail: info@mfa.kfki.hu
URL: http://www.mfa.kfki.hu/
Editor: Krisztina Szakolczai, Ph.D.
Published by: EK MFA, Budapest, Hungary, 2022.

Content

GENERAL INFORMATION

Director's foreword

As the director of MFA, it is my pleasure to welcome the reader. I recommend browsing the present yearbook which continues the series of the former ones and contains results achieved in 2021.

2021 was the second whole year what we spent as the member of Eötvös Lorand Research Network (ELKH). The network administration set up a system which provided financial support to member institution not only to cover the running cost, but also a part of the budget was distributed based on the qualification of the staff, based on the publication and citation records. The whole Centre for Energy Research and MFA as one of its member institutions gained increased support via that system. I used to say to my colleagues already science became a production income. Than MFA could announce a publication award and the best ten papers were awarded by cash prize in order to encourage colleagues for publication in high impact factor journals.

The COVID_19 pandemic caused still a lot of turbulence in the life of our institute. That also had a delay effect for the scientific qualification of my colleagues. There was no one defending the Doctor of Academy title, and we had only one successful PhD process, therefore I congratulate our youngest postdoc Tamás Kolonits and his supervisor Dr. Zsolt Czigány. As we learned how to live together with the low level of pandemic I expect more qualification process in 2022.

Unfortunately, we also lost our former colleague Dr. Csaba Daróczi – who organized the MFA summer schools for years - due to COVID. Moreover 2021 was a sad year for us with a lot of losses. Our former colleague Ferenc Glázer died and we lost our emeritus colleagues, namely Dr. Péter Varga, Dr. Gábor Pető, Dr. Árpád Barna and Professor József Gyulai. In order to tribute to Árpád Barna a Hungarian firm Technoorg-Linda founded an Árpád Barna Prize, the winner(s) will be selected by a committee in which members of our institution (via the Hungarian Society for Microscopy) will work as well. József Gyulai was our former institute director, ordinary member of the Hungarian Academy of Sciences, former president of the Technical section, the loss is very painful for us. We plan to set up a relief at the gate of our main building in which he did work.

I congratulate to my colleagues Dr. György Szabó who was awarded by the Széchenyi Prize for his excellent achievements in the field of statistical physics and game theory. Beatrix Péter won the Róbert Bárány prize from ELKH, Viktória Kis closed her Bolyai Fellowship period with a Bolyai medal. Katalin Balázsi was elected for ECerS (European Ceramic Society) Fellow. Péter Nemes-Incze got the Physics prize from the Physics Section of the Hungarian Academy of Sciences. Our Attila Szolnoki received already third time the Highly Cited Researcher title from Clarivate. What we could expect (see the forward of the previous yearbook) Professor Péter Barna was elected IUVSTA (International Union for Vacuum Science Technology Applications) Honorary President.

The microscopy laboratory of MFA with its aberration corrected THEMIS 200 F got the excellent research infrastructure title and now it is listed among the top50 research infrastructures of the country.

We are also proud of the scientific results achieved by our colleagues, I hope you will enjoy learning them in this book. Here I note that the former MFA Yearbooks are available electronically at http://www.mfa.kfki.hu/hu/yearbook.

Prof. Béla Pécz, D.Sc., Director

Organizational structure

Director: Prof. Béla Pécz, D.Sc.

Scientific departments	
Thin Film Physics Department	Katalin BALÁZSI, Ph.D.
Complex Systems Department	Géza ÓDOR, D.Sc.
Photonics Department	Péter PETRIK, D.Sc.
"Lendület" group - NanoBioSensorics	Róbert HORVÁTH, Ph.D.
Microsystems Department	Péter FÜRJES, Ph.D.
Nanosensorics Laboratory	János VOLK, Ph.D.
Nanostructures Department and "Lendület" group - 2D Materials	Levente TAPASZTÓ, Ph.D.
"Lendület" group - Topological Nanostructures	Péter NEMES-INCZE, Ph.D.

Directly supervised functions	
Head of Scientific Advisory Council	Levente TAPASZTÓ, Ph.D.
Scientific secretary, projects and PR	Krisztina SZAKOLCZAI, Ph.D.
Quality control, patents, MTMT, REAL admin	Andrea BOLGÁR
Technical support	Károly BODNÁR
Financial administration	Zsuzsanna KELEMEN
Informatics	Gergely TAMÁS
Technology transfer (IPR)	Antal GASPARICS, Ph.D.

Key Financial Figures of MFA

The domestic subsidies changed in 2020, not long after the centre left the MTA network and became part of the Loránd Eötvös Research Network (ELKH). It has been adjusted partly to the number and salary of the researchers as well as excellence and output of the centre. The overhead of the institute is still around 35-40% of the annual budget. It means strong financial dependence on the amount of income the research grants could provide. The number of researchers together with the research supporting staff dropped from ca. 140 to 100 in the last 10-12 years. Due to the correction of the subsidy, the researchers received an average 30% salary correction in 2021. The fluctuation is although still high especially under age 35, because the industry promises double payment.

The institute and its administration handles over 40 grants and 20 other R&D contracts each year. A bit less than half of the project are fundamental research grants, rest implements industrial and application driven ideas. Despite all the efforts of colleagues R&D grants require stable strong and research motivated SMEs, which is hard to find in Hungary. The large domestic projects (VEKOP) and also the H2020 grants mainly ran out in 2021, but fortunately three new and large grants (TKP2021) will start from the first months of 2022, which provides some sort of stability for the upcoming 3 years.

Since 2015 MFA is part of the Centre of Energy Research, and the financial operation became partly transparent, therefore the data shown here for 2015-2021 for MFA are based upon our own estimates.

MFA budget 2003-2021 (million HUF)

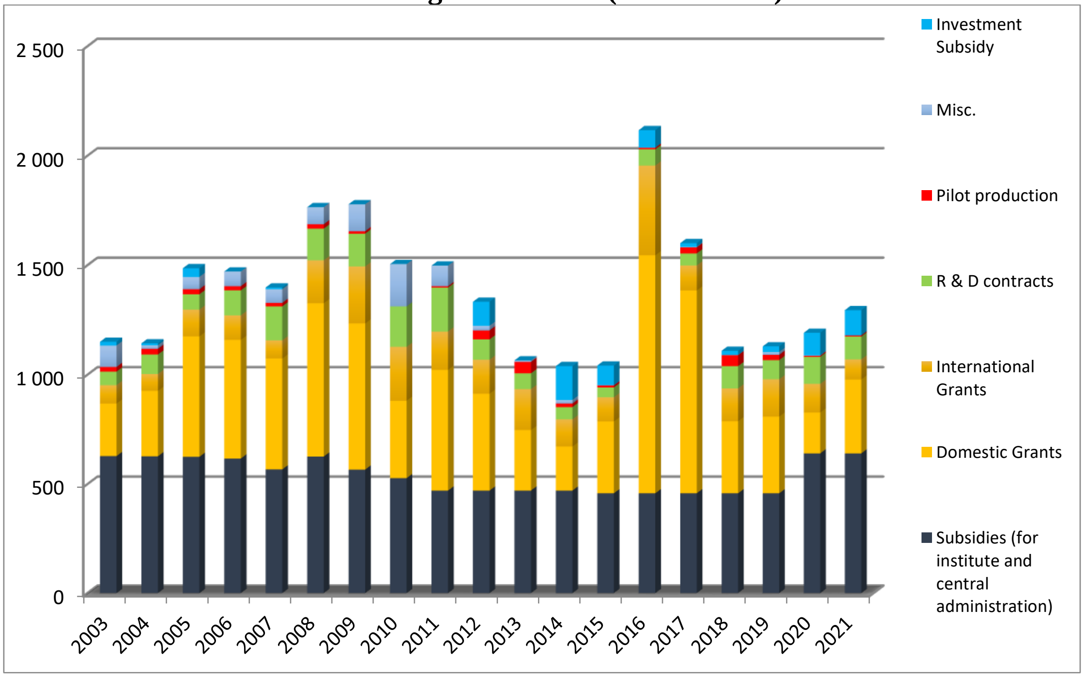

MFA 2003-2021 restoration and investment spendings (million HUF)

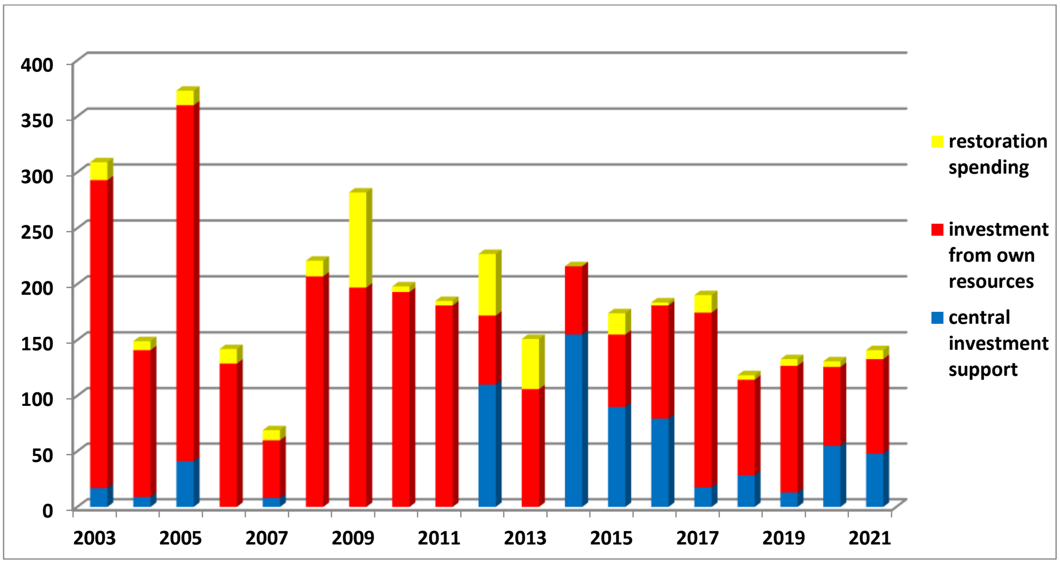

Publications and Citations of MFA

According to the Thomson-Reuters ISI "Web of Knowledge", and MTMT2 databases, the Institute has an average publication activity of ca. 100 scientific papers in IF journals a year. The number decreased a bit in the last years, but recently MFA researchers publich in journals with higher impact factor.

MFA and its predecessor's publications per year

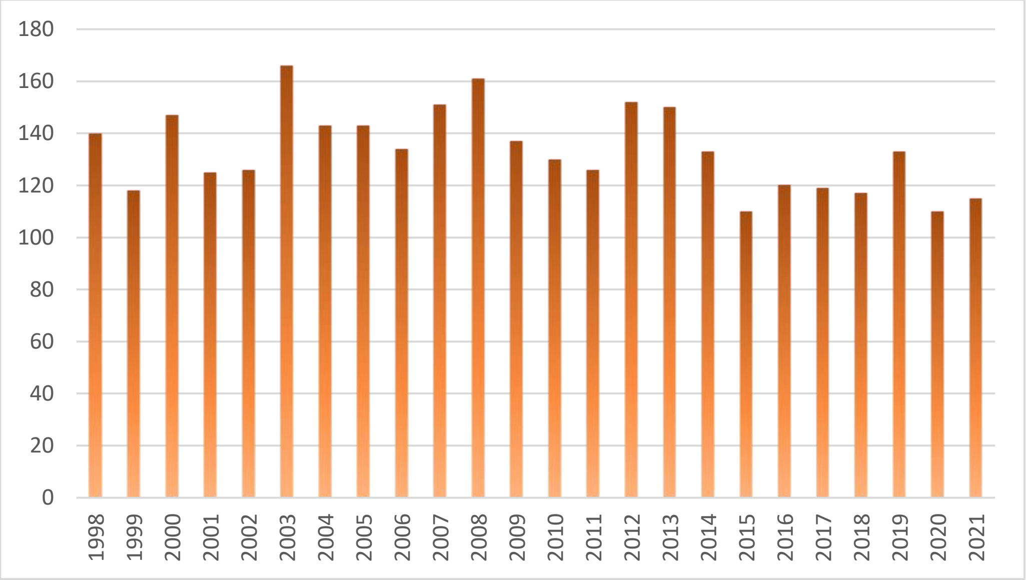

MFA and its predecessor's independent citations number per year

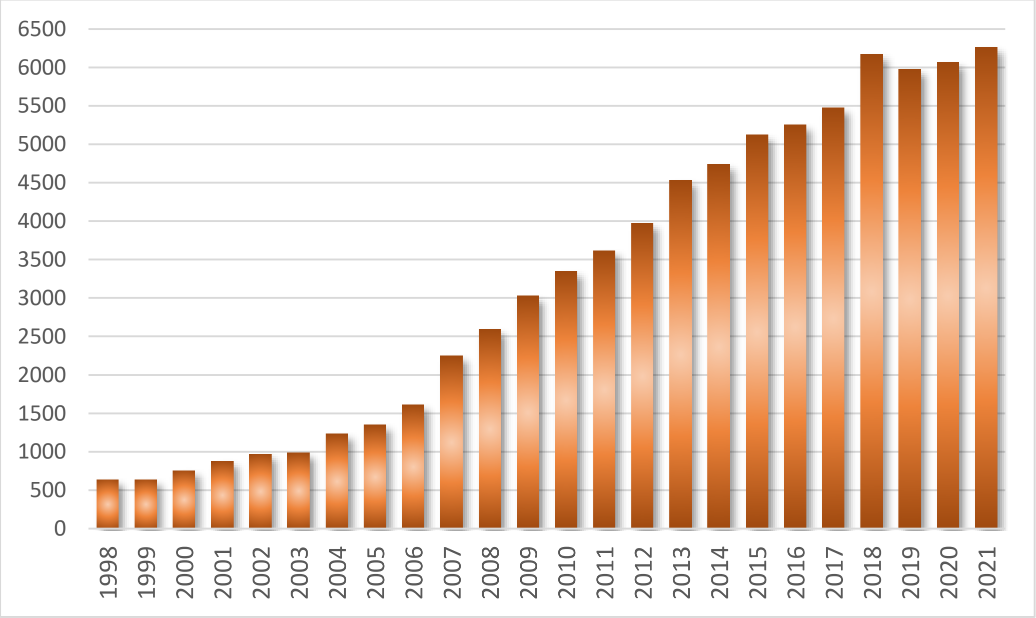

Prizes and Distinctions

	**SZABÓ, György**	Széchenyi Prize
	**BARNA, B. Péter**	Honorary president of the International Union for Vacuum Science, Technique and Applications (IUVSTA)
	**KOVÁCS, Kis Viktória**	Bolyai plaque (MTA)
	**Péter, NEMES-INCZE**	Physics Price (MTA)
	**BALÁZSI, Katalin**	Acta Materialia, Mary Fortune Global Diversity Medal American Ceramic Society, Global Ambassador European Ceramic Society, fellow
	**SZOLNOKI, Attila**	CLARIVATE Highly Cited Top 1% researcher
	**PÉTER, Beatrix**	MBFT young researcher award
	**BALÁZSI, Csaba**	Vebleo, Fellow American Ceramic Society, Fellow

	**PÓSA, László**	MFA Postdoctoral prize
	**DOBRIK, Gergely**	MFA Postdoctoral prize
	**TUNYOGI, Erika**	MFA prize for excellent research support
	SZEKRÉNYES, Dániel	MFA young researcher prize

Dr. György Szabó receives the highly prestigious Széchenyi prize from Dr. János Áder President of Hungary, Dr. Viktor Orbán Prime minister of Hungary and Dr. László Kövér speaker of the National Assembly of Hungary.

Dr. Viktoria Kovacs Kis receives Bolyai plaque at MTA from Prof. Tamás Fraund president of the Hungarian Academy of Sciences and Prof. Tivadar Tulassay regular member of HAS Chairman of Bolyai board.

SCIENTIFIC REPORTS

1 - Nanostructures Laboratory

Head: Dr. Levente TAPASZTÓ, Ph.D., research fellow

Research Staff:

- Zsolt Endre HORVÁTH, D.Sc., Deputy Head of Laboratory
- Prof. László Péter BIRÓ, Member of the HAS
- József GYULAI, Member of the HAS
- (┼ 2021.02.12)
- Gergely DOBRIK, Ph.D.
- Krisztián KERTÉSZ, Ph.D.
- Antal Adolf KOÓS, Ph.D.
- Géza István MÁRK, Ph.D.
- Péter NEMES-INCZE, Ph.D.
- Zoltán OSVÁTH, Ph.D.
- Gábor PISZTER, Ph.D.
- Péter SÜLE, Ph.D.
- Péter VANCSÓ, Ph.D.

Ph.D. students:

- Péter KUN, Ph.D. student
- András PÁLINKÁS, Ph.D. student
- János PETŐ, Ph.D. student
- Márton SZENDRŐ, Ph.D. student

The research activity of the Nanostructures Laboratory is based on the two-decade-long expertise in the synthesis, characterization and engineering of various nanostructures using scanning probe microscopy as the main experimental technique. Since more than a decade, our research efforts are focused on the investigation of two-dimensional materials. Besides graphene, in the last couple of years, novel 2D materials, mainly form the family of transition metal chalcogenides (TMC) have been intensely studied. Recently, we have further extended our activity with the investigation of layered topological insulator crystals. We have also successfully continued our research on bioinspired photonic nanoarchitectures.

The composition and structure of the ubiquitous hydrocarbon contamination on van der Waals materials

Lendület LP2017-9, Élvonal OTKA KKP138144, H2020-SGA-FET-GRAPHENE-2019-881603 Graphene Flagship Core3, OTKA K134258

A. Pálinkás, Gy. Kálvin, K. Kandrai, G. Németh (Wigner FKI), Á. Pekker (Wigner FKI),
M. Németh (EK EKBI), P. Petrik, L. Tapasztó, P. Nemes-Incze

Layered (van der Waals) materials have gained special interest in the last decade because many of them can be exfoliated down to single unit cell thickness. As the thickness decreases, surface effects become more pronounced; hence, both environmental adsorbates and substrates can substantially influence their properties.

Here we show that a self-organized monolayer of molecules adsorbed from the environment often forms on the surface of van der Waals materials exposed to ambient air for several hours. The molecules self-organize into parallel stripes with 5 +/- 1 nm periodicity on several distinct vdW material surfaces (graphite, hBN, MoS_2). The presence of molecules self-assembled into stripes has previously been identified by AFM measurements through the observation of distinct friction domains. However, the molecules forming such stripes have not been identified, since their atomic structure could not be resolved by AFM (contact or tapping mode). We were able to resolve the atomic structure of the molecules forming the self-assembled layer by low-temperature STM measurements on graphite, revealing the inner structure of the stripes: their arrangement, precise length and the atomic periodicity of the individual molecules.

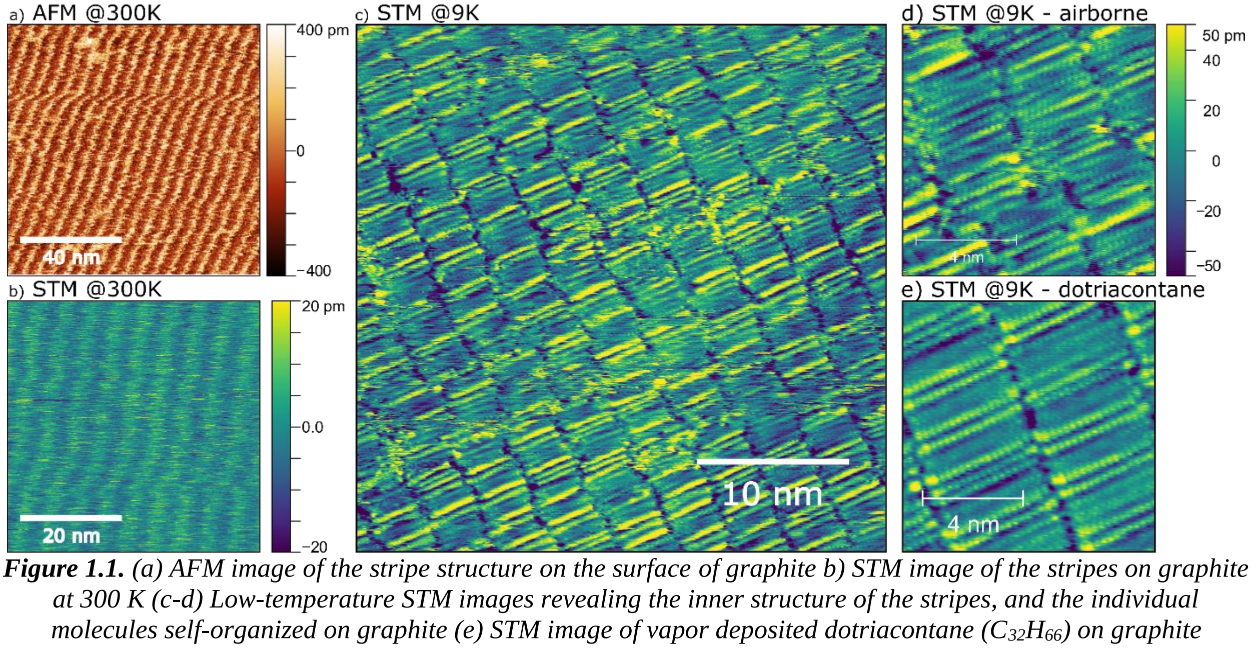

Figure 1.1. *(a) AFM image of the stripe structure on the surface of graphite b) STM image of the stripes on graphite at 300 K (c-d) Low-temperature STM images revealing the inner structure of the stripes, and the individual molecules self-organized on graphite (e) STM image of vapor deposited dotriacontane ($C_{32}H_{66}$) on graphite revealing rectangular-centered structure.*

The low-temperature topographic STM measurements revealed that the self-assembled monolayer adsorbed from the air consists of long-chain molecules of 20-24 atoms. Such molecules are self-organized into an incommensurate orthorhombic structure. In STM images no signs of any additional functional groups (e.g., -OH, -COOH, -O-, -SH,), have been observed. To further investigate this, we have performed grazing-angle IR-spectroscopy and XPS-measurements, in collaboration. Such measurements did not reveal any signature of functional groups, the obtained spectra were fully consistent with that of the alkyl backbone. From these findings, we can conclude that the airborne monolayer consists of mid-length (20-24 carbon atoms), saturated, linear hydrocarbons, most likely simple alkanes. To support this, we have also performed low temperature STM measurements on vapor-deposited dotriacontane ($C_{32}H_{66}$) on graphite (Fig. 1.1.e) and found a close similarity with the structure of the monolayer formed during ambient exposure, except for the larger chain length in the $C_{32}H_{66}$ case.

The self-organized monolayer of molecules can be accountable for the domain-like friction anisotropy observed on various surfaces. Fig. 1.2.a shows an AFM topography map on a graphene (on h-BN), where three domains of different molecule stripe orientation can be recognized, matching the armchair direction of the underlying graphene lattice. The lateral force signal (Fig. 1.2.b) on the same area reveal three distinct friction domains. We showed that not only airborne monolayer of molecules on vdW-materials, but a vapor-deposited monolayer of dotriacontane ($C_{32}H_{66}$) on HOPG can show similar friction anisotropy.

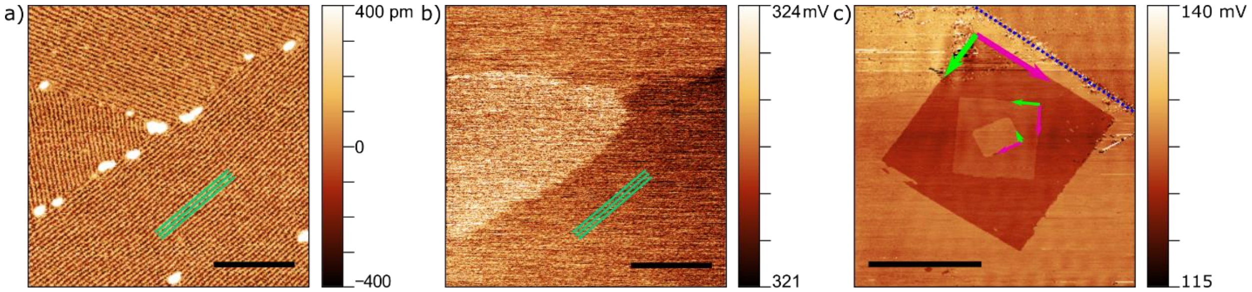

Figure 1.2. *(a) PeakForce AFM topography map on graphene/hBN shows three distinct domains of stripe orientations. (b) Three distinct friction domains on the same area we measured by contact AFM. (c) The friction force map on a thick hBN crystal after the molecules reorganized by the scanning AFM tip. The fast scan direction (pink arrow) rotated by 60° respect to a zigzag crystal edge (blue dotted line) for the successive "drawing" steps.*

STM measurements indicate that the molecules lie parallel to the zigzag axis of the substrate. We found that the local orientation of the molecular layer can be on purpose switched between the three distinct zigzag directions through repeated scans along the desired direction (mechanical interaction) in contact mode AFM. As a demonstration, we defined three distinct friction domains by three successive rectangular AFM scans (edge length: 15, 7, 3.5 μm) reorienting the molecular arrangement and thus the friction domain structure (Fig. 1.2.c).

The ubiquitous hydrocarbon chains observed here play a role in the surface chemistry, adsorption, wetting etc. characteristics of 2D materials. Furthermore, the robust and complete saturation of the basal plane, from extremely low concentrations in air might open new routes for designing filters for long chain alkanes.

Directly imaging visible-frequency graphene plasmons by SNOM in nanocorrugated graphene sheets

Élvonal OTKA KKP138144, 680263-NanoFab2D-ERC-2015-STG, H2020-SGA-FET-GRAPHENE-2019-881603 Graphene Flagship Core3, Lendület LP2017-9, OTKA K132869

G. Dobrik, P. Nemes-Incze, P. Süle, Péter Vancsó, Gábor Piszter, Luc Henrard (Univ. Namur), Levente Tapasztó

We have shown that engineering strong nanoscale corrugations into the atomic structure of graphene, enables the edge-free lateral confinement of graphene plasmons into sub-5nm corrugations, scaling up their resonance frequency from native THz, into the commercially relevant visible range. Visible-frequency graphene plasmons, facilitate orders of magnitude stronger Raman enhancements than previously achieved with graphene, allowing the detection of molecules well below part per trillion level sensitivity, and high selectivity. SERS substrates based on nanocorrugated graphene offer a series of practical advantages over conventional nanoparticle films, such as simpler and cheaper fabrication, better reproducibility, and highly improved environmental stability, up to several months.

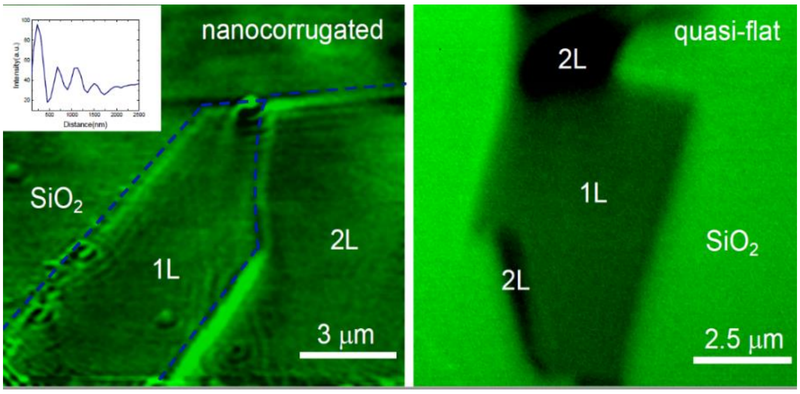

Figure 1.3. *a) SNOM image (λ= 488nm) of nanocorrugated graphene revealing clear interference maxima and oscillations in the proximity of edges (marked by dashed lines) and defects. Inset shows a line cut perpendicular to the graphene edge. b) SNOM image of quasi-flat graphene recorded under the same conditions, showing no interference patterns.*

Given its significance and the wide range of potential applications, exploring and understanding the detailed properties of visible graphene plasmons is of paramount importance. The most important step in this direction is directly confirming their presence in nanocorrugated graphene. Graphene plasmons in the IR frequency range have previously been detected by Scanning Near-field Optical Microscopy (SNOM), through imaging the interference patterns of the plasmons launched from the apex of a metallic AFM tip with the propagating graphene plasmons reflected from graphene edges and structural defects of the graphene sheet. However, such a technique can only detect propagating plasmon modes, why in our system we were primarily expecting visible plasmons localized into the nanocorrugations.

Our SNOM measurements reveal clear interference maxima in the proximity of edges, as well as fainter ~ 400 nm oscillations inward from edges and defects (Fig. 1.3). The observed patterns are highly similar to the SNOM images of plasmon interference patterns on doped quasi-flat graphene at IR frequencies. However, in our case the interference patterns are observed at visible frequencies in nanocorrugated graphene, while quasi-flat graphene samples imaged under the very same conditions show no signs of plasmon interference (Fig. 1.3.b). Detecting interference patterns, clearly indicates the presence of propagating visible plasmons in nanocorrugated graphene. This is a surprising finding, since localized plasmons were primarily expected. However, localized and propagating plasmons are not mutually exclusive. It has been theoretically predicted and experimentally confirmed that when separated nanostructures, hosting localized plasmons, are located in the close vicinity of each other (< □$_{exc.}$), their interaction can give rise to propagating plasmon modes. In nanocorrugated graphene the corrugations are typically located at least an order of magnitude closer than the excitation wavelength, enabling the interaction of localized plasmons to give rise to propagating modes, observed in our SNOM measurements. Furthermore, in such systems, the dispersion of transversal propagating modes crosses the light line, enabling the existence of plasmon wavelengths larger than the excitation wavelength. This can account for the oscillations of about 400 nm observed in SNOM images.

We have also performed confocal microscopy measurements with the same excitation wavelength. Fig. 1.4 shows the comparison of the same nanocorrugated graphene flake imaged by AFM, Confocal Microscopy and SNOM.

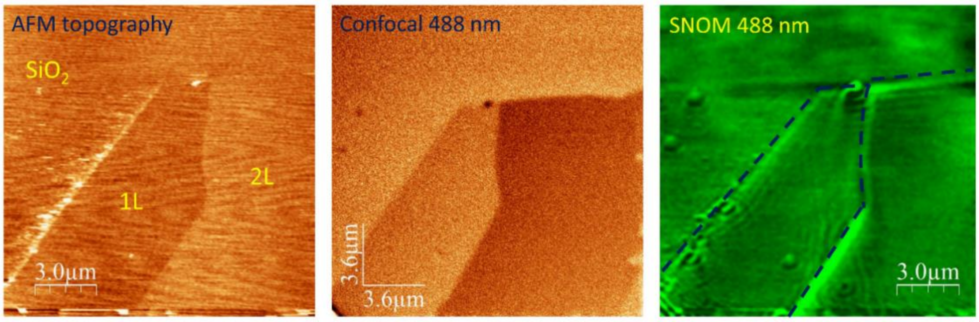

Figure 1.4. *AFM, confocal (λ_{ex}= 488 nm) and SNOM (λ_{ex} = 488 nm) images of the same nanocorrugated graphene sample.*

In contrast to SNOM images, confocal images show no interference patterns on nanocorrugated samples, while using the same excitation laser in both cases. The reason for this is the difficulty of coupling in light into the graphene (to excite the plasmons). While in the case of the evanescent modes of the SNOM tip, this coupling is possible, in the case of far-field propagating light modes the momentum out-of-plane vs. in-plane momentum mismatch preclude the coupling of light into the graphene, and hence the excitation of graphene plasmons. The results have been published in Nature Nanotechnology.

Unfolding the topological phase diagram of $ZrTe_5$ using bubble

Lendület LP2017-9/2017, H2020-SGA-FET-GRAPHENE-2019-881603 Graphene Flagship Core3

Z. Tajkov, D. Nagy (ELTE), K. Kandrai, L. Oroszlány (ELTE), J. Koltai (ELTE),
Zs.E. Horváth, P. Vancsó, L. Tapasztó, P.Nemes-Incze

The paradigm of topological phases has permeated much of contemporary condensed matter physics [Ref. 1.1]. This fundamentally new way of classifying systems according to global topological properties rather than a local order parameter yielded a deeper understanding of a host of peculiarly robust phenomena. At the heart of these phenomena lies bulk-boundary correspondence, which guarantees robust states localized at the perimeter of the topological materials.

Three-dimensional time reversal symmetric topological band insulators are classified into “strong” (STI) and “weak” (WTI) according to the nature of their surface states. The surface states of the STI are topologically protected from localization, while this does not hold for the WTI [Ref. 1.2]. These phases are separated by a metallic, conducting Dirac or Weyl semimetal phase. To change the indices, it is necessary to close and reopen the bandgap through of the metallic phases.

Among the transition-metal pentatellurides, $ZrTe_5$ is an excellent material to investigate the topological phase transitions. This material has been widely studied because it has numerous exotic and therefore interesting physical properties. In the literature of this peculiar crystal, it is well-known that the topological nature of the bulk $ZrTe_5$ has not been unambiguously identified [Ref. 1.3]. In our contribution we aimed to investigate the characteristics of the crystal using state-of-the-art experimental STM techniques and computer modeling on a sample of bulk $ZrTe_5$ that hosts bubble on the substrate. The unique strain pattern of the bubble makes possible the tuning of the originally strong topological insulating phase of the crystal into a metallic phase at the perimeter of the bubble. This transition can be observed using STM measurements (see Fig 1.5.b). The halo of the bubble of this highly anisotropic material only presents at one side of the bubble, where the crystallographic orientation matches the Te-Te chains direction. In the perpendicular direction there is no observable phase transition.

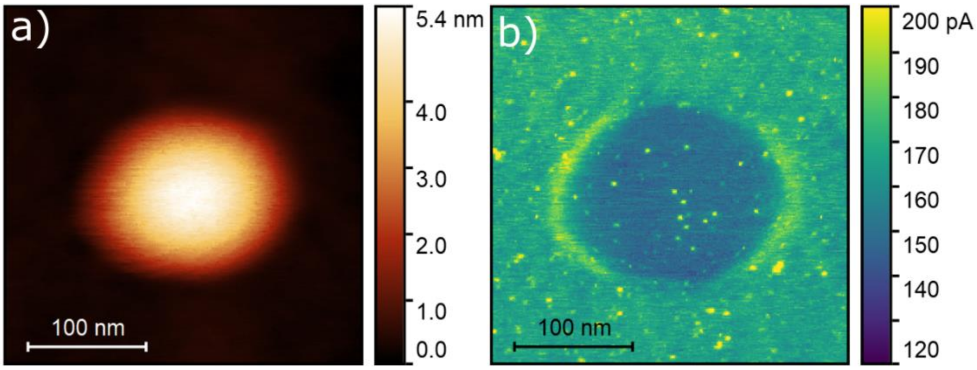

***Figure 1.5**. **a)** STS topography image of the bubble. **b)** STM measurements of the same area.*
The perimeter of the bubble is a high density of states area, indicating a metallic phase.
The halo shows a dependency of direction.

To understand this behavior, we first must establish a proper description of the elasticity tensor of the material. For this reason, we determined the elasticity tensor elements using density functional theory (DFT) calculations, as the free energy obtained from DFT of a mechanically distorted crystal is a function of the strain pattern of the distortion. This method gave us the total elasticity tensor of the material. Using the data, by numerically solving the three-dimensional equation of motion by the finite element method (FEM), implemented in the COMSOL package, we were able to determine the strain pattern of the bubble. This procedure has allowed us to explain the observed features without the necessity of any phenomenological-based semiphysical, or fitting parameters.

We obtained the electronic properties by DFT of a distorted crystal using the strain pattern that we determined from the FEM method at the two semi-axes of the bubble. The *ab initio* results are in excellent agreement with the measurements. At the major semi-axes point DFT predicts that the band gap is closed, hence the density of states increases. On the contrary at the vicinity of the minor semi-axes the *ab initio* analysis shows a small topologically strong band gap, therefore the density of states remains low.

Establishing the equilibrium state of the crystal we can map the topological phase diagram of the crystal using *ab intio* methods. Fig 1.6. shows the contour map of the size of the bandgap under different mechanical strain. The horizontal (vertical) axes indicate the strain (in %) along the in plane (van der Waals) lattice directions obtained by DFT. At every point a sign has been assigned to the gap as the topological invariants were calculated. Positive (negative) sign indicates weak topological (strong topological) insulating phase. The phase diagram shows three main domains. Around the equilibrium the system is a STI (1), and it can be tuned to the WTI phase (3). Between the two insulating phases there is a moderate conducting phase (2). The black tentative line in the conducting phase shows where the Dirac cones in the gamma point touch each other.

This procedure was also tested with a fundamentally different DFT code and the outcome was found to be in perfect agreement with the previous results. Our results will help to clear out some of the controversies about the material and provides a full, experimentally tested, and precise elasticity tensor.

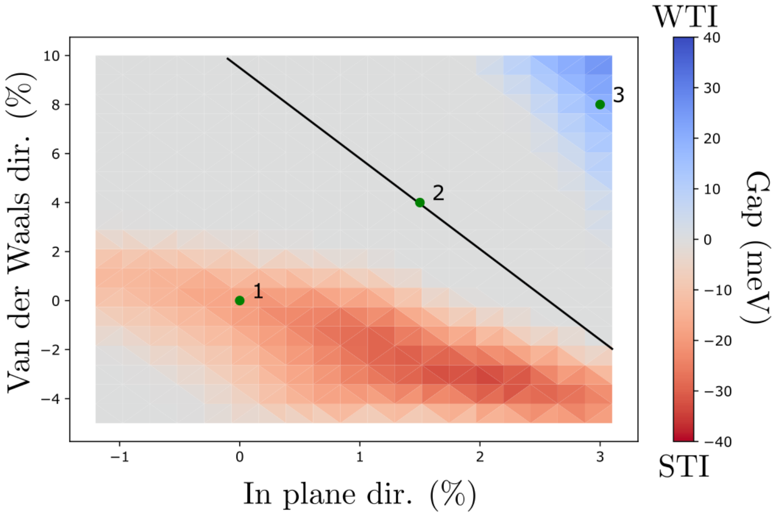

Figure 1.6. *The phase diagram of the electronic structure of the crystal under mechanical strain. The three main domains are marked by numbers. (1) is STI, (2) is metallic and the black tentative line indicates that the Dirac cones touch each other at the gamma point and (3) is WTI.*

Tuning the nanoscale rippling of graphene with PEGylated gold nanoparticles and ion irradiation

OTKA K119532, OTKA FK128327, OTKA K134258

Z. Osváth, D. Zámbó, A. Sulyok, A. Pálinkás, A. Deák

Ripples and wrinkles can highly affect the electronic and optical properties of graphene. The spatially varying strain associated with nanoscale ripples can tune the band structure of graphene through strain-induced pseudo gauge fields. Nanoscale corrugations can also enhance the chemical activity and functionalization of graphene. The controlled realization of nanoscale ripples in graphene has been of high interest in the last decade. However, inducing periodic nanoscale rippling in two dimensions and large areas is still challenging. In this work we present a new method combining gold nanoparticles, strain engineering and ion irradiation for the realization of periodically rippled graphene. The effect of irradiation on the graphene cover layer was revealed by scanning tunneling microscopy (STM), tunneling spectroscopy (STS), and Raman spectroscopy.

Gold nanoparticles of 16 nm in diameter were synthesized by seed-mediated, wet-chemical approach, and thiol-terminated polyethylene glycol (mPEG-SH) molecules were grafted onto their surface. High-density monolayers of the PEGylated gold nanoparticles were successfully prepared on Si substrates by the Langmuir-Blodgett technique. Achieving fully ordered state of such small nanoparticles is difficult, nanoparticle voids frequently occur on large scale. These voids appear as dark-contrasted areas on both scanning electron microscopy (SEM) and atomic force microscopy (AFM) images (Fig. 1.7). The gold nanoparticles were closely spaced in ordered clusters with an average interparticle distance of 18 nm.

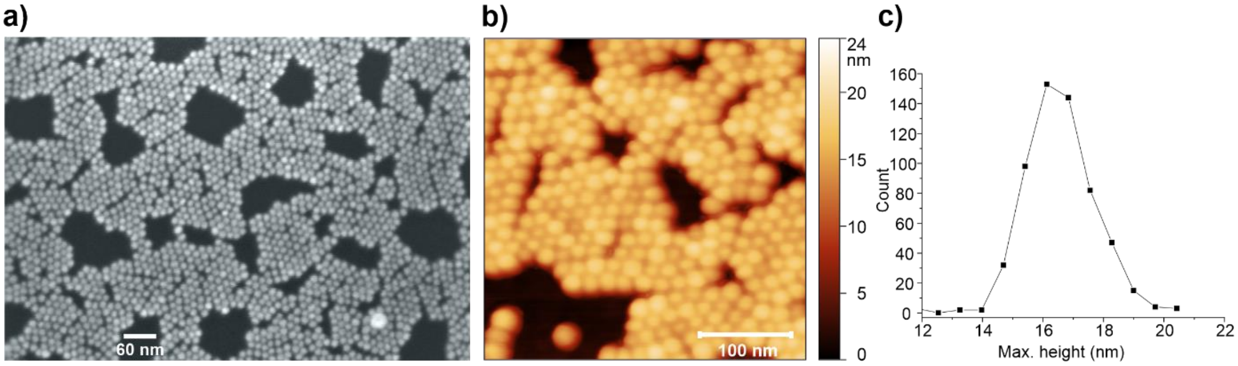

Figure 1.7. *SEM (a) and AFM (b) images of the prepared gold nanoparticle monolayer. The height distribution of 589 nanoparticles measured by AFM is shown in c).*

Graphene grown by chemical vapour deposition was transferred onto the nanoparticle monolayer. In order to fine-tune the nanoscale rippling of graphene, point defects were introduced by Ar^+ ion beam of 1 keV, with fluence of $\approx 10^{12}$ ions/cm^2, achieved by 20 sec irradiation. The structure of graphene transferred onto the PEGylated gold nanoparticle monolayer can be observed in Fig. 1.8.a, which shows the STM image of a completely graphene-covered area. The top of nanoparticles (closely spaced brighter spots), as well as nanoparticle voids (dark-contrasted regions) are both observed through the graphene layer. STM investigations performed after irradiation revealed that the rippling of graphene changed significantly (Fig. 1.8.b).

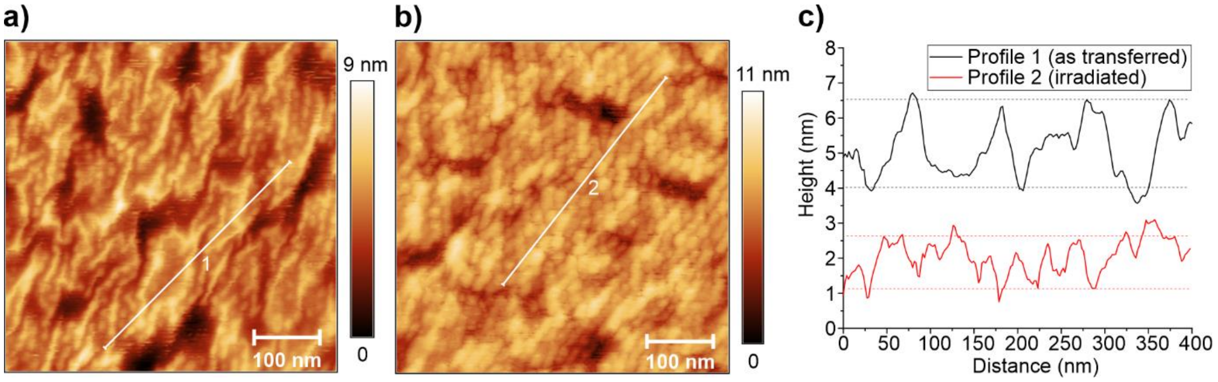

Figure 1.8. *(a) STM image of graphene as transferred onto the gold nanoparticle monolayer. (b) STM image of graphene supported by nanoparticle monolayer, after ion irradiation. (c) The height profiles corresponding to line section 1 in a) (black line) and line section 2 in b) (red line). Horizontal dotted lines are guides for the eye denoting typical rippling amplitudes. Tunneling parameters: U = 0.5 V, I = 0.5 nA.*

Elongated ripples disappeared, and the typical amplitude of out-of-plane deformations decreased from 2.5 nm to 1.5 nm (Fig. 1.8.c). A rippling wavelength of around 30 nm can also be identified (Fig. 1.8.c, height profile no. 2). Although this period is larger than the one of the underlying Au NPs, it can be considered as a regular, periodic deformation, characterizing the entire irradiated graphene.

Atomic resolution STM measurements revealed hillock-like protrusions, associated with the irradiation-induced point defects, as shown in Figs. 1.9.a and 1.9.b (height profile no. 2). As a comparison, the atomic lattice of intact graphene is also resolved (height profile no. 1).

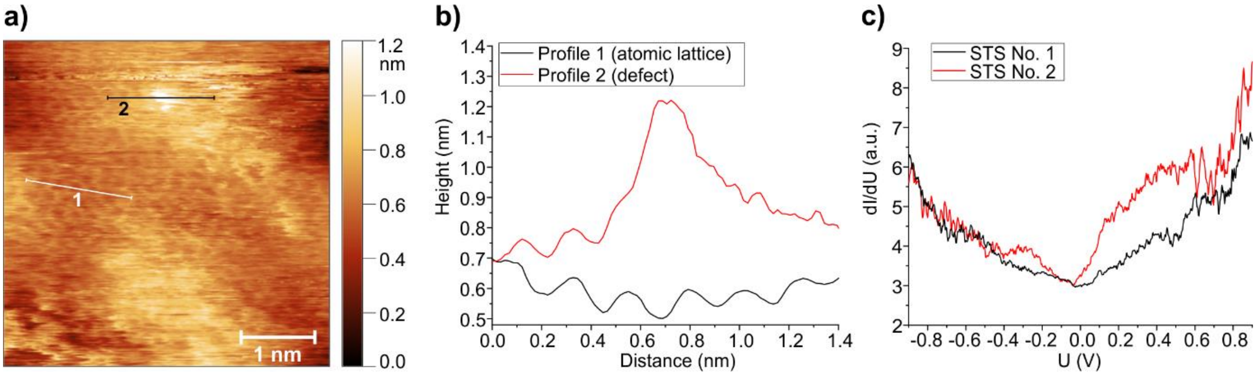

Figure 1.9. *(a) High resolution STM image of the irradiated graphene shown in Fig. 2b. The height profiles corresponding to unperturbed atomic lattice (section 1) and irradiation-induced point defect (section 2) are shown in (b). (c) STS spectra measured on intact graphene area (black) as well as on graphene area with irradiation-induced defect (red).*

Local *dI/dU* spectra obtained from STS measurements show increased density of states at a defect site (Fig. 1.9.c, red line) for positive bias voltages (*U*), which is the main cause of hillock formation: an apparent increase of height during constant current STM imaging. The paper was published in Carbon Trends 5, 100080 (2021).

Concordance of the spectral properties of dorsal wing scales with the phylogeographic structure of European male Polyommatus icarus butterflies

G. Piszter, K. Kertész, G. Sramkó, V. Krízsik, Zs. Bálint, L. P. Biró

The wings of butterflies exhibit a richness of colors and patterns unrivalled in the living world. Many of these colors are efficiently used and optimized in sexual communication. These colors may be generated by selective light absorption on pigments, by selective light reflection on photonic nanoarchitectures, or by a combination of the two.

The males of more than 80% of the Lycaenidae species belonging to the tribe Polyommatini exhibit structural coloration on their dorsal wing surfaces. These species-specific colors are produced by the cellular self-assembly of chitin/air nanocomposites. The spectral position of the reflectance maximum of such photonic nanoarchitectures depends on the nanoscale geometric dimensions of the elements building up the nanostructure. Our previous work showed that the coloration of male *Polyommatus icarus* butterflies in the Western and Eastern Palearctic exhibits a characteristic spectral difference. Here, we investigated the coloration and the *de novo* developed DNA microsatellites of 80 *P. icarus* specimens from Europe from four sampling locations, spanning a distance of 1600 km.

The reflectance data for the four dorsal wing surfaces of all male *P. icarus* measured in the present study were used to generate the statistical presentation of the peak wavelength in Fig. 1.10.A. The averaged spectra of the four sampling sites (TZ: Taizé, France; EF: Érd-1, Hungary; EP: Érd-2 Hungary; EB: Baraţcoş, Romania) are shown in Fig. 1.10.B. One may observe from both kinds of representations that the color of the butterflies originating from the four sampling sites show only minor deviations from each other but differs characteristically from the coloration of Asian males investigated previously (Fig. 1C). The excellent concordance of the coloration from Southern France through Hungary to the Carpathian Mountains in Romania is attributed to similar photonic nanoarchitectures being self-assembled individually in each dorsal wing cover scale in all male specimens investigated.

The chitin building up these species-specific photonic nanoarchitectures is deposited in protein-based molds, self-assembled in a process governed by the DNA of the scale producing cell. The observed spectral similarity within Europe and the difference from the Asian samples, which must originate from difference in photonic nanoarchitectures, may be an indication of subtle divergence that can only be traced by fast-evolving DNA regions. As a first step in the investigation of this hypothesis, we investigated microsatellites – also called Single Sequence Repeats (SSRs) – of European male *P. icarus* butterflies. As SSRs are known to have exceptionally high mutation rate, these are good choice for tracing genetic variability of natural populations.

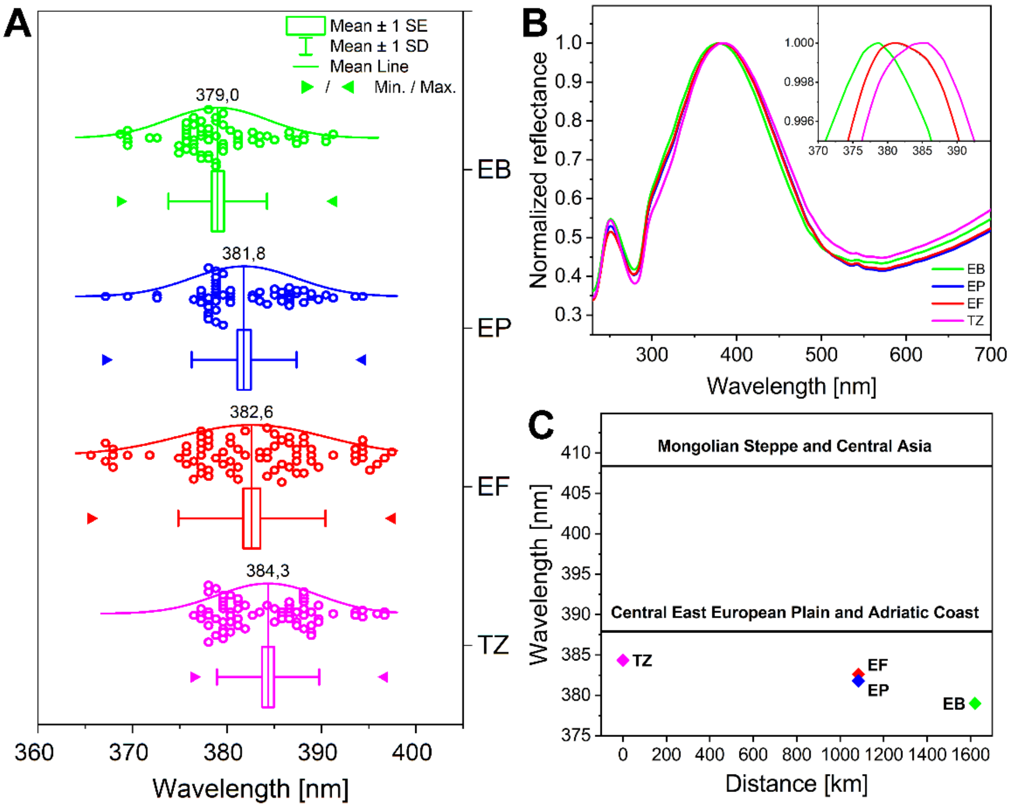

Figure 1.10. *(A) Box plots of the spectral position of the blue reflectance maximum of male P. icarus butterflies. (**B**) Averaged spectra of the specimens from the four sampling sites. (**C**) The colored diamonds show the spectral position of averaged reflectance maxima measured now, while the lines stand for the averages of European and Asian samples investigated previously.*

Altogether, we successfully genotyped 79 individuals of *P. icarus* for ten, *de novo* developed species-specific microsatellite loci from four populations representing three geographically distinct groups (France, Hungary, Romania).

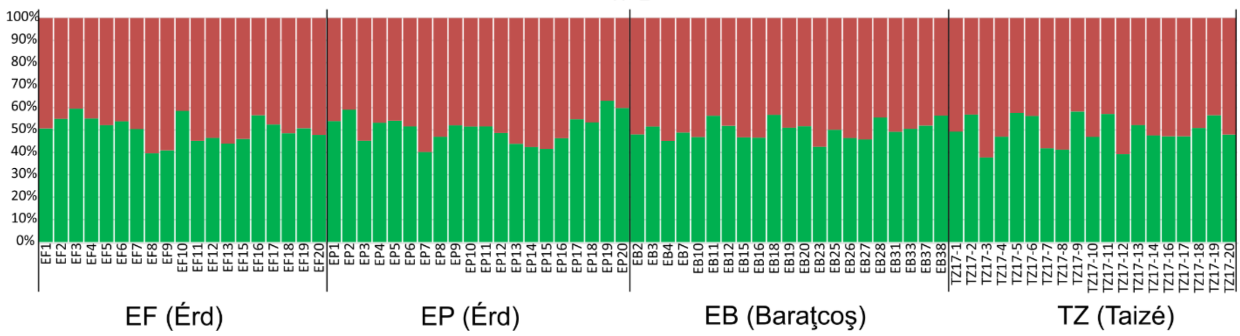

Figure 1.11. *A posteriori assignment of the studied Polyommatus icarus individuals into two genetic clusters that is the most likely number of clusters in our genetic dataset.*

Population genetic differentiation was found to be exceptionally low between the four populations analyzed, as it can be seen (Fig. 1.11), showing remarkably good concordance between the spectral properties of the blue sexual signaling color (coincident within 5 nm in the four sampling sites) and the population genetic structure as revealed by 10 microsatellites for the *P. icarus* species.

Multi-instrumental techniques for evaluating butterfly structural colors: A case study on Polyommatus bellargus

K. Kertész, Zs. Bálint, G. Piszter, Z . E. Horváth, L. P. Biró

Color is an important communication channel for day-flying butterflies. Chemical (pigmentary) coloration is often supplemented by physical color generated by photonic nanostructures. These nanoarchitectures (characteristic for a given species) exhibit wavelength ranges in which light propagation is forbidden. The photonic nanoarchitectures are located in the lumen of the wing scales and are developed individually by each scale during metamorphosis. This self-assembly process is governed by the genes in the nucleus of the scale producing cell. It is crucial to establish well-defined measurement methods for the unambiguous characterization and comparison of colors generated in such a complex manner. Owing to the intricate architecture ordered at multiple levels (from centimeters to tens of nanometers), the precise quantitative determination of butterfly wing coloration is not trivial. We present an overview of several optical spectroscopy measurement methods and illustrated techniques for processing the obtained data, using the species *Polyommatus bellargus* as a test case, the males of which exhibit a variation in their blue structural color that is easily recognizable to the naked eye (Fig. 1.12.A).

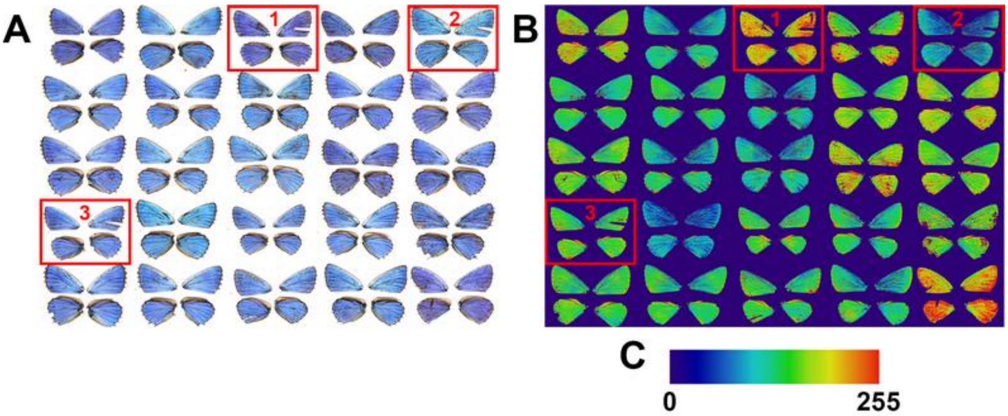

Figure 1.12. *Photographs and image analysis of 25 Polyommatus bellargus specimens. (**A**) Unprocessed photographs of the four detached wings of the specimens showing dorsal wing surfaces acquired under identical conditions. (**B**) False-color image of the hue channel of wings shown in (**A**). (**C**) Color bar showing the colors associated to hue values of 0-255.*

In previous studies, color characterization was often conducted using one or only a small number of measurement methods and sometimes using only just one or several samples. This may have led to important properties and aspects of intraspecific variation being overlooked. Therefore, the use of multiple techniques to determine the structural and spectral properties of complex objects could be very advantageous.

When investigating the light reflected from a butterfly wing, one may frequently face the question of how to accomplish nondestructive analysis, as these samples are often rare or unique in museum collections. A fast and simple approach is to consider the wing as a flat surface. Starting from the nondestructive optical methods ending with fully destructive electron microscopy, we present an overview of the multi-instrumental analysis of male specimens of the butterfly *Polyommatus bellargus* and demonstrate the possibilities of a detailed characterization of biological structural colors. This allows the reader to assess which is the most useful combination of test methods in terms of sample availability, vulnerability, and desired accuracy. In our test species the hue of the blue color varies from violet to turquoise, which can be qualitatively analyzed using the photographs (Fig. 1B) while a more precise differentiation is possible by using various spectroscopy setups. Adding microcopy techniques, the final aim is in the understanding of the relationship between biology and physics via exploring the phenomenon that results from this variation of blue colors and how this color variance is generated on the nanostructure level.

The properties of the different methods in Table 1.1 cover aspects worth to consider before planning optical or structural measurements. Not all methods are necessary, the correct selection is governed by the available time, the sample properties, and the required depth of the analysis. Nondestructive and faster methods often provide less precise results than slower and more labor-intensive, destructive ones. In the case of the presented test species, *P. bellargus*, we found the origin of the wing color differences in the scale nanostructure level which resulted in variation of the blue structural color. This in turn is tentatively associated with the unusually large genetic drift reported for this species in the literature.

Method	**Speed**	**Interpretability**	**Acquisition size**	**Instrument cost**	**Sample preparation**
Photograph analysis	fast	easy	> cm	low	nondestructive
Normal incidence spectral measurement	fast	easy	~ 1 mm	medium	nondestructive
Integrating sphere spectral measurement	slower	easy	6 mm	medium	wing removal, preferably flat sample
Spectrum fitting	slower	mathematical model is needed before application	-	-	-
Hyperspectral measurement	slow	postprocessing is needed	> cm	higher	nondestructive
Spectrogoniometer	slow	postprocessing is needed	~ 5 mm	higher	wing removal
Single scale microspectrometry	slow	easy	< 100 µm	higher	wing scale removal
SEM	slow	easy	< cm	high	destructive
TEM	slow	easy	< 10 µm	high	destructive

Table 1.1 *Overview of the discussed materials science methods for a detailed characterization of biological structural colors.*

2-Photonics Department

Head: Dr. Peter PETRIK, D.Sc., scientific advisor

Research Staff:

- Miklós FRIED, D.Sc., Head of Ellipsometry Laboratory
- András DEÁK, Ph.D., Head of Chemical Nanostructures Laboratory
- Miklós SERÉNYI, D.Sc.
- Gábor VÉRTESY, D.Sc.
- Antal GASPARICS, Ph.D.
- Norbert NAGY, Ph.D.
- Zoltán LÁBADI, Ph.D.
- Ferenc RIESZ, C.Sc.
- Dániel ZÁMBÓ, Ph.D.
- Emil AGÓCS, Ph.D., on leave
- György KÁDÁR, D.Sc., Prof. emeritus
- Tivadar LOHNER, D.Sc., Prof. emeritus
- János MAKAI, C.Sc., retired
- András HÁMORI, dr. univ., retired
- György JUHÁSZ, dr. univ., retired

Students:

- Benjamin KALAS, Ph.D.
- Alekszej ROMANENKO, Ph.D.
- Dániel SZEKRÉNYES, Ph.D.
- Deshabrato Mukherjee, Ph.D.
- Petra Bácsics,
- Áron Fogarasy,
- Dávid Kovács,
- Rita Némedi,
- Máté Szűcs,
- Gergely Südi,
- Dániel Takács

The Photonics Department develops unique methods and tools for non-destructive optical and magnetic measurement of surface nanostructures and materials (spectroscopy; magnetic material testing; biosensors; surface curvature measurement; surface testing; water contamination). One of the most important tasks of the Department is patenting and application of the methods in international projects with partners representing the industry and the high technology.

Key achievements of the Photonics Department in 2021:

- Non-destructive magnetic methods have been developed for the investigation of structural materials in nuclear power plants. A correlation is sought between the sample parameters determined by non-destructive magnetic measurements and the dose of neutron irradiation. An EU project was performed investigating whether the dose-dependent degradation of reactor steel materials can be determined non-destructively and whether the surface roughness can be taken into account. It is extremely important that these tests can be performed on cladded surfaces. The measurements performed can play an important role in the non-destructive testing of the pressure tank of nuclear power plants, which is currently one of the most important tasks in nuclear technology. Their results make it possible in the future to replace the labor-intensive, costly and destructive testing with the magnetic method they have developed.
- A micro-combinatorial mapping method was used for high-resolution composition-dependent optical analysis of materials used in solar cell technology and sensing. A database containing the

composition-dependent optical properties of amorphous compound semiconductors was constructed.
- Surface nanoparticles were generated in a controlled way that can be used in sensing, medicine, and solar cell technology, among others. Using a self-built single-particle spectrometer, we investigated the role of the exchange of molecules inherently present in the surface of gold nanorods (due to the synthesis method) in interactions by examining individual nanoparticles.
- We developed a capillary probe method for high-precision testing of hydrophobic and hydrophilic surfaces. Computational and experimental investigation of hydrophobic surfaces based on previous measurements and in collaboration will be of paramount importance. We investigated the novel possibilities of the method for the determination of solid-liquid adhesion work and surface free energy, partly among certain materials and liquids used in the paper industry.
- We developed an optical sensor structure that shows resonant surface amplification in a controllable way, depending on the properties of the biological materials to be tested. The arrangement typically achieves sensitivities of about 10^{-6} and 10 pg/mm^2 in refractive index and surface material density, respectively.
- Nickel- and arsenic-binding flagellar filaments were used to create sensor surfaces suitable for electrochemical measurements. We optimized the adsorption of the filaments by monitoring optical measurements on the surface of the sensors. Cyclic voltammetry measurements detect contaminants in natural waters and drinking water. We are developing sensor concepts that can be used in the field.
- We developed the method of Makyoh topography into a new direction utilizing the Schlieren layout. In this way, a new aspect of the sample surfaces (e.g., Si swirl defect) is implemented, which complements the traditional method. We make anti-reflective layers for lasers, for industrial orders.

Non-destructive evaluation (NDE) system for the inspection of operation-induced material degradation in nuclear power plants

EU H2020 755330 NOMAD

A. Gasparics, G. Vértesy and I. Borsos

The long-term operation (LTO) of existing nuclear power plants (NPPs) has already been accepted in many countries as a strategic objective to ensure adequate supply of electricity over the coming decades. In order to estimate the remaining useful lifetime of NPP components, LTO requires reliable tools. The objective of NOMAD project is the development, demonstration and validation of a non-destructive evaluation (NDE) tool for the local and volumetric characterization of the embrittlement in operational reactor pressure vessels (RPVs).

In order to address these objectives, developed NDE tools were tested on Charpy geometry samples, which ones represent the material properties, and on cladded material block type specimen which ones emulates the real application. The MFA contributes to the NOMAD project with own micromagnetic testing method: so called Magnetic Adaptive Testing (MAT). MAT is a recently developed method for nondestructive characterization of ferromagnetic materials which is based on systematic measurement and evaluation of minor magnetic hysteresis loops.

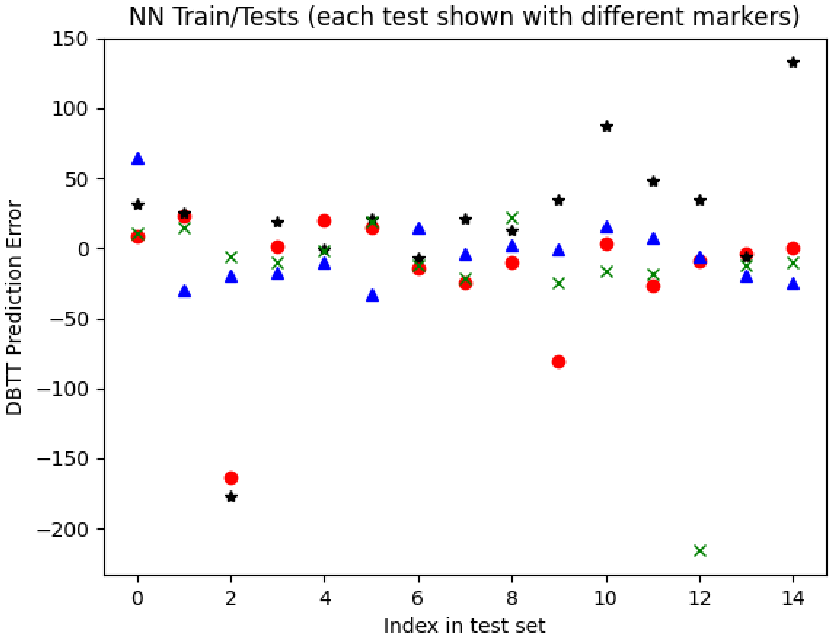

***Figure 2.1**. Example of the Neural Network Regression results on 15 test elements with index of 0…14. The key parameters of the studied structure: 1st Layer width: 128; Depth: 3; Dropout factor: 0.4, Epoch: 10.000*

MAT measurements were performed on reactor steel material before and after neutron irradiation and the nondestructively determined magnetic parameters were compared with the destructively measured ductile-to-brittle transition temperature (DBTT) values and with other available mechanical test results, such as the Upper Shelf Energy, Vicker Hardness and Yield strength were provided by Belgian Nuclear Research Centre (SCK•CEN). Within the framework of the project five different electro-magnetic, electric and acoustic non-destructive measurement techniques were applied on the common specimen set and their results are processed and evaluated individually. A common data-base has been established on the outcomes of the individual non-destructive, as well as, of the destructive test results in order to evaluate the performances of the different NDE methods, but also to be able to recognize their possible synergies.

Our team performed Neural Network (NN) based analysis on the established common data base of all output values of the five different NDE methods are obtained on all specimens were measured in the hot cell campaigns, as well as, previously to the irradiation. The determination of the DBTT was targeted, and the achieve resolution of the combined methods was studied. Also the applicability of the NN system was studied by using different configuration and structures and their results were compared. The results are quite encouraging: the real and successful application demands to be able to distinguish unambiguously 50° of DBTT shift, and the NN could provide better resolution. However, some outlying elements were observed (Fig. 2.1). On one hand, this problem can be related to the extraordinary low number of train set elements, that makes hardly applicable any statistical approach. Nevertheless, these outliers were studied further by a Bagging – Bootstrap aggregation method developed by Leo Breimann (1994), so called 'Ensemble machine learning' technique. Each of the dataset elements was excluded, the NN was trained for the rest in the same predefined way. Than the excluded element was predicted by the NN. The training with randomly selected train sets, and the testing of the excluded element was repeated 20 times (Fig. 2.2.). Following that, the results were averaged. This way, at the very end, all performance of the NN for all elements could be compared (Fig. 2.3.).

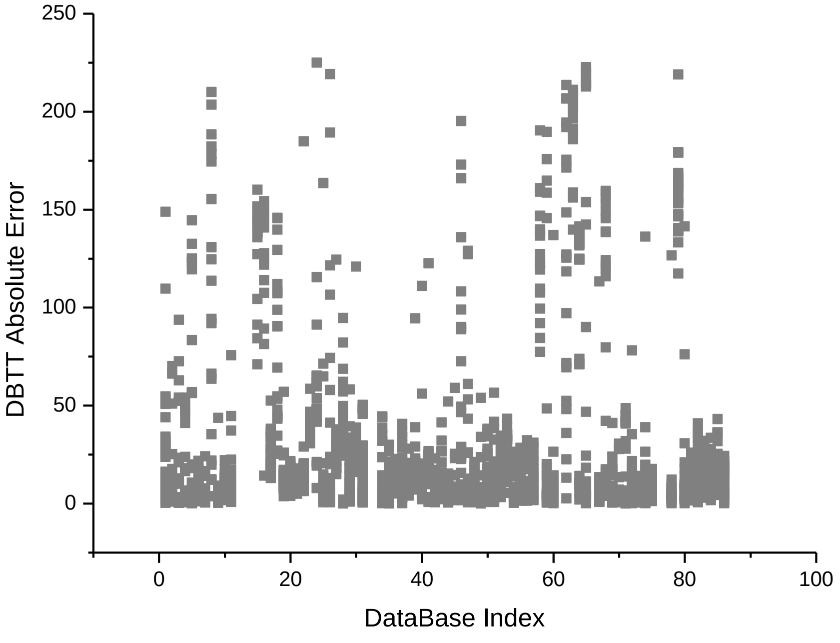

Figure 2.2. *NN performance (in all test runs) in case of each database element*

By excluding the worst 9 elements of the dataset (out of 89) as outliers the error of prediction was improved significantly. Without database reduction, the prediction error was found ~34°C on average. The exclusion reduced this average error below the margin, as: ~22°C.

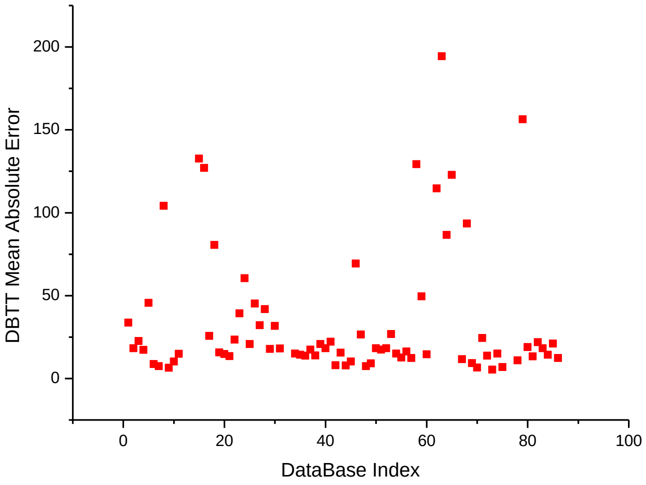

***Figure 2.3**. NN performance (average of errors) in case of each database element*

The possible interpretation of the observed outliers is that the NN technique can be applied for data interpolation only, since it cannot classify those values are outside of the teaching sample range. The outliers represent measurements on the border of the ranges, so by excluding them from the train set, the data range is reduced as well. By excluding these outliers, the NN approach could provide sufficient resolution of the DBTT prediction, i.e. ~22°C that is below the need of the possible application (i.e. 25°C).

The most important NOMAD specimens from application point of view are the irradiated bocks. These were measured in the third hotcell campaing (HCC3) by the MAT method. The Data-analysis of the HCC3 MAT measurements could provide promising outcome for the prediction of the base material degradation that measured though the cladding. Considering the applied neutron fluence values, which were the so called 'independent' parameter of our evaluation, systematic function between the evaluated data and the independent parameter could be found with reasonable errors (Fig. 2.4).

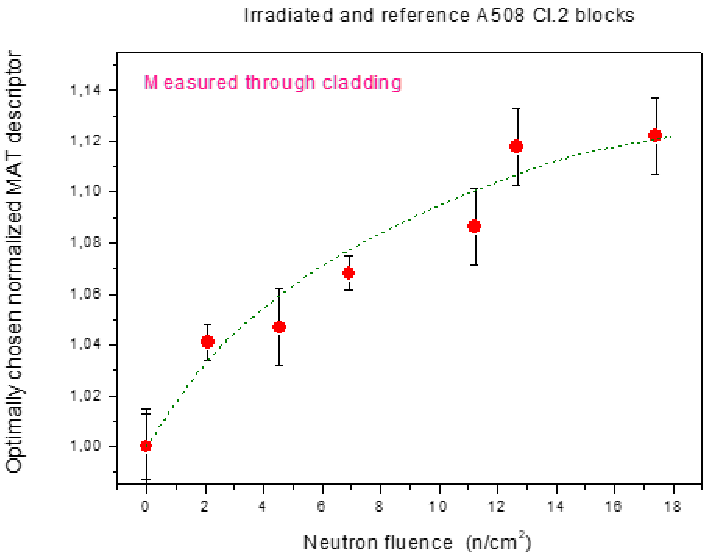

***Figure 2.4**. MAT results obtained on block type specimens through the cladding as a function of the neutron irradiation fluence values*

The importance of this outcome is that there is an application potential of the MAT method for inspecting the nuclear reactor vessel from inside, through the cladding. This has particular importance, since the easiest direction for testing the reacture vessel wall is measure it from insed, i.e. through the cladding on it. We should note, that the very limited sample set does not allow the statistical validation of any method. Also, the inhomogeneity of the tested samples are necessary to study further more.

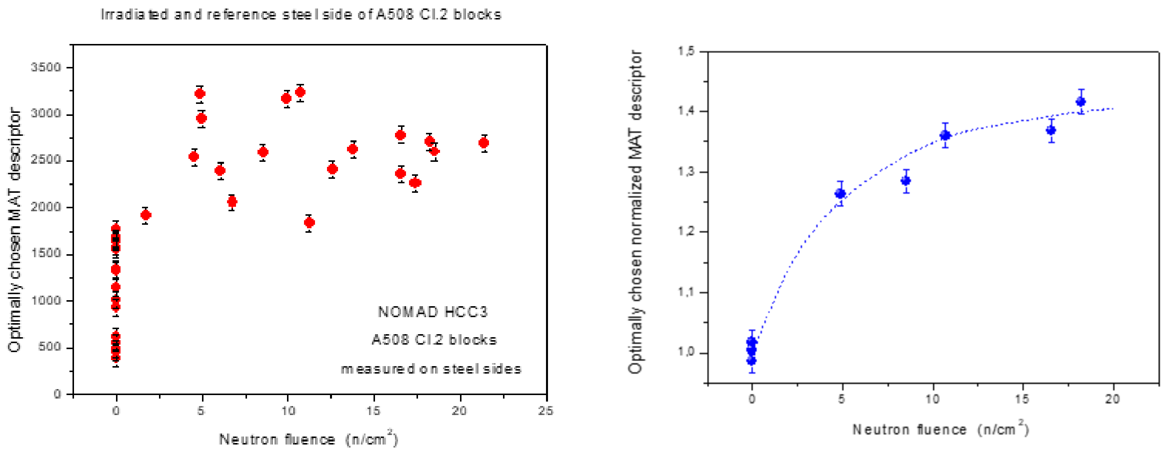

a) *b)*

***Figure 2.5**. Preselection of magnetically similar base material samples reduces the scattering a) MAT results on all samples, b) MAT results on the preselected samples*

The MAT method makes also possible the preselection of the experimental results, that means excluding the outliers before(!) the MAT evaluation process on the base of the acquired RAW data, practically even in real time with the measurements. The reasons for the outlying probe respones can be various: the magnetic coupling problem, surface contamination or can be also originated from the material inhomogeneity. Unfortunately, this cannot be studied within the framework of the NOMAD project on its merit. However, by using the above mentioned preselection (if the dimension of the dataset makes it possible) it can reduce dramatically the MAT prediction error (Fig. 2.5.). Therefore, this is also an argument for the MAT applicability [Ref. 2.1-2.3].

Clustering and spectroscopy of nanoparticles

OTKA FK 128327, OTKA KH 129578

D. P. Szekrényes, Zs. Zolnai, D. Zámbó, A. Deák

In the framework of our running projects we investigate the surface modification and self-assembly of nanoparticles that have engineered surface ligand layers. For the studies we employ plasmonic nanoparticles of different shape and size, that are wet-chemically synthesised in our lab. Our research efforts make use of the localised surface plasmon resonance changes that occur when the surrounding of plasmonic nanoparticles is modified. This modification can stem from changes in the composition and distribution of the molecular capping layer of the colloidal particles, or the presence of another particle due to clustering or aggregation. In addition to well-established ensemble characterization methods, like solvent based visible-light extinction spectroscopy and dynamic light scattering, we heavily rely on single-nanoparticle microspectroscopy, that allows a more detailed and fundamental investigation of the optical properties of the nanoparticles and their structures.

The clustering of PEGylated nanoparticles was investigated at the ensemble and single particle level. The aim of this research project is to study the colloidal stabilization properties of surface grafted PEG chains. Two types of gold nanospheres were prepared: one features permanent positive surface charge due to covalently bound MTAB ((11-Mercaptoundecyl)-N,N,N-trimethylammonium bromide), the other has a negative surface charge (citrate, MUA or PEG-COOH coating). The electric double layer (EDL) interaction dominated attractive interaction between these two species leads to heteroaggregation in the bulk liquid phase, and the resulting plasmon shift can be followed by conventional extinction spectroscopy (Fig. 2.6.a), confirming the affinity of the two particle types. For the PEG-COOH no significant shift is observed, but still, heteroaggregation takes place when the MTAB coated particle is fixed on a substrate and the PEG-COOH coated particle is allowed to assemble on it for several hours (Fig. 2.6.b). It was found that not only dimers, but larger clusters (up to heptamers) are also formed. All particle assemblies indicate a 2D (in-plane) arrangement of the particles, that might be attributed to the relatively weak coordination of the assembling particles and the consequent rearrangement upon drying under the action of immersion type capillary forces. Current efforts target the optimisation of the surface charges and PEG chain length to obtain a better control over the resulting cluster size and structure.

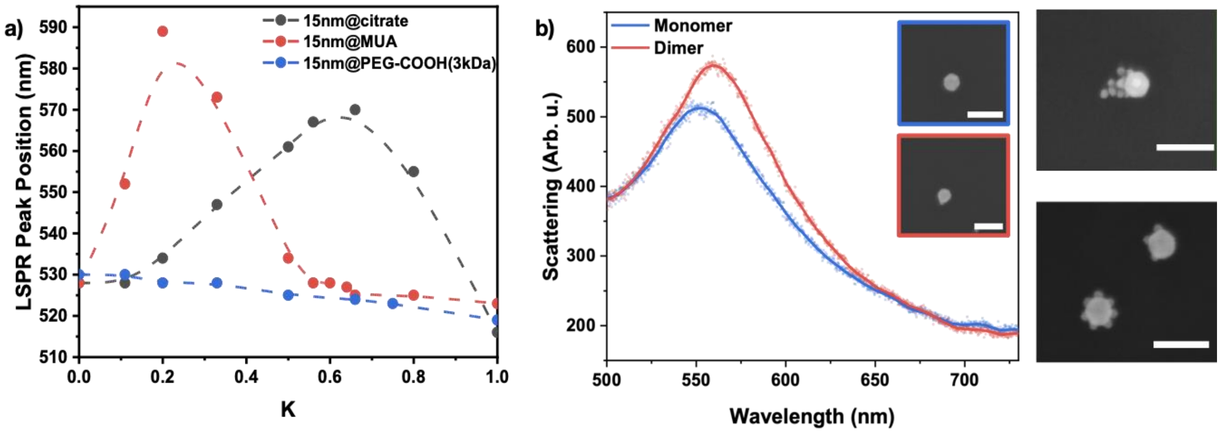

Figure 2.6. *a) Shift of the surface plasmon resonance as a function of the ratio of MTAB modified, positively charged 49 nm particles with 15 nm nanospheres. b) Single particle spectrum and structure of heteroclusters created at the solid/liquid interface.*

Another focus of our research activity is related to the controlled surface chemical patch formation of plasmonic nanoparticles. The engineered surface modification can allow the fabrication of complex nanoparticle assemblies and provide the background for applications in biology and optoelectronic fields. We employ gold nanoprisms and use two different thiol ligands, namely cysteamine and thiolated PEG (mPEG-SH) to create the molecular patches. Our strategy is based on the different accessibility of the particles' surface having low and high curvature regions. In these regions the original capping ligand layer has different packing density, allowing to create molecular patches first at the tips and edges of the nanoprisms – provided the ligand concentration is kept low enough. As shown in Figure 2.7.a, the dipole plasmon mode blueshifts over time as cysteamine is added to the system as a consequence of the decreasing effective refractive index in the optical near-field around the tips and edges.

From these measurements alone the site selective accumulation of the short chain thiols cannot be determined unambiguously. Hence we perform additional single particle spectroscopy studies and rely on the chemical interface damping related plasmon linewidth broadening as an additional indictor to assess the total amount of molecules accumulated at the particles' interface. At the present stage it was successfully verified that the scattering spectra of the individual patchy particles' can be fitted with Lorentzian oscillator model, where the contribution of the interband transition is taken into account (Figure 2.7.b). This enables to study in situ in a flow cell arrangement the molecule adsorption on individual nanoprisms based on the CID induced resonance peak broadening.

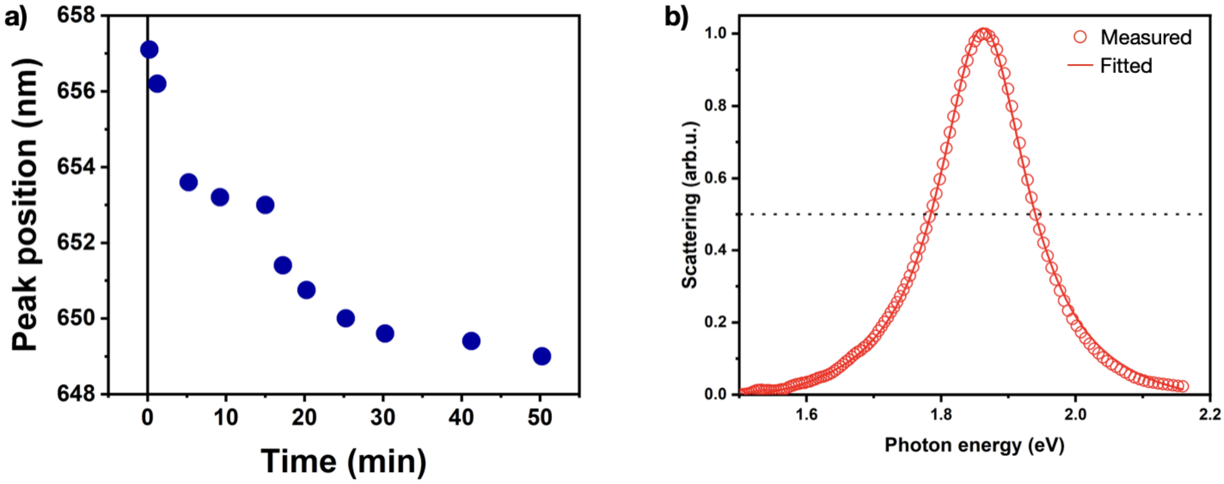

Figure 2.7. *a) Shift of the dipolar plasmon resonance wavelength as a function of time when cysteamine (5×10^{-2} mM) is added to gold nanoprisms (average edge length ca. 65 nm). b) Measured and fitted single particle scattering spectrum of a patchy gold nanoprism. The interband transition contributes with 40 meV to the resonance width for the given particle.*

Capillary Bridge Probe method on hydrophobic surfaces: liquid bridges without neck or haunch

OTKA FK 128901

N. Nagy

The developed indirect Capillary Bridge Probe method combines the accuracy of the Wilhelmy method and the general usability of the sessile drop method without their limitations. The method is based on the use of a liquid bridge as a probe: the capillary bridge of the test liquid is stretched between the base of a cylinder and the investigated surface under equilibrium conditions. The advancing contact angle on the sample can be measured during the slow (quasi-static) decrease of the bridge length. The receding contact angle is determined during the retraction of the cylinder. The contact angle is calculated from Delaunay's analytical solution, while the three necessary parameters are the measured capillary force (F_c), the radius of neck or haunch (r_0), and the radius of the contact line (r_s) on the investigated surface. The latter two parameters are obtained from the automated analysis of the captured image of the liquid bridge. The radius of the upper contact line (r_c) is constant since it pins on the rim of the cylinder.

The evaluation of full measurement cycles on hydrophobic surfaces is difficult, because several measured state of a water liquid bridge e.g. on a PTFE surface do not contain the neck or haunch region, as it is shown in Fig. 2.8. Therefore, one necessary parameter, the neck/haunch radius is unknown. How can be these measurements evaluated?

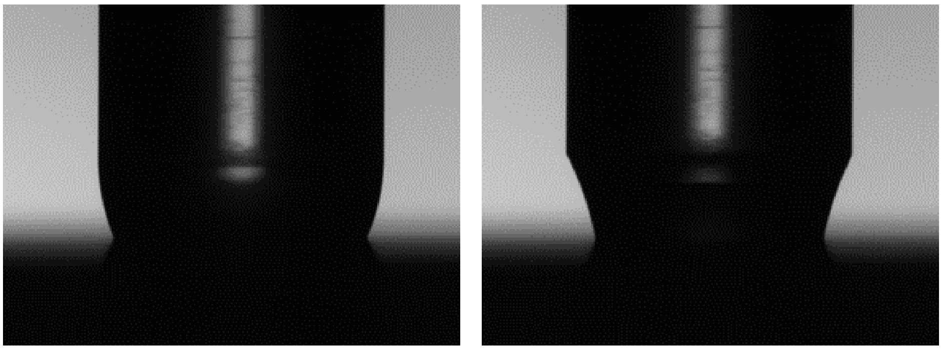

Figure 2.8. *Water liquid bridges without the haunch (left) and the neck (right) region, captured on a PTFE surface*.

Four different subcases can be identified to solve this problem: neck or haunch is missing and the upper or the lower part of the bridge is observable. These four cases can be seen in Fig. 2.9.

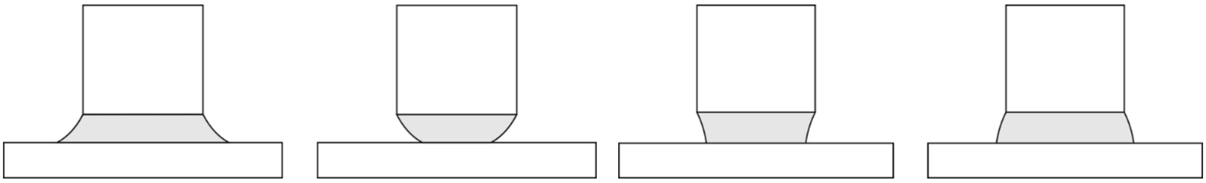

Figure 2.9. *Four different subcases of capillary bridges without neck or haunch*.

The two schematics to the left represent the lower part, while the two other show upper part of a liquid bridge. If we see the lower part, the surface radius (r_s) can be measured. Let's complete the shape of the bridge with the missing part so that let the upper contact radius match the radius of the cylinder (see

Fig. 2.10)!The resulted liquid bridge has the same radius, curvature, and capillary force as the real one has because of the constant mean curvature of the Plateau-surfaces. Polynomial fitting of the contour results an estimated contact angle on the investigated surface by derivation. According to this value, a contact angle range can be defined, thereby the potential liquid bridges can be found in the previously calculated look-up tables! Finally, the most appropriate capillary bridge with one definite r_0 is chosen according to the position of the lower contact points. Therefore, all parameters (including volume and surface area) can be calculated analytically.

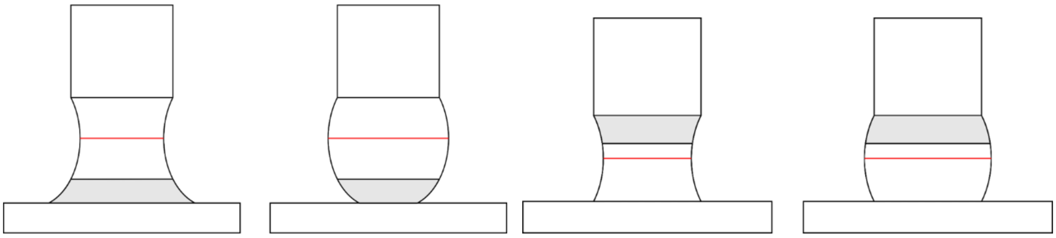

Figure 2.10. *Completing the shape of capillary bridges with the missing part.*

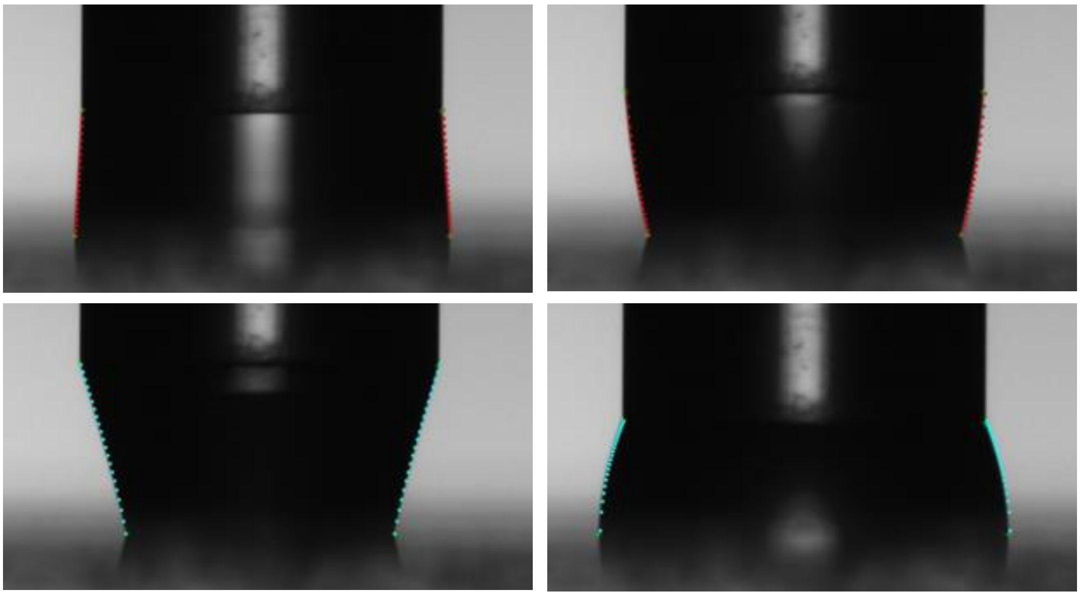

Figure 2.11. *Evaluated images of a water capillary bridge formed on a Zeonex-coated surface during one measurement cycle. The order of images follows the previous order of different subcases, not the measured sequence.*

In those cases when the the upper part appears, the problem seems to be more complicated because the surface radius is also unkown. In this situation, the solution is to find a symmetric liquid bridge, i.e. where the surface radius is equal to the radius of the cylinder! The capillary force of the completed bridge is identical to the force of the real liquid bridge due to their constant mean curvature. Due to the symmetry, the contact angle on the rim of the cylinder is equal to that which is formed on the imaginary surface. From this point, the procedure is similar to the previous cases: the polynomial fit helps to find a contact angle range and the position of the (real) contact points chooses the right nech/haunch radius of the capillary bridge. Now, we have all three input parameters to calculate every parameter of the real, original liquid bridge: contact angle on the sample surface, length, volume, area, etc. A water liquid bridge streched between the cylinder and a Zeonex-coated surface forms all of the four different subcases during one measurement cycle. Fig. 2.11. shows evaluated examples of these equlibrium states. The order of images in Fig. 2.11 follows the previous order of different subcases, not the measured sequence.

Noble metal nanorod cryoaerogels as novel electrocatalysts

D. Zámbó

Properties of nanoparticle building blocks can be retained and novel functionalities arise if they are assembled into functional nanostructures. One of the novel candidates of this materials class is the nanocrystal gel structures, which overcome the limitations emerging in case of practical applications of colloidally dispersed nanoparticles. The potential preparation methods of modern nanocrystal gels can be classified into two main families: the chemical and physical approaches. While the former includes the destabilization of the nanoparticle solutions via chemical triggers, so-called cryoaerogels are a novel class of physically gelated structures, including three main steps: concentration of the solution, flash-freezing and freeze drying of the frozen nanostructure to achieve air-filled pores and thus, aerogel structures. These gels (xerogels, aerogels and cryoaerogels) can revolutionize the application of these nanomaterials in sensorics, photo(electro)catalysis and energy harvesting.

Whilst plasmonic nanoparticles with small sizes and quasi-spherical shape have already been employed as cryoaerogel building blocks, larger plasmonic noble metal nanorods suffered from the limitation of synthetic procedures, stability of concentrated nanorod solutions and their relatively weaker catalytic activity compared to their spherical counterparts.

In this study, we demonstrated the fabrication of solid-supported cryoaerogel electrodes based on gold and silver nanorods via overcoming the above-mentioned limitations. Additionally, a proof-of-concept of electrocatalytically active nanorod cryoaerogels was presented. These porous cryogel networks are of great interest in direct liquid fuel cell-related application, such as ethanol oxidation reaction as well as electrochemical redox and glucose sensing. [Ref. 2.4]

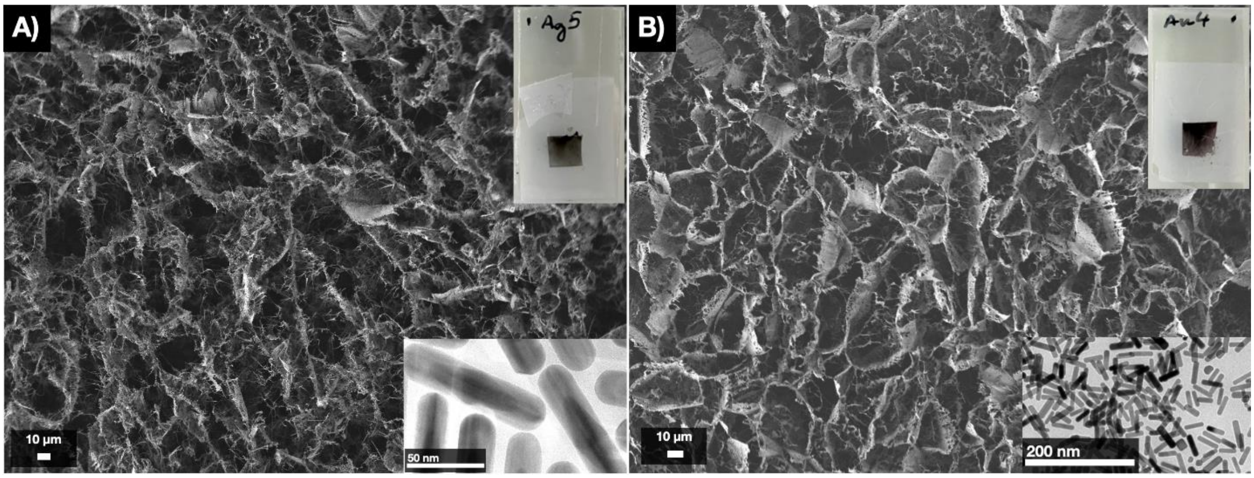

Figure 2.12. *SEM images of cryoaerogel-coated ITO electrodes consisting of Ag@Au nanorods (A) and Au nanorods (B). Insets show the physical appearance of the electrodes (upper right corners) and the TEM images of the colloidal building blocks (lower right corners).*

This work includes the upscaled colloidal synthesis of the noble metal nanorods, the modification of their surface with a conductive polymer shell (PEDOT:PSS), their concentration up to 5-9 g/L and the fabrication procedure of the cryoaerogel-coated ITO substrates.

It was found, that the cryoaerogels increase the overall conductivity of the ITO electrodes and facilitates their use as electrocatalysts due to the availability of the nanorods' active sites upon assembling the building blocks into porous macrostructures. Thus, electrochemical test reactions were performed to study the oxidation and reduction of the noble metal surfaces, their activity in redox couple reactions ($[Fe(CN)_6]^{4+}/[Fe(CN)_6]^{3+}$), ethanol oxidation reaction and glucose sensing.

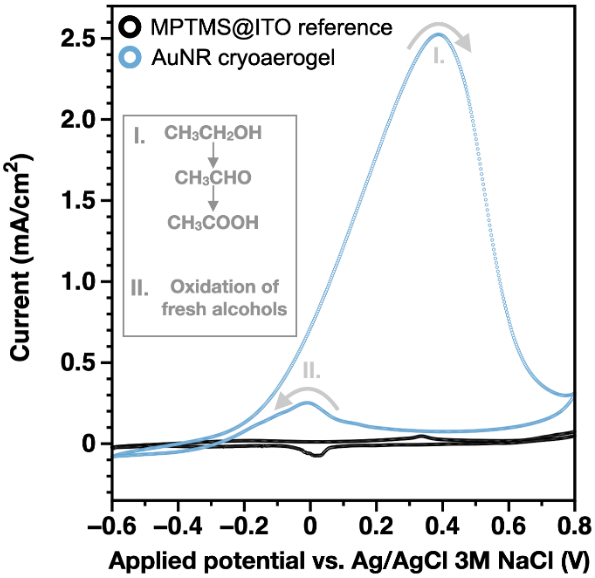

Figure 2.13. *Performance of the Au nanorod cryoaerogel electrode (blue) and the pure ITO substrate (black) in ethanol oxidation reaction in the presence of KOH.*

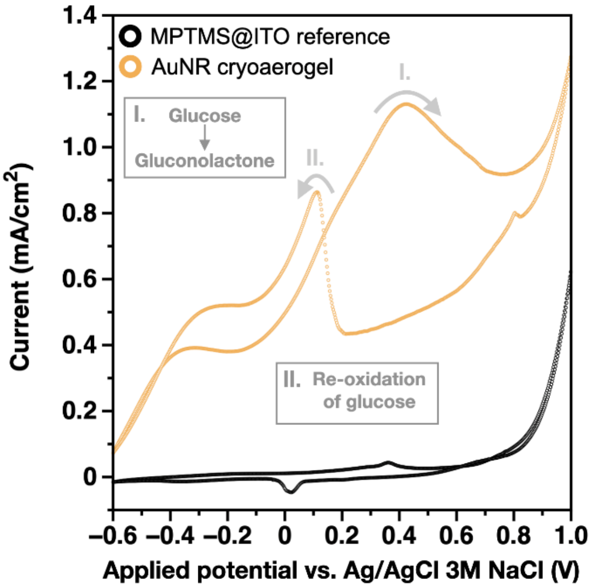

Figure 2.14. *Performance of the Au nanorod cryoaerogel electrode (orange) and the pure ITO substrate (black) in redox D-glucose sensing reaction in the presence of KOH.*

Cryoaerogelation is a promising technique to prepare nanoparticle-based porous macrostructures without using a chemical trigger for the assembly. The hierarchical porosity allows the electrolyte to rehydrate the gel structure and reach the catalytically active surface sites of the nanoscopic building blocks.

Investigations of plasmons in nanocorrugated CVD graphene by spectroscopic ellipsometry at visible-frequencies

G. Dobrik, P. Nemes-Incze, B. Majerus, P. Süle, P. Vancsó, G.Piszter, M. Menyhárd, B. Kalas, P. Petrik, L. Henrard, L. Tapasztó

Ψ and Δ spectra of nanocorrugated CVD graphene transferred onto SiO_2/Si substrate were measured using a Woollam M-2000DI rotating compensator spectroscopic ellipsometer (SE) at angles of incident 65° and 70° [Ref. 2.5]. The surface of the sample was large enough to avoid focusing and the corresponding depolarization effects [Ref. 2.6].

The optical model consists of a Si substrate, an interface layer between the thermal oxide and the Si wafer, the thermal oxide layer, an interface layer between the graphene and the SiO_2 layer, and the graphene layers (both quasi-flat and nano-corrugated) with a fixed thickness value of 0.34 nm. The reference dielectric function of the silicon substrate was imported from [Ref. 2.7], while the oxide and graphene layers were modeled by the Cauchy dispersion fitting the nondispersive and the λ^{-2} terms of the Cauchy polynomial and using two Lorentz oscillators, respectively. The wavelength (λ) range of 400-850 nm was used in the evaluations. We also set the same thickness for the flat graphene and corrugated graphene layers for an easier comparison.

We found the best fit for the SiO_2 layer of 303.3 nm (nominally 300 nm), and interface layer of 3 nm thickness. This latter is in good agreement with the values between 2 - 4 nm found in [Ref. 2.8]. Once all the thicknesses and dispersions were determined, the refractive indices (n) and extinction coefficients (k) of the quasi-flat graphene layer was calculated by fixing all the parameters in the model allowing only n and k of the graphene layer to be fitted "point-by-point" for all the wavelengths independently. This method is useful for the accurate and model-independent determination of dispersion [Ref. 2.9].

SE investigations revealed a substantially increased extinction in nanocorrugated graphene, for wavelengths above 700 nm, compared to the nearly constant extinction of quasi-flat sheet [Ref. 2.9] (Fig. 2.15). The refraction index also displays unconventional behavior in the nanocorrugated samples. While n has a nearly constant value between 3 and 4 in the quasi-flat graphene (Fig. 1b), its value progressively decreases down to 1.5 in the nanocorrugated sample starting from wavelengths above 600 nm (Fig. 2.15.a). A similar behavior (increasing extinction, decreasing refraction index) has been observed in graphene by broadband spectroscopic ellipsometry in the UV range, when approaching the wavelengths corresponding to the interband (π) graphene plasmon [Ref. 2.10].

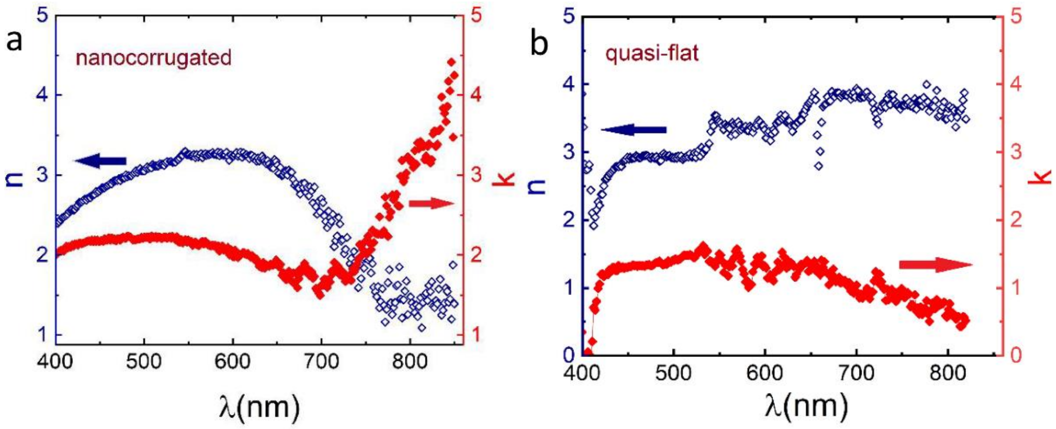

Figure 2.15. *SE on nanocorrugated CVD graphene sheets (a) reveals plasmonic activity through the drop of the refractive index and increase of the extinction coefficient at visible wavelengths, compared to quasi-flat CVD graphene samples (b).*

Oxidation of Zr at medium temperatures – concordant element of the growth kinetics

OTKA K131515

A. Romanenko, E. Agócs, Z. Hózer, P. Petrik, and M. Serényi

We report on the growth of ZrO_2 films upon the gradual thermal annealing of Zr in the temperature range of 500-700 K. The Zr samples were annealed in an isolated quartz tube shown in Fig. 2.16.A. Argon and Ar/O_2 gas mixtures with O_2 content of ~0, 1.25, 5 and 20 % were flowed at atmospheric pressure. The thickness of the oxide was monitored by in-situ spectroscopic ellipsometry (SE) with temporal and thickness resolutions of a few seconds and a few nanometers, respectively (Fig. 2.16.B). A remarkable feature of the process was that the growth of the oxide can be terminated immediately when decreasing the temperature by a few K shown in Fig. 2.17. This suggests that, in addition to the driving force, a built-in control adjusts the final thickness determined only by the temperature in sync with the formation and growth of the dense oxide films.

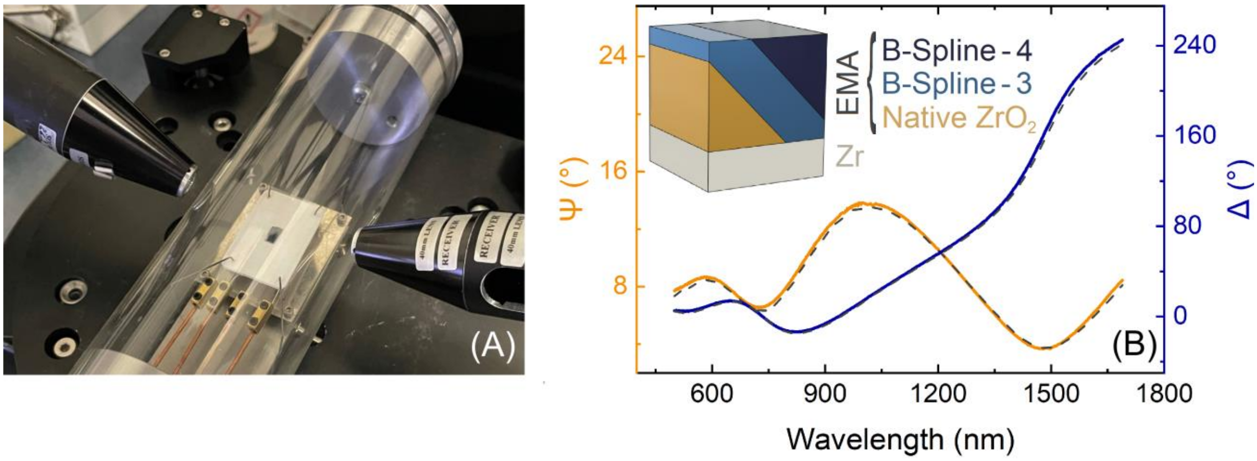

Figure 2.16. *(A) The heat cell constructed for multiple-angle SE measurements in controlled ambient and temperature. (B) Typical measured (solid lines) and fitted (dashed lines) SE spectra on the sample oxidized at 700 K for 18000 s and the optical model used for the evaluation of the SE spectra.*

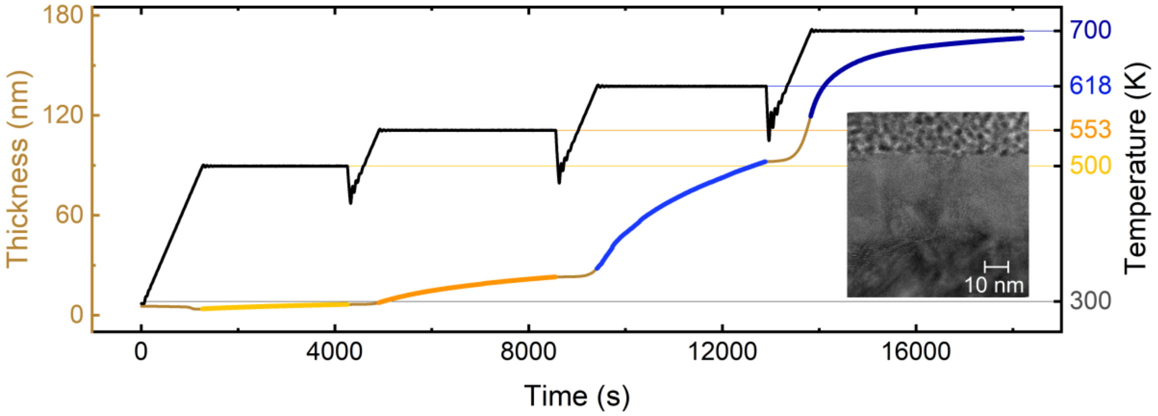

Figure 2.17. *Steps of thickness increase as a function of time under the influence of the increasing temperature values. The TEM image in the inset shows a typical oxide layer grown for 3600 s at the temperature of 553 K.*

A simple phenomenological model was developed that attempts to relate the parameters of the transport properties of the atomic oxygen to the results of kinetics measured by ellipsometry in a thickness range from a few nanometers to a few hundred nanometers. We apply the roughly simplified form of the Fick II. diffusion law to express the time dependence of the gradient of the O^- anion flux (*J*):

$$J_d(x) - J = c_O \frac{dx}{dt} \qquad (1)$$

where x and c_O denote the thickness of the oxide layer and the oxygen concentration, respectively. Using the formalisms used in the physics of semiconductors, we can solve this differential equation and we obtain for the time dependence:

$$t = -\alpha x - \alpha\delta \cdot ln\left(1 - \frac{x}{\delta}\right) \qquad (2)$$

where δ and α denotes the final thickness of the oxide layer and the growth rate, respectively. A comparison of this equation and the measurements is shown in Fig. 2.18.

The equations postulate that the oxide thickness approaches a value determined by temperature. The resulting oxide is stoichiometric when the growth occurs in an oxygen-rich environment. Stoichiometry is temporarily impaired in an oxygen-deficient environment, but if the heat treatment time is long enough for $\alpha \cdot \delta$, it becomes complete by the excess oxygen present in the final stage of the process. The driving force introduced into our phenomenological model based on ellipsometric measurements determines the kinetics of growth in a consistent and concordant way.

We focused on an alloy that is relevant in the nuclear power plant technology, and do not discuss the composition-dependent oxidation properties. The material we use in this study is sufficient for the demonstration of the proposed oxidation model. A greater knowledge of the oxidation process in this regime is of primary importance in many applications including nuclear technology and microelectronics. [Ref. 2.10]

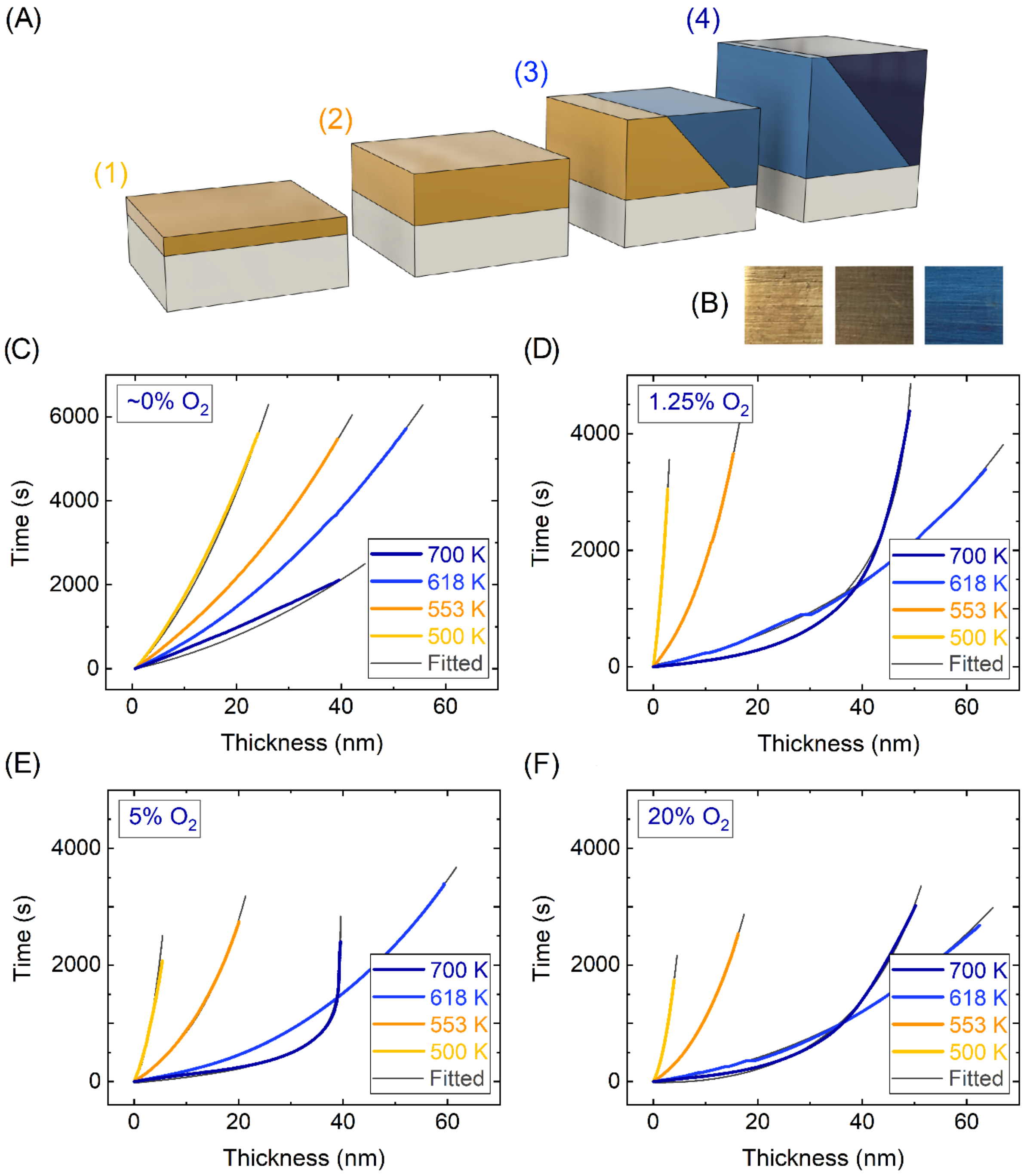

Figure 2.18. *(A) Optical models at different stages (1-4) of the oxidation process. (B) Photographs of 2 x 2-cm*^{2} *E125 alloy samples to demonstrate the change of color due to the different thicknesses of the oxides grown at various* O_2*/Ar ratios. (C-F) Time versus thickness for different* O_2 *concentrations at different temperatures, determined from the optical model shown in (A). The solid dark-grey lines show the curves fitted using Eq. (2).*

Flagellin-based electrochemical sensing layer for nickel and arsenic detection

M-ERA.NET OTKA NN117849 and K131515, BIONANO_GINOP-2.3.2-15-2016-00017

Z. Lábadi, M. Fried, P. Petrik

Regular monitoring of heavy metal concentrations in water sources is essential due to their severe health effects. Our goal was to develop a rapidly responding, sensitive and stable sensing layer for the detection of arsenic and nickel.

Flagellin-based proteins were designed and prepared at the University of Pannonia capable of forming stable filament structures with high surface binding site densities. The D3 domain of Salmonella typhimurium flagellin was replaced with arsenic-binding peptide motif of different bacterial ArsR transcriptional repressor factors. As-binding fibers were immobilized on the surface of a gold electrode and used as a working electrode in cyclic voltammetry (CV) experiments. Fig. 2.19. shows the scheme of the process.

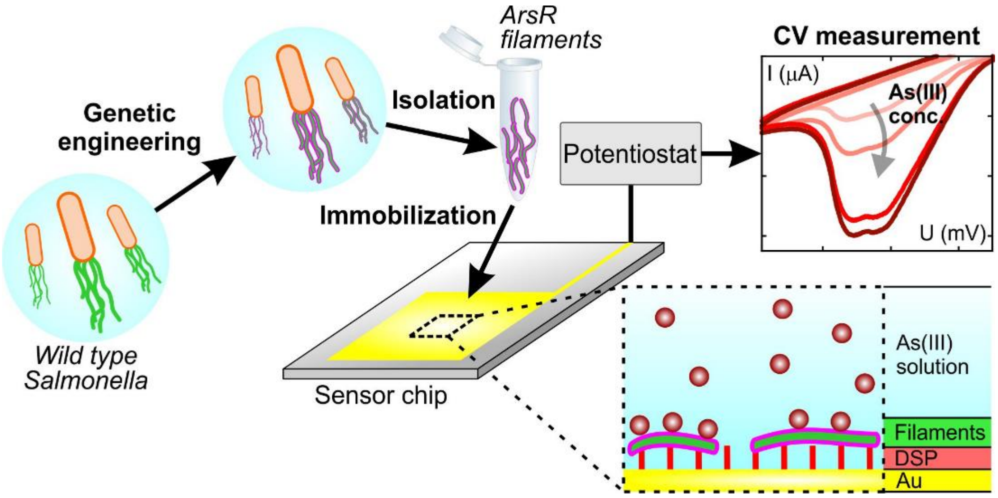

Figure 2.19. *Schematic workflow of the production of genetically engineered flagellar filaments, their deposition on the gold working electrode surface and CV measurements on As containing samples*

In order to form a stable and dense layer of flagellar nanotubes on the gold surface, thiol-based covalent immobilization chemistry was applied. The dynamics of the filament layer formation on a gold layer was monitored by in situ spectroscopic ellipsometry in the Kretschmann configuration, as shown in Fig. 2.20.

Fig. 2.21. summarizes the cyclic voltammetry results obtained on the protein-based sensor layers in the presence of arsenic. Set of CV curves measured in the presence of As(III) on wild type flagellar nanotubes (A) as well as on FliC-ArsR9 As-binding flagellar nanotubes before (B) and after (C) storage and regeneration. Subfigure (D) shows the areas for FliC-ArsR9 filament cathodic peaks after first use and after regeneration (calculated by averaging four measurements) as a function of the As(III) concentration. Up to 20 times the MAC, this setup may be suitable for quantitative determination of the concentration of arsenic. Based on the CV results obtained after DMSA treatment, it can be stated that the sensor layer is stable and partially regenerable.

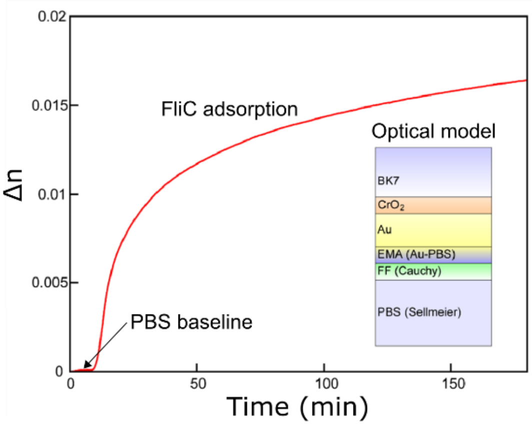

Figure 2.20. *Change in the refractive index (Δn) near to the surface of a DSP-functionalized gold layer caused by the adsorption of flagellar filaments from their 0.5 mg/mL suspension. The kinetic curve was recorded by in situ spectroscopic ellipsometry. The inset shows the optical model used for data evaluation.*

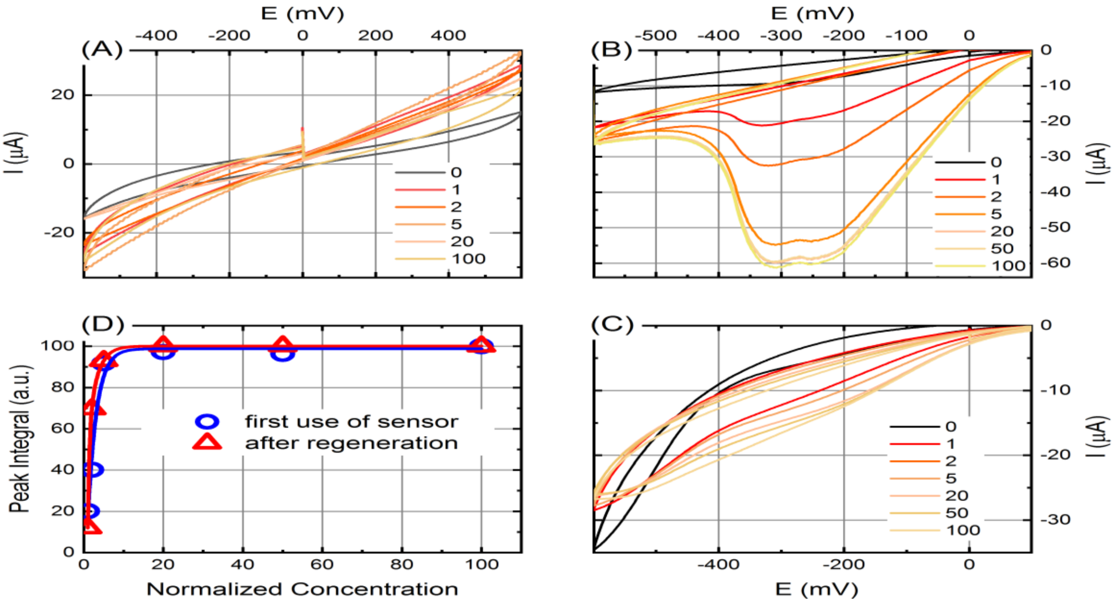

Figure 2.21. *Cyclic voltammetry on the protein-based sensor layers. Wild type flagellar nanotubes (A), As-binding flagellar nanotubes before (B) and after (C) storage and regeneration. Subfigure (D) shows anodic peak sizes.*

Further experiments were carried out on different protein layers containing Ni binding motifs. Application of stripping voltammetry methods (i.e. accumulation of the Ni ions at the sensor surface by delayed potential cycle) showed that the sensor layer is capable of semi-quantitative detection of Ni ions in concentrations below the health limit. Furthermore, we also showed that the sensing experiments can be repeated in natural water samples instead of model buffer solutions, and the presence of Fe, Cu and Zn ions does not affect the Ni sensitivity of the sensors. Based on these results, it can be concluded that the stable arsenic-binding flagellin variant can be used as a rapidly responding, sensitive, but simple sensing layer in a field device for the MAC-level detection of heavy metals in natural waters [Ref. 2.11].

Makyoh topography and related methods

Ferenc Riesz

Makyoh topography is an optical tool for the qualitative flatness testing of specular surfaces, based on the defocused detection of a collimated light beam reflected from the tested surface (Fig. 2.22). By inserting a square grid into the path of the illuminated beam, the height map can be calculated by integrating the gradients obtained from the distortion of the grid's reflected image (quantitative extension).

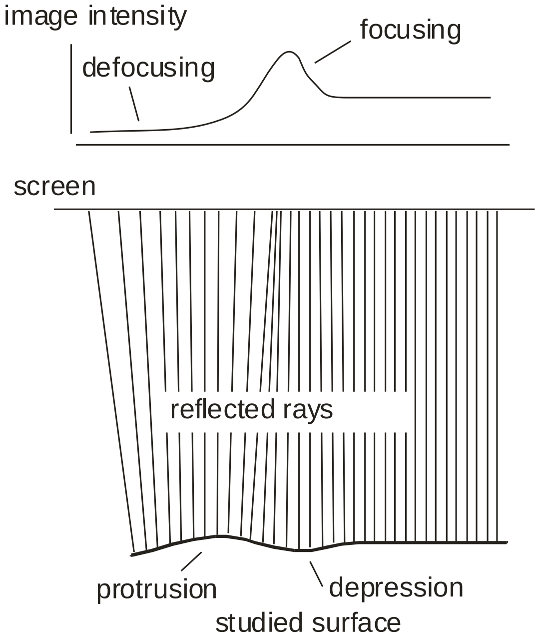

Figure 2.22. *The scheme of Makyoh-topography*

In the past year, activities were concentrated mostly on methodology.

It was shown earlier that utilising the existing Makyoh setup under certain geometrical conditions, a schlieren-like measurement can be realised where the imaging lens' aperture plays the role of the schlieren knife edge, or with some modifications, a traditional knife edge can be inserted while maintaining the original Makyoh imaging scenery as well. This leads to a useful tool complementing the traditional Makyoh scheme. Efforts were made to find optimum working conditions.

An approach to the modelling of Makyoh imaging is to utilize the mirror backside relief rather than the front side as the input data. The back relief is transferred to the front convoluted with a Gauss curve (or similar). The construction of a mathematical model using the geometrical model developed earlier (Riesz, J. Phys D 33 (2000) 3033) within the framework of this approach is under way.

The swirl defects in *p*-type Si wafers were further studied using Makyoh topography and the schlieren-like method. The interpretation of the high amount of data collected is in progress.

3-Thin Film Physics Department

Head: Dr. Katalin BALÁZSI, Ph.D., senior scientist

Research Staff

- Csaba BALÁZSI, D.Sc. (from February)
- Haroune R. BEN ZINE (from July)
- Ildikó CORA, Ph.D. (maternity leave)
- Zsolt CZIGÁNY, D.Sc.
- Zsolt FOGARASSY, Ph.D.
- Mónika FURKÓ, Ph.D.
- Viktória KOVÁCSNÉ-KIS, Ph.D.
- Béla PÉCZ, D.Sc.,
- György Zoltán RADNÓCZI, Ph.D.
- Adél RÁCZ, Ph.D.
- György SÁFRÁN, C.Sc.
- Attila SULYOK, Ph.D.
- Orsolya TAPASZTÓ, Ph.D. (leave until September)
- Dheeraj VARANASI, Ph.D. (from March)
- Árpád BARNA, D.Sc., Prof. emeritus (┼2021. 09.25)
- Péter B. BARNA, D.Sc., Prof. emeritus
- Miklós MENYHÁRD, D.Sc., Prof. emeritus
- György RADNÓCZI, D.Sc., Prof. emeritus
- János LÁBÁR, D.Sc, Prof. emeritus

Ph.D. students

- Dániel OLASZ (from September)
- Erzsébet DÓDONY
- Klára HAJAGOS-NAGY
- Nikolett HEGEDÜS
- Tamás KOLONITS
- Mohamed ARFAOUI (Hungaricum stipendium)
- Maroua H. KAOU (Hungaricum stipendium from September)

Technical Staff

- Andrea J. FENYVESINÉ
- Nikoletta KŐSZEGI (partial time)
- Valéria OSVÁTH (maternity leave)
- Noémi SZÁSZ
- Andor KOVÁCS
- Viktor VARGA

The scientific results of the Thin Film Physics Department are related to thin film and ceramic fields. The main research topics are in line with modern trends of material science with the respect to a 50 years long history of the department. In 2021 the important base research field was the development of the 2D semiconductor and multicomponent thin films supported by several international basic scientific projects and collaborations.

The second research line, the development of different ceramics supported by the basic and applied projects, was continued. Gradient sandwich ceramics (Si_3N_4- Si_3N_4 / multilayered graphene) and different calcium phosphate based bioceramics were developed framework of the international co-operations. The last line and uniqueness of the Department (in national and international level) was the transmission electron microscopy. The effect of the structure on the developed material´s properties was demonstrated by this TEM study and they showed that the optimal structure can be directed in a controlled way. All topics was supported by methodical developments based on electron diffractions.

In 2021, 45 papers appeared in refereed journals with a cumulative impact factor of 253. In addition, 2 papers in conference proceedings were published with no impact factor. Members of the group presented 18 invited lectures, 19 oral talks and 4 posters at national and international conferences. The group received 3200 independent citations in the examined interval of the last two years.

Research members of the group lectured some courses at universities and held few laboratory practices. All courses were for full semester (Eötvös Lóránd University - ELTE, and Budapest University of Technology and Economics - BME, and University of Pannonia- UP and Óbuda University - OE). In addition, 7 PhD students were supervised. 1 PhD student successfully defended his PhD degree.

Social activity of the group is landmarked by 15 memberships in different committees of the Hungarian Academy of Sciences and in boards of international societies (European and American Ceramic Society, International Ceramic Society, International Union for Vacuum Science).

Calibration procedure to improve the accuracy of SAED in aberration corrected Themis

OTKA K125100, VEKOP-2.3.3-15-2016-00002

Zs. Czigány, V. Kovácsné Kis

The aim of this work is to demonstrate that fine tuning of experimental and evaluation parameters can improve the accuracy and reproducibility of selected area electron diffraction (SAED) close to that of conventional laboratory X-ray diffraction (XRD) equipment. Among diffraction techniques used for structure investigation (including crystal structure determination, defect structure, grain size, and texture) electron diffraction excels with its locality, however, its accuracy and reproducibility are generally considered to be lower than that of XRD. A conservative estimate, according to the famous handbook by Williams and Carter (2009), for the accuracy and reproducibility of interplanar (d) spacing determination from electron diffraction is 1-3% without internal standard. The primary reason for this degree of uncertainty is that a focused diffraction pattern can be achieved by different combination of specimen height, illumination conditions and diffraction focus giving rise to different camera length (CL) values and widths of diffraction rings. This can be improved by application of standard acquisition parameters to achieve of reproducible TEM settings. At our department Lábár et al. (2012) elaborated a calibration procedure and achieved 0.3% accuracy. Higher accuracy (~0.1%) can only achieved by application of internal standard. Since systematic study of the effect of these parameters on the data is missing, similar estimates apply for the error of camera length in a recent aberration corrected transmission electron microscopes. State-of-the-art aberration corrected microscopes have an order of magnitude better acceleration voltage and lens current stability compared to conventional TEMs, which implies an order of magnitude better reproducibility and accuracy in electron diffraction. Besides the stability of acceleration voltage and lens currents, field emission gun (FEG) electron sources provide a coherent electron beam with typical energy spread of 0.7eV which also decrease the instrumental broadening.

We performed our study in a Themis (Thermo Fisher) TEM with Cs correction in the imaging system (spatial resolution in HRTEM mode 0.8Å), operated at 200kV and equipped with Schottky field emission gun (FEG) having an energy spread of ~0.7eV. SAED patterns were recorded by a 4kx4k Ceta camera using Velox software (Thermo Fischer). The diffraction patterns were exported in 16 bit tiff format and 1D diffraction profiles, containing intensity distribution as function of scattering angle, were obtained using Process diffraction software. The software allows visual fit and refinement of center of the pattern (X, Y), eccentricity (ε) and its angle (α) together with calibration of camera length. By careful control of specimen height and illumination conditions (by monitoring lens currents) it was possible to reach a session to session reproducibility better than 3x10-4 for camera length.

Refinements of the center of the diffraction pattern and corrections for lens distortions (ellipticity of rings) allowed for determining the ring diameters with an accuracy of 10-3. For determination of the ellipticity parameters by visualization of the intensity distribution an ideal calibration specimen is composed of nanocrystalline grains free of texture and produce narrow diffraction rings. For this purpose, we deposited a polycrystalline Cu layer on TEM grid coated with nanocrystalline graphene. The achieved accuracy of 10-3 for lattice spacing measurement without internal standard is compatible with that of XRD, and reduction of instrumental broadening due to the elaborated evaluation procedure allows for separation of close reflections and provides more reliable ring width and thus improved input parameters for further nanostructure analysis as demonstrated on dental enamel bioapatite Fig. 3.1. [Ref. 3.1].

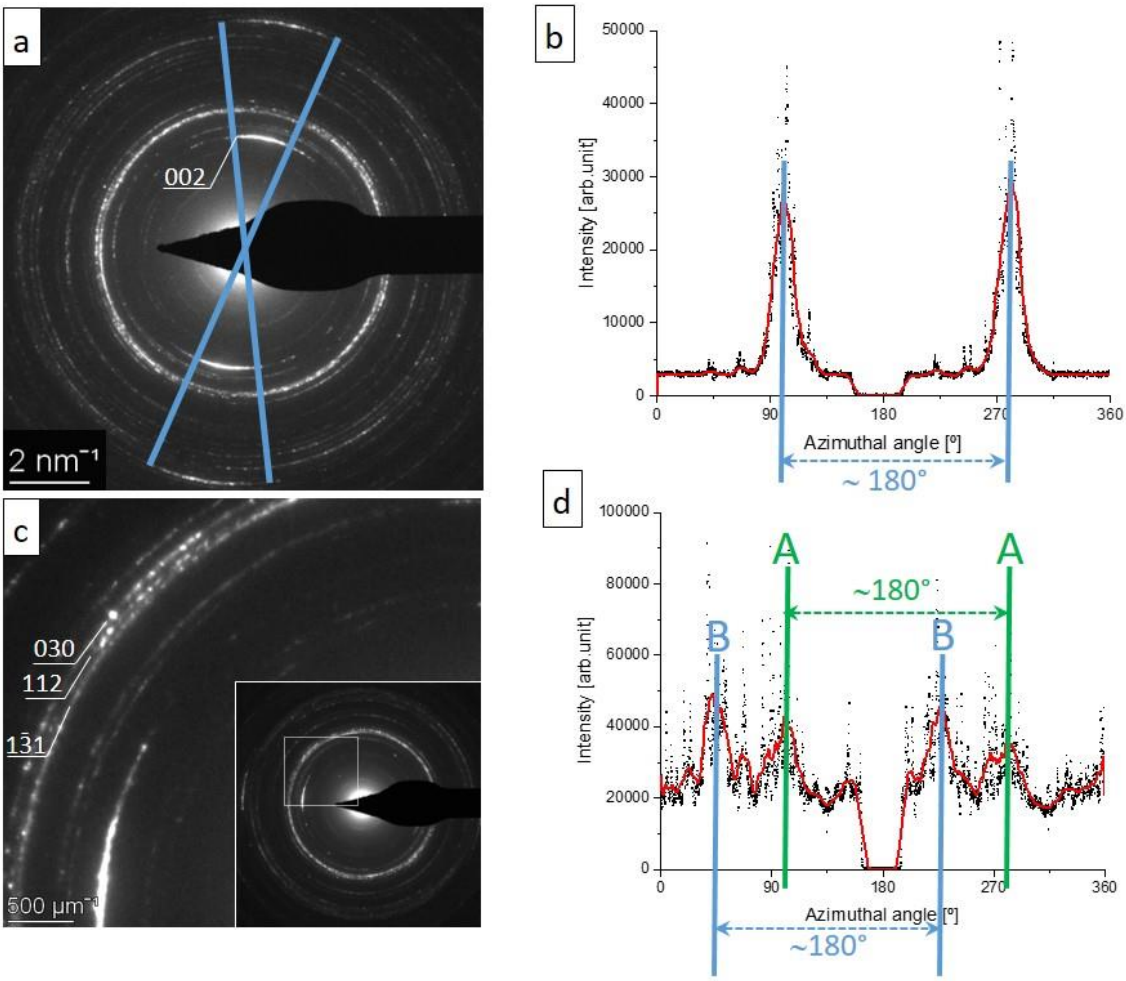

Figure 3.1. *(a) A typical SAED pattern of dental enamel cross section showing strong [001] texture. (b) Azimuthally integrated intensity profile of 002 reflections in a 15-pixel wide ring. (c) 030 diffraction ring can be resolved (separated from 112), and (d) azimuthal intensity profile of the 030 reflections obtained after integration in an 8-pixel wide ring shows two sets of crystallite population A and B separated by approximately 45°.*

DiffMap: Phase maps and orientation maps from 4D-ED pattern set

VEKOP-2.3.3-15-2016-00002

J. L. Lábár

Many new scanning transmission electron microscopes (STEM) can record four-dimensional diffraction (4D-ED) information in addition to the usual bright field (BF), dark field (DF) and high angle annular dark field (HAADF) imaging modes. 4D-ED information is collected in the form of a large number of 2D electron diffraction patterns, one pattern per location, each corresponding to a pixel of the 2D HAADF image. Although individual scientific solutions exist in the literature to mine information out of such 4D-ED pattern sets, the manufacturers of the STEMs do not offer commercial programs to solve the problem. Available commercial solutions also need additional hardware elements and use an optical camera to photograph the screen of the (S)TEM to record the diffraction patterns. Here we present a free, stand-alone program that does not require any additional hardware and runs under the Windows operating system. The diffraction patterns can be recorded with the native camera of the TEM controlled by the STEM software independently from our program. The new program processes such data sets (using TIF files as input) to produce phase maps and orientation maps for nanocrystalline samples. Since the diffraction patterns in TIF format can be recorded with STEMs from different manufacturers, our solution is available to many microscopists irrespective to the make of their instrument.

The examples here were recorded on a Titan Themis G2 200 STEM using a 4kx4k CETA 16 CMOS camera (both Thermo Fisher Scientific, Waltham, MA, USA) controlled by the TIA program (FEI, Eindhoven, The Netherlands). The data collection was done in microprobe STEM mode, which means that a fine parallel nanobeam (NB) was scanned over a rectangular area while recording a NB electron diffraction at each pixel. A TEM lamella was cut by focused Ga$^+$ ion beam (FIB) from the same multiphase sample, but from a different location than which was published in [Ref. 3.2].

The procedures in DiffMap are based on the solutions originally coded in an *unpublished* version of the ProcessDiffraction program [Ref. 3.3- 3.4], as cited in publications, where it was already used [Ref. 3.2] before it was revamped for publication of the program itself.

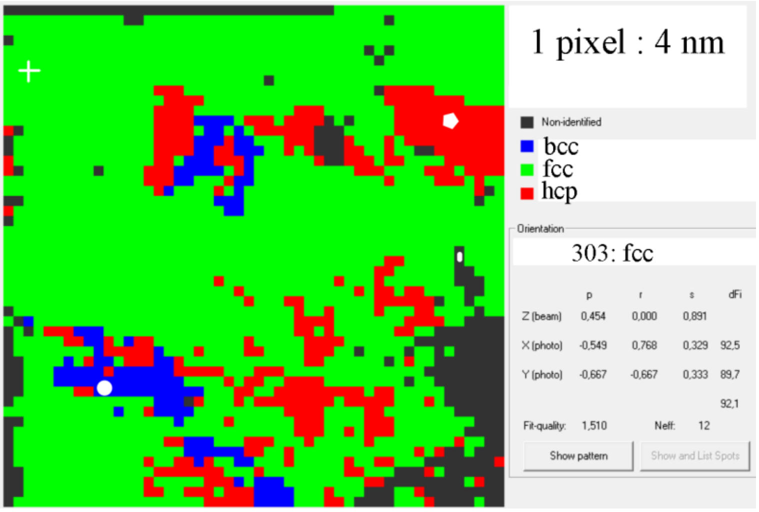

303: fcc

	p	r	s	dFi
Z (beam)	0,454	0,000	0,891	
X (photo)	-0,549	0,768	0,329	92,5
Y (photo)	-0,667	-0,667	0,333	89,7
				92,1

Fit-quality: 1,510 Neff: 12

Figure 3.2. *Phase map from a nanocrystalline Co-Cr-Fe-Ni sample. Pixel size is 4 nm.*

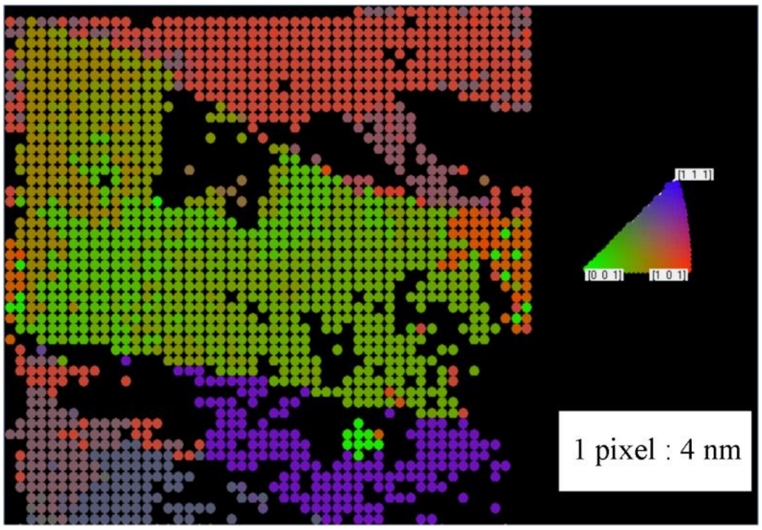

Figure 3.3. *Orientation map for the fcc phase in the sample as seen from the beam direction (Z-direction in the Lab-system). Pixel size is 4 nm.*

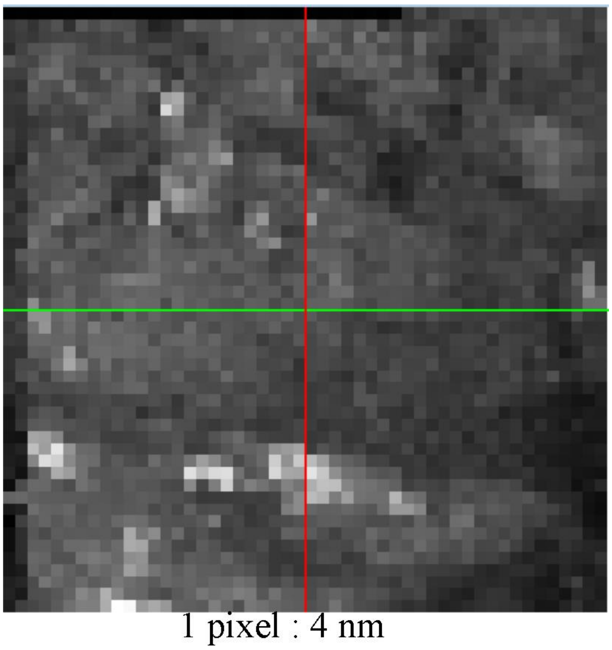

Figure 3.4. *Fit-quality map. Pixel size is 4 nm.*

The program operates in two, logically distinct steps. First, the several thousand NBD patterns are compared to a set of simulated patterns to calculate, which fits the measured the best. Patterns are simulated for each crystal structure (phase) that can be present in the sample for each symmetrically independent orientations (the rest of orientations are automatically provided by the symmetry operations of the crystal). The results of the matching are stored in a result file. In the second step phase map (Fig. 3.2), orientation maps (Fig. 3.3) and quality map (Fig. 3.4) are created from this results file. Additionally, the original patterns can be consolidated into virtual BF and virtual DF images, by collecting information only from the pre-selected parts of the diffraction patterns.

As a means for optional cross-checking the original data and the correctness of the identification, any measured diffraction pattern can be loaded by double-clicking on a pixel in the phase map. An example of an indexed diffraction pattern is in Fig. 3.5.

The graphical user interphase is easy to use and the program is available free from https://public.ek-cer.hu/~labar/DiffMap.htm.

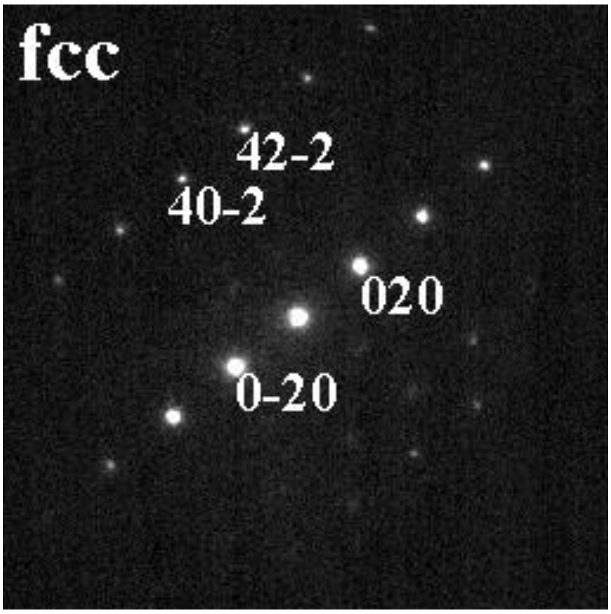

Figure 3.5. *Example for an indexed diffraction pattern*

The experimental part of this research was supported by VEKOP-2.3.3-15-2016-00002 of the European Structural and Investment Funds. The sample is kindly provided by Johann Michler, László Pethő and Péter Nagy at EMPA Swiss Federal Laboratories for Materials Science and Technology, Laboratory for Mechanics of Materials and Nanostructures, Thun, Switzerland. The author is indebted to Noémi Szász for the preparation of the FIB lamella.

Application of internal standard for the in-situ TEM investigation of solid phase transformations and reactions

OTKA NN112156

K. Hajagos-Nagy, F. Misják, G. Radnóczi

In an in-situ experiment paying attention to a few aspects/steps can make the measurement procedure and the evaluation of results more effective. However, these are hard to find in the literature. Our goal was to give a description that can facilitate the in-situ investigation of phase transformations and reactions at high temperatures. The steps are demonstrated on amorphous Cu-Mn/C thin films focusing on phase identification in a multicomponent system. Cu-Mn films are of recent technological interest due to their potential application as barrier layers in interconnect structures. Mapping the Cu-Mn-C-O system may help their integration with low-κ dielectrics (eg. SiOCH) [Ref. 3.5].

CuMn/C films were in-situ annealed and examined by TEM in a Philips CM-20 electron microscope operated at 200 kV. The temperature range of in-situ annealing was 20-600°C. Separate samples were used in microscope and diffraction mode to be able to follow the initial area of observation during in-situ annealing. The phase compositions of the films were evaluated from SAED patterns using the Process Diffraction program [Ref. 3.3].

The amorphous Cu-Mn films crystallized at 300°C into Cu(Mn) and α-Mn-based solid solutions. The lattice parameter of the Cu(Mn) solid solution changed throughout the temperature interval of 300-600°C. At 400°C new phases appeared accompanied with disappearance of the α-Mn-based solid solution. To identify the new phases and to examine the changes in solid solutions we applied the method of internal standard. This method allows calibrating the camera constant for each annealing step and to increase the accuracy of the lattice parameter values by approximately one order of magnitude [Ref. 3.6]. MnO was chosen as an internal standard because MnO is present in the whole temperature range of annealing, most of its diffraction maxima can be easily separated from other phases and it produces stable and well defined diffraction rings without the risk of contamination. By separating the effect of thermal expansion and changes in solute concentration, the composition of the Cu(Mn) solid solution in the temperature range of 300-600°C was calculated. To identify the new phases that appear at 400°C, a list of candidate phases was made by comparing the probability of formation of all phases in the Cu-Mn-C-O multicomponent system. Phase identification confirmed the candidate phases: Mn23C6 and Mn5C2 carbides were present in the temperature range of 400-500°C, and Mn5C2 and Mn7C3 carbides from 500°C to 600°C which formed through the reaction of the Cu-Mn film and the C substrate. The presented example can serve as a guideline for the in-situ investigation of phase transformations and reactions at high temperatures.

Evaluation of AES depth profiles with serious artefacts in C/W multilayers

A. S. Rácz, Zs. Fogarassy, M. Menyhárd

Tungsten-carbide (WC) is often used as protective coating due to its high hardness and chemical resistivity. In our work we produced WC by means of ion irradiation by irradiating a C/W multilayer structure by nobel gases. Due to irradiation at the interfaces ion mixing happened and carbide was formed, as well. The produced carbide was detected by Auger electron spectroscopy (AES) and the component in-depth distribution was determined by depth profiling. In the case of a non-irradiated sample we observed that during depth profiling the applied argon ions induced mixing and carbide compound was formed at the interfaces.

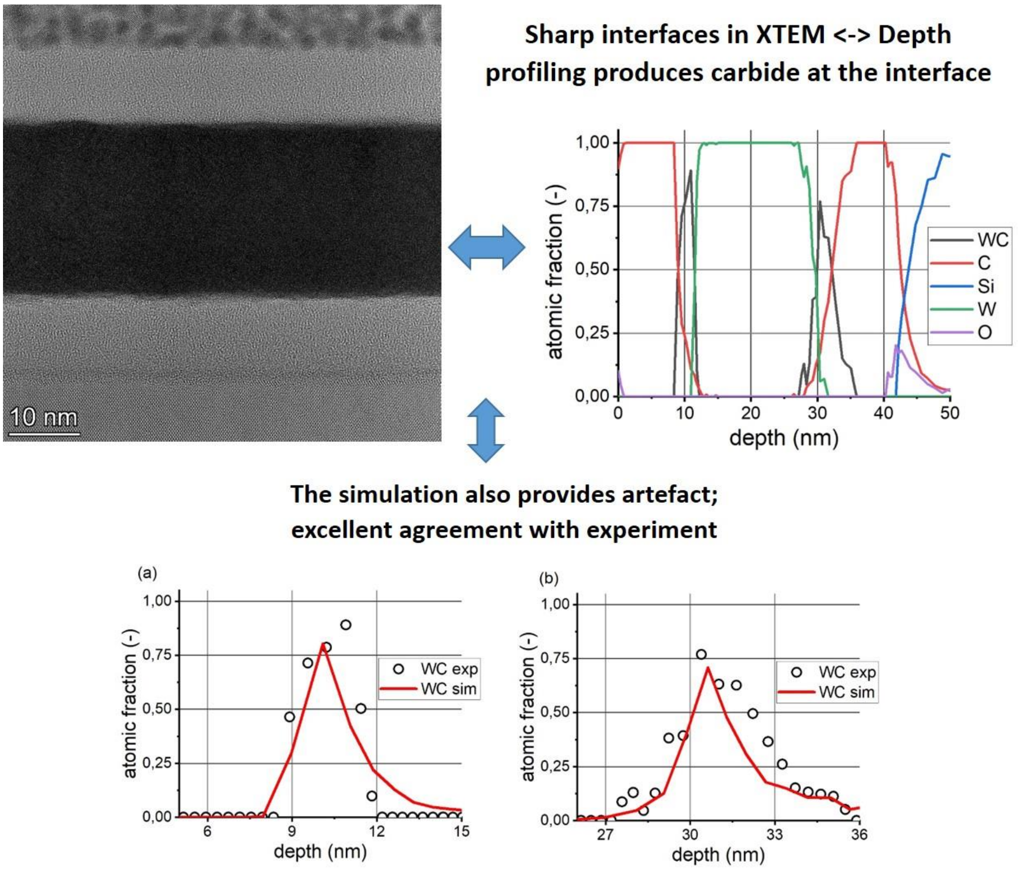

Figure 3.6. *XTEM, AES and TRIDYN simulation results for a non-irradiated C/W/C/Si substrate multilayer structure*

This was modelled by the TRIDYN simulation which helped us to determine the carbide artefact production of AES depth profiling (Fig. 3.6.). The simulation was used for reconstructing the real depth profile of ion-irradiated samples. We have shown that the artfact production can be neglected in the case of highly mixed (high carbide content) samples [Ref. 3.7].

Microstructure and optical properties of composition spread YTiO thin films

OTKA K129009

D. Olasz, V. Kovácsné Kis, P. Petrik, B. Kalas, G. Sáfrán

Materials with perovskite structures are receiving increasing attention in semiconductor research. They have a chemical formula ABX_3, where ‘A’ and ‘B’ are cations and X is an anion that bonds to both. A number of elements can be combined to form perovskite structures showing a wide variety of physical, optical, and electrical properties. Perovskite solar cells can be manufactured by simple, additive deposition techniques, like printing, for a fraction of the cost and energy compared to traditional silicon technology.

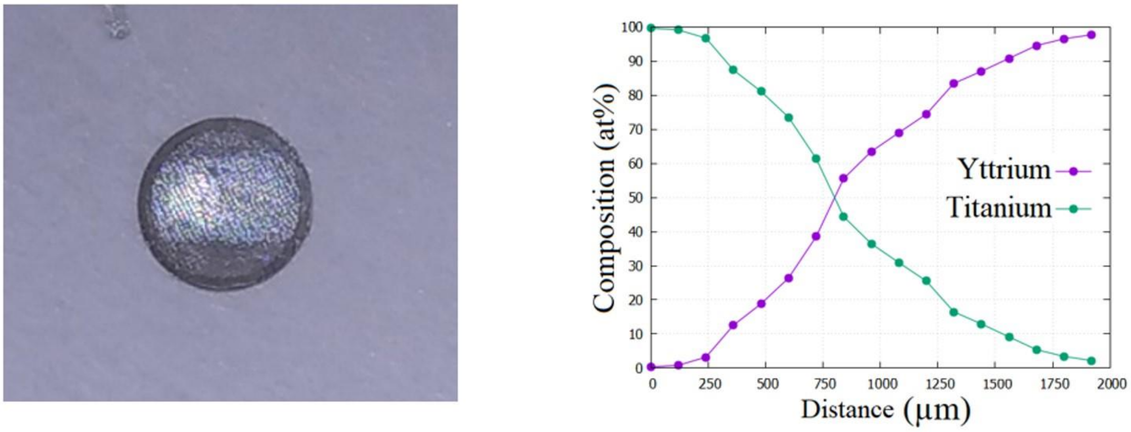

Figure 3.7. *A combinatorial YTiO sample on a TEM grid and its EDS diagram representing concentration of the cations as a function of distance along the layer. O-concentration values are shown in Fig. 3.9.*

Recently, the photoconversion efficiency of perovskite solar cells has exceeded 25%, close to that of silicon (27%). From the large family of perovskites, we aimed to produce and characterize the Y-Ti-O system. Thin composition spread samples were deposited on both carbon coated TEM grids and Si slabs by reactive DC magnetron sputtering of yttrium and titanium in $3 * 10^{-3}\ mbar$ Ar gas with $1 * 10^{-4}\ mbar$ O_2 inlet. Using microcombinatory [Ref. 3.8-3.9] we could produce and examine the oxides of the cations in the whole Y_xTi_{1-x} (x=0…1) concentration range in a single sample (Fig. 3.7.). The microstructure as a function of composition was determined by TEM and SAED: at high Y or Ti concentrations crystalline, while in between an amorphous structure was found (Fig. 3.8).

The radial intensity distribution curves of SAED-s evaluated with ProcessDiffraction software [Ref. 3.10] are shown in Fig. 3.9. for the whole Y_xTi_{1-x} -oxide composition range. At the Ti surplus side of the sample, rocksalt-type cubic TiO structure (space group: $Fm\bar{3}m$, $a = 4.1766$ Å) was formed and the intensity of its characteristic peaks decreases with the increase of Y concentration. Between Y/Ti/O 14/28/58 and 28/8/64 at% compositions only diffuse peaks are present, characteristic for amorphous structure. With a further increase of the Y content, at 33/5/62 at% composition, the peaks of the Y_2O_3 crystalline phase appears, showing $Fm\bar{3}m$ space group, cubic ($a = 5.2644$ Å), CaF_2 type structure. At even higher Y concentration (33/5/62) additional small peaks appear representing a Mn_2O_3 bixbyite-type cubic structure of Y_2O_3 (space group: $Ia\bar{3}$, $a = 10.5981$ Å). It has a lattice constant twice as large as the one mentioned above, and its formation is related to the arrangement of O-vacancies.

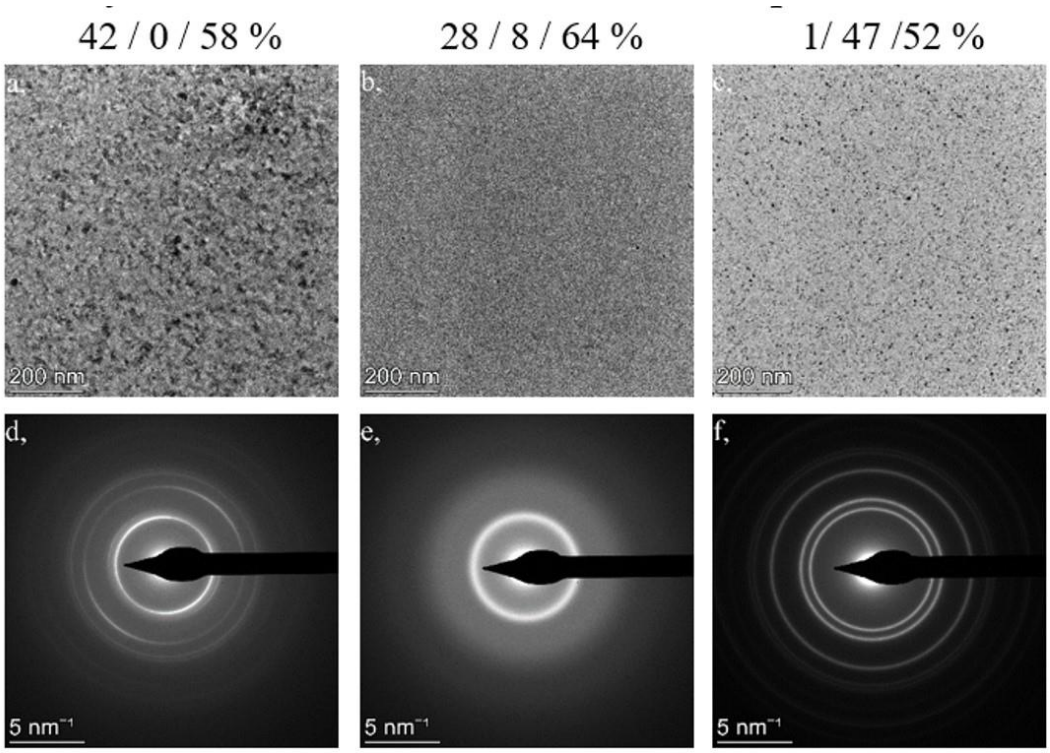

Figure 3.8. (a,b,c): *BF TEM image of selected Y/Ti/O (at%) compositions (d,e,f) the corresponding SAED patterns.* *Sharp rings (**d, f**) show polycrystalline, while diffuse rings **(e)** represent amorphous structure*

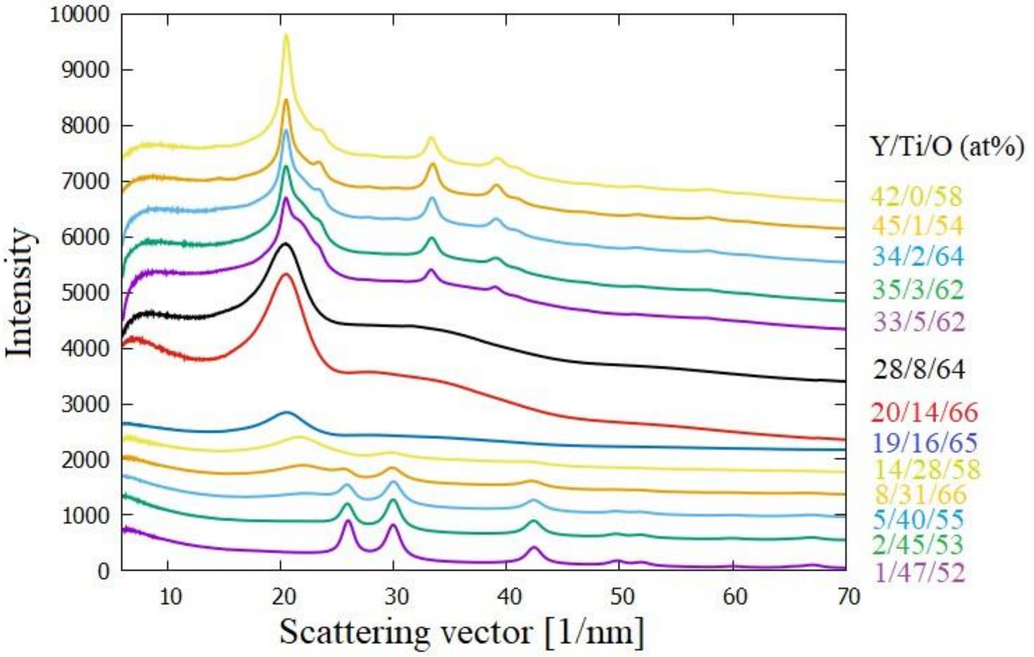

Figure 3.9. *Radial intensity distribution curves of SAED as a function of layer composition (curves are shifted along the intensity axis).*

The optical properties of the composition spread layer deposited on a Si slab were determined by spectroscopic ellipsometry (SE) during in situ heat treatment up to 600°C. A colour map of the measured data is shown in Fig. 3.10. showing the composition and temperature of the phase transitions and the potential regions where perovskite structure is found. The SE colour map can be used, in future studies, to select the thermal treatment parameters of combinatorial TEM samples to generate and characterize the perovskite structure in the Y-Ti-O system.

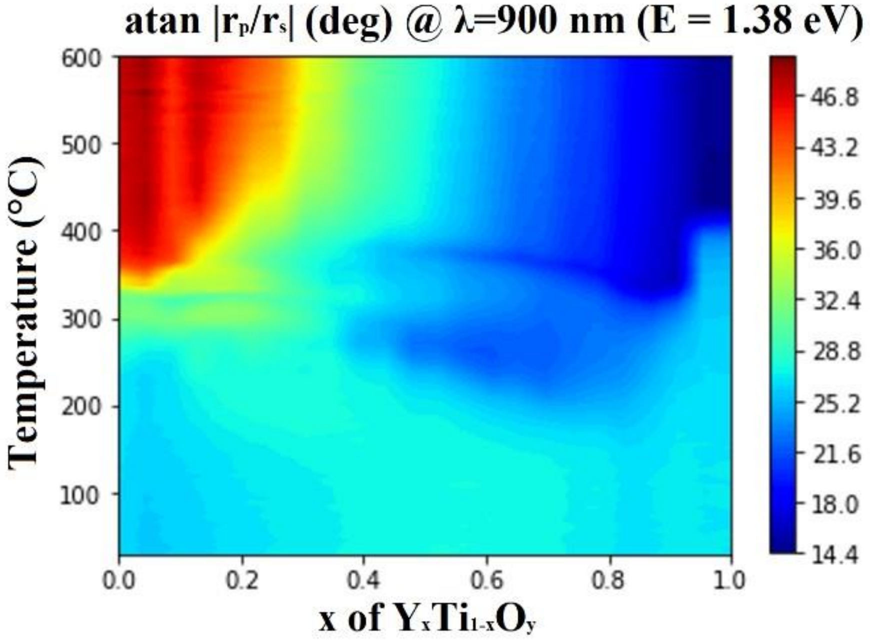

Figure 3.10. atan $\left|\frac{r_p}{r_s}\right|$ *map as the function of temperature and composition in the case of a microcombinatorial YTiO sample deposited on a 10x25 mm^2 Si slab. Separated regions imply morphological and phase transitions.*

In- and ex-situ study of nickel silicide formation in thin films

E. Dódony, I. Dódony (ELTE), G. Z. Radnóczi, G. Sáfrán

Due to their excellent physical and electrical properties nickel silicide layers have become one of the most promising components of microelectronics devices. To date, the mechanisms and reaction pathways of Ni-silicide formation remain unexplored, as the outcome depends on a wide range of experimental parameters (temperature, layer thickness, microstructure etc.). [Ref. 3.10- 3.12].

We studied in- and ex-situ the formation of nickel-silicides below 1073K in the solid state reactions between thin amorphous silicon (a-Si) layers and the supporting nickel TEM micro-grids. This unique experimental setup allowed us to reveal the sequentially forming phases of nickel-silicides, in lateral arrangement, by high resolution TEM (HRTEM) and selected area electron diffraction (SAED). During heat treatments at 860K and 973K we identified, almost all known silicide phases in reaction Zone 1 and 2 shown by Fig. 3.11 together with the Ni grid-bar at the lower right corner. The first reaction product observed was α-NiSi2, that was continuously present in Zone 1, at the reaction front advancing in the a-Si layer. (Fig. 3.11). The HRTEM image in Fig. 3.12.a shows α-NiSi2 in [110] orientation. Planar defects - stacking faults and micro-twins- are recognized both in the image and in the Fourier transform inset. While the average width of zone 1 remained constant, the width of zone 2 increased continuously during the reaction. Zone 2 is dominated by Ni31Si12. Fig. 3.12 represents HRTEM image of [100] oriented γ-Ni31Si12 full of planar defects. Besides Ni31Si12 we identified further phases in Zone 2. They followed a tendency of increasing Ni content towards the Ni-grid bar as follows: NiSi, ε-Ni3Si2, δ-Ni2Si, β1-Ni3Si, β2-Ni3Si. Together with these phases of Zone 2, the Ni31Si12 phase was abundant.

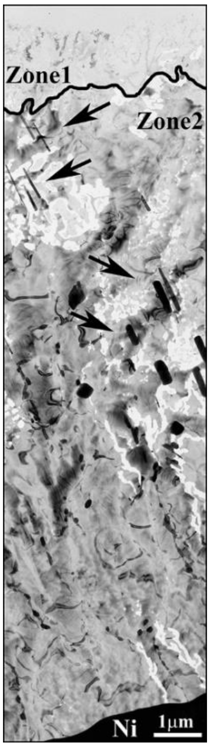

Figure 3.11. *Bright field TEM image depicts reaction Zone 1 and 2 formed as a result of solid state reaction between Ni grid and a-Si layer. Arrows show whiskers protruding from the thin layer.*

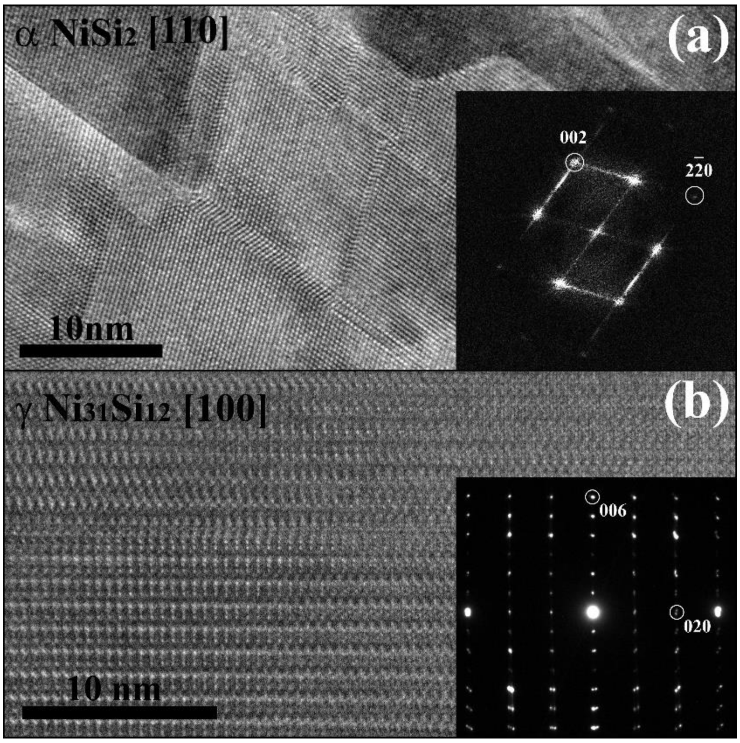

Figure 3.12. *HRTEM image of (a) NiSi2, the typical phase of Zone 1, showing planar defects, stacking faults and micro twins depicted by the image and the FFT inset, (b) the dominant γ-(Ni31Si12) phase of Zone 2 and its SEAD showing [100] orientation****.***

During the heat treatment elongated protrusions, whiskers (shown by arrows in Fig. 3.12) were ejected preceded by an intense diffraction contrast change in the parent crystal, suggesting the accumulation of compressive stress. It was found that whisker and its parent grain consist of the same phase. As the reaction progresses and the parent grain transforms into a phase with a higher Ni concentration, whisker undergoes the same transformation (NiSi → Ni_3Si_2 → Ni_2Si → Ni_3Si). This explains the coexistence of whiskers of different phases. It is to mention that whisker formation in the solid-state reaction of Ni and Si was first observed in our experiments.

In conclusion, because of their excellent physical and chemical properties, phase variability, as well as their applicability in microelectronics, the present results on Ni-silicide could be of both scientific and technological importance. However, to get a complete picture of the formation of silicides as thin films and whiskers in the Ni-Si system, further detailed studies are needed.

Application of microcombinatorial layer structure for tunable AlAg/SiN biosensors

G. Sáfrán, B. Kalas, M. Serényi, P. Petrik

In a collaboration of the MFA Thin Film Physics Department (VRF) and the Photonics Laboratory (FL), we have developed a wide detection range surface plasmon resonance (SPR) AlAg/SiN layer biosensor for various liquids and proteins. The complex geometry so-called Kretschmann-Raether (KR) arrangement [Ref. 3.13] of the SPR sensors was used to achieve energy and momentum conservation during the interaction between incident light and surface plasmons propagating on the semi-infinite metal surface (Fig. 3.13).

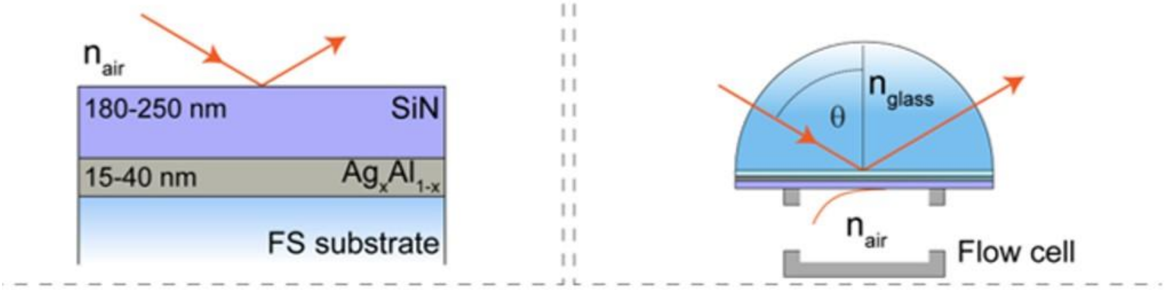

Figure 3.13. *SE measurement of a variable thickness* Ag_xAl_{1-x}*/SiN sensor in (a) simple (from sample-side) and (b) Kretschmann-Raether arrangement*

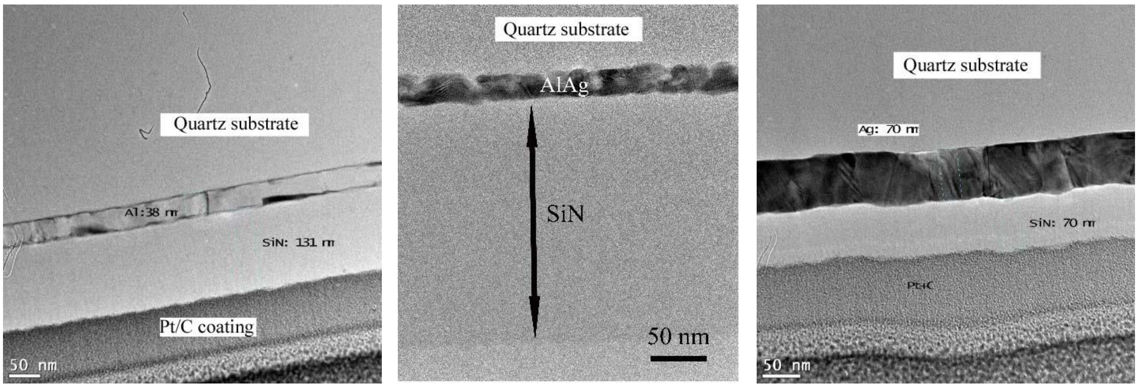

Figure 3.14. *XTEM images of Al end, centre and Ag end of a sensor prepared at a stage of sensor development. (left: Al: 38nm, SiN: 130nm, middle: Ag: 27nm, SiN: 220nm, right: Ag: 70nm, SiN: 70nm)*

The microcombinatorial technique [Ref. 3.8, Ref. 3.14-3.17], was used to fabricate an $Al_{1-x}Ag_x$ /SiN layered system sensor on quartz substrate with variable properties along the length of sample. This allows the plasmonic frequency to be tuned as a function of the illumination position for spectral ellipsometry measurements. The thickness of pure Ag, on the basis of optical model calculations, is estimated in the range of 40-50 nm, that is considered optimal for plasmonic applications, while for pure Al, due to its high optical absorption, a lower thickness is preferred. The thickness of the Ag-Al layer was specified as 40 nm on the Ag side and, with a continuous transition of composition and thickness, 15 nm on the Al side. Thus, as the Ag-Al composition changes along the sample, the thickness of the layer also changes. The layer was deposited from Ag and Al sources on a 25×10 mm^2 quartz substrate by DC magnetron sputtering through a 0.5 mm wide slot passing over the substrate. The maximum power applied to the Ag and Al targets was

150 W and 330 W, respectively. The variable composition and thickness were achieved by synchronized computer power control using stepper motor slot motion. The resonances in the KR alignment could also be easily tuned by applying an additional RF-sputtered SiN layer of gradient thickness. Diagrams in Fig. 3.14. are based on FIB TEM cross-sections of the two ends and the middle of the sensor covered with SiN of different composition and thickness show that the geometry is as designed.

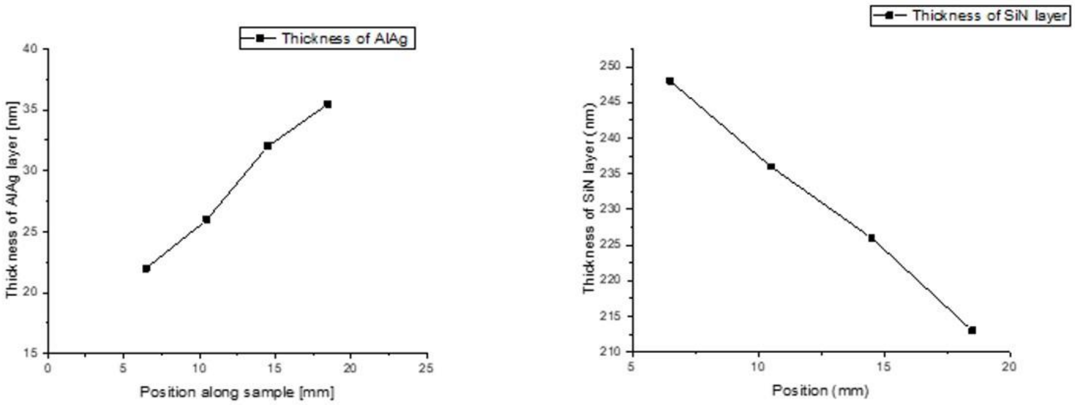

Figure 3.15. *AlAg and SiN layer thicknesses at selected positions of a sensor revealed by FIB-TEM measurements*

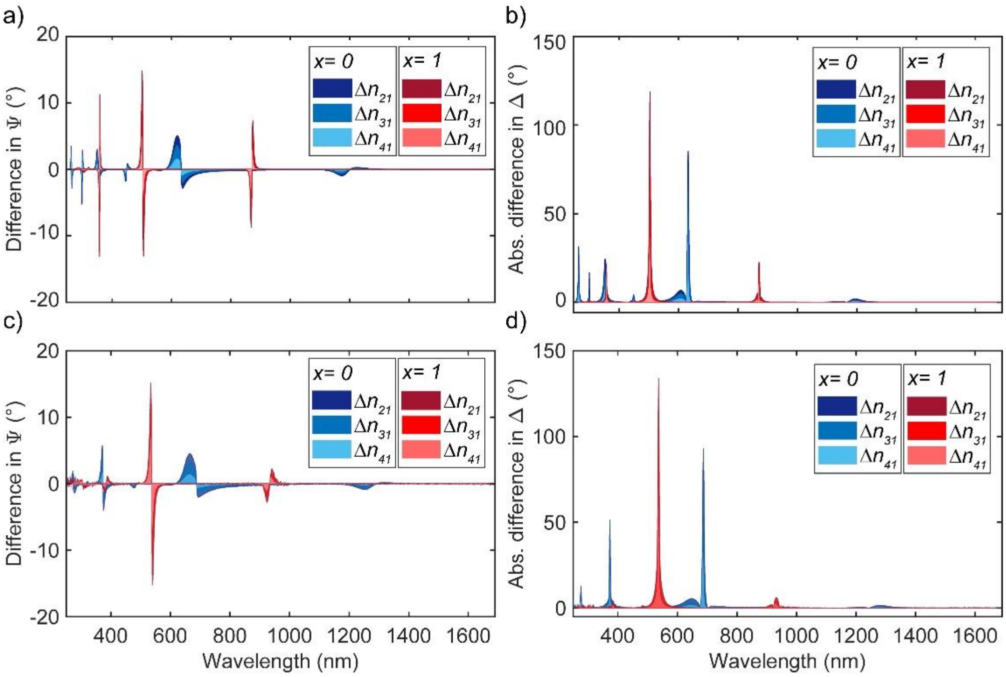

Figure 3.16. *Difference of simulated (a, b) and measured (c, d) Ψ and Δ spectra at compositions x = 0 and 1 for various DI water-isopropanol solution ambient. Δn_{j1} denotes the refractive index difference at λ = 632 nm (j = 2, 3, 4)*

The operation and tunability of the sensor in water and isopropanol test medium is demonstrated in Fig. 3.16. using the spectral ellipsometer with the difference spectra of the Ψ and Δ angles measured at both ends of the sample. A detailed discussion can be found in the PhD thesis of Benjamin Kalas [Ref. 3.18].

Combinatorial catalysis; development of bimetallic Ni-In catalysts for the dry reforming of methane with carbon dioxide

A. Horváth, M. Németh, A. Beck, G. Nagy, M. Serényi, G. Sáfrán

As a joint initiative of the Thin Film Physics Department (VRF) of the MFA and the Laboratory of Surface Chemistry and Catalysis (FKKL) and in the framework of bilateral Italian and Egyptian MTA grants, the microcombinatorial TEM method was applied for the first time in catalyst research. The catalytic system is the SiOx-supported nickel-indium catalyst of FKKL, which has been investigated in the so-called dry reforming reaction of methane with CO_2 ($CH_4+CO_2 \leftrightarrow 2CO+2H_2$) for several years with considerable success [Ref. 3.19-3.21] in environmentally conscious methane conversions: (1) CO_2 reactants to obtain synthesis gas ($CH_4+CO_2 \leftrightarrow 2CO+2H_2$), the aim here is to avoid deactivating carbonization of our NiIn catalyst [1] and (2) pyrolysis to obtain pure H_2 without CO_2 emissions ($CH_4 \leftrightarrow C+2H_2$), the opposite aim here is to increase the carbon deposition propensity of our NiMo catalyst. In the reforming reaction, the harmful carbonization of the catalyst is strongly inhibited due to the indium component, however, the effect of the Ni-In ratio has not yet been studied in detail. Our first SiO_2-supported catalyst had a Ni/In=3 composition, but indium may have a beneficial effect even at low concentrations e.g. Ni/In=24. The micro-combinatorial method developed at VRF allows the linear variation of the thickness of a component or the composition within one sample deposited by DC or RF magnetron sputtering. [Ref. 3.8, Ref. 3.14-3.15].

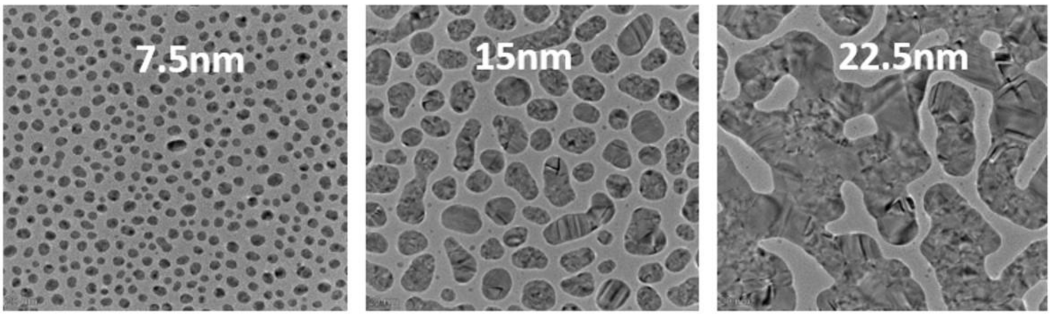

Figure 3.17. *Morphology of variable layer thickness revealed by combinatorial TEM*

This way we investigated the thickness dependence of size and morphology of pure nickel (Fig. 3.17.) on a variety of substrates e.g. C, SiO_2, Al_2O_3. The samples of varying thickness were subjected to oxidation and reduction according to the standard catalyst pretreatment. HRTEM, STEM-EDS and SEM-EDS measurements were performed to monitor the structural and morphological changes, so we optimised the size and distribution of the particles so that they do not aggregate during heat treatments.

The Ni catalyst layer optimised in the investigated range shows well-separated 5-20 nm grains after standard oxidation-reduction treatment (Fig. 3.18). The HR-TEM image clearly shows carbon deposit of 3-4 graphite planes (d=3.3 Å) built onto Ni grains, which originates from the bare or SiO_x-capped C-support. It is detrimental to the catalyst activity, therefore, in future, the use of the SiN/SiOx support is considered.

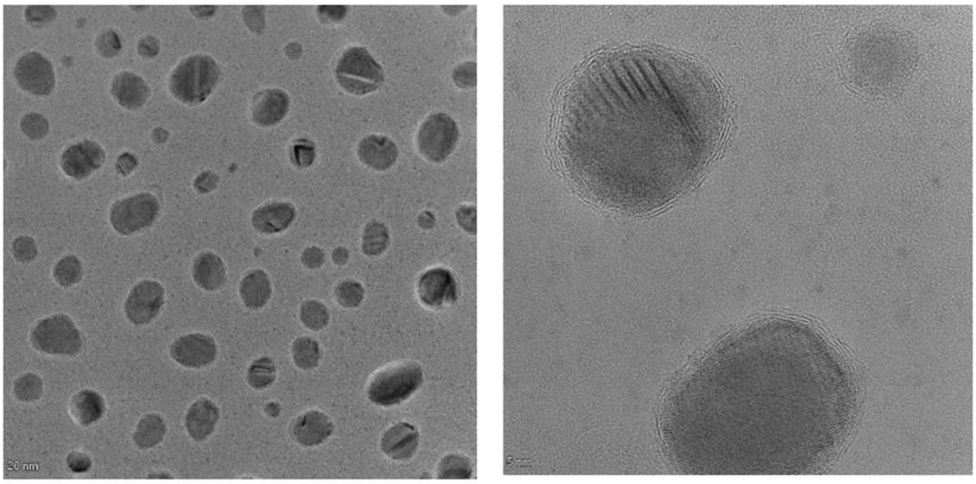

Figure 3.18. *TEM of 5~20 nm size Ni catalyst grains on C/SiO_x support after standard oxidation-reduction treatment. The HR-TEM image shows the carbon deposit on the Ni grains consisting of 3-4 graphite planes (d=3.3 Å).*

In subsequent experiments, we will add the catalyst in a controlled way, with indium, up to Ni/In=3 ratio, creating a regular concentration variation between the two endpoints of the sample. This will be followed by reacting the samples in a methane stream at various temperatures. Based on our experience, the Ni or NiIn particles are expected to exhibit different levels of carbon deposition depending on the local composition. TEM microstructural studies of the resulting carbon nanotubes, graphitic or amorphous carbon forms provide important information on the expected behaviour, efficiency and self-cleaning ability of a given Ni-In composition in methane dry reforming and thus allow to select the best performing Ni-In compositions. In a third step, nanoparticles with optimal Ni-In composition and morphological-structural properties are prepared by classical wet chemistry and tested under real catalytic conditions in a flow-through system (FKKL). The experience gained can also be used for the optimization of further two-component material systems, e.g. Ni-Mo. The use of the single-sample combinatorial method in catalysis development is new in the literature. The results of ongoing research will be used in the development of energy-efficient, low-temperature stable catalysts that convert methane and carbon dioxide into useful synthesis gases.

The growth of a multi-principal element (CoCrFeMnNi) oxynitride film by direct current magnetron sputtering using air as reactive gas

OTKA NN112156

*G. Radnóczi, R. Dedoncker (Ghent University), G.Z. Radnóczi, Zs. Czigány, A. Sulyok,
V. Kovács-Kis (MFA, University of Pannonia), D. Depla (Ghent University)*

Multi-principal element alloys (MPEAs) are a class of alloys that are composed of several elements in near-equimolar concentrations. The field of MPEAs was discovered about 15 years ago but still holds many interesting features. Against the intuitive expectation, some of these compositionally complex alloys have a simple crystallographic structure such as a face centred (fcc) or body centred cubic (bcc) structure with the constituent elements randomly distributed over the lattice positions [Ref. 3.22-3.23] When some specific requirements are reached, these materials can also be labelled high entropy alloys. These materials received already much interest due to their excellent mechanical behaviour as bulk material, but in thin film form many aspects remain undiscovered. Especially, research on compound thin films based on MPEAs holds a vast uncharted territory.

From literature and previous studies, it became clear that nitrides and oxides of alloys consisting of 4-5 components show the same remarkable structures when they are deposited by magnetron sputtering. In the case of the CoCrCuFeNi alloy, the addition of nitrogen or oxygen to the discharge resulted in the same B1 (NaCl) structure. This intriguing similarity triggers the interesting fundamental question whether this behaviour can be extended to a mixture of oxygen and nitrogen, and how both gases influence the structure formation during film growth.

In this paper, a detailed atomic level structural analysis of CoCrFeMnNi oxynitride thin films is performed. The goal is to get insight into the atomistic processes, responsible for the growth mechanism and the morphological development of the film structure.

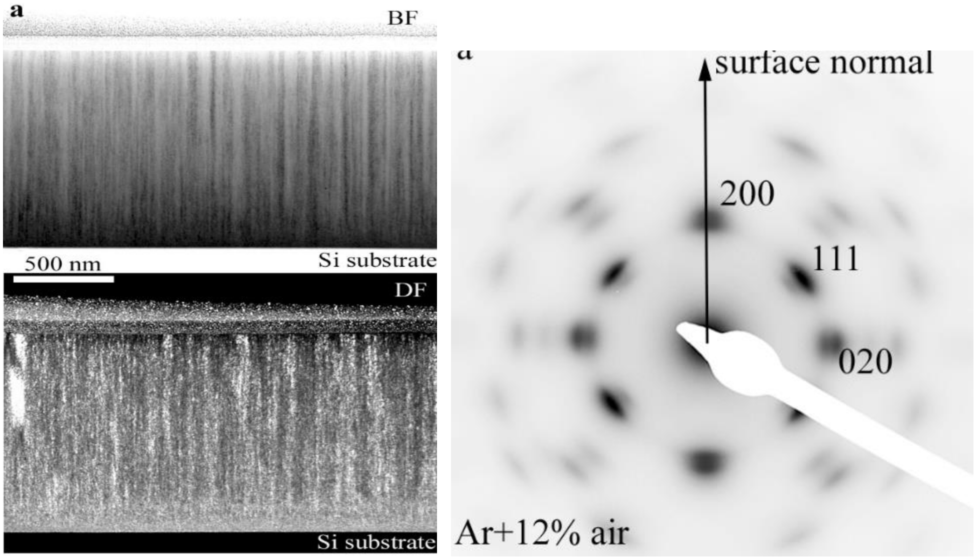

***Figure 3.19**. (a) Cross section bright field (BF) and dark field (DF) TEM images of film, grown in Ar+12% air sputtering gas. (b) Selected area electron diffraction (Ø1 μm area) of the film shown in a). The strong reflections belong to metallic CoCrFeMnNi alloy, the internal weak reflections belong to the CoCrFeMnNi-oxynitride compound.*

CoCrFeMnNi films were grown by DC magnetron sputtering using Ar+air as sputtering gas. A background pressure of less than 4×10^{-4} Pa was achieved by the combination of a rotary pump and a turbomolecular pump. A CoCrFeMnNi powder target was used according to a procedure described in [Ref. 3.23]. At a total pressure of 0.5 Pa the fractional flow rate of air was varied between 0-50 vol.%. The samples were deposited at room temperature on a Si [100] substrate with a native oxide. The growth rate was around 1.5 nm/s and the thickness of the grown layers varied between 1 and 2 mm.

Addition of 4–50% air to Ar in sputtering gas during deposition of CoCrFeMnNi alloy thin films resulted in a change of the phase state of growing film. At 12 % and 20 % of air in sputtering gas a 〈100〉 preferred orientation fcc CoCrFeMnNi alloy, doped with oxygen and nitrogen develops, which is stochastically intermixed with a B1 oxynitride nano-phase. The B1 oxynitride nano-phase is embedded epitaxially into the fcc CoCrFeMnNi alloy.

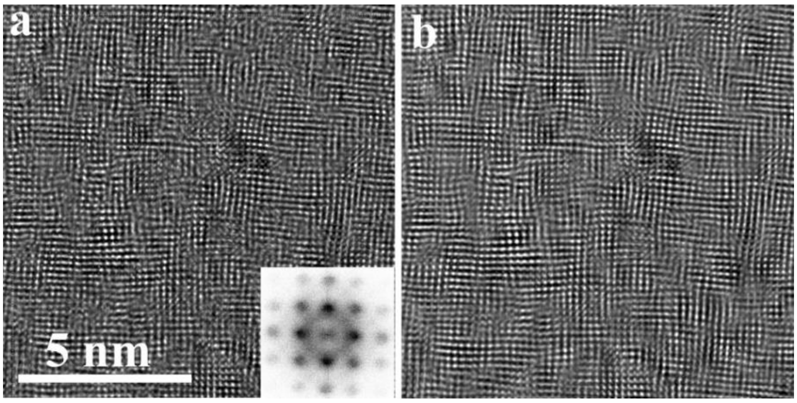

Figure 3.20. *High resolution image of the film grown in Ar+12% air sputtering gas and its FFT diffraction pattern (a), and the filtered image of the same area created by the 200 type reflections (b).*

At and above 30% of air a B1 phase CoCrFeMnNi-oxynitride forms with 〈100〉 preferred orientation. Oxygen is preferentially incorporated into the growing structures, while nitrogen content is inferior. The 〈100〉 preferred orientation is the result of selected nucleation (12 and 20% air) or competing growth (30 and 50% of air) of the developing crystals. All films produce broad Bragg peaks and a strong diffuse scattering which can be attributed to the nanoscale stochastic and/or partly ordered (rigid unit mode and ordered fcc) CoCrFeMnNi metal or CoCrFeMnNi-oxynitride lattice. The stochastic and ordered nano-structures are thought to be the result of spinodal processes taking place already during the growth process of the originally homogeneous structure. These kinds of structures and processes can be quite general in MPEA alloys and compounds.

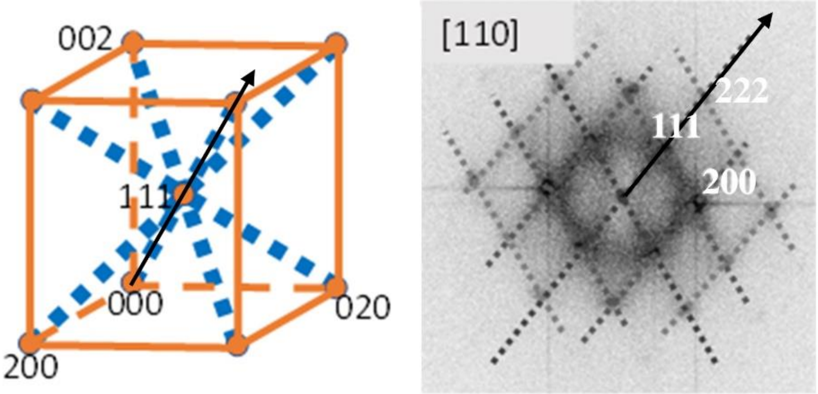

Figure 3.21. *The reciprocal unit cell of the fcc crystal with infinite rods (dotted lines) in 〈111〉 directions, due to the planar disorder on {111} planes in the lattice (left) and their geometry in an {110*} reciprocal lattice plane of 30% air sample (right). The dotted lines correspond to linear streaks in the diffraction pattern.*

Bioresorbable and biocompatible bioactive ion-doped, carbonated hydroxyapatite loaded biopolymer composites

OTKA PD131934

M. Furkó

The aim of this research work is to develop bioactive ion-doped bioceramic – biopolymer composite coatings onto implant materials. The ion-doped, carbonated hydroxyapatite (cHAp) powders were prepared by wet chemical precipitation using different calcium and phosphorus sources and co-precipitating with different bioactive ions such as Mg, Sr, Zn along with the base CaP. The micro and nanostructure of base cHAp powders were studied with regard to the post treatment after precipitation.

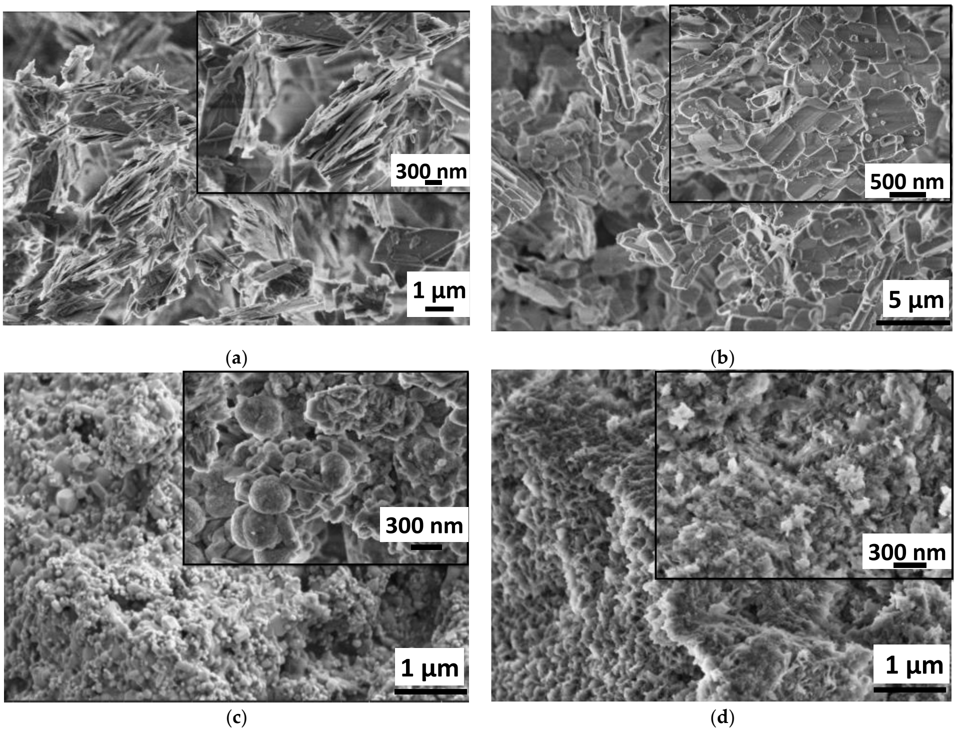

(a) (b)

(c) (d)

Figure 3.22. *SEM images of calcium phosphate particles (a) as-prepared by wet chemical precipitation (sample CaP1): magnification 20kX, inset 50kX (b) CaP1 sample heat treated at 650 °C for 5 hours (sample CaP2): magnification 10kX, inset 20kX (c) CaP1 sample heat treated at 900 °C for 5 hours (sample HAp1): magnification 20kX, inset 100kX and (d) CaP1 sample alkaline treated in* Na_2CO_3 *solution for 24 hours (sample HAP2): magnification 50kX, inset 100kX.*

Fig. 3.22 clearly demonstrates the difference in morphology of CaP powders prepared and treated in different ways. The as-prepared powder using Ca acetate as precursor has particles in the shape of large, thin plates in several micrometre sizes. These plates tended to be oriented parallelly (Fig. 3.23.a). This type of morphology is characteristic of the monetite phase. After heat treatment, the morphology of particles changed noticeably. Keeping the sample at 650 °C for 5 hours resulted in long, rod-shaped particles and smaller cubes attached together as well as large agglomerated blocks. This change in morphology can be attributed to the phase transformation to calcium pyrophosphate. Effect of ionic substitution: the addition of different bioactive ions into the starting solution has also changed the morphology of the precipitated powders. The substituting ions were also deposited in the form of low soluble phosphate precipitates along with different CaP phases. The forms and sizes of particles were very diverse, the powders contained large plate-like, rod-like grains in 0.5 – 5 µm sizes and small, needle-like particles as well as agglomerated spherical and flake-like particles. The elemental distribution of substituting elements was homogeneous within the CaP matrix according to the SEM elemental mapping.

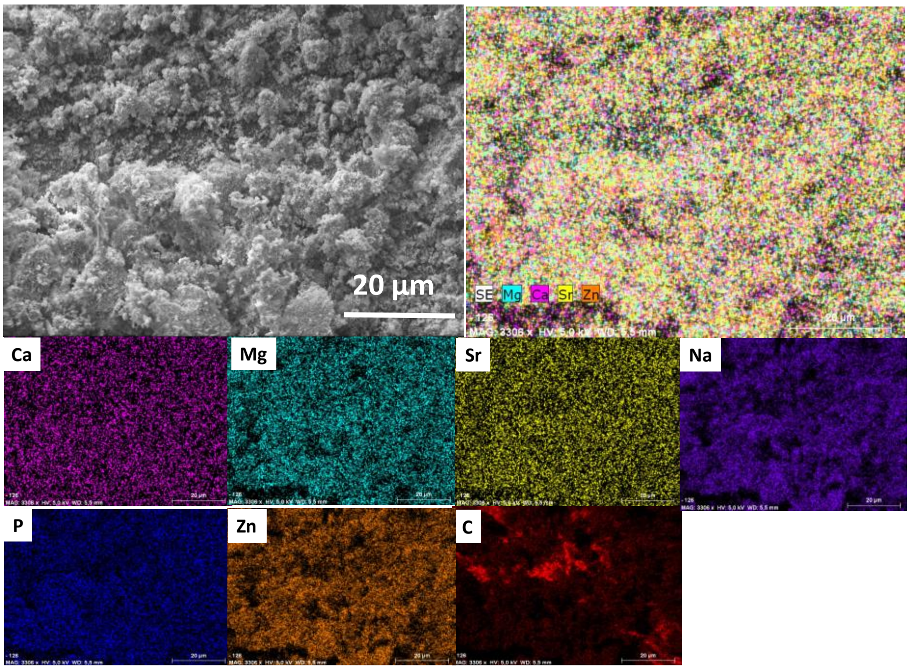

***Figure 3.23**. SEM image and elemental mapping on ionic doped CaP powder prepared from Ca gluconate precursor.*

CaP/biopolymer (Cellulose acetate, CA) composites were prepared by electrospinning technique. The bioactive ions were added to the base CaP suspension in the form of their chloride salts. The incorporation of added ions occurred during the co-precipitation with CaP phases. The suspension was mixed with biopolimer solution in appropriate concentrations and ratio in ethanol media. The fiber generation was performed by electrospinning apparatus, using high voltage difference between the two electrodes (needle and collector). According to SEM analyses, the CaP particles (white agglomerates, nodules) were sufficiently incorporated between the polymer fibers. the particles of HAp2 sample are attached to the CA fibres as clusters and the cover is discontinuous. In other words, the ceramic particles are incorporated into a mat of *interwoven* fibres. However, it can also be observed that the huge difference between the diameters of individual fibres, compared to pure CA fibres, lowered (between 100 and 400 nm) which can be attributed to the dispersed cHAp particles and the increased viscosity of suspension.

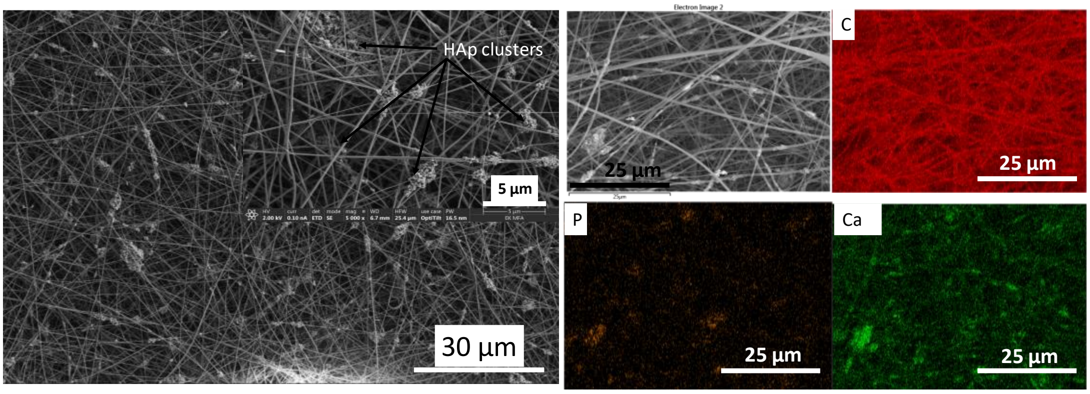

Figure 3.24. *SEM images on cHAp loaded cellulose acetate as well as the corresponding elemental mapping.*

Al_2O_3-AlN composite and AlON ceramic development using the powder technology

NKFIH NNE

K. Balázsi, M. Furkó, V. Varga, S. Gurbán, F. Cinar (ITU), Cs. Balázsi

Aluminum nitride (AlN) is an alternative refractory ceramic material being used in various range of applications such as optics, electronics and computer circuits for its unique thermal and electrical properties. It has a really high degree of thermal stability and wear resistance while exhibiting a low density. The aim of our work was the preparation of cheap Al_2O_3-AlN composites and transparent AlON by eco-friendly technology. Currently commercially available AlON materials show a larger grain size. The development of new methods to control the nano-grain size can improve the material´s properties. The most promising techniques for ceramic aluminum based preparation are the hot isostatic pressing (HIP) or spark plasma sintering (SPS). The currently available and used techniques are still all expensive, as well as being energy and time consuming. We intend to develop an eco-friendly preparation method (Fig. 3.25) of Al_2O_3-AlN and AlON in which we develop a novel way to reduce the temperature and/or time thus requiring lower energy.

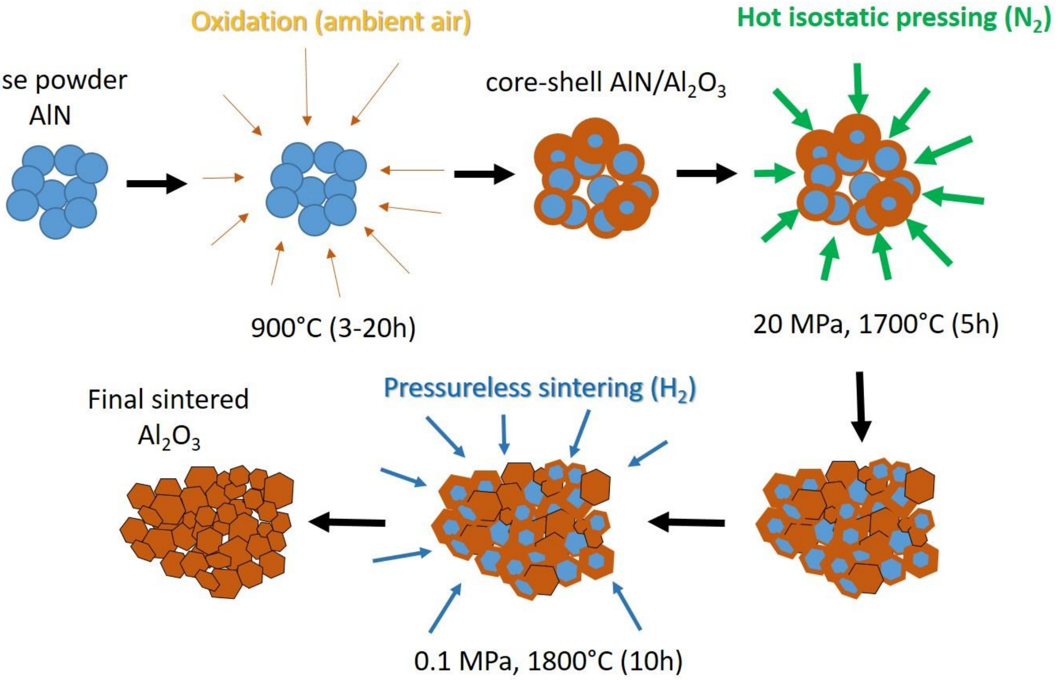

Figure 3.25. *Schematic view of preparation method*

The effect of the pressureless post-sintering in hydrogen atmosphere on the structural and mechanical properties of the hot isostatic pressed Al_2O_3 prepared by oxidized AlN powder has been studied. The micrometer size AlN powder has been oxidized in ambient air at 900° C for different times (3, 6, 10 and 20 hours) and sintered by hot isostatic pressing (HIP) at 1700°C, 20 MPa nitrogen atmosphere for 5h. Pressureless sintering (PS) has been applied for all HIP sintered samples in H2 gas at 1800° C for 10 hours. It has been shown that the oxidation caused a core-shell AlN/ Al_2O_3 structure and the amount of Al_2O_3

increased with increasing of the oxidation time of the AlN powder. For the first time, the green samples obtained from oxidized AlN powder have been successfully sintered first by HIP followed by post-sintering by PS under hydrogen without adding any sintering additives.

All post-sintered samples exhibited the main α- Al_2O_3 phase. The metastable oxide phases of Al_2O_3 have not been present in the post-sintered samples owing to the high temperatures involved in the processing. Sintering in H2 caused the full transformation of AlN to α- Al_2O_3 phase and their better densification. Therefore, the hardness values of post-sintered samples have been increased to 17-18 GPa having apparent densities between 3.11 and 3.39 g/cm3 [Ref. 3.24].

Porous sandwich ceramic of layered silicon nitride-zirconia composite with various multilayered graphene content

FLAG-ERA "Ceranea" , OTKA NN127723

K. Balázsi, M. Furkó, Zs. Fogarassy, V. Varga,
Z. Liao (IKTS), J. Dusza (IMR SAS), E. Zschech (IKTS), Cs. Balázsi

Development of the graphene-filled ceramic sandwiches that deliver materials with enhanced properties and functionalities was a part of the "Graphene Flagship" „CERANEA" project as a part of FLAG-ERA Joint Transnational Call 2017 for graphene supported by the European Commission.

The silicon nitride (Si_3N_4) is the widely used high-temperature ceramic material (up to 1500 °C). Due to its extreme high hardness and toughness in a wide range of temperatures, potential applications include reciprocating engine components, turbo chargers, bearings, metal cutting and shaping tools as well as hot metal handling. Silicon nitride has better mechanical properties at high temperatures compared to most metals, and its low coefficient of thermal expansion (CTE) results in a higher thermal shock resistance than for most ceramic materials. These ceramics can be prepared in different forms, sintered bulk or layered. Multilayer ceramic composites (MCC) consist of two ceramic materials. These ceramics are consisting of insoluble parts in each other and sequentially piled in a symmetric manner. In this work, we are firstly produced the gradient-structured Si_3N_4 ceramics with few layers' graphene by attritor milling and hot isostatic pressing (Fig. 3.26.).

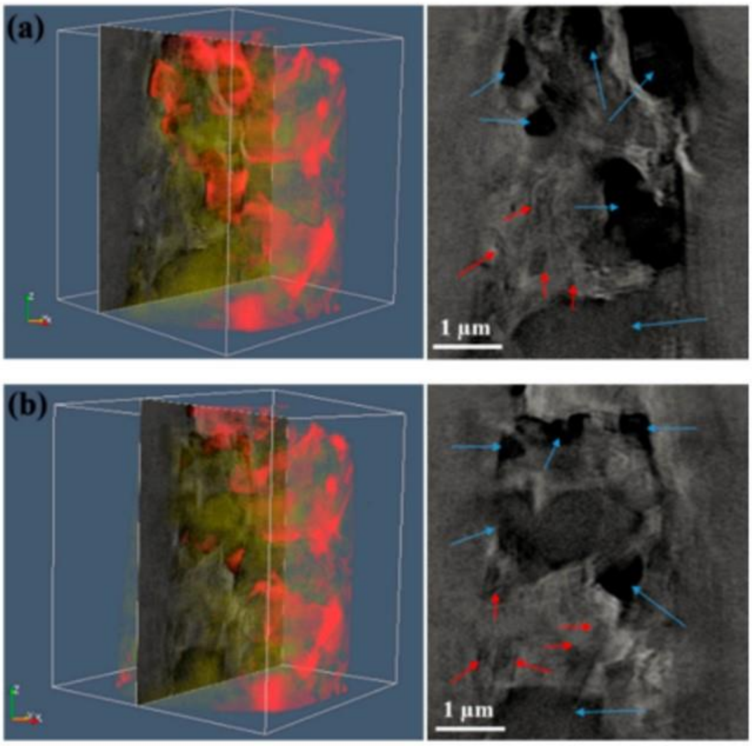

Figure 3.26. *Image of the multi-layered ceramic composite with different graphene content. Extracted slices from a volumetric reconstruction of the composite with 30 wt.% multilayer graphene (MLG) by synchrotron-based nano-X-ray computed tomography (XCT). ZrO2 phases are indicated by blue arrows, Si3N4 phases are indicated by red arrows*

The porosity of the samples increased by around two times with increasing of the multilayer graphene content (MLG) content. The density values were lower for samples with high MLG content owing to their very porous microstructure. The mechanical test confirmed that sandwich structure with combination of 5-30-5 wt% MLG layers showed 2 or 3 times better properties than structure with 30-5-30 wt% MLG. The main effect on mechanical properties had the layer with 30 wt% MLG with porosity of ~66% and high α/β-Si_3N_4 ratio of sintered ceramic matrix. [Ref. 3.25-3.28]

4-Nanosensors Laboratory

Head: Dr. János VOLK, Ph.D., senior research fellow

Research Staff:
- Gábor BATTISTIG, D.Sc.
- Zsófia BAJI, Ph.D.
- Nguyen Quoc KHÁNH, Ph.D.
- György MOLNÁR, D.Sc.
- Péter Lajos NEUMANN, PhD
- László PÓSA, Ph.D.
- János RADÓ, PhD
- Zsolt ZOLNAI, Ph.D.

Technical Staff:
- János FERENCZ, engineer
- Levente ILLÉS, engineer
- Attila NAGY, technician
- Erika TUNYOGI, engineer

Ph.D. students / Diploma workers:
- Péter HORNUNG, B.Sc. student
- Ádám, DACHER, B.Sc. student
- Binderiya OYUNBOLOR, M.Sc. student
- Zénó, PUSZTAI, M.Sc. student
- Tímea Nóra TÖRÖK, Ph.D. student

Nanosensors Laboratory was established at the beginning of 2019 from the former Department of Microtechnology. The core infrastructure, having two semiconductor clean rooms, is shared and operated together with the Microsystems Laboratory. The mission of the Lab is to utilize the emerging results of nanotechnology and materials science for novel physical sensors, particularly for micro- and nanometer sized electromechanical systems (MEMS/NEMS).

In the following sections nine selected topics are presented, which relate to
i) functional thin films (topics 1-5);
ii) nano- and micrometer sized electrical and sensor devices (topics 6-7); and
iii) novel sensor systems (topics 8-9).

These are conducted mainly in the framework of four domestic and international projects (OTKA: Atomic layer deposition and applications of functional sulfide nanolayers; OTKA: Development of Nanometer Scale Resistive Switching Memory Devices; NKFIH: Investigation of atomic or molecular processes induced by ultrashort laser and/or electron pulses; TéT: Atomic layer deposition and application of functional VO_2 thin films) as well as in a collaborative research with Puli Space Technologies (NASA challenge: Honey, I Shrunk the NASA Payload, The Sequel). The two highlighted topics of 2021 were the phase changing VO_2 and neutron converter ^{10}B thin films. Besides, the Nanosensors Laboratory provided services for several industrial partners (Lighttech, Technoorg Linda, Bosch, BHE - Bonn Hungary Electronics) and nanofabrication infrastructure for the National Quantum Technology Program and was engaged in university education as well (University of Debrecen, Budapest University of Technology and Economics).

Optimization of post vacuum annealed V thin films

Sloven bilateral 2019-2.1.11-TÉT-2020-00189, Bolyai fellowship, ÚNKP Postdoctoral fellowship

Gy. Molnár, Zs. Baji, L. Pósa, L. Illés, J. Volk, G. Drazic (National Institute of Chemistry, Slovenia), A. K. Surca (National Institute of Chemistry, Slovenia)

The oxidation of vanadium thin films is a promising method for the production of vanadium dioxide (VO_2) layers. VO_2 has been extensively studied for decades, because of its semiconductor (insulator) – metal transition at about 68°C. This is a first order phase transition accompanied by structural transformation from low-temperature monoclinic to high-temperature tetragonal phase. Besides the structural and electronic properties, the optical features change remarkably between the two phases. VO_2 has possible applications for microelectronics including memory and switching devices and for optical shutters and thermochromic smart windows.

Earlier, we studied the oxidation of vanadium film in atmospheric pressure air at different temperatures and time and found a rational fabrication method for the production of low switching temperature VO_2 [Ref. 4.1]. Recently, we have been trying to enhance the electrical and structural features of the vanadium dioxide films by reducing the pressure of the oxidizing ambient and optimize the time and temperature of the oxidation process.

Thermally oxidized Si wafers were applied as substrates. 100 nm thick vanadium films were evaporated from vanadium ingots using an electron gun. The post deposition heat treatments were carried out in a computer-controlled tube furnace in air at 1.0×10^{-1} mbar pressure. The annealing temperature varied between 400 and 480 °C and the annealing times were between 2 and 270 minutes. According to our measurements, the samples annealed at 400°C, for 270 minutes, in 1×10^{-1} mbar pressure air have the best electrical properties.

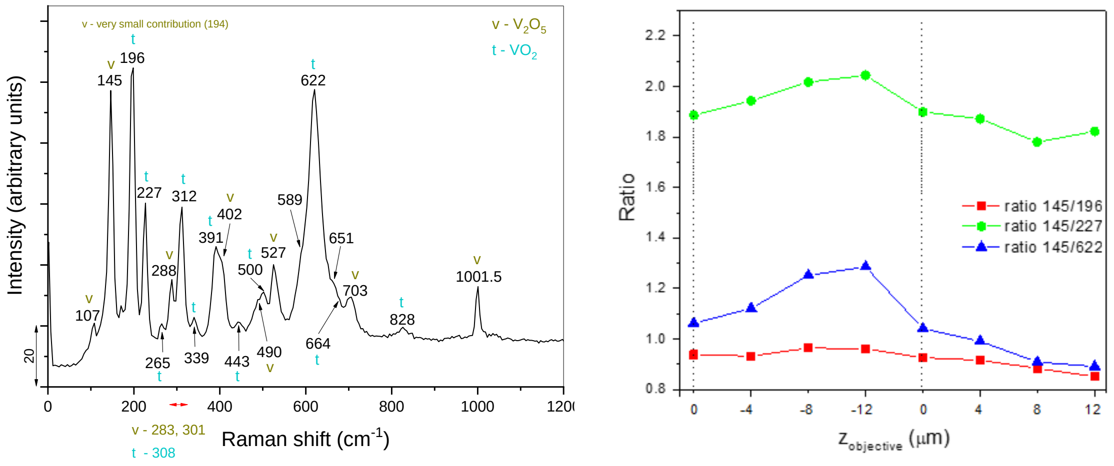

Figure 4.1. *Raman spectrum of V-oxide film on silicon wafer (left) Ratios of V_2O_5 (145)/VO_2 bands of Raman spectra taken at various z-axis positions of objective (right).*

The prepared films were analysed with electron energy loss spectroscopy and Raman spectroscopy. It is clear from both measurements that the film is pure vanadium-oxide with only two phases present: VO_2 and V_2O_5 (Fig.4.1). Fig. 4.2 shows the TEM image with the corresponding EELS spectra. The spectra of the topmost 50 nm of the layer show only the presence of VO_2 (spectra 1 and 2 in Fig. 4.1). The lower ~150 nm of the film consists of V_2O_5, as clearly shown by a characteristic shoulder of the L peak of V marked in spectra 3-5 in Fig. 4.2.

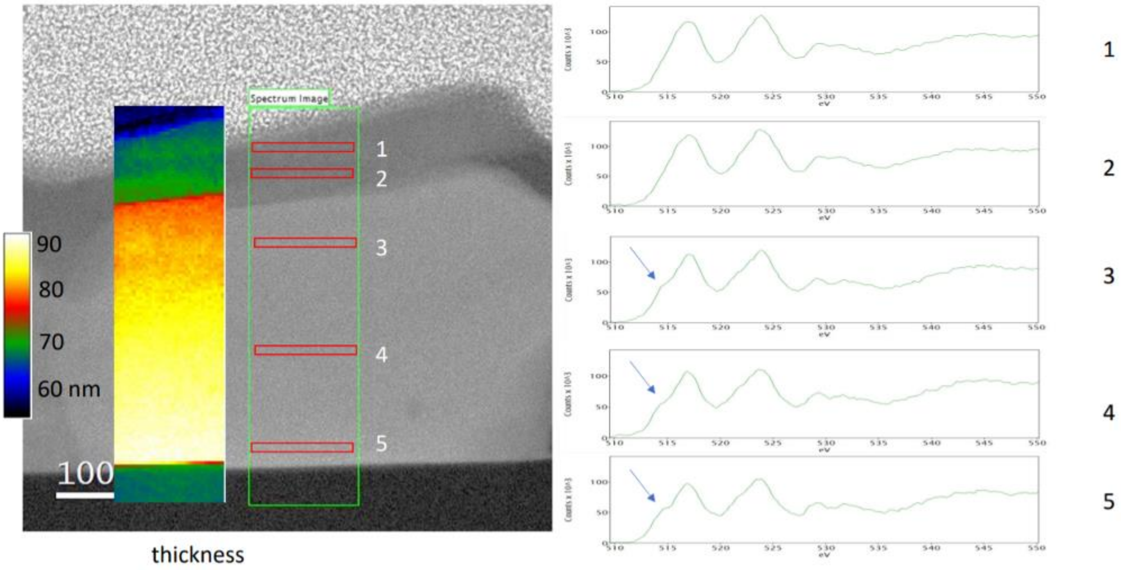

Figure 4.2. *EELS spectra from different depths of the VO_x layer*

The Raman spectrum of V-oxide film clearly shows that both vanadium oxides (VO_2 and V_2O_5) are present. The most intense band of V_2O_5 is 145 cm^{-1} and the most characteristic one is 1001 cm^{-1}. Also the band at 527 cm^{-1} belongs to solely V_2O_5. In other bands V_2O_5 is accompanied with VO_2. Raman spectra were also measured by moving the objective to sample different parts of the film along *z*-axis and the intensities of the most representative bands (145 cm^{-1} for V_2O_5, and 196, 227 and 622 cm^{-1} for VO_2) were measured and the ratios calculated. Fig. 4.1. shows the increase in the value of these ratios when the objective was directed more in-depth of the film. When the objective was directed upwards from the middle of the films, the opposite, the decrease of the ratios was noted, which shows that there is more V_2O_5 more in-depth and more VO_2 towards the surface, which agrees with the findings of TEM measurements.

According to these results, only the topmost 50 nm of the layer was VO_2. Nevertheless, the temperature dependent electrical measurements showed excellent switching properties. As Fig. 4.3 shows, there is a three orders of magnitude change in the resistance at the transition temperature reported in the literature. The hysteresis width is around 10–13°C, which is also a good value for polycrystalline VO_2 thin films.

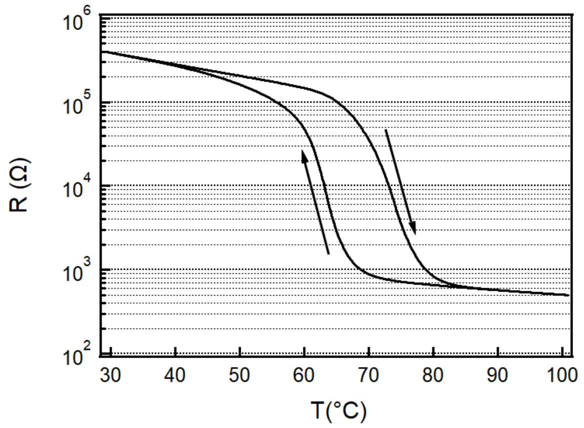

Figure 4.3. *The temperature dependent resistance curve of the VOx film*

Atomic layer deposition of HfS2 from Tetrakis(dimethylamino)hafnium

OTKA FK139075

Zs. Baji, Zs. Fogarassy, A. Sulyok, P. Petrik

2D materials with sizable bandgaps, such as transition metal dichalcogenides (TMD) have been in the focus of research, as they lack the drawback of the absence of an intrinsic band gap in graphene. HfS_2 is a less examined member of the TMD family, with most properties only theoretically predicted, and few reliable ways to synthesize. According to calculations, HfS_2 may have an ultrahigh room-temperature electron mobility and sheet current density, combined with a high chemical stability and reasonable bandgap, therefore it could be a very promising material for the transistors, photocatalysts and photodetectors of the future.

HfS_2 films can be prepared by mechanical or chemical exfoliation, or chemical vapour deposition but so far, no reliable preparation of HfS_2 layers on wafer sized surfaces has been found, although it would be extremely important for later applications. The atomic layer deposition of HfS_2 has not yet been explored, there are so far only a handful of papers describing the ALD of HfS_2 films using different precursors, but these layers were non-uniform and rough.

In this work, the use of the percursor tetrakis-dimethylamino-hafnium (TDMAH) was explored. Successful deposition with the use of H_2S as a reagent was performed between 200°C and 400°C. The growth rates were the following: 0.07nm/cycle at 200 °C, 0,08nm/cycle at 300°C and 0.06nm/cycle at 400 °C. The wafer scale uniformity of the films was determined by spectroscopic ellipsometry (SE), and the thickness was found uniform within ±1 nm on a 4” wafer size, which corresponds to a relative standard deviation of 2.5%. This is an excellent result previously not reported in the preparation of HfS_2 layers. The atomic layer deposition of HfO_2 from the same precursor always has a CVD like component, and the deposition of uniform films is not straightforward, it requires a precise tuning of the parameters and long pulsing and purging times. In the light of this, it is surprising that the ALD of HfS_2 provides such high-quality layers, and it may be attributed to the higher reactivity of H_2S.

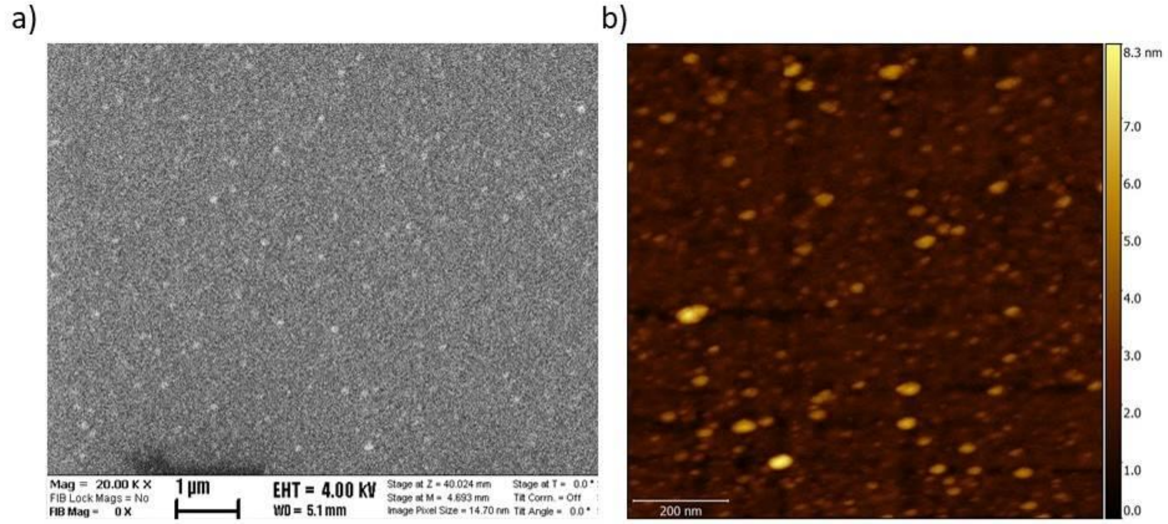

Figure 4.4. *HfS_2 films deposited at 300°C on Si(a), and on sapphire (b)*

The morphology of the layers was investigated with SEM and AFM. According to these, the films are not smooth at an atomic level, they have a slightly granular surface structure with typical grain sizes between 60-100 nm. However, all the layers are very smooth with RMS roughness below 9 nm in the case of silicon substrates, and 1 nm on sapphire (Fig. 4.4).

The composition of the deposited layers was determined by TEM EDS and XPS. Both methods showed that the films were mostly HfS_2, but the presence of HfO_2 was also detected, which can be attributed to the presence of some background oxygen in the deposition chamber. TEM analysis also proved that the films were amorphous, but after an annealing at 400°C, crystalline HfS_2 layers could be obtained, as shown by the FFT analysis of the film (Fig.4.5.b) The layer consists of crystalline 2D films stacked upon each other with an average distance of 0.59 nm between them.

After thicker films an ultra-thin layer was also synthesized. For this purpose, 10 ALD cycles were performed, with 0.3 s long TDMAH pulses followed by the closure of the ALD reactor for 1.5 s, then the evacuation of the reaction chamber is closed for 6 s to ensure enough time for the precursors to chemisorb to the surface and react with one another (picoflow mode). This method ensured that this ultra-thin film is also continuous and uniform. The thickness of the resulting thin film was measured by AFM (after etching a step with buffered oxide etchant in the layer), and it was found to be 3 nm. This means that the resulting film was about 5-6 monolayers thick. (Fig. 4.5.c.)

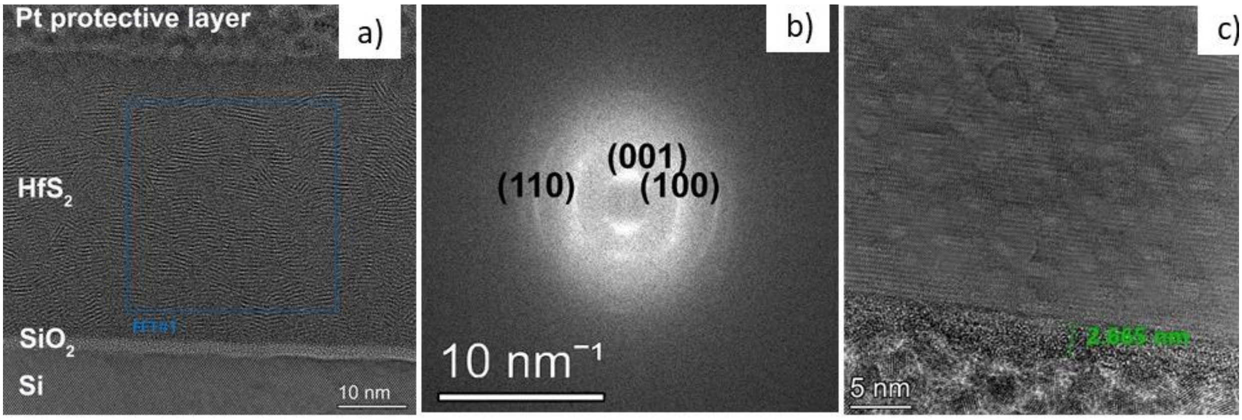

Figure 4.5. *HRTEM image of the film deposited on sapphire (at 300°C, annealed) (a), the FFT image of the same film (b) and the ultra-thin layer (c)*

The dielectric function spectra of the as deposited films on Si measured by SE also reveal an amorphous structure. The SE measurements showed high-quality, dense, compact, and homogeneous layers with a thickness of ≈40 nm. The optical band gaps of the layers were also calculated from the SE data. The gap of the film deposited at 200°C was 2.2eV, that of the film deposited at 300°C was higher, 3.3eV.

The film deposited at 400°C showed no definable band gap as measured by SE, instead appeared to present dielectric properties. This suggested a HfO_2-like behavior, and implied that the layer may be partly or completely oxidized, therefore, this film was further investigated and the XPS measurement also proved that this film was oxidized, and according to electrical measurement was an excellent insulator. The method proved to be a promising way to prepare this promising TMD material [Ref. 4.1].

Pulse DC deposited AlScN alloys for piezoelectric MEMS devices

NVKP_16-1-2016-0018 "KoFAH"

N. Q. Khánh, B. Oyunbolor, L. Illés, and J. Volk

For application of thin piezoelectric nitride film in sensors and energy harvesters, piezoelectric coefficient is the key feature. It can be improved by alloying nitride with scandium, but the result depends strongly on the parameters of given deposition system. We have studied the effect of pulse DC reactive ion sputtering system (VAKSIS – MiDAS) parameters on the properties of scandium nitride film for optimalization of the co-sputtering process.

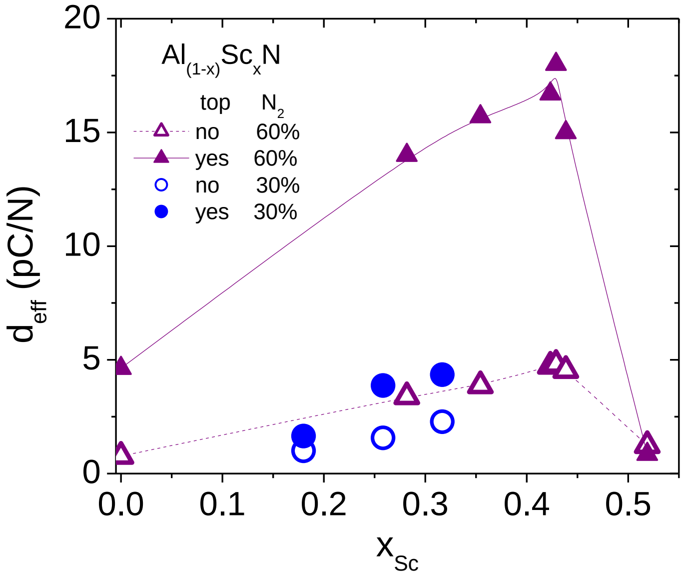

Figure 4.6. *d_{33eff} measured by piezometer as a function of Sc concentration on $Al_{(1-x)}Sc_xN$ nitride layers deposited using different $N_2/(N_2+Ar)$ gas ratio.*

Fig. 4.6 shows the benefit of alloying nitride with scandium, where the absolute values of piezoelectric coefficient (d_{33}) measured by Berlincourt method (Piezotester, PM-300) are shown as a function of *x*, i.e. Sc atomic concentration. Up to x~0.45, the higher Sc concentration, the higher the measured piezoelectric coefficient. Afterwards, d_{33} approaches zero at x~0.51. d_{33} measured using top electrode is significantly higher, than that measured on bare nitride. The reason may be that the top electrode keeps the nitride surface clean from ambient, hence excluding the effect of surface contamination on the transport of the generated charge between nitride surface and the measuring head, thus gives data close to the real values. One can also observe in Fig. 4.6, that the efficiency Sc alloying depends on gas ratio. Deposition using 60% N_2 gas ratio (triangles) results in better improvement of d_{33} than with 30% N_2 (circles). Besides, nitride surface is smoother for higher N_2 gas ratio.

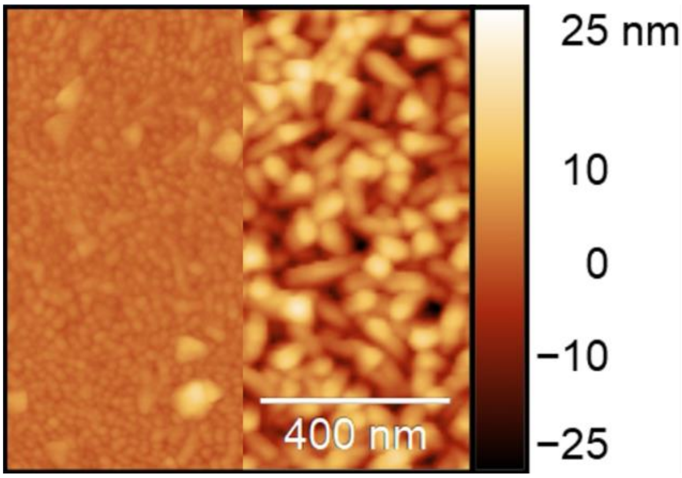

Figure 4.7. *AFM images of Al(1-18)Sc18N nitride layers deposited at 1.5 mTorr (left), and 3 mTorr (right).*

The most important parameter is the process gas pressure. As shown by AFM images in Fig. 4.7, only 1.5 mTorr difference in gas pressure resulted in much smoother surface, i.e. 1.7 nm, and 6.8 nm rms for 1.5 and 3 mTorr, respectively. The d_{33} measured by the piezotester is well improved for lower pressure, namely 9.9 pC/N compared to 1.8 pC/N. Because our system works with relatively long target-to-substrate distance (TSD), low gas pressure is needed for adequate mean free path of the sputtered particles to achieve good crystal. We note that using too high N_2 (>80%) gas ratio and low pressure may lead to instability of plasma, and low deposition rate.

Substrate effects on the intensity and radiative damping of gold nanoparticle plasmon resonance

OTKA FK128327

Zs. Zolnai, D. P. Szekrényes, D. Zámbó, A. Deák

In general, the far-field scattering intensity of plasmonic gold nanoparticles (GNP) is important factor in different applications like nanosensorics and surface enhanced Raman scattering (SERS). Note, besides non-radiative surface damping and chemical interface damping, to date less attention was paid to the radiative damping of surface plasmon resonance (SPR), despite the fact that it may have significant contribution to the overall damping (Γ), and it is related to the far-field scattering intensity of plasmonic GNPs. In this work we investigate the scattering intensity related radiative damping (Γ_{rad}) of SPR of individual gold nanorods (GNR) and nanospheres (GNS) supported by substrates to reveal the effect of the environment on Γ_{rad} and scattering intensity. Fig. 4.8.a shows dark-field optical scattering spectra of an individual GNR deposited on glass vs. the normalized power of exciting light (P_{exc}). The derived Γ and Γ_{rad} are also shown in Fig. 4.8.b No change (within 1 meV) in Γ_{rad} can be observed for different power levels. This can be understood as Γ_{rad} is related to the rate of energy transferred to radiated power through far-field electromagnetic scattering (P_{sc}) emitted by the GNP which supports plasmons with oscillator energy $E_{pl} = \hbar\omega_{pl}$, where ω_{pl} is the plasmon resonance frequency. Γ_{rad} [s^{-1}] can be defined as:

$$\Gamma_{rad} = P_{sc}/E_{pl} \qquad (1)$$

Since both P_{sc} and E_{pl} depend linearly on P_{exc}, Γ_{rad} will not change by varying the excitation power, as it is shown in Fig 4.8. On the other hand, for a GNP embedded, i.e., in a transparent medium, the particle will sense an effective dielectric constant ε_{eff} [Ref. 4.2]. In this case the relation between Γ_{rad} and the cross-sections for optical scattering (σ_{scatt}) and absorption (σ_{abs}) of the GNP can be computed as [Ref. 4.3]:

$$\Gamma_{rad}/\Gamma = \sigma_{scatt}/\sigma_{ext} = 1/[1+(\sigma_{abs}/\sigma_{scatt})] \qquad (2)$$

where Γ is overall damping and $\sigma_{ext} = \sigma_{scatt}+\sigma_{abs}$ is the extinction cross-section.

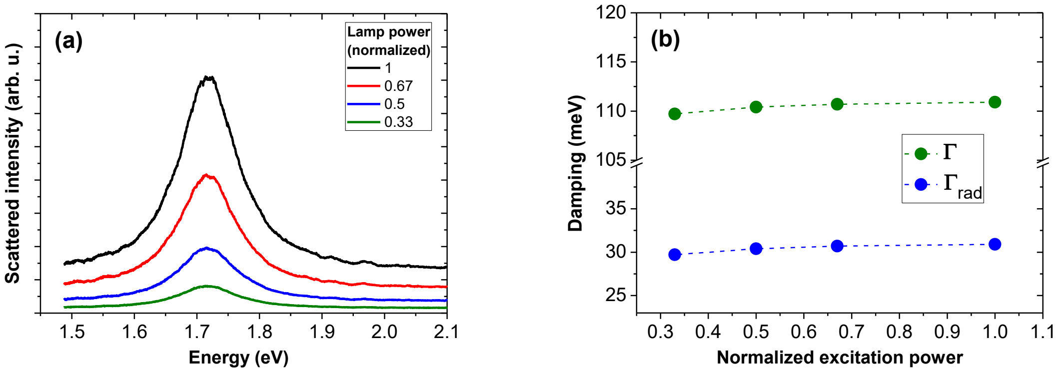

Figure 4.8 *(a) single particle dark-field scattering spectra of a gold nanorod (GNR) measured at different power levels of the light excitation source (normalized power values); (b) derived FHWM (Γ) and radiative damping (Γ_{rad}) values for the SPR of the same GNR vs. the excitation power.*

Considering that [Ref. 4.4]:

$$\sigma_{abs}/\sigma_{scatt} = 6\pi(L^2c^3\omega_b^2\Gamma_{nr})/(\varepsilon_{eff}^{5/2}V\omega_{pl}^2) \tag{3}$$

where L is depolarization factor, c is the speed of light in vacuum, ω_b is bulk plasmon frequency for gold, while V is the volume of the GNP, and utilizing that the parameters Γ_{nr}, ε_{eff}, V, and ω_{pl} can be determined from experimental optical scattering spectra and scanning electron microscopy analysis, one can calculate $\sigma_{abs}/\sigma_{scatt}$, and thus Γ_{rad}, considering that $\Gamma = \Gamma_{rad} + \Gamma_{nr}$, where Γ_{nr} is non-radiative damping (note Γ is the FWHM of the Lorentzian shaped optical scattering spectrum).

Fig. 4.9.a shows that for GNSs and GNRs embedded in glass [2] the values of Γ_{rad}/Γ derived from Eq. (2) and Eq. (3) agree well with those evaluated from $\Gamma_{rad} = \Gamma - \Gamma_{nr} = \Gamma - (\Gamma_b + \Gamma_{ib} + \Gamma_s)$. Here Γ_b, Γ_{ib}, and Γ_s are the non-radiative bulk, interband, and surface damping terms and they can be calculated according to previous works [1]. When the GNSs and GNRs are deposited on the surface of glass, the ratio Γ_{rad}/Γ changes significantly for both spherical and elongated particle shape, see Fig. 4.9.b. Especially for GNRs, better agreement is found when in Eq.(3) a value of $\varepsilon_{eff} = 1$ (air) was considered for the embedding medium and an additional substrate-related correction has been applied for the scattering cross-section.

This correction accounts for the mirror charge effect, induced by the SPR of the GNP in the underlying polarizable substrate. In case of glass substrate the correction for σ_{scatt} is $\sigma'_{scatt} = \sigma_{scatt}(1+\eta)^2$ where $\eta = \pm 0.38$, and + (-) sign holds for a GNS (GNR) with transversally (longitudinally) polarized SPR related to parallel (antiparallel) polarization in the substrate with respect to the polarization of the GNP. For GNSs and GNRs deposited on glass a correction factor of ~1.9 and ~0.38 applies, respectively, which means opposite effect of the substrate for the two different particle shapes. As Fig. 4.9.b shows the substrate effect on GNRs is significant and suppresses Γ_{rad} and thus the far-field scattering intensity. For GNSs either the increase of ε_{eff} (due to the proximity of glass) or the mirror charge effect will increase Γ_{rad} and the scattering intensity, moreover, their impact seems to be comparable when estimated separately.

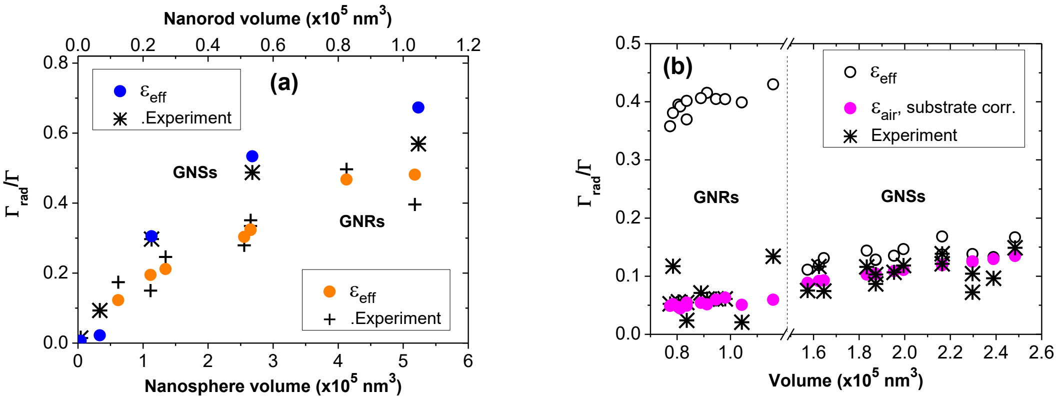

Figure 4.9. *Ratio of the radiative damping and full damping of the SPR in gold nanospheres and nanorods (a) embedded in a glass layer (data are from [2]) and (b) deposited on the surface of a glass substrate, as a function of the volume of the GNP. Crosses and stars represent experimental values, dots show calculations. In (b) the effect of the substrate is estimated in two different ways, for open dots an effective dielectric constant (ε_{eff}) was considered around GNPs, while for full dots air ambient and mirror charge effect in the underlying substrate have been taken into account*

Based on the above results we conclude that the presence of a polarizable substrate introduces asymmetric environment around a GNP deposited on it and further work is required to reveal the full effect of different substrates on the scattering intensity and radiative damping of plasmonic GNPs.

Deposition of 10B thin films for novel neutron detectors

N. Q. Khánh, L. Illés, P. Petrik, and J. Volk in collaboration with PuliSpace

^{10}B and its compounds (B_4C, BN) have been widely used in thermal neutron detection *via*

$^{10}\mathrm{B}(\mathrm{n}, \alpha_0)^7\mathrm{Li}$: Q_0=2.792 MeV

$^{10}\mathrm{B}(\mathrm{n}, \alpha_1\gamma)^7\mathrm{Li}$: Q_1=2.310 MeV

reactions, owing to its very large capture cross-section for thermal neutron. When the reaction products (α, ^{7}Li) are used for neutron detection, single element ^{10}B is better than its compound, because the particles do not scatter on other elements in compound on the way to detector, thus have higher energy, i.e. higher detection efficiency. However, being semimetal boron target is almost insulator at RT, which prevents stable plasma formation near target surface even in pulse DC system.

We have applied the built-in substrate radio frequency (RF) unit together with pulse DC input to ignite plasma at the beginning of deposition process, which can be switch off, when the target becomes hot enough, i.e. has sufficient electric conduction on its surface, thus ensuring the stable plasma in pulse DC mode alone. For comparison, the deposition rates of 35nm/h, 97nm/h, and 208 nm/h have been determined by Scanning Electron Microscope (SEM) for pulse DC, RF, and substrate RF ignited pulse DC depositions, respectively, where similar inputs (gas pressure, power) were set.

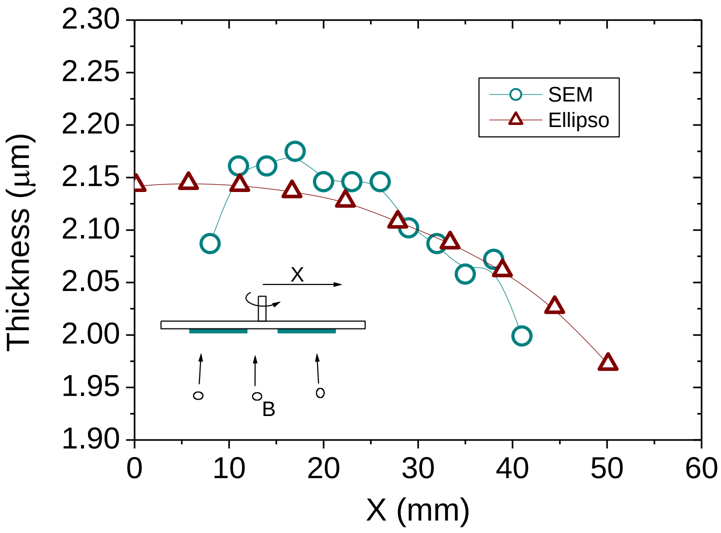

Figure 4.10. *Boron film thickness measured by Spectroscopic Ellipsometer (triangle) and SEM (circle) across control wafers.*

Enabling pulse DC sputtering of boron target by this manner, the boron film with thickness of ca. 2 µm, i.e. the optimal thickness given by simulation can be deposited in reasonable time. The thickness of boron layer across the control Si substrate was determined by SEM and Spectroscopic Ellipsometer (Fig. 4.10). The thickness homogeneity over the sensing area is ca. 2.5%.

As an example, applying substrate RF ignited pulse DC sputtering of boron target, we managed to neutron-sensitize a small (10x10x35cm), light weight (0.4 kg) neutron counter developed by PuliSpace Ltd. Fig. 4.11 shows the cross-section SEM image of the neutron sensing head of the similar device we sensitized with 870 nm boron layer on top.

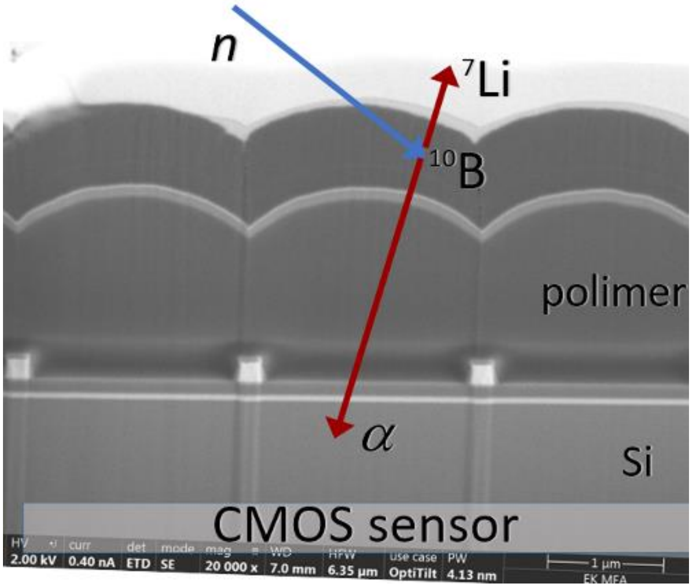

Figure 4.11. *Cross-section SEM image of CMOS sensor neutron sensitized with boron film. Sketch shows detection principle.*

Vanadium-oxide based memristive switches

OTKA K128534, Bolyai fellowship, ÚNKP postdoctoral fellowship

L. Pósa, T. N. Török, Gy. Molnár, Sadaf Arjmandabasi, J. Volk,
in collaboration with A. Halbritter and Dept. of Physics, BME

VO_2 resistive switches were fabricated by depositing Ti/Au electrodes onto VO_2 thin layer. Three different electrode designs were tested, whose geometries are shown in Fig. 4.12.a-c. The device operation is the same for all types: the VO_2 is switched only in a nanogap region, located between the metal electrodes. In the first two cases (Fig 4.12.a-b) nanogap is defined by electron beam lithography, whereas in the third case, a sub-5nm nanogap is formed subsequently by controlled electromigration of the nanowire. The best device performance was demonstrated by the second electrode design, where a sharp electrode faces with a flat one and the gap size is around 20-30 nm. The device could be switched between its two states more than $2{\cdot}10^5$ times with stable electrical parameters at room temperature. The typical I-V characteristic is shown in Fig. 4.12.d. Initially the device is in high resistance (OFF) state at zero bias voltage. By increasing the driving voltage, at a threshold bias voltage (set voltage, ≈1.06 V), the VO_2 at the nanogap region switches to the metallic state and the current jumps several orders of magnitude.

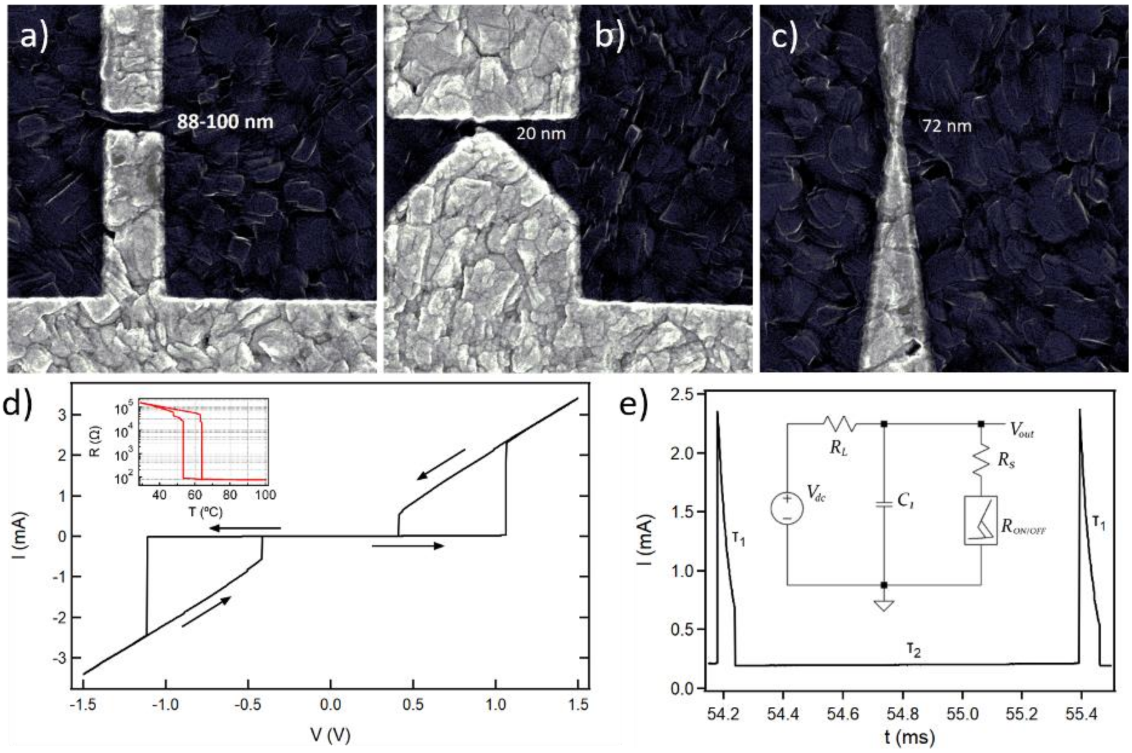

Figure 4.12 a-c) *SEM micrograph of the metal electrodes (light grey) on the surface of the VO_2 thin layer (dark grey). The three different structures mean three different gap size from 100nm to 5nm.* ***d)*** *A representative current-voltage (I-V) characteristic of the volatile VO_2 memristor. The arrows indicate the switching directions. The inset shows the resistace of the device versus temperature.* ***e)*** *Waveform of the current flowing through the VO_2 device in the oscillator circuit. The phase transitions occur during the sudden current jumps, while during the smooth current increase/decrease the capacitor is charging/discharging. The inset shows the circuit diagram of the oscillator.*

This low resistance (ON) state is preserved until the backward voltage sweep, when the device transforms back to its original high resistance state at the reset voltage level (≈ 0.41V). Due to the unipolar behavior of the device, the same characteristic is seen at the negative bias polarity with the similar switching parameters. During the I-V measurement a serial resistance of 380 Ω was connected to the electrical circuit to protect the VO_2 device from the high current. This serial resistance is seen in the high voltage part of the I-V traces.

The temperature dependent electrical resistance trace of the device (inset of Fig. 4.12.d) exhibits very sharp phase transitions with larger resistance change than was measured during the layer optimization process. This finding may result from the very small size of the nanogap, it is comparable with the grain size. The first device structure with flat electrodes and 100 nm large gap worked only at elevated temperature (≈60 °C), close to the phase transition temperature, which may result from less efficient Joule-heating and a lower electric field. In case of the third design, we could form the sub-5nm large nanogap, however during the electrical switching the narrow electrodes were too unstable and we could not operate the memristor reproducibly.

Owing to the volatile hysteretic resistive switching behavior of the VO_2 memristor, we can construct astable oscillator by connecting a parallel capacitor (C_1) and an external d.c. voltage source (V_{dc}) to the memristor through a load resistor (R_L) (Fig 4.12.e). The current flowing through the device is shown in Fig. 4.12.e, the state of memristor is periodically altered between the ON state (high current part) and OFF state (low current part). The characteristic time constants (τ_1, τ_2), which belongs to the charging and discharging of the capacitor can be tuned by the external electric elements. These oscillators could be used e.g. in the hardware realization of spiking neural network.

Besides the unipolar spikes, the action potential like signal can also be produced by constructing artificial neuron. The artificial neuron consists of two resistively coupled astable oscillators, each having a d.c. biased active memristor (X_1, X_2), a parallel capacitor (C_1, C_2), and a load resistor (R_{L1}, R_{L2}) (Fig. 4.13.a). According to the firing characteristic, the neurons can be a tonically or a phasically active neuron. In the former case the neuron fires evenly spaced spikes or burst of spikes when stimulated by a steady d.c. input. This firing behavior is demonstrated by a tonic burst signal in Fig. 4.13.a. The phasically active neurons, on the contrary, fire only a single spike or burst of spikes at the onset of the steady d.c. input due to transient dynamics and remain quiescent afterwards as the input reaches the steady state. Fig. 4.13.b shows a rebound spike behavior in a phasic VO_2 neuron. The basic parameters of the generated neural signal, such as period time, number of spikes per period, duration of a spike, voltage offset, etc., can be tuned by the electrical circuit elements (capacitances, resistances, voltage levels). The VO_2 arbitrary neurons are promising devices to construct highly efficient brain-machine interfaces.

We simulated the electrical circuit of the artificial neuron by MATLAB using Simulink environment. The VO_2 memristor was realized by a two-state switch with hysteresis, controlled by the potential difference between the nodes. The simulation enables us to set the proper resistance, capacitance and voltage values to get the desired output waveform. A simulated physically active neuron is seen in Fig. 4.13.d, whereas the time dependent energy consumption is shown in the inset. The energy needed to generate single, 40 µs long spike is around 8.2 nJ.

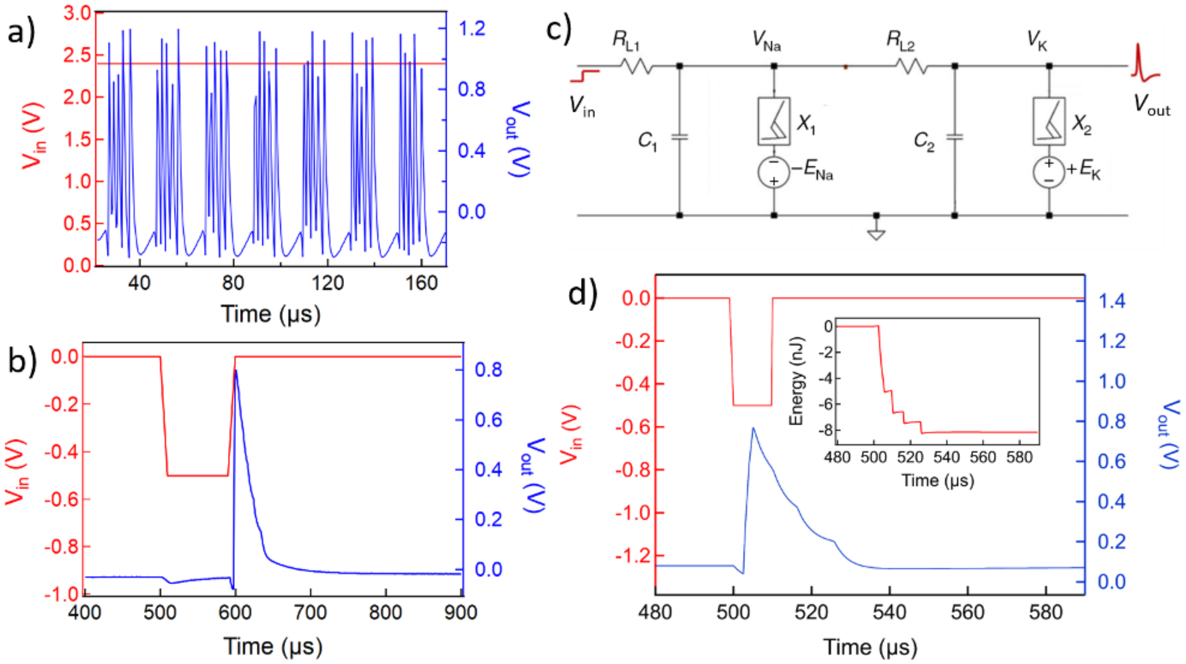

Figure 4.13 a) *Tonic bursting behaviour in response to the d.c. input voltage.* ***b)*** *Rebound spike behaviour: the neuron receives and then is released from an inhibitory, negative input, it fires a post-inhibitory (rebound) spike. in response to the release (the rise edge) of the inhibitory input waveform.* ***c)*** *The circuit diagram of the tonically active neuron, which produces the neuronal function, shown in panel a).* ***d)*** *Simulated physically active neuron using MATLAB Simulink software. The inset shows the time dependent energy consumption.*

AlGaN/GaN heterostructure based force sensor

P. Neumann, J. Radó, J. Ferencz, J. Volk

GaN, as a piezoelectric wide-bandgap semiconductor, can play an important role in next generation micro- and nanoelectromechanical systems (MEMS, NEMS). It is electrically more resistant in harsh environment and against ionizing radiation than Si, which triggers new applications in space technology. Moreover, epitaxial thin films are already commercially available on Si wafer making it compatible with standard Si MEMS technology.

In this work a novel AlGaN/GaN heterostructure based 3D force sensor (2DEG force sensor) is proposed. The principle of operation is like that of its Si counterpart: a thin membrane is deformed upon applying a loading force on the Si micro-stick formed on the back-side of the membrane. Local strains in four positions of the membrane are measured by semiconductor gauges. By collecting the electrical signals both the magnitude and the direction of the force can be determined. However, in contrast to conventional Si piezoresistive devices, here mechanical strain influences the density of the 2-diementional electron-gas (2DEG) at the AlGaN/GaN interface by changing the magnitude of the discontinuity in the polarization vector between the two layers.

For a side-by side comparison with our standard Si piezoresistive force sensor, we employed the same device geometry for the 2DEG force sensor. We used a commercial high-electron mobility transistor (HEMT) epilayer stack (GaN(3 nm)/AlGaN (22 nm)/GaN (1,5 um)) grown onto a 4” Si wafer (NTT-AT). During the fabrication process we fabricated four voltage divider bridge circuits on the device side, each having a reference AlGaN/GaN resistors on the bulk and a sensitive one on the top of the membrane (Fig. 4.14.a). AlGaN/GaN resistors were formed by physical Ar etching from the top down to the semi-insulating GaN layer (mesa structure) and by a subsequent ohmic contact formation. The flexible membrane and the Si microstick are formed by a deep reactive etching (DRIE) step from the backside of the Si wafer. The schematics of the device geometry from both sides and the result of a finite element calculation (Comsol) are shown in Fig. 4.14.b and 4.14.c.

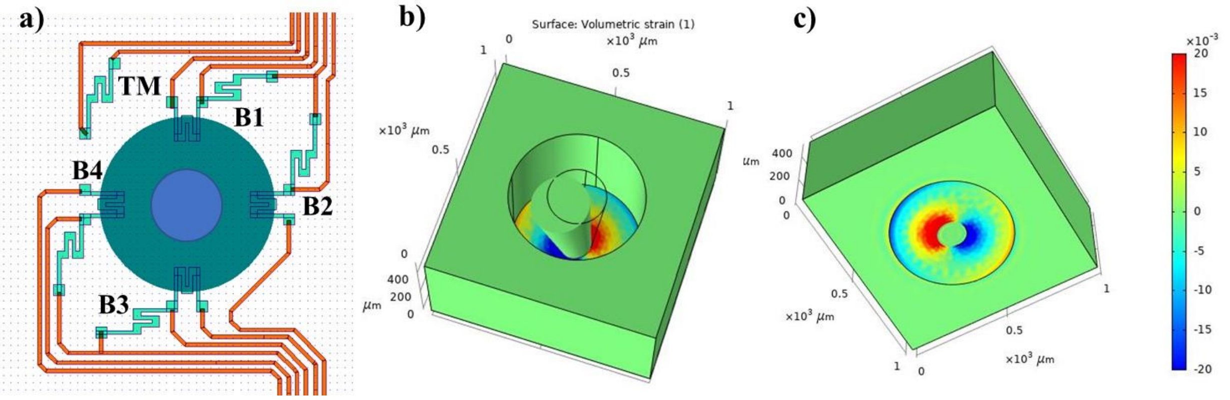

Figure 4.14. ***a)*** *Layout of the AlGaN force sensor from the epilayer side. Each B1-4 voltage divider bridge consists of a strain sensitive 2DEG resistor placed on the membrane (green area) and a reference meander on the bulk. Direction sensitive strain distribution occurs upon pressing the columnar Si stick (blue area). Volumetric strain distribution in the membrane calculated by finite element analysis shown from the backside (**b**) and from the device side (**c**) of the chip. By applying a load having lateral force component a significant asymmetric strain builds up in the membrane.*

The characterization of the device was started with a fracture strength test by pressing a sharp metal needle along perpendicularly against the flat top surface of the Si micro-stick. During the test the deflection of the tip position and the applied normal force (Andilog) were recorded (Fig. 4.15.a). As shown in Fig. 4.15.b all the tested GaN drumskin membranes had a linear force-displacement curve, the obtained spring constants and fracture strength are in the range of 4,2-5,3 mN/um and 35-50 mN.

In the next step, the sensitivity of the force sensor on normal force load was investigated. We applied a constant bias of 1V on each bridge and measured the voltage signal between the 2DEG resistors using a matrix switch module (NI PXI). For a better visualization, at the beginning of the measurement a reference voltage was taken for each bridge and only the change as a function of time upon increasing load pulses is shown in Fig. 4.15.c. The recorded voltage signals gave a fast response (<0.2 s) on the applied load and found to be proportional on that. The relatively high difference in the sensitivity of the bridges can be attributed to the asymmetric device geometry caused by the non-ideal setting of the DRIE system. The 3D loading test of the 2DEG force sensor is still in progress and we also plan to repeat the experiments in the current saturation regime where a higher sensitivity is expected.

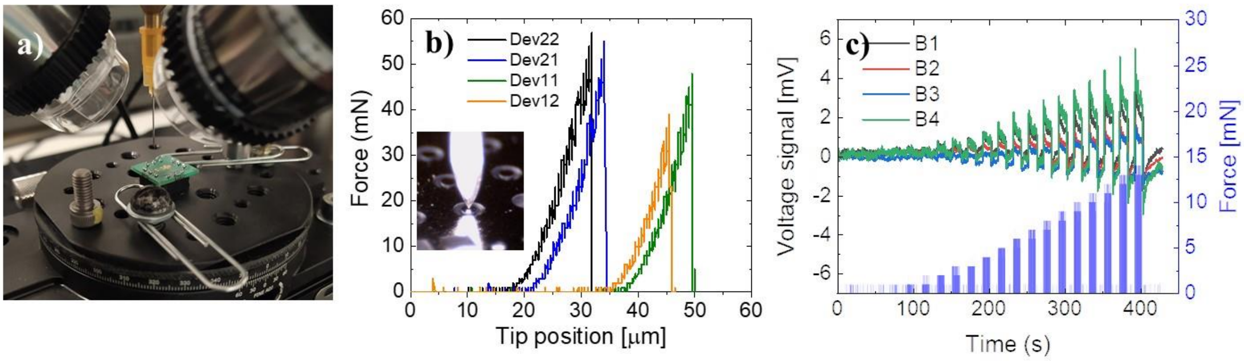

Figure 4.15. a) *Force sensor testing set-up with the bonded chip (green), perpendicular loading needle mounted on a force gauge (not shown), and USB cameras.* ***b)*** *Force-displacement curves of fracture tests of four devices. Fracture occurs in the range of 35-50 mN. Inset: USB camera image of the needle tip in contact with the force sensor. c) Voltage signals (left axis) of the measuring bridges upon increasing loading force pulses (right axis)*

The 3D loading test of the 2DEG force sensor is still in progress. We also plan to repeat the experiments in the current saturation regime where a higher sensitivity is expected.

Middle ear MEMS detectors for fully implantable cochlear implants

J. Radó, Á. Dacher, Z. Pusztai, J. Volk in collaboration with PTE and SOTE

Fully implantable cochlear implants could offer several advantages for patients suffering severe hearing loss. However, the miniaturization, complexity as well as self-powering, signal processing and cochlear multielectrode system are required for such a fully implantable device. Correspondingly, these requirements are to be fulfilled in order to eliminate the use of external unit, i.e. microphone, sound processor, transmitter and battery, which are used in conventional semi-implantable hearing aids. In this work, instead of the direct detection of the sound (microphone), we demonstrate an accelerometer array, which could be mounted on one of the vibration transmitting bones, like anvil (incus), in the middle ear. To reduce the sensor dimensions, the accelerometer array is made with a multi-electrode structure. As a result, more than one frequency can be identified with a single spiral using a simple truth-table based on the phases of the signals (Fig. 4.16).

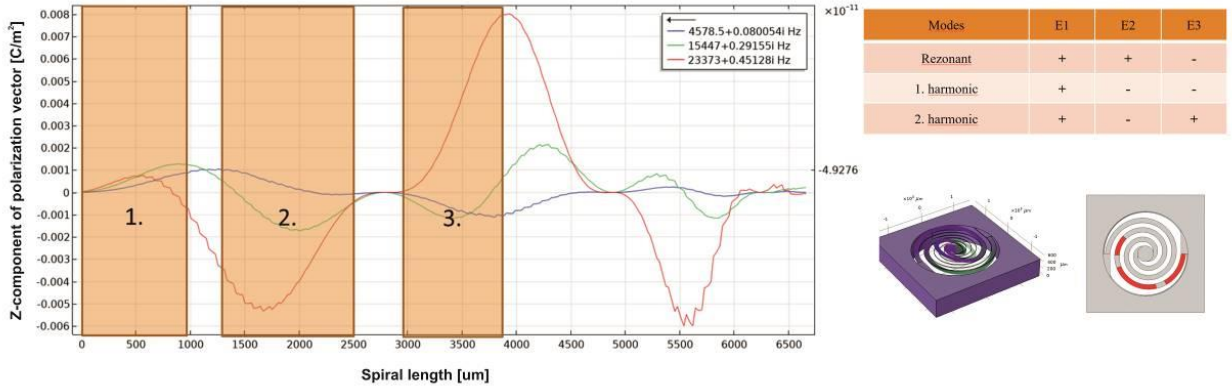

Modes	E1	E2	E3
Rezonant	+	+	-
1. harmonic	+	-	-
2. harmonic	+	-	+

***Figure 4.16** Z component of the polarization vector along the spiral length (on the left), the truth-table (on the top-right) contained the momentary sign of the signals and the FEM model (on the bottom-right) in which the red bars indicate the position of the electrodes. Every image refers to the same spiral.*

As the dimension and the location of the electrodes are crucial issues for the appropriate operation of the sensor, in 2021 we redesigned the multi-electrode structure based on Comsol Multiphysics FEM calculations. The simulation models were tuned with the results of vibration measurements using a SmarAct PicoScale vibrometer.

Having designed the new layout of the electrode structure, the sensor was fabricated in our cleanroom applying conventional MEMS technology steps (Figure 4.17). As a continuation of the topic, this year we will validate functionality of the new design with measurements using our vibrometer and minishaker setups.

In parallel, we also started the preliminary animal experimentations in collaboration with University of Pécs Medical School and Semmelweis University. The main goals of the experiments were to practice the implantation process to a mouse cochlea using a 3-contacts cochlear electrode provided by MED-EL Corporation and to test the stimulator electronics and the Auditory Brainstem Response (ABR) measurement system (Fig. 4.18). In order to reduce ambient noise contamination of the stimulus, we developed an electrically independent stimulator circuit. To ensure synchronization between the stimulus and the ABR signals, the stimulator receives only a trigger signal from the ABR equipment via optical cable. The stimulator generates biphasic nerve-like stimulus to avoid nerve fatigue. The ABR system receives the mouse brain response through a pre-amplifier and records averaged data, repeating the stimulation 800 times. During the data analysis we found that the 1.5V stimulus overrode the ABR pre-amplifier, so the low-level brain signals, which are in the nanovolt range, could not be retrieved from the recorded data. This year, we need to redesign our stimulator so that upon every stimulus onset the recording amplifier is blanked for a few microseconds [Ref. 4.5-4.6].

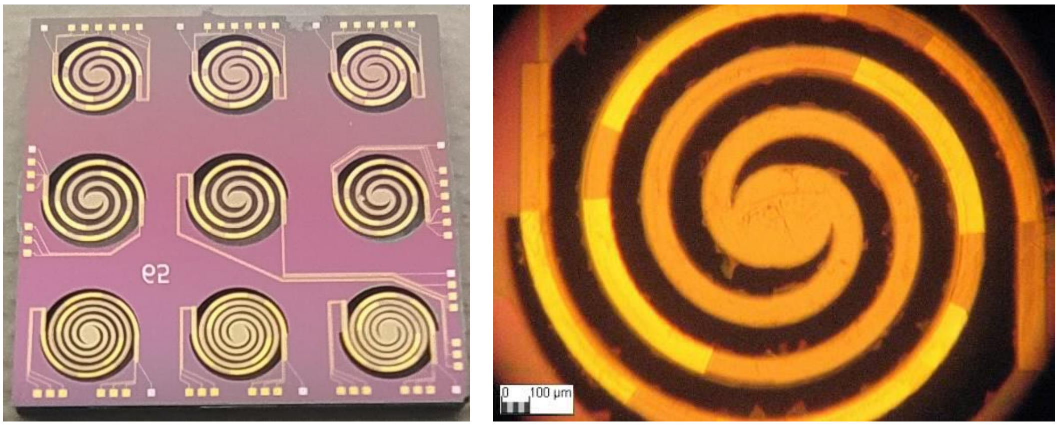

Figure 4.17. *The completed device with nine single spirals geometrically tuned to different resonant frequencies and harmonics (on the left) and a close view of the central spiral (on the right). The yellow bars indicate the realized gold top electrodes*

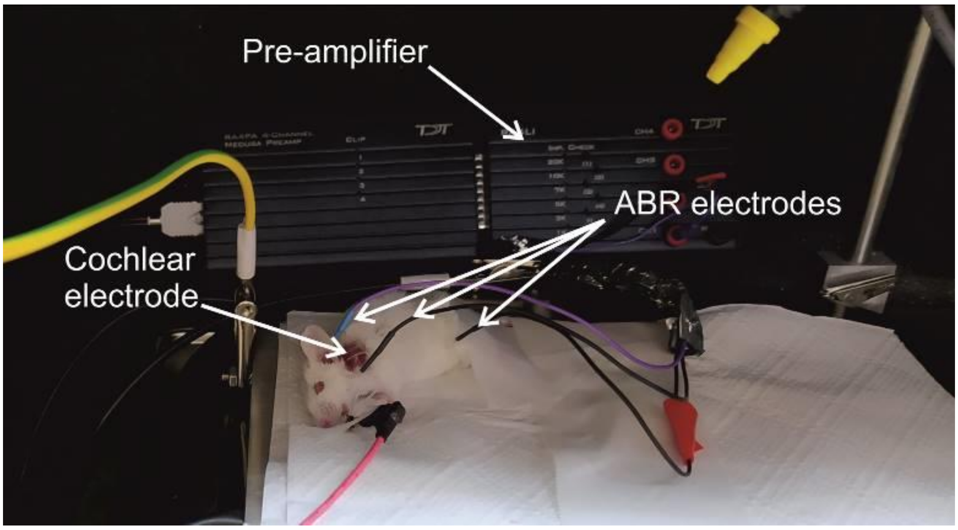

Figure 4.18. *ABR measurement arrangement. The electrode implantation to the cochlea was carried out under stereomicroscope on an operating table located next to the ABR system.*
The operating physician was Péter Révész from University of Pécs.

A novel force sensor-based measurement system for abnormal road surface detection

NVKP_16-1-2016-0018 “KoFAH”

J. Radó, A. Nagy, J. Volk in collaboration with ELTE and SzTAKI

Besides tire pressure monitoring, intelligent tires can be exploited to analyze tire/road interactions, wheel loading, tread wear, and they can support automotive vehicle applications. In this study we develop a measurement system for intelligent tires including a novel piezoresistive force sensor. In order to protect the sensor from the outer harsh environment and obtain the highest response signals, the inner sidewall was chosen as the embedding location. Based on our previous experience the greatest deformation within the sidewall occurs near the tread, as a result, the sensor was glued there (Fig. 4.19). To retrieve the data from the sensor built into the inner sidewall of the tire, we developed a readout electronics capable of driving the voltage bridges with 2.5V, conditioning the signals, and transmitting the data wirelessly. The readout electronics was powered by LiPo battery that can be charged from outside the tire with a commercially available RF charging coil. Both electronics and the RF coil were fixed to the tread as a less compliant area of the tire.

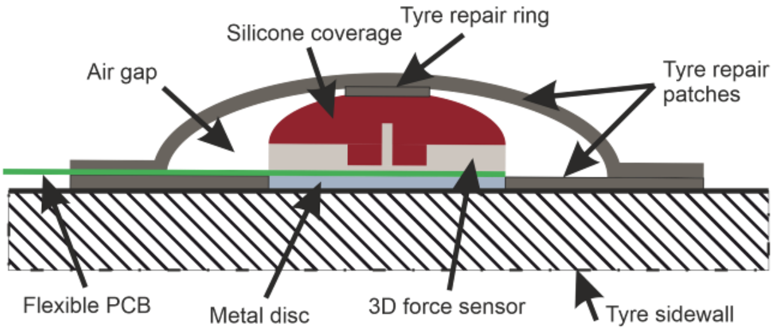

Figure 4.19. *Schematic of the embedding process. Due to the air gap, the sidewall deformation of the tire can be transmitted to the joystick through the tire repair ring and the flexible silicone coverage*

In order to carry out the dynamic experiments, two test tires were mounted on a Nissan Leaf provided by Institute for Computer Science and Control (SZTAKI). The external receiver electronics were placed in the engine bay of the car as close as possible to the tires to ensure the continuous signal transmission (Fig. 4.20). The received signals were transformed according to the CAN BUS protocol of the vehicle for on-board computer processing and data recording. The CAN transformation ensures the synchrony between the tire sensor signals and the other dynamics data, such as accelerations, speed, angular momentum and GPS coordinates.

For the final test, two different, well-separable road surfaces were chosen in Budapest. One, the so-called “normal” surface, was a newly paved, perfect asphalt pavement, while the other, “abnormal” surface, was an old, poor quality concrete road with potholes. We passed through both pavements many times and recorded the signals of the tire sensors along with other dynamic data from the CAN BUS.

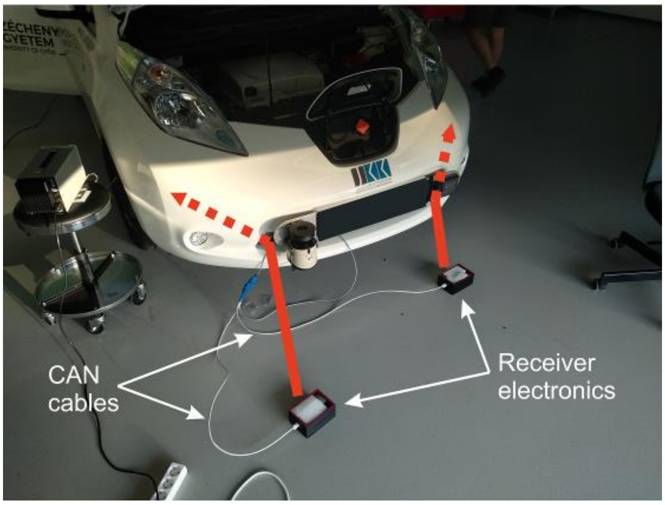

Figure 4.20. *Off-tire receiver and data conversion electronics. The PCBs were placed in a 3D printed box to protect them from the harsh environment. The red arrows indicate the final position of the electronics*

The output of the sensor was segmented into tire revolution cycles, which were then transformed to a subspace spanned by adaptive Hermite functions. The underlying idea behind this step is to emphasize relevant features of the data which capture the dynamics of the tires. We developed two abnormality detection methods relying on this signal representation. In the first case, the parameters of the applied adaptive transformation were optimized for each sensor output segment separately. The acquired representations were then classified to be normal or abnormal based on an analytic, statistical approach. In the second case, we optimized the parameters of the transformation and the weights of the underlying classifier simultaneously with the help a model driven neural network architecture referred to as a variable projection network (Fig. 4.21.). Experiments using measurements acquired from the public roads of Budapest show an abnormality detection accuracy of over 97%.

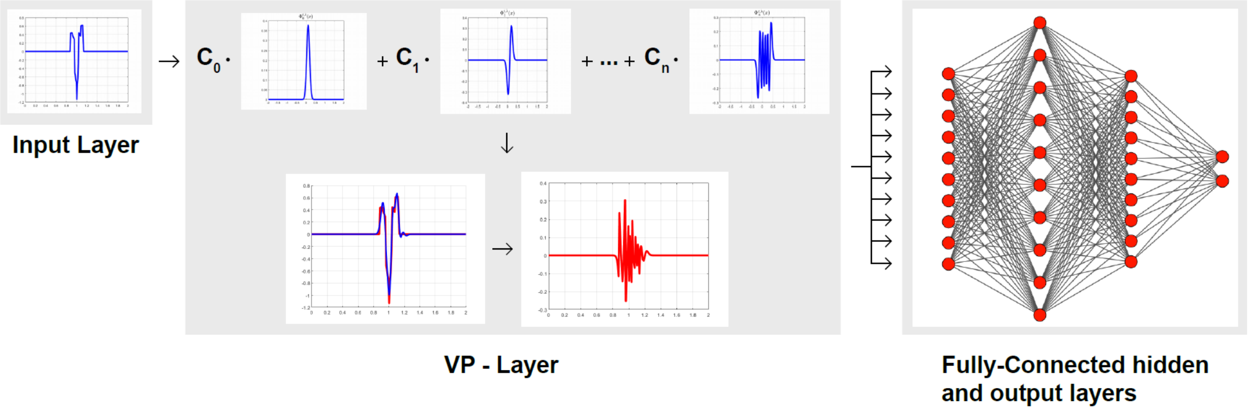

Figure 4.21. *VP-NET architecture. The first layer implements a variable projection operator (in our case an adaptive Hermite function based residual transformation). The output of this layer is then passed to a neural network. The parameters of the transformation implemented by the variable projection layer are thus trained together with the weights of the underlying classifier.*

5 - Microsystems Laboratory

Head: Dr. Péter FÜRJES, Ph.D., senior research fellow

Researchers:

- István BÁRSONY, member of HAS
- Orsolya BÁLINT-HAKKEL, Ph.D.
- Barbara BEILER, Ph.D.
- Ferenc BÍRÓ, Ph.D.
- Csaba DÜCSŐ, Ph.D.
- Péter FÖLDESY, Ph.D.
- Péter FÜRJES, Ph.D.
- Eszter LEELŐSSYNÉ TÓTH Ph.D.
- János RADÓ, Ph.D.
- Zoltán SZABÓ, PhD.

PhD Students:

- Anita BÁNYAI (ÓE Univ. Óbuda)
- Lilia BATÓ (ÓE Univ. Óbuda)
- Dóra BERECZKI (ÓE Univ. Óbuda)

Engineers / technicians:

- Gabriella BÍRÓ, technician
- János Márk BOZORÁDI, electrical engineer
- Tibor CSARNAI, electrical engineer
- Magda ERŐS, technician
- Petra HERMANN, bioengineer
- Róbert HODOVÁN, mechatronic engineer
- Csaba LÁZÁR, electrical engineer
- Margit PAJER, technician
- Zsuzsanna Brigitta SIK, bioengineer
- Zsombor SZOMOR, medical engineer

The main goal of the Microsystems Laboratory is to research and develop integrated sensors and sensor systems, MEMS and BioMEMS devices fabricated by silicon or polymer micro- and nanomachining technology. The activity covers the characterisation, materials systems and technology solutions and the development of sensing principles. The application of micromachining technology enables the miniaturisation of sensing and analytical systems and integration of various functions of sample preparation, sensing, readout, actuation or communication, respectively. The laboratory is focusing on the development of mechanical, physical, chemical (and biochemical) sensors, functional micro- and nanofluidic devices, implantable microsystems and infrared LED.

Our medium-term goal is to broaden the spectra of perspective research topics of MEMS systems and to develop a systematic organisation and form a dynamic and growing research group in the Microsystems Laboratory. Considering the financial environment our research directions fit to the European and Hungarian strategic roadmaps and directives (S3 - National Smart Specialisation Strategy) by the following research topics:

- Healthy society & wellbeing: BioMEMS, Lab-on-a-Chip, Organ-on-a-Chip, microfluidic systems, implantable, wearable devices, personal medicine, continuous monitoring, etc.
- Vehicle technologies: Driving safety sensors
- Clean and renewable energies: Low consumption electronics, sensors for energy industry, characterisation photovoltaic systems,
- Sustainable environment: Environment safety sensors (water monitoring), gas sensors (smart home, smart clothes)
- Healthy food: Food safety sensors, spectroscopy

Research group structure in the Microsystems Laboratory

The development of MEMS devices requires solid design capacity and advanced cooperation among the research and technical staffs for precise operation of the full micromachining fabrication line. Actually, 10 researchers, 9 engineers / PhD student and 3 technicians work for the Laboratory with close and flexible cooperation with the colleagues of the Nanosensors Laboratory.

- **MEMS / smart sensors (Csaba Dücső, Ferenc Bíró, János Radó):** The team's primary expertise is traditional MEMS sensor development, such as gas, environmental and mechanical sensors with an emphasis on the technology of 3D microstructure implementation.
- **BioMEMS, medical applications (Péter Fürjes, Csaba Dücső, János Radó):** Silicon based sensor development and their electro-mechanical integration, specifically for medical applications, are the long-term goals in this topic. The medical field demands the development of tools in low numbers that have extensive added value, which also aligns with the European strategic directives. The topic includes Si and flexible integrated microstructure development as subcontractors in the National Brain Programme.
- **Lab-on-a-Chip / Organ-on-a-Chip (Péter Fürjes, Anita Bányai, Lilia Bató, Dóra Bereczki, Orsolya Hakkel, Petra Hermann, Zsuzsanna Brigitta Sik, Zsombor Szomor):** The Lab-on-a-Chip and Organ-on-Chip systems are essential building blocks of Point-of-Care diagnostic and drug analytical tools in the medical field. We have vast experience in this topic, especially in microfluidics. Accordingly, we actively collaborate with companies and universities in this field (77 Elektronika Kft., University of Pécs) as well.
- **IRLED (Zoltán Szabó, Barbara Beiler, Ferenc Bíró):** We fabricate and develop a few thousand infrared LEDs per year (partners: Anton Paar, Senop). Additionally, we envisaged a larger scope spectroscopic development and application in the frame of an actual ECSEL grant. Environmental analytics and food safety applications could be important goals for IR spectroscopy and other optical developments.
- **Integrated systems / Heterogeous integration /IoT (Péter Földesy, János Márk Bozorádi):** Research grants ask for a certain level of preparedness, which usually includes demo systems

(sometimes prototypes). Therefore, the requirements of developed instruments and their electro-mechanical integration are becoming a greater task.
- **Technology, FEM / Multiphysics Modelling (Eszter Leelőssyné Tóth):** Modelling, such as digital twin, is a widely applied method in engineering practice. It speeds up development and manufacturing time of prototypes while also lowering costs. The application of these methods is not as straight forward for the development of microstructures due to the effects of microenvironments. However, the use of these simulations is indispensable. The group is effectively corroborating the research and development tasks.

Infrastructure and technological competencies

This is a unique infrastructure in Hungary accordingly its sustainable operation and development is strategic goal. The infrastructure is open for academic and industrial partners to realize complex, purpose-designed microsystems, nanocircuits, as well as Lab-on-a-Chip devices.

The high-tech microtechnology related fabrication and characterisation systems work in a class 10 cleanroom facility. The laboratory is dedicated for 3D processing of 3” and 4” Si / glass / polymer substrates with maximal resolution of 1µm, together with lithographic mask manufacturing. Electron beam lithography and focused ion beam (FIB) milling are also available with resolution of 20nm. The structural design and development are also supported by multi-domain Finite-Element Modelling (FEM), and process simulation. Wide spectra of characterisation techniques are also available: optical (fluorescent) and electron microscopy (SEM and EDS), atomic force microscopy (AFM), profilometry, optical and electrical measurements, electrochemical impedance spectroscopy, microfluidic characterisation, mechanical vibration and climate test chambers, UV / VIS / IR / FTIR spectroscopy, etc.

Available micromachining techniques:

- Patterning – mask design, laser pattern generator, photolithography, (double side) alignment, electron beam lithography (E-Beam), Focused Ion Beam processing – FIB milling, nanoimprinting
- Structured polymer layers – PMMA, PI, SU8 patterning, micromoulding, soft lithography – PDMS
- Wet chemistry – chemical wafer cleaning, isotropic and anisotropic etching techniques
- Dry etching – deep reactive ion etching, plasma etching techniques (DRIE, RIE)
- High temperature processes – thermal oxidation, diffusion, annealing, rapid thermal annealing (RTA)
- Physical thin film depositions – Thermal and electron beam evaporation, DC and RF Sputtering
- Chemical thin film depositions – Atmospheric and Low Pressure Chemical Vapour Deposition (CVD, LPCVD, LTO), thermal and plasma enhanced Atomic Layer Deposition (ALD)
- Liquid Phase Epitaxy of III-V compound semiconductors (LED manufacturing)
- Wafer bonding – Si-glass, glass-glass, polymer-glass anodic and thermal bonding
- Chip dicing, wire bonding especially for sensor applications
- Special packaging techniques and methods

Cooperations

Apart from the European and bilateral international R&D projects wide cooperative and knowledge network was established by the large number of joint research projects with Hungarian research centres (ELKH-ATOMKI, BME, PPKE, SE, ELKH-SZBK, PTE, ELKH-WIGNER, ELKH-TTK, ELKH-SZTAKI) and research groups to perform interdisciplinary research. We are supporting the National Quantum Technology Programme (HunQuTech), the National Brain Programme and National Laboratory on Human Reproduction Programme by our infrastructural background. Besides the scientific projects, the Lab offers technology development services, with these industrial partners (SEMILAB, 77 Elektronika, Mirrotron, Trimble, Bay Zoltán Appl. Res., Z-Microsystems (Austria), Anton Paar (Austria), Senop (Finland), FRK (Poland), Philips (The Netherlands)) the higher technology readiness levels are also achievable (TRL 2 → 6).

The technological and scientific results are directly transferred into the higher education, by means of several lectures, laboratory practices, TDK, diploma and PhD works. Our researchers give lectures at various departments of TalTech, BME, PPKE, ÓE, DE, ELTE.

Major research projects

The researchers of the Microsystems Laboratory are involved in development, fabrication and integration micro- and nanosystems, sensor structures to open new perspectives in the field of medical diagnostics, Minimal Invasive Surgery techniques, energy-efficient autonomous systems (sensor networks, autonomous driving). Our interest covers the topics of optical analytics (spectroscopy), environmental and safety (gas detectors) sensors.

- A pilot line for the next generation of smart catheters and implants – POSITION-II, ECSEL 2017-2-783132
- Accelerating Innovation in Microfabricated Medical Devices – Moore4Medical, ECSEL Innovation Actions (IA), Call ECSEL-2019-1-IA
- Low power consumption-type nano-sensors for gas detection in harsh environment – Hungarian-Russian Collaborative Research Program - 2017-2.3.4-TéT-RU-2017-00006
- Advanced Aerosol Metrology for Atmospheric Science and Air Quality - AEROMET II, European Metrology Programme for Innovation and Research (EMPIR 9ENV08)
- Development of Rapid Urine Bacteria Analyzer – VEKOP-2.2.1-16-2017-00001 – „Versenyképességi és Kiválósági Együttműködések"
- Low-dimensional nanomaterials for the optical sensing of organic molecules on liquid and gas interfaces - OTKA K 131515 (participant)
- IR spectroscopy of extracellular vesicles: from exploratory study towards IR-based diagnostics – OTKA K 131594 (participant)
- Thin film integrity check by capillary bridge test – OTKA FK 128901 (participant)

Scientific cooperation:

- Manufacturing optrode devices applied in the NKP_17 „National Brain Programme" - 2017_1.2.1-NKP-2017-00002 for Pámány Péter Catholic University

Industrial cooperation:

- Development and optimisation polymer based autonomous microfluidic cartridge, its production technology and measurement methodology for high sensitive Point-of-Care detection of cardiovascular blood biomarkers for 77 ELEKTRONIKA Ltd. (subcontraction)
- Development CVD technology and equipment for deposition low roughness polycrystalline Silicon layers for MIRROTRON Ltd. (subcontraction)
- Development and manufacturing specific calibration test samples for characterisation methods of semiconductor industry for the SEMILAB Co.
- Development and manufacturing Near InfraRed LED devices for spectroscopic applications for Senop Ltd. (Finland)

Low power consumption-type nano-sensors for gas detection in harsh environment

Hungarian-Russian Collaborative Research Program 2017-2.3.4-TéT-RU-2017-00006

F. Bíró, I. Bársony, Cs. Dücső

The ultimate goal of the project is to develop a novel calorimetric gas sensor family what is able to detect CH_4, NH_3 and CO up to their lower explosion limits (LEL), i.e. 5, 15 and 12,5 %, respectively. The sensors can be operated in harsh environment without any risk of ignition even over LEL concentrations. Apart from the optical and electrochemical approaches and the corresponding systems, there are two viable solutions, both exploit temperature changes and read-out by:

- measuring the temperatures of a heated catalyst surface and a passive reference,
- measuring the temperatures of a filament exposed to gas environment and a perfectly sealed reference heater.

Although the catalytic device is expected to detect lower gas concentration and exhibit better sensitivity, the second, heat-conductivity type device is simpler and still in use in practice. A more sophisticated device applies both sensors, thereby extending the detection range and improves the detection reliability. Another advantage is the commonly used filament or micro-hotplate structure. Therefore, to develop a micro-hotplate meets all the mechanical, electrical and chemical requirements is essential for a reliable and commercialized device [Ref. 5.1-5.2].

The basis of the sensor is a newly developed small diameter (150µm) microhotplate exhibiting ±1% temperature uniformity on the heated area below 550ºC. The stability of the heater is 5000 hours at least at the operation temperature of 530°C, thereby in pulsed mode operation ca. 5 years operation can be achieved. The power dissipation at 500°C is 27mW/1.5V, so the chip can be utilized in portable or wearable devices for personal safety. [Ref. 5.3] An alternative, suspended crystalline-Si microheater was also developed to form and test the miniaturised conventional bead-type pellistor.

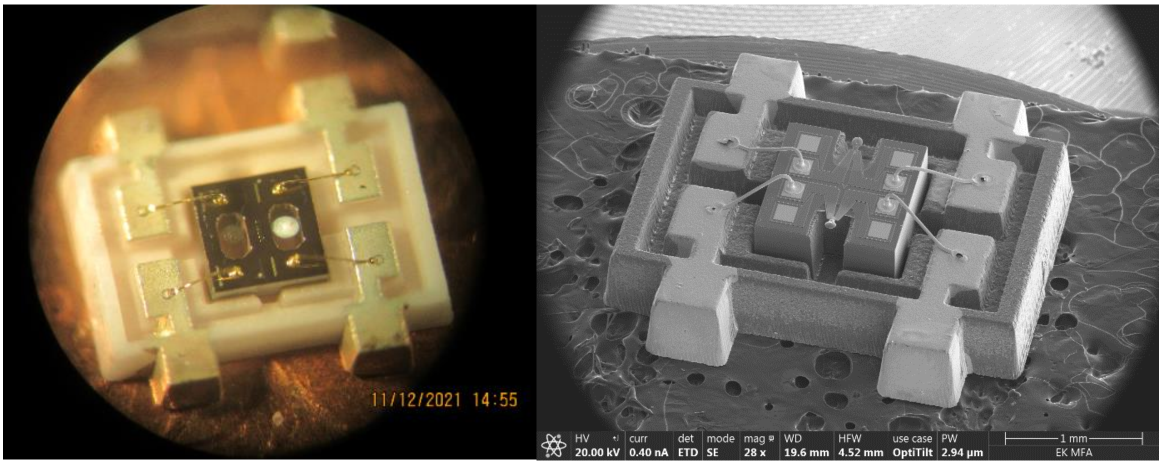

Figure 5.1. *Gas sensor chips in laser micromilled ceramic headers. Catalyst (black on the optical image) and reference suspensions (white) dropped on hotplates (a) and c-Si filaments (b). The artificially coloured inset shows the shape of the micro-bead. The size of both chips is 1x1 mm^2.*

The other key element of the development is the SMD compatible mechanical encapsulation. The ceramic elements were jointly designed followed by laser milling fabrication at the Russian partner. The catalytic sensors measure the heat generated by the controlled catalytic combustion of the burning/explosive gases. In order to avoid false thermal signals caused by temperature variation, flow and compositional changes (e.g. humidity) of the ambient the sensor consists of two identical heaters; one is covered with chemically active catalyst, whereas the other has a passive cover and serves as a reference (Fig. 5.1). Although the stability of all the catalysts have been investigated need to be improved to consider them in commercial devices the dynamics of the sensor chips enables the pulsed mode operation (Fig. 5.2).

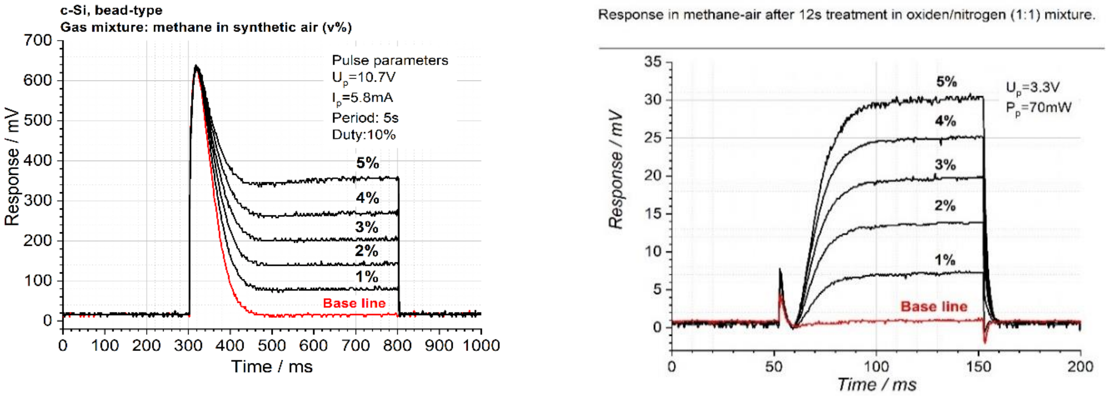

Figure 5.2. *Responses of freshly prepared pellistors in pulsed mode operation for LEL 20-100% of CH_4. The origin of the first peaks is the difference of the heating-up speed of the two elements (active, passive). The bead-type pellistor formed on c-Si microfilament provides stable response after 200ms (left). Reliable signal of the thin film-ALD catalyst covered hotplate is given after 50ms. (right). Apart from the better dynamics the first small peak also indicates the better control of the processing technology.*

In the follow-up activity we plan to elaborate the appropriate material composition of the thin film catalyst to achieve the necessary sensor lifetime required by any commercial device. We hope to build a reliable earth gas sensor with combining the already proven (report 2020) heat conductivity device and this thermocatalytic sensor. Having in hand the **stable heaters** we now focus on other applications.

Design and development of a 3D Flex-to-Rigid compatible force sensor

H2020-ECSEL-2017-2-783132 "POSITION-II - A pilot line for the next generation of smart catheters and implants", 2018-2.1.6-NEMZ-ECSEL-2018-00001

J. Radó, L. Illés, P. Fürjes, Cs. Dücső

The main objective of the POSITION-II project is the realization of a pilot line for the fabrication of the next generation of smart medical instruments. This second generation of smart medical instruments offers improved performance through better sensors and transducers combined with an improved manufacturability and lower cost. The task of our research group is to develop and demonstrate the applicability of a capacitive force sensor integrable in the tip of an electrophysiological catheter.

The goal of our task was to develop a force sensor structure we can built in the tip head of a catheter. Due to the required function the sensor must have minimum 3 sensing elements. In the first two years we have developed alternative force sensor structures and characterized them in terms of their sensitivity and capability to resolve the loading force components. As described before the best structure utilizes the Philips' CMUT-type surface micromachined capacitor elements arranged in concentric 6 segmented blocks. We also investigated the appropriate coating material and its geometry to get the best force conveying performance. Finally a hemisphere bumpers were formed by moulding the elastomer to cover the capacitor array, then individually glued on the surface. The sensor responses could be dramatically improves if a thin hard coting layer was applied on the elastomer (Fig. 5.3).

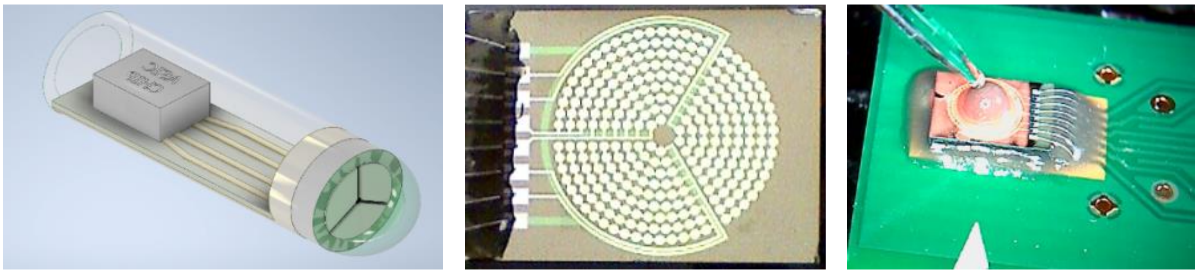

Figure 5.3. *Concept of the tip head force sensor in the catheter (left). The layout of the six capacitor blocks of the chip contain 42 (inner) and 48 (outer) micromachined capacitances and is covered with force transferring biocompatible elastomer. The chip before encapsulation (middle) and after assembled in the tester (right). The controlled load is applied via a 250µm diameter glass pin.*

In the previous year we determined the sensitivity and demonstrated the 3D resolving functionality by loading the sensor at the centre point from 33 different directions and uniformly increasing the force from 0 N to 500 mN in each case (Fig. 5.4). In order to retrieve the loading force and also obtain the load/contact point from the collected data, we applied a deep feed-forward neural network. The neural network consisted 1 input layer, 3 hidden layers and 1 output layer containing different number of neurons. The number of the hidden layers and the neurons were optimized for the force sensor by comparing the root-mean-square errors of each construction. The input and the output layers were determined by the system. The response signals of the six segments provided the six inputs, whereas the three components of the force and the coordinates of the contact point could be obtained as outputs. For training the network, a Levenberg-Marquardt algorithm based back-propagation learning method was employed by using the build-in train function of MATLAB. According to the routine procedure, we split the measurement data into three subsets. The first subset containing 70% of data was the training set, and the remaining 15%-15% of data were used in validation and for testing, respectively.

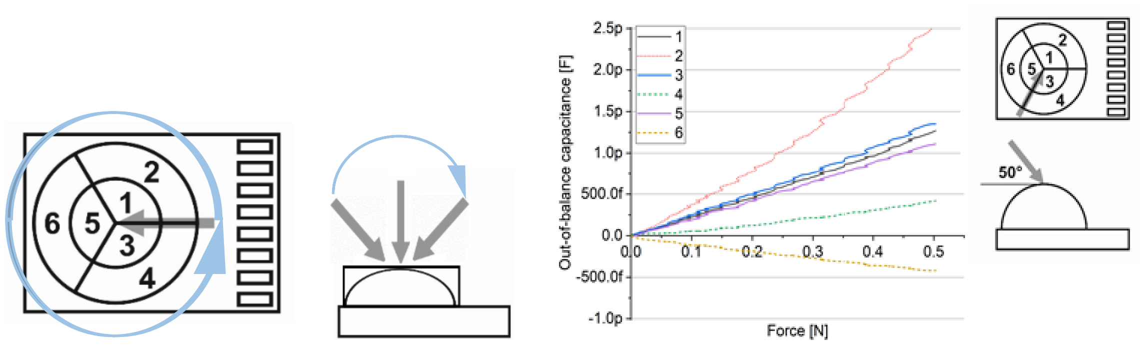

Figure 5.4. Representation of the loading directions and the typical responses of the six elements (right).

In order to examine the contribution of the segments (capacitor blocks) of the outer and the inner rings to the network performance, we made different calculations with different number of network inputs. The network performance was very good for the response signals of the six segments as well as for the three segments of the outer ring. However, the prediction of F_x and F_y components was poor when based on the signals of the inner three segments only. In Fig. 5.5 the significantly better performance of the outer 3 elements for the F_x and F_y (tangential) components is clearly seen, as the predicted and calculated values can't be distinguished.

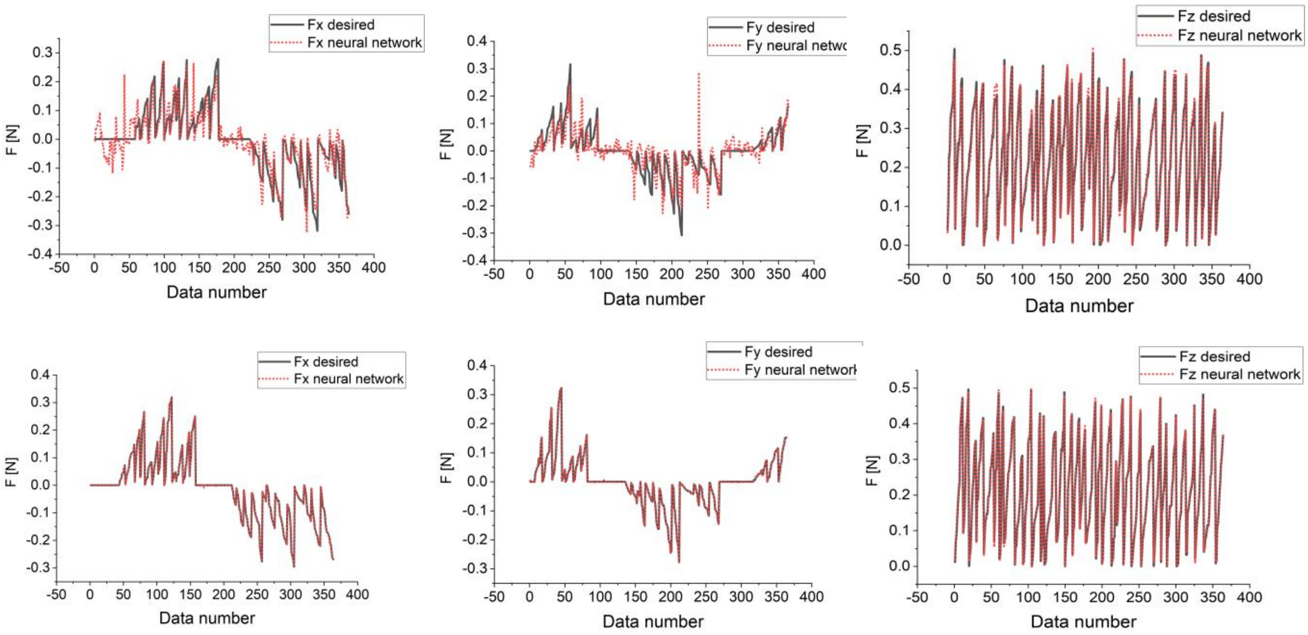

Figure 5.5. Estimation of the force components based on response signals of (top row) the inner segments and (bottom row) the outer segments

Having got an impressive direction dependence in the responses and considering that we have six signals, we also tested whether we can also retrieve the point of application as an additional extra. Parallel with the determination the force vectors, the network performance was also satisfactory in retrieving the position of their contact points. In this case, the RMSE values along the x- and the y-axes were 0.48 and 0.63, respectively. These levels of errors mean that the network estimates the position of the contact points in both directions much more accurately than the characteristic distance between the two neighboring points we measured for training.

The feasibility of the sensor integration in the catheter tip was demonstrated by the circular shape and the F2R (flex to rigid) compatible processing. The concentric double ring arrangement, and the need for three signals offer the possibility to further reduce the diameter of the circular chip. We have proven the functionality of the 1.6mm diameter chip, but we think that with appropriate design of the chip (i.e. introduction of TSV, through silicon via) and the electronics, further reduction to 1.2-1.5mm size is also feasible. The sensor sensitivity is in the range of 1-500mN. Training a NN the system can provide accurate and quick information on the contact force.

Polymer based autonomous microfluidic systems for medical diagnostics

Polimer alapú autonóm mikrofluidikai kazetta gyártástechnológiájának fejlesztése és optimalizálása, mérési módszer fejlesztése kardivaszkuláris betegségek vérmarkereinek nagy pontosságú betegágy melletti kimutatásához (Partners: Semmelweis Egyetem, Budapest University of Technology and Economics, Aedus Space Ltd.) R&D contract (as subcontractor of 77 Elektronika Ltd.)

A. Bányai, P. Hermann, Zs. B. Sík, O. Hakkel, P. Fürjes

Precise and fast PoC monitoring of marker molecules or bacteria levels in body fluids or cell culture media could be crucial in effective diagnostics and choosing therapies. Due to the specific tools and novel microtechnology processes the cost-effective, complex but miniaturised analytical systems, such as Lab-on-a-Chip (LoC) and microfluidic devices have become available and applicable for implementing the overall sample analysis from the preparation to the molecular detection. The microfluidic system has to transport the sample and the washing buffer to the active area of the chip meanwhile mix and incubate the sample with the reagents. As the incubation and read-out needs a specified time, precise sample handling and flow control are crucial. The perspective of our work is to develop a polymer based microfluidic cartridge suitable to autonomously controlled sample transport or preparation for integrated bioanalytical device.

To define precise sample flow rates in the microfluidic systems adequate surface modification and macro and microscale structuring of the geometry are crucial. The COP (cyclic-olefin-polymer) material were choosen and modified by specific surface treatment methods, as oxygen plasma treatment, Ar plasma induced polymerisation of Pluronic F127 and PEGMA (Poly(ethylene glycol) methacrylate) layers, dip-coating of BSA (Bovine Serum Albumin). Accordingly the applicability of different surface modification methods were analysed with special consideration of the long term stability of the surface properties as contact angle, roughness, non-specific binding of biomolecules and labelling nanoparticles. The modified surfaces were characterised by surface contact angle measurements, **FTIR (Fourier Transform Infrared Spectroscopy)**, AFM (Atomic Force Microscopy), spectro-ellipsometry. Fig. 5.6 demonstrates the chemical change of the O_2 plasma treated substrates during 12 months' storage: the intensity of the characteristic peaks of hydroxyl groups and carbon-dioxyde molecules indicates the contamination of the surface which is much more moderated in case of low temperature storage with water absorbent.

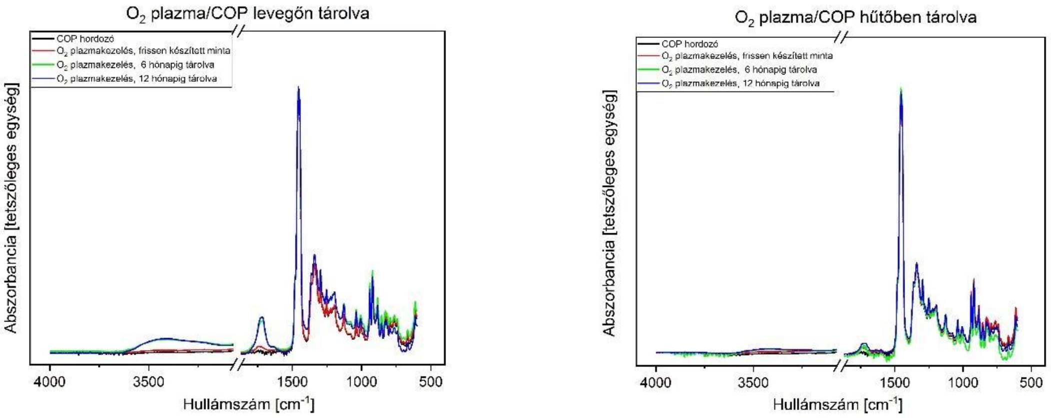

Figure 5.6. *The ATR FTIR spectra of the uncoated and the O_2 plasma treated COP substrates stored at air athmosphere (left) and at 4°C (right) – as prepared and after 6 or 12 months.*

In a previous project (Multiparaméteres Point of Care in vitro diagnosztikai rendszerek fejlesztése) an autonomous microfluidic system was designed and manufactured for transporting blood or plasma by precisely controlled sample rate. These autonomous sample transport systems were integrated into Point-of-Care Lab-on-a-Chip based diagnostic devices. The developed systems are to be applied for detection cardiovascular diseases in cooperation with 77 Elektronika Ltd. Based on these results we are continuously developing the microfluidics based **Lab-on-a-Chip device** for the specific cardiovascular diagnostic panel. In the actual period the geometry of the microfluidic systems was finalised according to the additional requirements of the optical detection method and the real sample. To step forward the industrial polymer manufacturing technology the injection moulding technology was tested as promising manufacturing solution. The Microsystems Lab developed 3D silicon dry etching technology applicable for structuring mould master for the injection moulding elaborated by Z-Microsystems GmbH. The parameter set for the cryo type deep reactive ion etching was optimised to achieve adequate geometry profiles (Fig. 5.7.) of the silicon master.

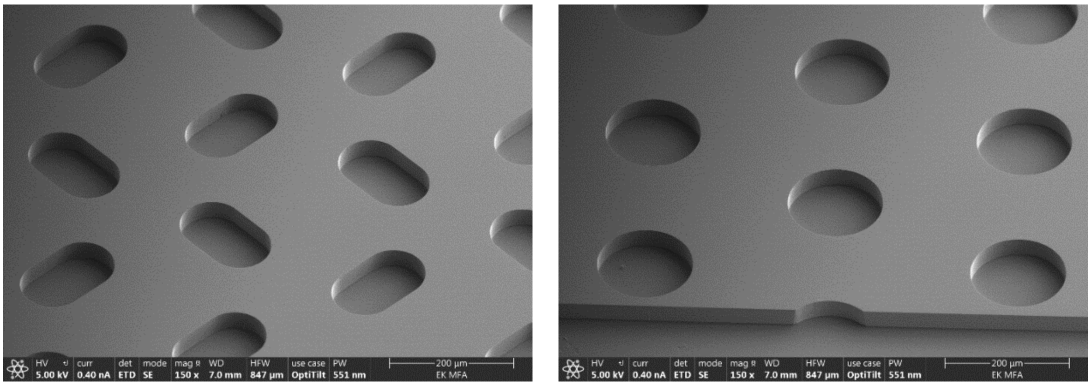

Figure 5.7. *3D silicon moulding master fabricated by cryo type deep reactive ion etching for injection moulding of polymer microfluidic cartridges.*

Microfluidic sample preparation system for rapid urine bacteria analysis

VEKOP-2.2.1-16-2017-00001 – "Versenyképességi és Kiválósági Együttműködések - Gyors húgyúti baktérium elemző mérőkészülék fejlesztése (Rapid urine bacteria analyzer)"

A. Bányai, P. Hermann, Zs. B. Sik, E. L. Tóth, O. Hakkel, P. Fürjes

In this finished project the main goal was to develop a **single-channel microfluidic cartridge** for certain subtasks of **sample preparation and handling**, which then can be integrated into a measuring instrument. During the optical measurements of bioanalytical tests, the sample handling is solved in an integrated Lab-on-a-Chip cartridge. The cartridge includes transport and filtration of the liquid sample, positioning of bacteria in the detection chamber over the sensing layer, and a microfluidic component for storage of used sample. Accordingly, we focused our attention to develop a **hydrodynamic unit** that is capable of filtering larger elements (>6um) in **urine samples** and positioning permeated bacteria laterally. In order to achieve this goal, we designed and characterized such units. Simultaneously, single-channel cuvettes were made to test the optical system with the sample solution. For the proper passive operation of such device, a bubble-free channel upload had to be provided, by taking account the appropriate setting of the surface properties of the structural materials, and making a special design of the fluidic microstructure. The microfluidic channel was developed by soft lithographic method in PDMS (polydimethylsiloxane) polymer and the raw material was further modified by PDMS-b-PEO copolymer molecules, to ensure the hydrophilic properties of the walls.

For the dielectrophoretic concentration of bacteria, metallization technology was used to develop a high-resolution electrode network on COP polymer film with the thickness of 100 µm. To manage the autofocus function for image processing system, the electrode design were further equipped with an additional pattern. The manufactured microfluidic compartments and COP foils the containing high-resolution gold electrodes were handed over to project partners (77 Elektronika Kft. and SZBK) for further measurements.

Hydrodynamic principle based microfluidic filters and lateral concentrating structures were developed and evaluated by their filtration efficiency for different particle sizes; and by the target loss ratio in the size range of bacteria. After filtering every larger component of the urine sample, the permeated bacteria must be vertically and possibly laterally focused in the detection chamber in order to achieve high trapping efficiency on the functionalized surface. The inertial focusing phenomenon was investigated, which can be used as a passive method for sample preparation and target manipulation in case of particulate suspensions. Asymmetric channel geometry was designed to apply additional inertial forces besides lift forces to promote laterally ordered particles to achieve sheathless focusing or size dependent sorting. The lateral focusing was achieved by a hydrodynamic method and the efficiency of the hydrodynamic focusing depends mainly on the characteristics of the fluidic system and on the particle to channel size ratio. The position of the particle within the flow profile is determined by forces acting on the particle in the fluidic system. The focusing was carried out in an asymmetric microfluidic system with alternating geometric parameters. The evolving hydrodynamic forces were tailored with altered channel parameters (width and height), and different flow rates, to get a better understanding of smaller beads' lateral migration. The behavior of the microfluidic system were tested by using artificial fluorescent beads with different sizes (diameter of 15.8 µm – 6.08 µm – 1.97 µm beads) and GFP-labeled E. coli also. These particles were used to distinguish the focusing position in continuous flow (Fig. 5.8.), and experimental results were compared to in-silico models for particle movement prediction, made in COMSOL Multiphysics (Fig. 5.8.). The focusing behaviour of the applied microfluidic system was mainly characterised for particles size in the range close to blood cells and bacterias.

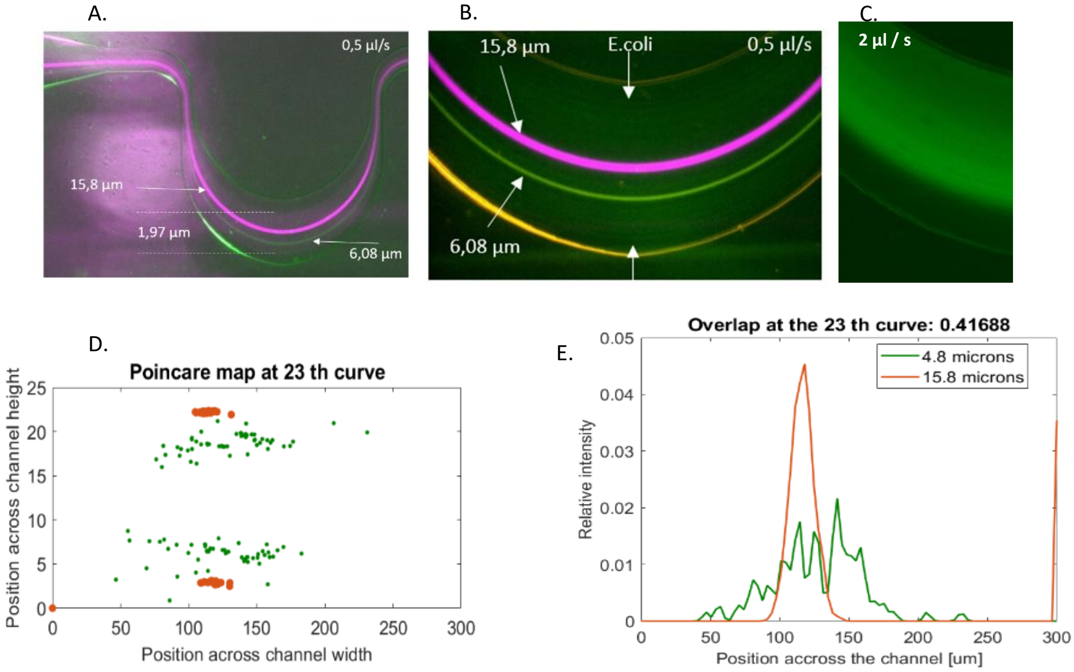

Figure 5.8. *Lateral focusing of 15.8 and 6.08 µm beads at 0.5 µl/s flow rate and concentration of 1.97 µm beads at the end of the lateral focusing unit (A). E.coli could not be focused in the very same structure (B.), although could be concentrated at decreased channel height (15 µm) and increased flow rate (2 µl/s) (C.). Computational data with the cross sectional distribution of the beads in the channel height (D.) and the lateral distribution of the beads (E.)*

Computational fluid dynamics (CFD) simulation was also performed using COMSOL Multiphysics (version 5.3a) to analyse and predict particle movement in the specially designed microchannels. Finite Element Modeling (FEM) is applied to numerically calculate the Navier-Stokes equation considering laminar flow due to the low Reynolds number regime. Particle tracing module was used to calculate particle trajectories in the pre-solved velocity field using spherical particles with two different diameters and properties set to be in correspondence with fluorescently labeled polystyrene beads applied in experimental validation (density: 1055 kg/m3, diameter: 4.8 µm, 15.8 µm). In Fig. 5.8.C-D the Poincare map represents the calculated positions of the particles at the outer surface of the microfluidic systems, and the lateral distribution function comparable to the fluorescent intensity measurements [Ref. 5.4-5.5]

Hierarchically Combined Periodic SERS Active 3D Micro- and Nanostructures

R. Öcsi, Zs. Zolnai, I. Rigó (Wigner FKK), M. Veres (Wigner FKK), O. Hakkel, P. Fürjes

Raman spectroscopy is finding many applications in biology, life sciences and other areas. Raman scattering is inherently weak, but its sensitivity can be improved by implementing surface-enhanced Raman scattering (SERS). Surface Enhanced Raman Scattering (SERS) is applied to enhance the Raman signal by several orders of magnitude and significantly improve the sensitivity of the ordinary scattering method. As a result of the electromagnetic enhancement emerging in the vicinity of metallic nanostructures the sensitivity of molecule detection can achieve attomolar concentrations. This highly sensitive detection performance of SERS was utilized for analysing molecules located in the few nanometer distance or immobilised on the surface of nanoparticles trapped in a specially designed microstructure. By means of the effect efficient detection method can be developed for the analysis of low concentration biological samples assuming that sample transport and preparation system is also integrable.

To increase the local field intensity of Raman scattering, gold nanospheres were entrapped in gold coated periodic inverse pyramid structures, being SERS substrates by themselves. The applicability of this complex structure for sensitive molecule detection was proved by comparison of the detected Raman signals with and without particle entrapment. Moreover its relevance in molecular diagnostic was also proposed considering the specific surface functionalisation of the gold nanoparticles.

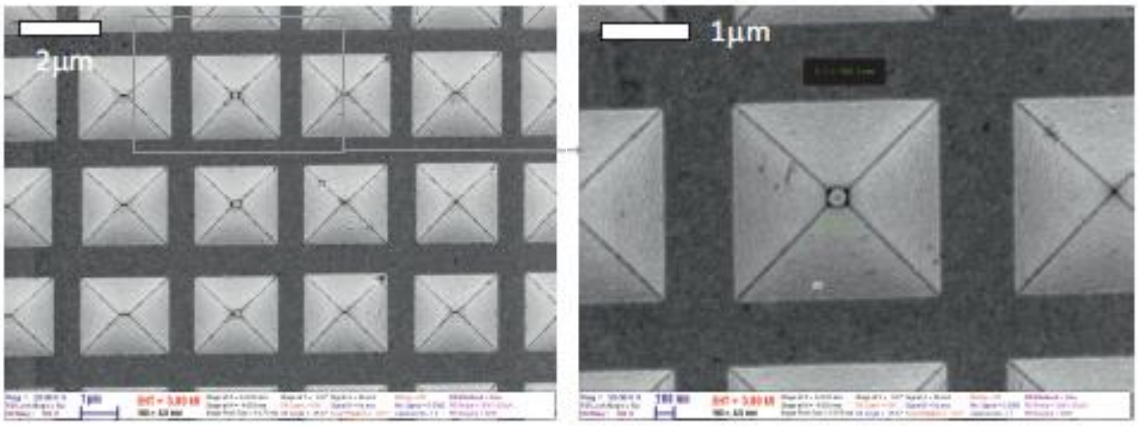

Figure 5.9. *SEM images of the inverse pyramid SERS substrate with 200 nm GNPs located in some of the voids.*

Silicon was used as substrate material of the inverse pyramids with 150 nm gold coating, and periodically ordered gold nanospheres (with 100 and 200 nm diameter) were placed into the pyramids. A remarkable increase of the surface enhancement has been observed in gold coated micron sized inverse pyramid after placing a gold nanosphere inside it. The amplification of both surface enhanced Raman and fluorescence signals was found to be dependent on the size of the gold nanoparticle, and the enhancement can be two orders of magnitude larger than that of the empty pyramid (Fig. 5.10.).

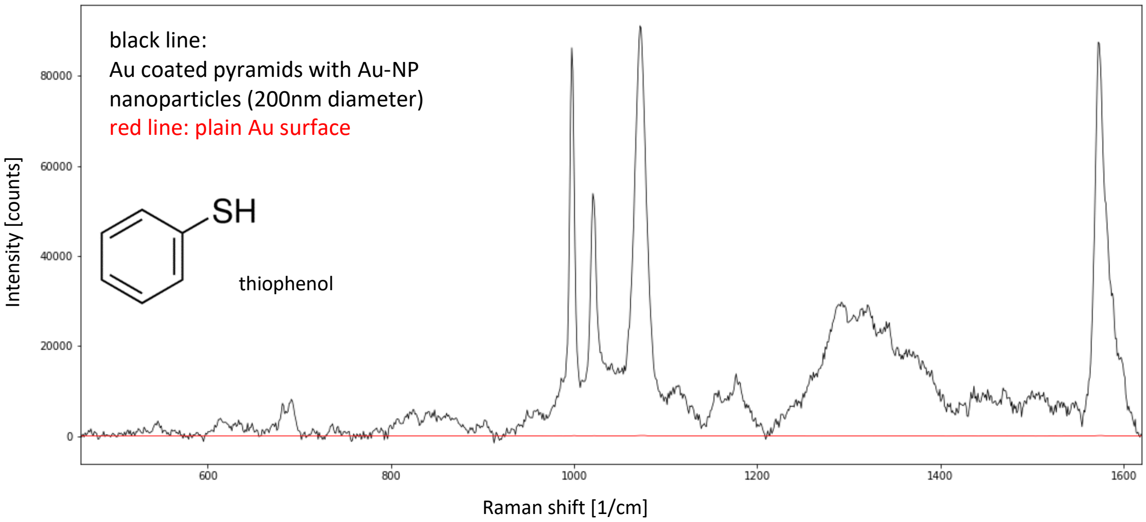

Figure 5.10. *Surface enhanced Raman spectra of thiophenone solution dripped and dried onto inverse pyramid arrays entrapping a Au NP with diameter of 200nm.*

To understand the analytical performance the near-field intensity distributions of inverse pyramid arrays were studied by FDTD simulations using the Lumerical FDTD Solutions v.8.15.736 software. The origin of the phenomenon was investigated by finite differential time domain simulations that showed that coupling of the electric field occurs when the nanosphere protrudes into the high intensity near-field region of the pyramid. The plasmon-related near-field enhancement was found to be concentrated into the gaps formed around the contact points of the curved sphere and the flat pyramid surface [Ref. 5.6].

Development and small scale production of near infrared LEDs and LED based devices: and their spectroscopic applications

Moore4Medical, ECSEL-2019-1-IA -876190 2019-2.1.3-NEMZ_ECSEL-2020-00005

F. Bíró, J. Bozorádi, G. Battistig, Cs. Dücső, B. Beiler, Z. Szabó, P. Fürjes

Near infrared LEDs for spectroscopy

Infrared spectroscopy is a very popular measurement technique especially in food industry, pharmaceutical industry and agriculture for the detection and measurement of organic materials. The -OH, -NH and -CH functional groups found in organic substances can frequently be detected by spectroscopy through absorbance measurements at the resonance wavelength of valence-bond vibrations. The measured wavelengths are 4-2.5µm, while the signal to noise ratio of photon detectors is low due to thermal noise at room temperature. The 1st-3rd harmonic absorption bands are located in the range of the near infrared (NIR), where smaller signals can be measured effectively in practice. NIR LEDs have narrow wavelength, therefore they are suitable for measurements at given wavelength. Further advantages of LEDs compared to incandescent lamps are their small dimensions, high efficiency, and low power consumption, which is critical in small handheld devices.

GaInAsP/InP is an ideal material system for the fabrication of double heterostructure devices as the emission wavelength is easily tuneable between 950-1650 nm. As InP has higher bandgap than the lattice-matched GaInAsP active layer the absorption losses inside the device structure can be minimized. In order to tune the emission wavelength of the LED, the composition of the semiconductor light-emitting layer has to be properly set. Our high quality single peak LED chips (1220nm) have a stable market, our business partners are SENOP Oy (Fi) and Anton Paar Ltd. (At).

The purpose of the **LED2Spectro (Knowledge Transfer) project** is to connect the Centre for Energy's Microsystems Lab with a potential application partner Photonic Insights (Germany) who also serves as an interface between the Microsystems Lab and Fraunhofer IZM. Berlin-based company Photonic Insights develops products for advanced quality measurement. Microsystems Lab provides LED based illumination technology that is targeted in the near-infrared (NIR) region 950nm to 1650nm. This illumination is an optimal complement for cutting-edge spectrographic sensors. These LEDs can be integrated into the existing spectrographic device created by Photonic Insights. The unique double-wavelength LEDs have the advantage is that emission peaks are stable relative to each other because only one LED driver circuit is needed and both of peaks are generated by the same emission spot. New innovative NIR LED light source is under development which illuminates in the whole NIR spectral range. It could replace the miniature incandescent light sources in the handheld spectroscopic devices. The first solution that will benefit from the cooperation is Photonic Insights' metrology suite which adds value to certain agricultural and water-related use cases due to its price performance ratio.

Tea quality measurement is an untapped segment of measurement technology. This is primarily an Asian (China, Sri Lanka, India) agricultural market. In tea quality measurement technology there are so far, two competitors present. One of them offers a stationary, not handheld device with mediocre analytic capabilities, the other offers a mobile-phone-integrated solution, hence handheld; however, the analytical capabilities are low. Optical reflectance measurements in NIR range on wet and dry tea leaves are capable to identify to monitor the drying process of the leaves; optical absorbance measurement in the UV-NIR range helps to investigate the optically detectable target molecules in tea solutions.

Reflectance measurements on tea leaves were carried out simultaneously with mass measurement during the drying process. The known water content vs. reflectance spectra (Fig. 5.11.a) were analysed by Photonic Insights to identify the most important wavelength lines and develop the calculation method for the moisture measurement. It is possible to distinguish between different types of tea solutions based on the visible and NIR absorbance spectra (Fig. 5.11.b.). To measure absorbance in UV range further dilution was necessary. The chemical composition of tea is very complex, and it contains, among other things, polyphenols, alkaloids (caffeine, theophylline and theobromine); amino acids (L-theanine); flavanols/tannins; carbohydrates; proteins; chlorophyll and volatile compounds. Photonic Insights has the knowledge base and experience to analyse such a complex data using various analytical methods.

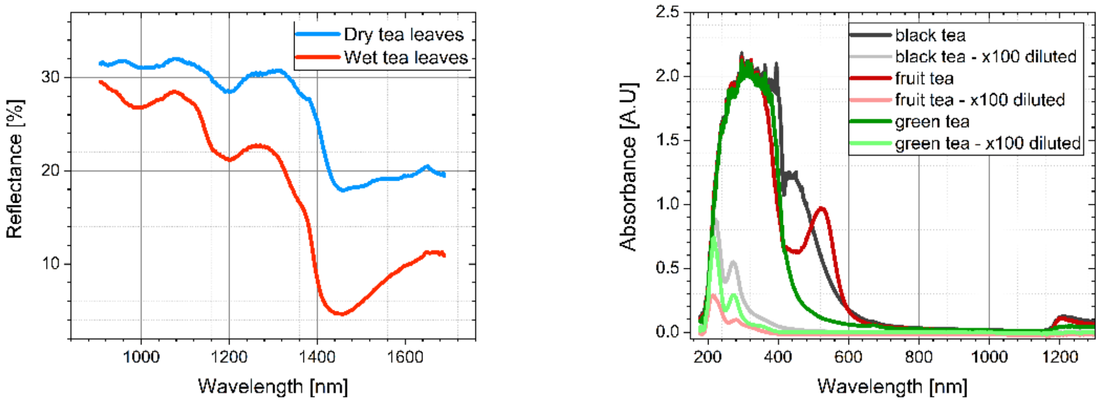

Figure 5.11. *NIR reflectance spectra of wet and dry tea leaves (left) and UV-NIR absorbance spectra of different tea solutions (b.).*

Marker molecule detection in Organ-on-Chip applications

The 3 year long international Moore 4 Medical project was started in June 2020. The consortium has participants from 12 countries and from around 64 companies and research institutes. The project leader, Phillips Research try to create the base of new open technology platforms which will accelerate innovations in various medical domains such as implantable devices, organ-on-chip, drug adherence, next generation ultrasound, towards x-ray free surgery and continuous patient monitoring. Our main task is in the field of development organ-on-chip applications, where the collaboration develops a smart multiwell plate system. A smart multiwell plate works as an autonomous system with micropumps, microfluidic infrastructure that provide perfusion, as well as the electronics to drive the micropumps and integrated readout sensors. Another part of the system is a smart multiwell plate lid that can be used in combination with ordinary, as well as the smart multiwell plates. The non-disposable lid contains micropumps and sensors that monitor in situ and in a parallel fashion monitor the medium of cell cultures in incubators.

Our laboratory participates in designing the microfluidic layer of the smart well plate, development flexible sensor module for the smart lid and the **integration of optical NIR spectral sensors**. We intend to develop near IR LED sources and spectroscopic solution for monitoring nutrient composition (e.g. glucose concentration) in microfluidic channels. There is only a small space (~1 cm^3) available in the smart well plate for an optical sensor, if we are still intended to construct a modular plug-in module. According to the limited space the miniaturisation and usage microfluidic channels and cuvettes are crucial. The final vision is to construct a modular optical plug-in module integrated with microfluidic sample monitoring system and the measurement has to be restricted to a few specific wavelengths using absorption or fluorescence detection.

For the first period the main goal was to **define system specifications and architecture**. Accordingly the components of the cell culture media and its additives were investigated by measuring their optical characteristics in the 200-2500 nm (UV-VIS-NIR and even in mid infrared) range. Absorbance, transmittance and fluorescence spectra were recorded so far on DMEM/F-12 plus and Vitrolife G1 (plus) solutions, glucose, lactate, glutamine molecules and antibiotics such as penicillin streptomycin, streptomycin sulphate, neomycin sulphate in different concentrations. Other target molecules, various grow factors are also considered: EGF, FGF, BDNF, VEGF, GDNF. High throughput optical studies were stated by platereader (TECAN Spark) also in the 200-1000 nm range.

- Glucose has only a very small absorption in near infrared (NIR) range in the usual concentration range and has no fluorescence signal.
- Lactate (which indicates the anaerobic glucose consumption) has high absorbance in the UV region and absorbance peaks in the NIR range.

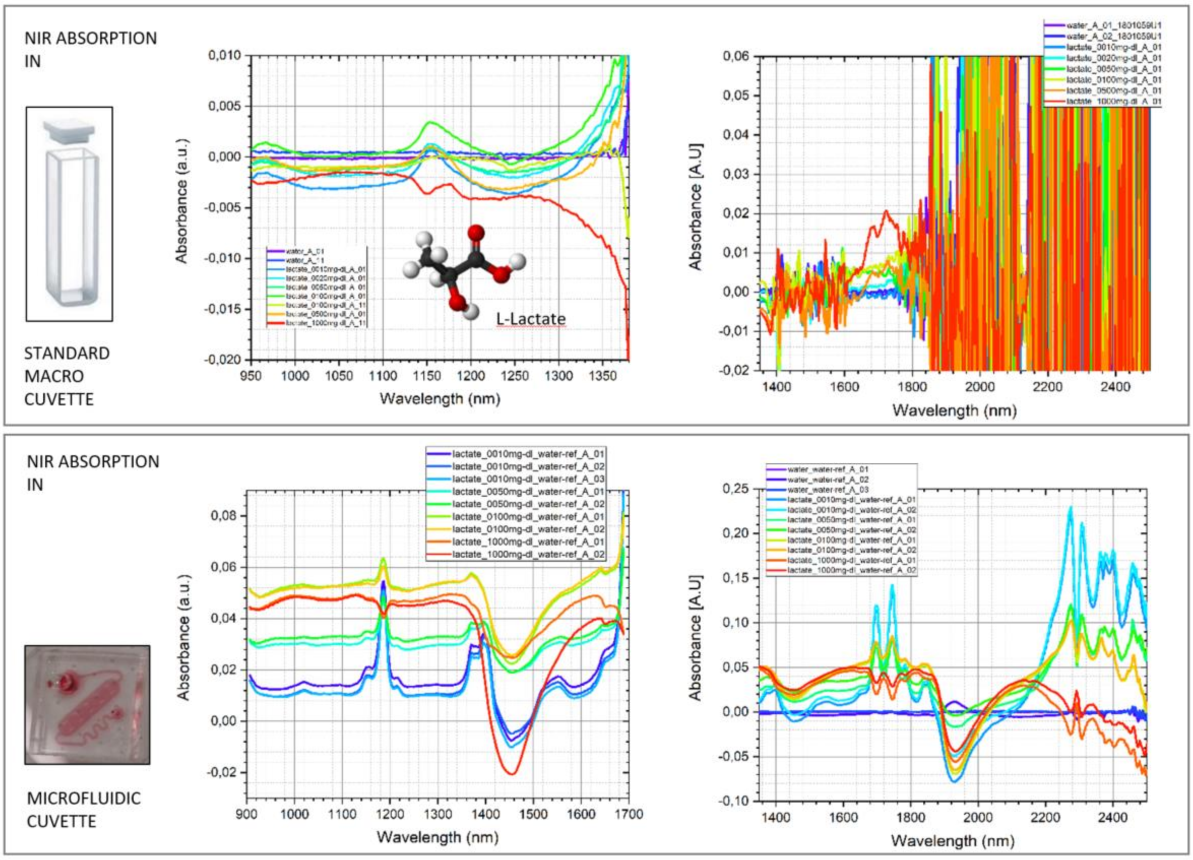

Figure 5.12. *Spectral characteristics of the lactate in macroscopic (top) and microfluidic environment (bottom) as being a significant marker molecule of OoC applications. The IR light absorption is depressed due to the smaller pathway in microfluidics, and it allows us to measure detailed spectrum.*

For further optical characterisation specific microfluidic cuvettes were designed and manufactured. According to the requirements of low sample volume and autonomous sample transport a specific surface modified PDMS (polydimethylsiloxane) microfluidic cuvette was fabricated by soft lithographic technique. The optical parameters were measured in microfluidic cuvette and compared to the macroscopic case. In microfluidic environment **improved signal-to-noise ratio was achieved due to the suppressed absorption of water** as demonstrated in Fig. 5.12 in case of Lactate. The top right figure demonstrates the high optical absorption of water in the wavelength range of 1400-2400nm, accordingly the detected signal is low, and the signal-to-noise ratio is low. In contrary in microfluidic environment the effect can be eliminated (see the bottom right figure). To step forward the integration of the optical screening method in smart wellplate system the wellplate compatible microfluidic cuvette was designed including material selection, geometric parameters and fabrication technology in cooperation with Micronit & TUDelft. The possible cuvette materials were characterised optically and COP was chosen. The geometry was defined to be compatible with the fluidic layer of the smart wellplate. Hot embossing and laser welding (in cooperation with Aedus Ltd.) were proposed as industrial scale production compatible technologies.

6- Nanobiosensorics Momentum Group

Head: Robert HORVATH, Ph.D., Senior Scientist

Research Staff
- Robert HORVATH, Ph.D.
- Sándor KURUNCZI, Ph.D.
- Inna SZÉKÁCS, Ph.D.
- Beatrix PÉTER, Ph.D.
- Boglárka KOVÁCS, Ph.D.
- András SAFTICS, Ph.D.
- Zoltán SZITTNER, Ph.D.
- Enikő FARKAS, Ph.D
- Alexandra VÖRÖS, MSc
- Andrea ÁCS, MSc
- Nicolett KANYÓ, MSc

Ph.D. students / Diploma workers
- Ágoston NAGY, Ph.D. student
- Tamás GERECSEI, Ph.D. student
- Kinga Dóra KOVÁCS, PhD student
- Milán SZTILKOVICS, MSc student
- Fatime GAJNUT, MSc student
- Imola RAJMON, BSc student
- Anna BALOGH, BSc student
- Szabolcs NOVÁK, MSc student
- Zsolt, JANKA MSc student
- Viktor Sándor KOVÁCS, BSc student
- Bálint BÉRES, MSc student
- Tamás HAJDÚ, MSc student
- Lili FARKAS, MSc student
- Igor SALLAI, MSc student
- Norbert PAP, BSc student
- Róbert TARR, BSc student
- Kinga TÓTH, BSc student
- Barbara MAJOROS, MSc student
- Beatrix MAGYARÓDI, MSc student
- Bence JOÓ, MSc student
- Péter JOÓ, MSc student

The research profile of the Nanobiosensorics Group is the development and application of label-free optical biosensors, the mathematical modeling of the relevant biological and biophysical processes. Building on their broad national and international collaborative network the group conducts research in the fields of instrument development, monitoring of cell secreted extracellular vesicles, development of protein-based functional coatings, adhesion studies on human cancer and immune cells, and theoretical modeling. In 2014, the application for an ERC Consolidator Grant by the head of the research group received qualification category “A (fully meets the ERC excellence criteria and should be funded if sufficient funds are available)” after the interview in Brussels, but the funding line did not reach this proposal due to budgetary constraints. However, using this achievement the Group could successfully apply for funding from NKFIH in the framework of the ERC_HU call. In the framework of this project they aim single cell manipulation and label-free sensing. Building on this expertise, in 2018 they won an Élvonal (NKFIH) research project for single cell biosensing. In 2020, the research group won the Tématerületi Kiválósági Program (TKP2021 NKFIH) excellence project as well in collaboration with other groups of the MFA.

Dissociation constant of integrin-RGD binding in live cells from automated micropipette and label-free optical data

LP2012-26/2012 Lendület, OTKA KH126900, OTKA ERC_HU117755, OTKA PD131543, OTKA KKP129936

T. Gerecsei, P. Chrenkó, N. Kanyó, B. Péter, A. Bonyár (BME), I. Székács, B. Szabó (ELTE), R. Horváth

The binding of integrin proteins to peptide sequences such as arginine-glycine-aspartic acid (RGD) is a crucial step in the adhesion process of mammalian cells. While these bonds can be examined between purified proteins and their ligands, live-cell assays are better suited to gain biologically relevant information. Here we apply a computer-controlled micropipette (CCMP) to measure the dissociation constant (Kd) of integrin-RGD-binding. Surface coatings with varying RGD densities were prepared, and the detachment of single cells from these surfaces was measured by applying a local flow inducing hydrodynamic lifting force on the targeted cells in discrete steps. The average behavior of the populations was then fit according to the chemical law of mass action. To verify the resulting value of Kd2d = (4503 ± 1673) $1/\mu m^2$, a resonant waveguide grating based biosensor was used, characterizing and fitting the adhesion kinetics of the cell populations. Both methods yielded a Kd within the same range. Furthermore, an analysis of subpopulations was presented, confirming the ability of CCMP to characterize cell adhesion both on single cell and whole population levels (Fig. 6.1). The introduced methodologies offer convenient and automated routes to quantify the adhesivity of living cells before their further processing [Ref. 6.1.].

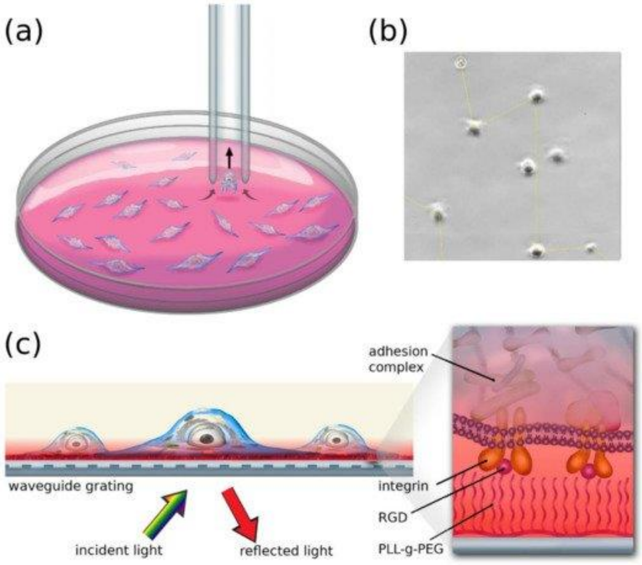

Figure 6.1. *Illustration of the methods used to measure cell adhesion. (a) The computer-controlled micropipette (CCMP) automatically visits each detected cell and probes them by applying a preset negative pressure. (b) Section of a field of view in a Petri dish containing adhered HeLa cells. (c) Schematic representation of the resonant waveguide-based measurement.*

Data evaluation for surface-sensitive label-free methods to obtain real-time kinetic and structural information of thin films: A practical review with related software packages

LP2012-26/2012 Lendület, OTKA ERC_HU117755, OTKA KH126900,
OTKA KKP129936, OTKA PD131543

A. Saftics, S. Kurunczi, B. Péter, I. Székács, J. J. Ramsden (University of Buckingham), R. Horváth

Interfacial layers are important in a wide range of applications in biomedicine, biosensing, analytical chemistry and the maritime industries. Given the growing number of applications, analysis of such layers and understanding their behavior is becoming crucial. Label-free surface sensitive methods are excellent for monitoring the formation kinetics, structure and its evolution of thin layers, even at the nanoscale.

In this paper, we review existing and commercially available label-free techniques and demonstrate how the experimentally obtained data can be utilized to extract kinetic and structural information during and after formation, and any subsequent adsorption/desorption processes. We outline techniques, some traditional and some novel, based on the principles of optical and mechanical transduction. Our special focus is the current possibilities of combining label-free methods, which is a powerful approach to extend the range of detected and deduced parameters. We summarize the most important theoretical considerations for obtaining reliable information from measurements taking place in liquid environments and, hence, with layers in a hydrated state.

A thorough treamtment of the various kinetic and structural quantities obtained from evaluation of the raw label-free data are provided. Such quantities include layer thickness, refractive index, optical anisotropy (and molecular orientation derived therefrom), degree of hydration, viscoelasticity, as well as association and dissociation rate constants and occupied area of subsequently adsorbed species. To demonstrate the effect of variations in model conditions on the observed data, simulations of kinetic curves at various model settings are also included. Based on our own extensive experience with optical waveguide lightmode spectroscopy (OWLS) and the quartz crystal microbalance (QCM), we have developed dedicated software packages for data analysis (Fig.6.2), which are made available to the scientific community alongside this paper [Ref. 6.2.].

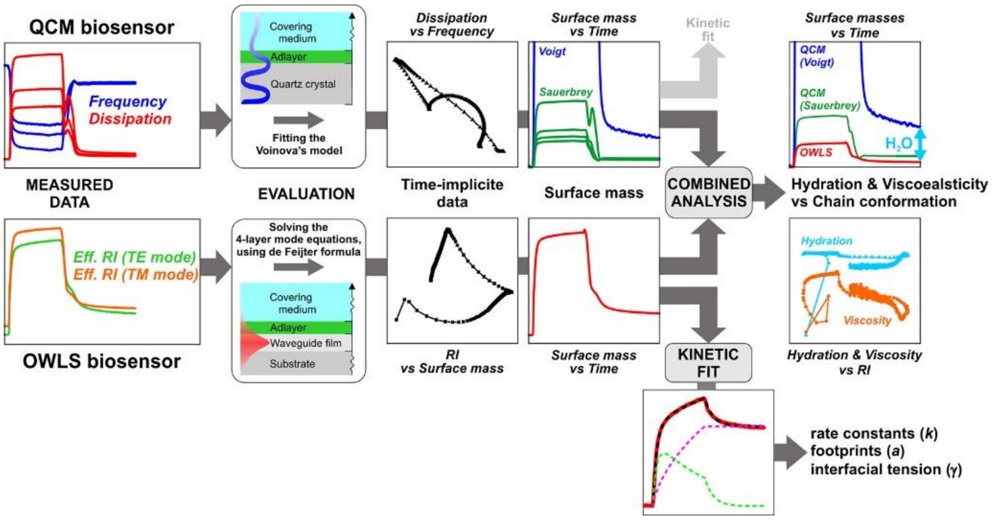

***Figure 6.2**. Simulations of kinetic curves at various model settings are also included in the review article.*

Nanonewton scale adhesion force measurements on biotinylated microbeads with a robotic micropipette

LP2012-26/2012 Lendület, OTKA PD124559, OTKA PD131543, OTKA ERC_HU117755, OTKA KH126900, OTKA KKP129936

R. Ungai-Salánki, B. Csippa (ELTE), T. Gerecsei, B. Péter, R. Horváth, B. Szabó (ELTE)

Binding force between biomolecules has a crucial role in most biological processes. Receptor-ligand interactions transmit physical forces and signals simultaneously. Previously, we employed a robotic micropipette both in live cell and microbead adhesion studies to explore the adhesion force of biomolecules such as cell surface receptors including specific integrins on immune cells. Here we apply standard computational fluid dynamics simulations to reveal the detailed physical background of the flow generated by the micropipette when probing microbead adhesion on functionalized surfaces. Measuring the aspiration pressure needed to pick up the biotinylated 10 μm beads on avidin coated surfaces and converting it to a hydrodynamic lifting force on the basis of simulations, we found an unbinding force of 12 ± 2 nN, when targeting the beads manually; robotic targeting resulted in 9 ± 4 nN (mean ± SD). We measured and simulated the effect of the targeting offset, when the microbead was out of the axis (off-axis)of the micropipette.

According to the simulations, the higher offset resulted in a higher lifting force acting on the bead. Considering this effect, we could readily correct the impact of the targeting offset to renormalize the experimental data. Horizontal force and torque also appeared in simulations in case of a targeting offset. Surprisingly, simulations show that the lifting force acting on the bead reaches a maximum at a flow rate of ~ 5 μl/s if the targeting offset is not very high (<5 μm). Further increasing the flow rate decreases the lifting force. We attribute this effect to the spherical geometry of the bead. We predict that higher flow rates cannot increase the hydrodynamic lifting force acting on the precisely targeted microbead, setting a fundamental force limit (16 nN in our setup) for manipulating microbeads with a micropipette perpendicular to the supporting surface (Fig.6.3). In order to extend the force range, we propose the offset targeting of microbeads [Ref. 6.3.]

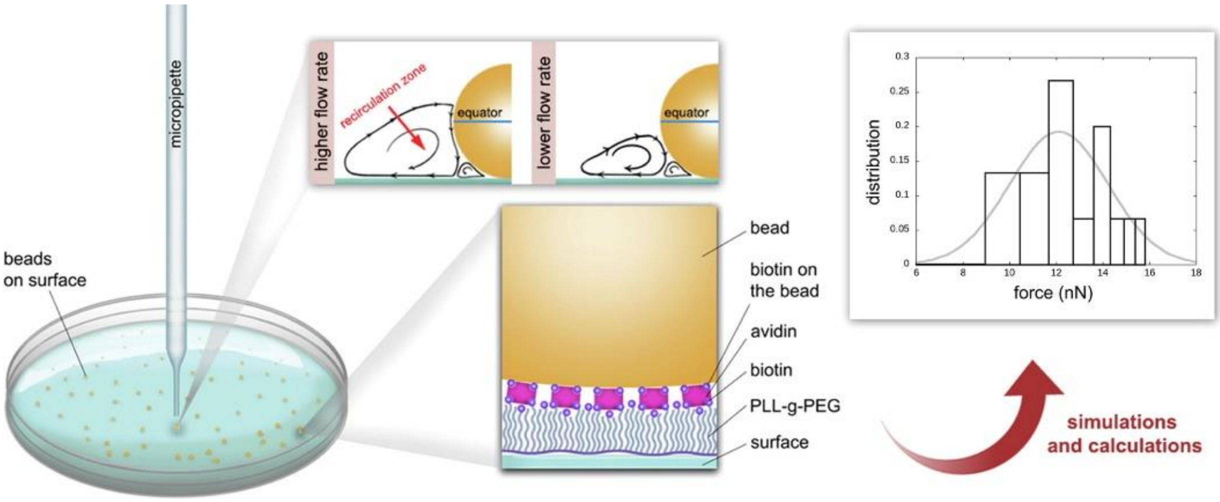

Figure 6.3. *For measuring the aspiration pressure needed to pick up the biotinylated 10 μm beads on avidin coated surfaces with robotic micropipette.*

Natural compounds as target biomolecules in cellular adhesion and migration: from biomolecular stimulation to label-free discovery and bioactivity-based isolation

LP2012-26/2012 Lendület, OTKA ERC_HU117755, OTKA PD131543, OTKA KKP129936, OTKA K135712, TKP2020-IKA-05, EFOP-1.8.0-VEKOP-17-2017-00001

B. Péter, I. Boldizsár (ELTE), G. M. Kovács (ELTE), A. Erdei(ELTE), Zs. Bajtay (ELTE), A. Vörös, J. J. Ramsden (University of Buckingham), I. Szabó (ELTE), Sz. Bősze (ELTE), R. Horváth

Plants and fungi can be used for medical applications because of their accumulation of special bioactive metabolites. These substances might be beneficial to human health, exerting also anti-inflammatory and anticancer (antiproliferative) effects. We propose that they are mediated by influencing cellular adhesion and migration via various signaling pathways and by directly inactivating key cell adhesion surface receptor sites. The evidence for this proposition is reviewed (by summarizing the natural metabolites and their effects influencing cellular adhesion and migration), along with the classical measuring techniques used to gain such evidence. We systematize existing knowledge concerning the mechanisms of how natural metabolites affect adhesion and movement, and their role in gene expression as well. We conclude by highlighting the possibilities to screen natural compounds faster and more easily by applying new label-free methods, which also enable a far greater degree of quantification than the conventional methods used hitherto.

We have systematically classified recent studies regarding the effects of natural compounds on cellular adhesion and movement, characterizing the active substances according to their organismal origin (plants, animals or fungi) [Ref. 6.4]. Finally, we also summarize the results of recent studies and experiments on SARS-CoV-2 treatments by natural extracts affecting mainly the adhesion and entry of the virus (Fig. 6.4).

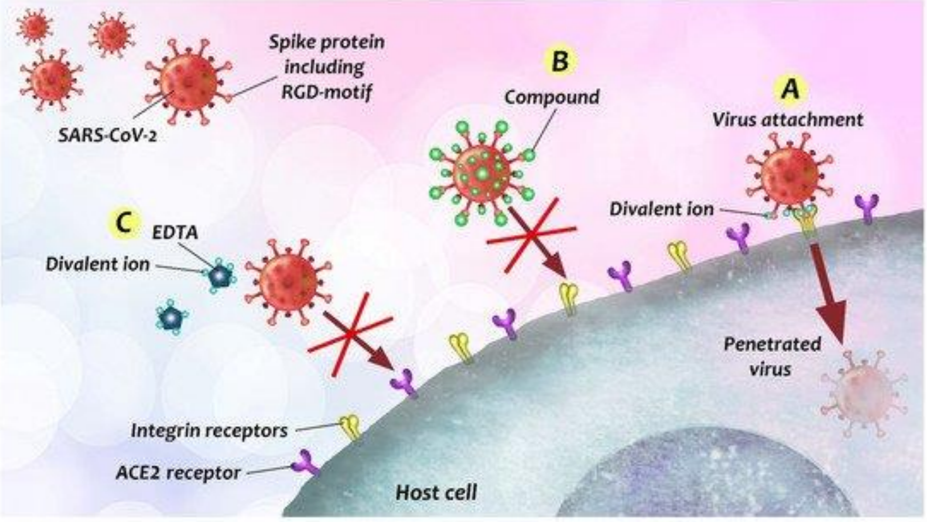

***Figure 6.4**. Schematic illustration of SARS-CoV-2 attachment and two possible examples of ways to inhibit this process. (A) Virus can attach to ACE2 receptor or integrins of the host cell. RGD-integrin interaction occurs in calcium-dependent manner. As the result of the process, the virus penetrates into the cell and starts to copy itself. (B) Several compounds bind to the spike protein or even may alter it and prevent virus-receptor attachment. (C) Lowering divalent ion concentrations in the lungs with pulmonary EDTA chelation therapy may inhibit virus-host interaction.*

Design of non-autonomous pH oscillators and the existence of chemical beat phenomenon in a neutralization reaction

LP2012-26/2012 Lendület, OTKA NN125752, OTKA K131425, OTKA KKP129936, TKP2020 IES, Grant No. BME-IE-NAT

H. S. Lawson (BME), G. Holló (BME), N. Német (BME), S. Teraji (KIT, Japan), H. Nakanishi (KIT, Japan), R. Horváth, I. Lagzi (BME)

The beat in physical systems is a transparent and well-understood phenomenon. It may occur in forced oscillatory systems and as a result of the interference of two waves of slightly different frequencies. However, in chemical systems, the realization of the latter type of the beat phenomenon has been lacking. Here we show that a periodic titration of acid and alkaline solutions with each other using programmable syringe pumps in a continuous stirred-tank reactor exhibits the beat phenomenon in the temporal pH oscillation pattern if the time periods of sinusoidal inflow rates of the reagents are slightly different. Interestingly, the frequency of the chemical beat pattern follows the well-known relationship from physics, namely the frequency of the beat is equal to the absolute value of the difference of the two wave frequencies. Based on our strategy, we can design and engineer non-autonomous pH oscillatory systems, in which the characteristics of the temporal oscillations (amplitude, time period) can easily and precisely be controlled by the experimental conditions such as the inflow rates and feed concentrations (Fig. 6.5). The demonstrated phenomena can be exploited in practical applications, we use the non-autonomous pH oscillators to drive the reversible assembly and disassembly of pH-sensitive building blocks (oleic acid and gold nanoparticles), both highly relevant in nanotechnology and biomedical applications [Ref. 6.5.]

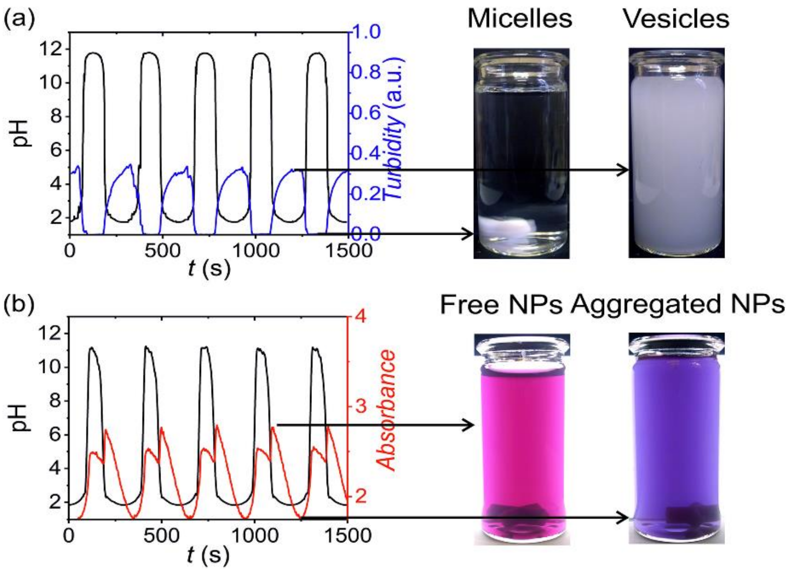

***Figure 6.5**. Reversible transformation of vesicle and micelles (a) and assembly/disassembly of pH-sensitive AuNPs (b) using the non-autonomous pH oscillator.*

Near cut-off wavelength operation of resonant waveguide grating biosensors

LP2012-26/2012 Lendület, OTKA ERC_HU117755, OTKA KH126900,
OTKA KKP129936, OTKA K132050

B.Kovács, F. A. Kraft (Kiel University), Zs. Szabó (PPKE), Y. Nazirizadeh (Byonoy GmbH), M. Gerken (Kiel University), R. Horváth

Numerical simulations and analytical calculations are performed to support the design of grating-coupled planar optical waveguides for biological sensing. Near cut-off and far from cut-off modes are investigated, and their characteristics and suitability for sensing are compared. The numerical simulations reveal the high sensitivity of the guided mode intensity near the cut-off wavelength for any refractive index change along the waveguide. Consequently, it is sufficient to monitor the intensity change of the near cut-off sensing mode, which leads to a simpler sensor design compared to those setups where the resonant wavelength shift of the guided mode is monitored with high precision. The operating wavelength and the sensitivity of the proposed device can be tuned by varying the geometrical parameters of the corrugated waveguide (Fig.6.6). These results may lead to the development of highly sensitive integrated sensors, which have a simple design and therefore are cost-effective for a wide range of applications. These numerical findings are supported with experimental results, where the cut-off sensing mode was identified [Ref. 6.6.].

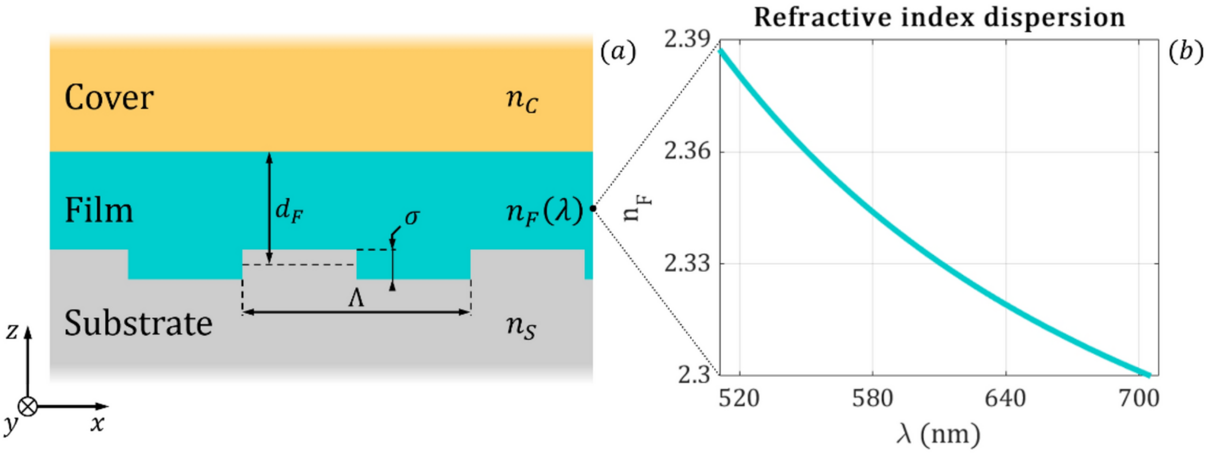

Figure 6.6. *(a) The cross-section of the modeled corrugated waveguide. The electromagnetic simulations apply Floquet boundary conditions along the x- and y-axis and open boundaries with Floquet ports in the vertical z direction. (b) The frequency dependence of the* Nb_2O_5 *film refractive index.*

Single-cell adhesion strength and contact density drops in the M phase of cancer cells

LP2012-26/2012 Lendület, OTKA PD124559, OTKA ERC_HU117755,
OTKA KH126900, OTKA PD131543, OTKA KKP129936

R. Ungai-Salánki, E. Haty, T. Gerecsei, B. Francz (CellSorter), B. Béres, M. Sztilkovics,
I. Székács, B. Szabó (ELTE), R. Horváth

The high throughput, cost effective and sensitive quantification of cell adhesion strength at the single-cell level is still a challenging task. The adhesion force between tissue cells and their environment is crucial in all multicellular organisms. Integrins transmit force between the intracellular cytoskeleton and the extracellular matrix. This force is not only a mechanical interaction but a way of signal transduction as well. For instance, adhesion-dependent cells switch to an apoptotic mode in the lack of adhesion forces. Adhesion of tumor cells is a potential therapeutic target, as it is actively modulated during tissue invasion and cell release to the bloodstream resulting in metastasis.

We investigated the integrin-mediated adhesion between cancer cells and their RGD (Arg-Gly-Asp) motif displaying biomimetic substratum using the HeLa cell line transfected by the Fucci fluorescent cell cycle reporter construct. We employed a computer-controlled micropipette and a high spatial resolution label-free resonant waveguide grating-based optical sensor calibrated to adhesion force and energy at the single-cell level (Fig.6.7). We found that the overall adhesion strength of single cancer cells is approximately constant in all phases except the mitotic (M) phase with a significantly lower adhesion. Single-cell evanescent field based biosensor measurements revealed that at the mitotic phase the cell material mass per unit area inside the cell-substratum contact zone is significantly less, too. Importantly, the weaker mitotic adhesion is not simply a direct consequence of the measured smaller contact area. Our results highlight these differences in the mitotic reticular adhesions and confirm that cell adhesion is a promising target of selective cancer drugs as the vast majority of normal, differentiated tissue cells do not enter the M phase and do not divide [Ref. 6.7.]

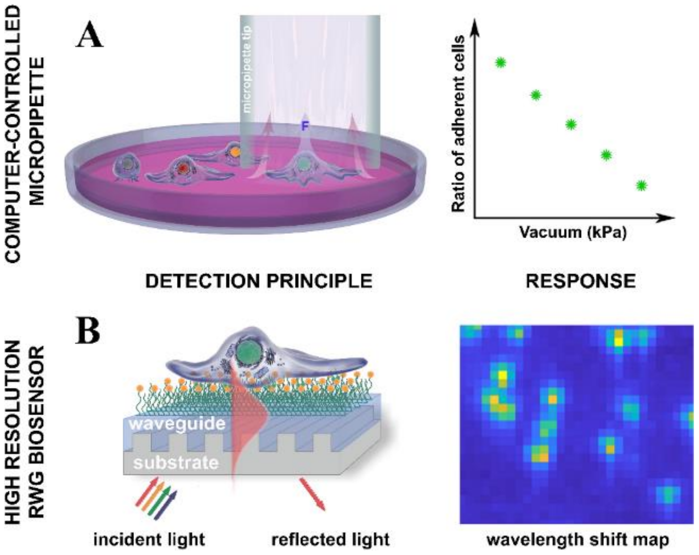

Figure 6.7. *Schematic representation of the adhesion strength measurements on single cells using a computer-controlled micropipette and the high-resolution RWG biosensor (Single-Cell RWG).*

Label-free tracking of whole-cell response on RGD functionalized surfaces to varied flow velocities generated by fluidic rotation

LP2012-26/2012 Lendület, OTKA KKP129936, OTKA KH126900,
TKP2020 IES, Grant No. BME-IE-BIO

K. D. Kovács, M. Novák, Z. Hajnal, Cs. Hős (BME), B. Szabó, I. Székács,
Y. Fang (Corning Inc.), A. Bonyár (BME), R. Horváth

Fluidic flow plays important roles in colloid and interface sciences. Measuring adsorption, aggregation processes and living cell behavior under a fluidic environment with varied flow velocities in a parallel and high-throughput manner remains to be a challenging task. Here a method is introduced to monitor cell response to well-defined flow with varied velocities over an array of label-free resonant waveguide grating (RWG) based optical biosensors (Fig.6.8). The arrangement consists of a circular well with an array of biosensors at the bottom surface. By rotating the liquid over the biosensor array using a magnetic stirrer bar, flow velocities from zero to a predefined maximum can be easily established over different locations within the biosensor array as characterized in detail by numerical simulations. Cell adhesion and detachment measurements on an Arg-Gly-Asp (RGD) peptide functionalized surface were performed to demonstrate i) measurements at a wide range of simultaneous flow velocities over the same interface; ii) the possibility of parallel measurements at the same flow conditions in one run; and iii) the simple tuning of the employed range of flow velocities. Our setup made it possible to analyze the magnitude and rate of cell detachment at various flow velocities in parallel and determine the critical velocity and force where cells start to detach from the RGD motif displaying biomimetic surface. Furthermore, cellular response to simultaneous mechanical (flow) and chemical stimulation was also investigated using trypsin as a model. This study opens a new possibility to investigate interface phenomena under predefined and conveniently varied flow conditions [Ref. 6.8].

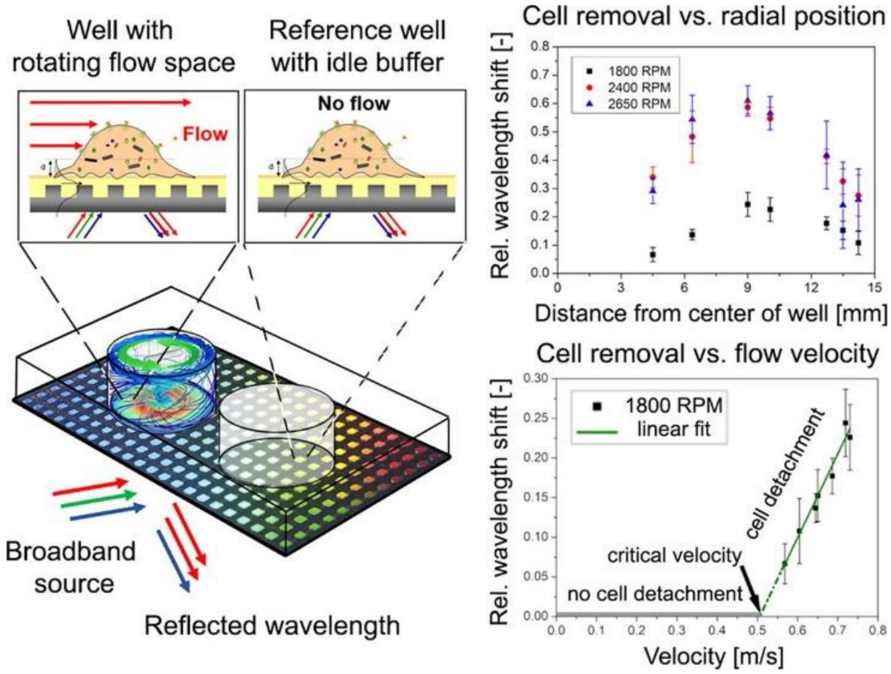

***Figure 6.8**. Illustration of the flow field and cell interactions in the assay and reference wells, respectively.*

Label-free real-time monitoring of the BCR-triggered activation of primary human B cells modulated by the simultaneous engagement of inhibitory receptors

LP2012-26/2012 Lendület, OTKA ERC_HU117755, OTKA KH126900, OTKA PD 131543, OTKA KKP129936, OTKA K 112011

K. Kliment, I. Szekacs, B. Peter, A. Erdei (ELTE), I. Kurucz (ELTE), R. Horvath

Today, there is an intense demand for lab-on-a-chip and tissue-on-a-chip applications in basic cell biological research and medical diagnostics. A particular challenge is the implementation of advanced biosensor techniques in point-of-care testing utilizing human primary cells. In this study, a resonant waveguide grating (RWG)-based label-free optical biosensor technique has been applied for real-time monitoring of the integrated responses of primary human tonsillar B cells initiated by B cell receptor (BCR) and modified by FcγRIIb and CR1 engagement (Fig.6.9).

The BCR-triggered biosensor responses of resting and activated B cells were revealed to be specific and dose-dependent, in some cases with strong donor dependency. Targeted inhibition of Syk attenuated the label-free biosensor response upon BCR stimulation. Indifferent protein human serum albumin (HSA) did not interfere with the recorded signal to BCR stimulation. Simultaneous engagement of BCR and FcγRIIb modulated the kinetic signal of the cells. Activated and resting B cells exhibited different response profiles upon simultaneous engagement of BCR and CR1. This advanced approach has the potential to decipher interfering signaling events in human B cells, manage differences between activated and resting B cell states, helping to understand the actual integrated response of these immune cells, and could be useful in the point-of-care diagnostic testing on human primary cells [Ref. 6.9].

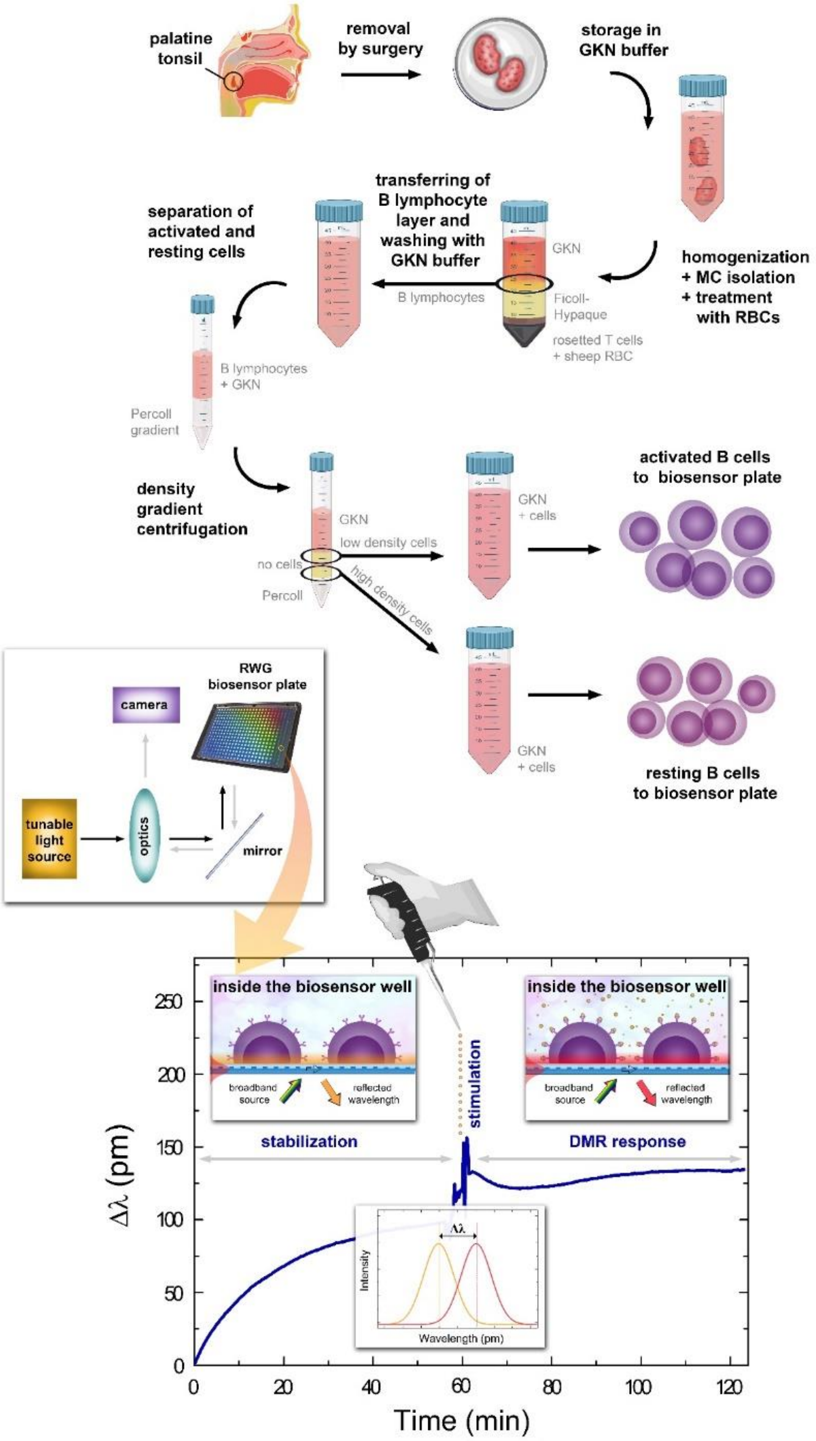

Figure 6.9. *Schematic overview illustrating the major steps of the biosensor assay: surgery material collection, storage in glucose potassium nutrient (GKN) buffer, mononuclear cells (MC) isolation through rosetting with 2-aminoethylisothiouronium bromide-treated sheep red blood cells (RBCs) by centrifugation over Ficoll-Hypaque solution, with further B cells fractionation on a Percoll gradient. In the end, activated and resting cells were used for the biosensor measurement. The bottom part represents the actual biosensor arrangement and data collection. The schematic readout of the biosensor microplate with incorporated sensor wells and the label-free primary signal (shift in resonant wavelength or DMR response) originating from the cells adhering on the surface is also shown.*

7 - Complex Systems Department

Head: Dr. Géza Ódor D.Sc., Scientific advisor

Research Staff
- Balázs Király PhD
- István Borsos
- Zoltán Juhász PhD
- György Szabó D.Sc., Professor emeritus
- Attila Szolnoki D.Sc., Scientific advisor
- Shengfeng Deng PhD

Ph.D. students / Diploma workers
- Zoltán Gárgyán LFZE diploma
- Krisztián Kiss LFZE diploma
- István Hegedűs LFZE, diploma
- Béla Szerényi, LFZE diploma
- Attila Kazsoki BME PhD student
- Lilla Barancsuk BME PhD student

The research field of the group is the investigation of complex systems by the methods of statistical physics in equilibrium as well as non-equilibrium states.

The theoretical investigation of multi-agent evolutionary game models studies processes supporting fair behavior of individuals by numerically analyzing mathematical models when a player’s own interest opposes that of the community. Mathematical models have been used to investigate the effect of one kind of penalties, the combinations of the rules of strategy updates, and systems in which the income of the players is obtained from two or three interconnection systems (communities).

The applicability of matrix decomposition is also being investigated in other related fields. In population ecology, the nature and intensity of pairwise interactions between different species can be gauged in biological growth experiments conducted in bicultures, but the specifics of the interplay between these interspecific interactions and how they determine outcomes in mixtures of multiple species are unclear as yet. We introduced the componental cosines of the irrelevant, external benefit, coordination, and conflict components of matrices to measure the relative weight of the different interaction types. The decomposition analysis of 33 empirical pair interaction matrices found in the literature has revealed statistically significant correlations between the different componental cosines beyond those introduced by their mere definitions, and also between some of the componental cosines and the community’s productivity and biodiversity. These latter correlations reflect expectations based on the game theoretic interpretation of the corresponding elementary matrices.

The Nash equilibria are investigated systematically for different combinations of elementary interactions. These analyses have clarified the existence and possible number of pure and strict Nash equilibria for n-strategy symmetric games and indicated different types of social dilemmas. Additionally, infinite number of mixed Nash equilibria are found in zero-measure subsets of the payoff parameter space.

Using concepts and methods of statistical physics the non-universal scale-free properties of avalanche phenomena were analysed in Kuramoto types synchronization models applied to the human and fruitfly brains. Similarly, catastrophe analyses were performed in models appearing in the interconnected network of electric plants and consumers. They extended the investigation of the general characteristics of the Griffiths phase to inhomogeneous networks of modular structure and realistic networks of the US, EU high voltage power-grids. The critical behavior of Covid-type SIR models were also studied finding relevant effects of topological disorder on the scaling in contrast with infection heterogeneity. While the mobility causes a dramatic increase of the epidemic, frozen hot-spot sizes do not much effect.

The increase of data in folk music and genetic data sets implies the continuous improvement of algorithms to analyze them. The newly developed algorithms are able both to identify clusters and to follow the evolutionary inheritance of clusters, both in genetic (haplogroup) features and in popular characteristics of folk music tunes. A book was also written, titled “Zenegenetika” by Z. Juhász.

Cooperation and competition between pair and multi-player social games in spatial populations

A. Szolnoki and X. Chen

The conflict between individual and collective interests is in the heart of every social dilemma established by evolutionary game theory. We cannot avoid these conflicts but sometimes we may choose which interaction framework to use as a battlefield. For instance, some people like to be part of a larger group while other persons prefer to interact in a more personalized, individual way. Both attitudes can be formulated via appropriately chosen traditional games. In particular, the prisoner's dilemma game is based on pair interaction, while the public goods game represents multi-point interactions of group members. To reveal the possible advantage of a certain attitude we extend these models by allowing players not simply to change their strategies but also let them to vary their attitudes for a higher individual income. We show that both attitudes could be the winner at a specific parameter value. Interestingly, however, the subtle interplay between different states may result in a counterintuitive evolutionary outcome where the increase of the multiplication factor of public goods game drives the population to a fully defector state. We point out that the accompanying pattern formation can only be understood via the multipoint or multi-player interactions of different microscopic states where the vicinity of a particular state may influence the relation of two other competitors.

When calculating the payoff of $A_{D,}$ marked by a yellow background, then we sum the payoff elements of four prisoner's dilemma games played with the neighbors. When we calculate the payoff of O_C player, also marked by yellow background, then we should consider the fact that two of its neighbors have "alone" attitude, hence O_C should play prisoner's dilemma game with them. The remaining two neighbors have "together" attitude hence the focal player can play a three-member public goods game with them in the marked G_0 group. The focal player also participates in a three-member public goods game of G_1 group and in a two-member game of G_2 group. For the shake of comparable payoff values we multiply the incomes of public goods games by an α factor. The interactions, where prisoner's dilemma game is used are marked by dashed lines, while the in the case of public goods game they are denoted by solid green (Fig. 7.1).

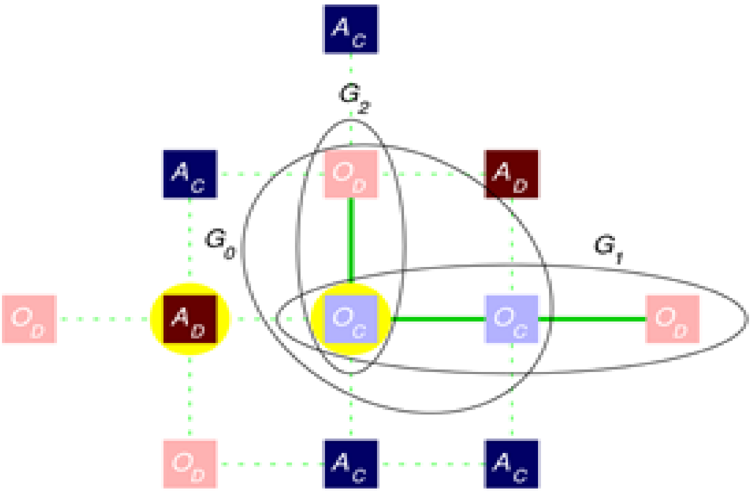

Figure 7.1. *The competition of "alone" and "together" attitudes.*

On the phase diagram of the four-state model (Fig 7.2.) in dependence of the key parameters of basic games r denotes the multiplication factor of the public goods game, while T is the temptation to defect for the prisoner's dilemma game. As expected, at low r values those states which represent pair interactions prevail. As we increase r, however, both attitudes, hence pair and multi-point interactions, coexist. Interestingly, as we support cooperation by increasing r further the system evolves onto a full defection state. Cooperation can only recover for very high r values when the traditional public goods game with multi-point interactions prevail. We may conclude that the freedom to choose alone attitude could be harmful for the vitality of together attitude, but the former could be an escape route in case of harsh conditions.

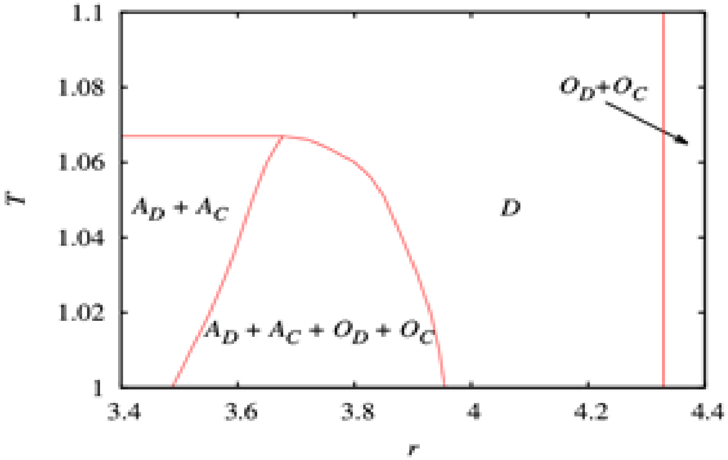

Figure 7.2. *Phase diagram of the four-state model in dependence of the key parameters of basic games.*

Time evolution of the pattern formation was shown at two representative values of multiplication factor r when T = 1.03. The common prepared initial state is shown in the left side on Fig. 7.3. where we arranged homogeneous patches of competing states denoted by different colors. Here dark colors mark players having "A" attitude, while light colors denote players with "O" attitude. Furthermore, different shades of red color mark defector strategies, while various blue colors for cooperator strategies. The legend for the microscopic states are shown in the middle row of the plot. The top row from panels (Fig 7.3.b-d) illustrates how the initial patchwork evolves at small (r = 3.4) multiplication factor. Here, as white ellipses shown in panel (Fig 7.3.b), A_C and O_C players can coexist due to the low value of r. Because of the modest temptation value A_D and A_C states can coexist and this mixed phase gradually beat O_D players. This process is marked by a white ellipse in panel (Fig 7.3.c). In the final state only players with "A" attitude can survive. When r is higher, as shown in the bottom row, O_C beats A_C who gradually diminishes. This is shown by a white ellipse in panel (Fig 7.3.e). The lonely O_C, however, becomes vulnerable against O_D and the previously victorious domains of O_C players gradually shrink. In the absence of other states A_D and O_D would be neutral, but the vicinity of cooperators helps the latter to beat the former defector state. This is shown by a white ellipse in panel (Fig 7.3.f). Finally, only defector state survives, but a slow voter-like stochastic dynamics will drive the system onto a homogeneous state [Ref. 7.1].

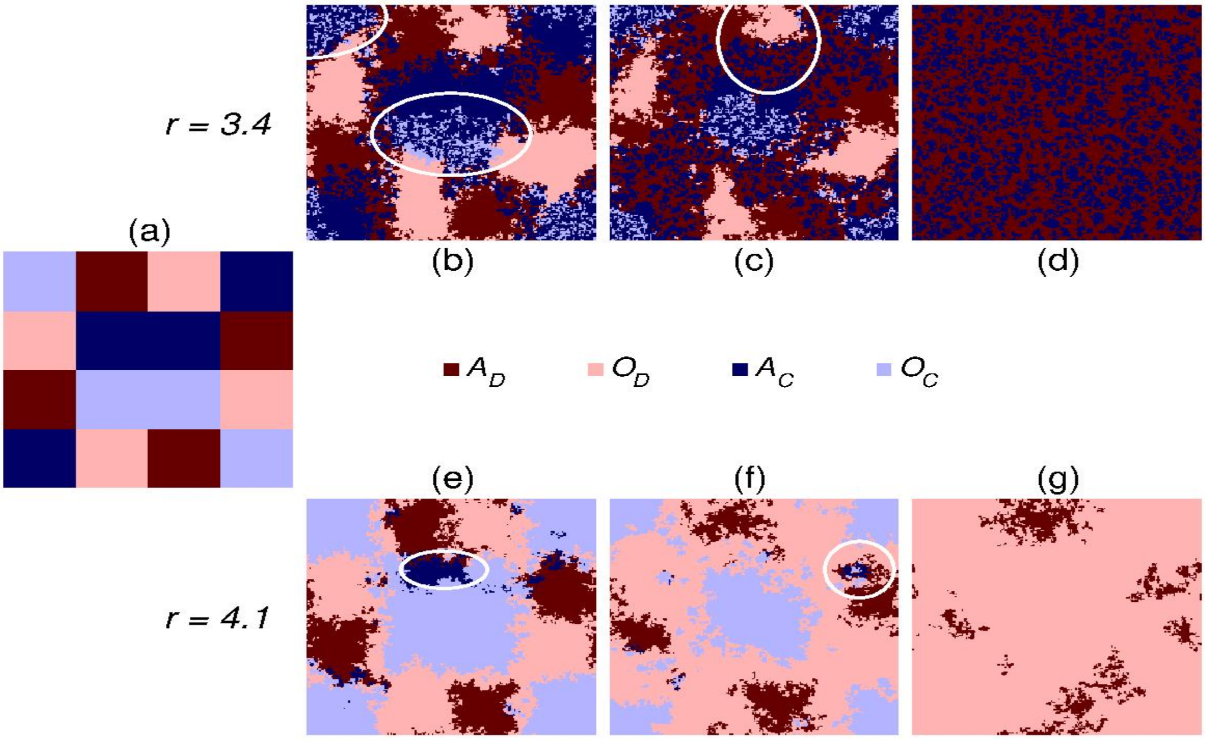

Figure 7.3. *Time evolution of the pattern formation.*

General features of Nash equilibria in combinations of elementary interactions in symmetric two-person games

OTKA PD 138571

G. Szabó and B. Király

One of the key concepts of game theory is the Nash equilibrium, a set of strategy choices from which no unilateral deviations can benefit the players. Nash's theorem states that in a game with a finite number of players who can choose from a finite number of pure strategies there exists, at least in the set of mixed strategies, at least one such equilibrium state. Generally, however, a game can have multiple different Nash equilibria. One such example is the two-person, three-strategy symmetric matrix game described by the dynamical graph shown in Fig. 7.4. The upper pair of numbers on the nodes of the graph show the strategy choices of the players, while the lower pair indicates the corresponding payoffs, and its directed edges point toward higher payoffs realized during unilateral strategy changes. Pure Nash equilibria, highlighted in yellow, are easily identified in in Fig. 7.4, since these can only have incoming edges attached to them. The game also has a mixed Nash-equilibrium that provides a lower payoff. Games like this may lead to social dilemmas, as they make mutually choosing the "best" equilibrium more difficult for selfish players who do not communicate with each other, which can be circumvented by considering other viewpoints, trust and fraternity. The importance of the problem of choosing from different Nash equilibria is demonstrated by earlier computer studies that proved that the expected number of Nash equilibria increases with the logarithm of the number of strategies when the payoffs are random.

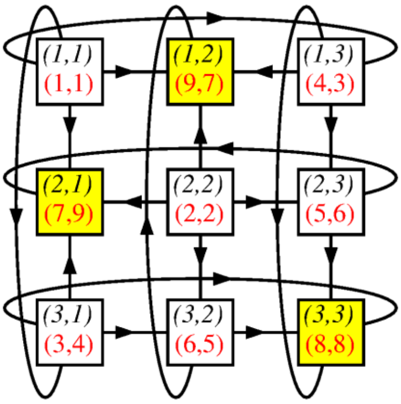

Figure 7.4. *Two-person, three-strategy symmetric matrix game*

Our research employed direct analytic calculations to analyze the number of Nash equilibria in symmetric matrix games with an arbitrary *n* number of strategies in light of the decomposition of payoff matrices into four kinds of non-trivial, self-dependent, cross-dependent, coordination and cyclic, elementary interaction types. Our results revealed that in self-dependent games (aside from degenerate cases, in general) there is a single pure Nash equilibrium. Games made up solely of coordination components can have at most *n* different pure Nash equilibria, and this statement remains true even when beside the coordination component self- and cross-dependent components are also present. An infinite number of mixed Nash equilibria can be observed in certain games composed of appropriate combinations of coordination or cyclic elementary games, which still only constitute a zero-measure subset of all possible games. Purely cross-dependent games also have an infinite number of Nash equilibria, however, adding these or constant components to other games does not change their Nash equilibria. A detailed treatment of our results was published in a game theory special issue of The European Physical Journal B [Ref. 7.2.].

Critical dynamics, synchronization and Griffiths effects in brain models

G. Ódor, G. Deco, J.Kelling

We have extended the study of the Kuramoto model with additive Gaussian noise running on the KKI-18 large human connectome graph. We determined the dynamical behavior of this model by solving it numerically in an assumed homeostatic state, below the synchronization crossover point we determined previously. The de-synchronization duration distributions exhibit power-law tails, characterized by the exponent in the range $1.1 < \tau_t < 2$, overlapping the in vivo human brain activity experiments by Palva et al. We show that these scaling results remain valid, by a transformation of the ultra-slow eigen-frequencies to Gaussian with unit variance. We also compare the connectome results with those obtained on a regular cube with $N = 10^{6}$ nodes, related to the embedding space, and show that the quenched internal frequencies themselves can cause frustrated synchronization scaling in an extended coupling space [Ref. 7.3.].

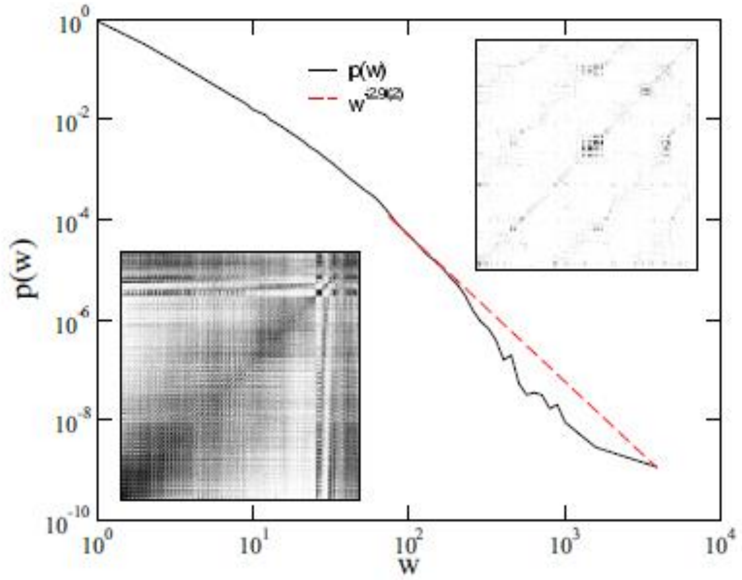

Figure 7.5. *Weight distribution of the fruit-fly connectome. Right inset: adjacency matrix plot of the fruit-fly connectome. Left inset: full adjacency matrix down sampled with a max pooling kernel of size 10 × 10. Black dots denote connections between presynaptic and postsynaptic neurons. Right inset: zoom-in to the center of the matrix without down sampling*

Previous simulation studies on human connectomes suggested that critical dynamics emerge subcritically in the so-called Griffiths phases. Now we investigate this on the largest available exact brain network, the *21662* node fruit-fly connectome, using the Kuramoto synchronization model. As this graph is less heterogeneous, lacking modular structure and exhibit high topological dimension, we expect a difference from the previous results. Indeed, the synchronization transition is mean-field-like and the width of the transition region is larger than that of random graphs, but much smaller than as of the KKI-18 human connectome. This demonstrates the effect of modular structure and dimension on the dynamics, providing a basis for better understanding the complex critical dynamics and consciousness of humans [Ref. 7.3-7.5].

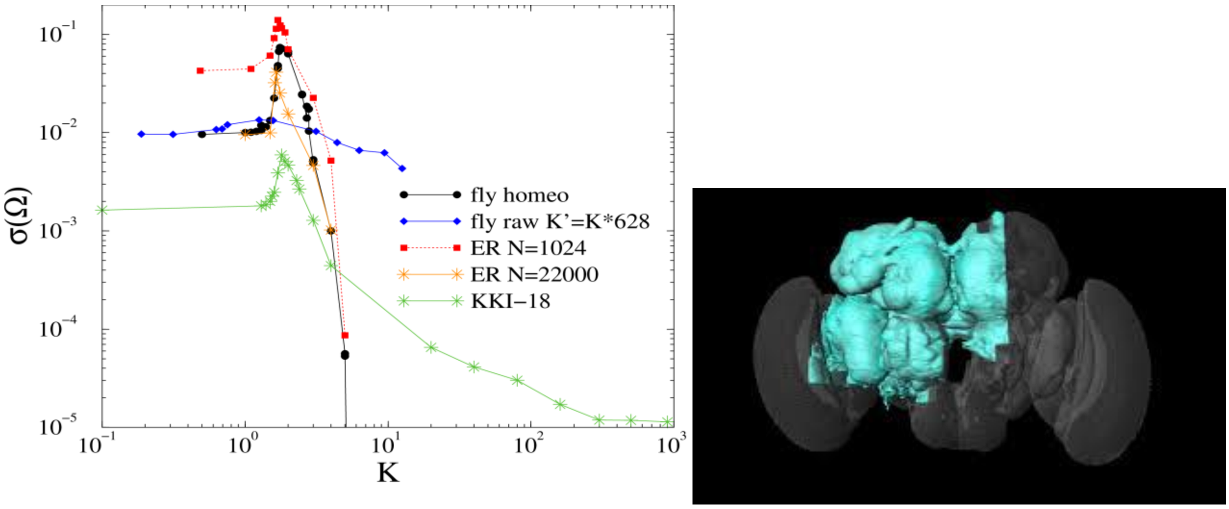

Figure 7.6. *left: Fluctuations of the frequency entrainment order parameter $\sigma(\Omega(t \rightarrow inf.))$ as the function of global coupling K, for different graphs. One can see that the fly results are similar to the random (ER) graph results, while in case of the human connectome KKI-18 an extended region of fluctuations emerge, as in the Griffiths phases. right: image of the fruit-fly brain of which the connectome is used.*

Nonuniversal power-law dynamics of susceptible infected recovered models on hierarchical modular networks to model COVID-like epidemics

Géza. Ódor, S. Deng

Power-law (PL) time-dependent infection growth has been reported in many COVID-19 statistics. In simple susceptible infected recovered (SIR) models, the number of infections grows at the outbreak as $I(t) \propto t^{d-1}$ on d-dimensional Euclidean lattices in the endemic phase, or it follows a slower universal PL at the critical point, until finite sizes cause immunity and a crossover to an exponential decay. Heterogeneity may alter the dynamics of spreading models, and spatially inhomogeneous infection rates can cause slower decays, posing a threat of a long recovery from a pandemic. COVID-19 statistics have also provided epidemic size distributions with PL tails in several countries. Here we investigate SIR-like models on hierarchical modular networks, embedded in *2d* lattices with the addition of long-range links (Fig.7.7).

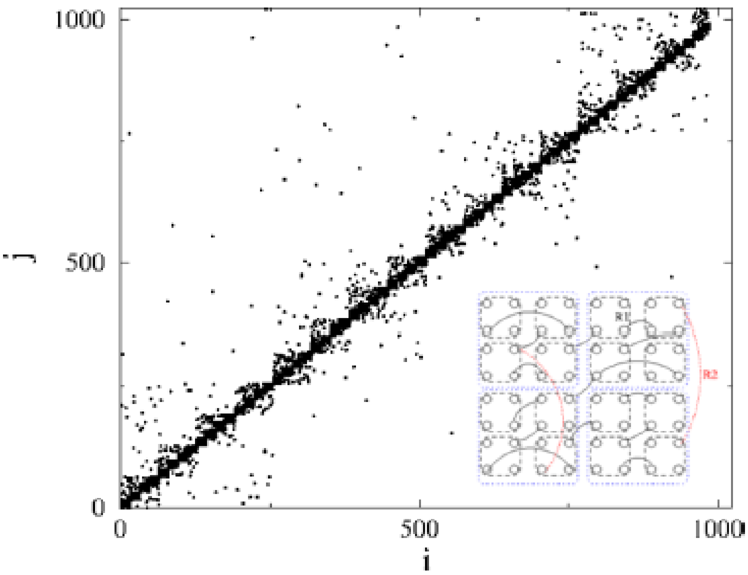

Figure 7.7. *Plot of the adjacency matrix of an $N = 1024$ sized sample of the HMN2D graphs, used for the simulations. Black dots denote edges between nodes i and j. The $l_{max} = 4$-level structure is clearly visible by the blocks near the diagonal. Low density, scattered points away from the diagonal represent long-range links. Inset: scheme of the lowest three levels of a hierarchical, four-block structure of nodes, embedded in 2d space with additional long links. Black solid lines: $l = 1$ links; red, dashed lines, $l = 2$ links; $l = 0$ edges are not shown*

We show that if the topological dimension of the network is finite, average degree-dependent PL growth of prevalence emerges (see Fig. 7.8). Supercritically, the same exponents as those of regular graphs occur, but the topological disorder alters the critical behavior. This is also true for the epidemic size distributions. Mobility of individuals does not affect the form of the scaling behavior, except for the $d=2$ lattice, but it increases the magnitude of the epidemic. The addition of a superspreader hot spot also does not change the growth exponent and the exponential decay in the herd immunity regime [Ref. 7.6.].

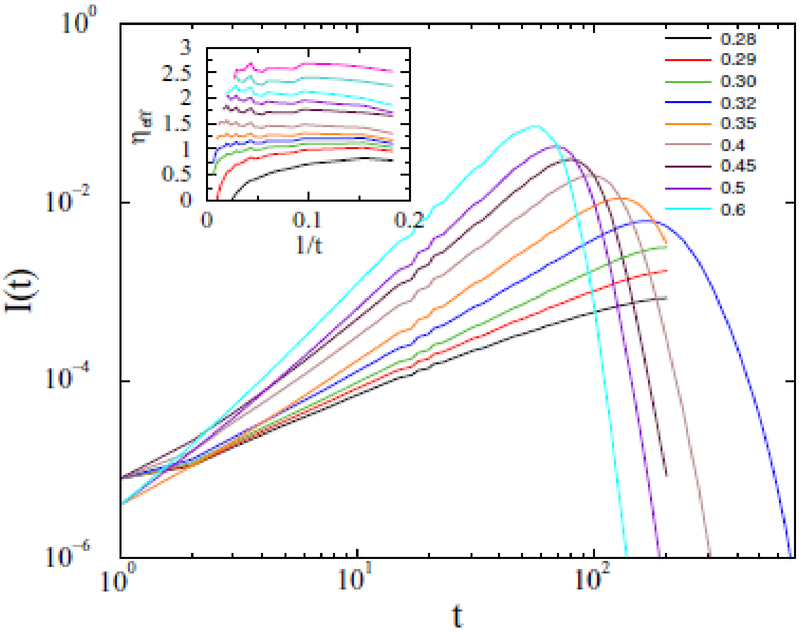

Figure 7.8. *Density of infected sites in graphs with parameters s=4 and b=1 for infection probabilities λ = 0.28, 0.29, 0.3, 0.32, 0.35, 0.4, 0.45, 0.5, and 0.6 (bottom to top curves). Inset: local slopes of the same curves as well as for λ = 0.7, 0.8. One may think of continuously changing exponents above λc=0.310(5), because short times hinder our ability to see the supercritical point scaling behavior with the growth exponent η=2.5.*

REFERENCES

[Ref. 1.1] Asbóth, J., et al. Springer, LNP, 919, (2016) https://link.springer.com/book/10.1007/978-3-319-25607-8

[Ref. 1.2] Zohar, R., et al. Phys. Rev. B. 86, 045102, (2012) https://journals.aps.org/prb/abstract/10.1103/PhysRevB.86.045102

[Ref. 1.3] Monserrat, B., et al. Phys. Rev. Research 1, 033181 (2019)

https://journals.aps.org/prresearch/abstract/10.1103/PhysRevResearch.1.033181

[Ref. 2.1] Madalina, Rabung ; Melanie, Kopp ; Antal, Gasparics ; Gábor, Vértesy ; Ildikó, Szenthe ; Inge, Uytdenhouwen ; Klaus, Szielasko: „Micromagnetic Characterization of Operation-Induced Damage in Charpy Specimens of RPV Steels” APPLIED SCIENCES-BASEL 11 : 7 Paper: 2917 (2021) https://www.mdpi.com/2076-3417/11/7/2917?type=check_update&version=2

[Ref. 2.2] Vértesy, Gábor ; Gasparics, Antal ; Szenthe, Ildikó ; Rabung, Madalina ; Kopp, Melanie ; Griffin, James M.: „Analysis of Magnetic Nondestructive Measurement Methods for Determination of the Degradation of Reactor Pressure Vessel Steel” MATERIALS 14 : 18 Paper: 5256 , 15 p. (2021) https://pubmed.ncbi.nlm.nih.gov/34576479/

[Ref. 2.3] Vértesy, Gábor ; Gasparics, Antal ; Szenthe, Ildikó ; Uytdenhouwen, Inge: „Interpretation of Nondestructive Magnetic Measurements on Irradiated Reactor Steel Material APPLIED SCIENCES-BASEL 11 : 8 Paper: 3650 , 13 p. (2021) https://www.mdpi.com/2076-3417/11/8/3650

[Ref. 2.4] D. Zámbó, P. Rusch, F. Lübkemann, N. C. Bigall, „Noble-Metal Nanorod Cryoaerogels with Electrocatalytically Active Surface Sites,” ACS APPLIED MATERIALS & INTERFACES 2021, 13 (48), 57774–57785. https://doi.org/10.1021/acsami.1c16424.

[Ref. 2.5] G. Dobrik, P. Nemes-Incze, B. Majérus, P. Süle, P. Vancsó, G. Piszter, M. Menyhárd, B. Kalas, P. Petrik, L. Henrard, L. Tapasztó, Large-area nanoengineering of graphene corrugations for visible-frequency graphene plasmons, Nat. Nanotechnol. (2021) https://doi.org/10.1038/s41565-021-01007-x.

[Ref. 2.6] Z. Pápa, J. et al., Spectroscopic ellipsometric investigation of graphene and thin carbon films from the point of view of depolarization effects, Appl. Surf. Sci. 421 (2017) 714–721

https://www.sciencedirect.com/science/article/pii/S0169433216326897

[Ref. 2.7] W. Paulson, et al. Ellipsometric determination of optical constants for silicon and thermally grown silicon dioxide via a multi-sample, multi-wavelength, multi-angle investigation, J. Appl. Phys. 83 (2002) 3323–3336. https://aip.scitation.org/doi/10.1063/1.367101

[Ref. 2.8] V.G. Kravets, et al., Spectroscopic ellipsometry of graphene and an exciton-shifted van Hove peak in absorption, Phys. Rev. B 81, 155413 https://journals.aps.org/prb/abstract/10.1103/PhysRevB.81.155413 (2010)

[Ref. 2.9] E. Agocs, et al., Approaches to calculate the dielectric function of ZnO around the band gap, in: Thin Solid Films, 2014: pp. 684–688. https://www.sciencedirect.com/science/article/pii/S0040609014003009

[Ref. 2.10] Li, W., et al. Broadband optical properties of graphene by spectroscopic ellipsometry. Carbon 99, 348 (2016).

https://www.sciencedirect.com/science/article/pii/S0008622315304991?via%3Dihub

[Ref. 2.10] Alekszej Romanenko, Emil Agócs, Zoltán Hózer, Peter Petrik, Miklós Serényi, Concordant element of the oxidation kinetics—Interpretation of ellipsometric measurements on Zr, Applied Surface Science, Volume 573, 2022, 151543, ISSN 0169-4332, https://doi.org/10.1016/j.apsusc.2021.151543 .

[Ref. 2.11] Jankovics H.; Szekér, P. ; Tóth, É. ; Kakasi, B. ; Lábadi, Z. ; Saftics, A. ; Kalas, B. ; Fried, M. ; Petrik, P. ; Vonderviszt, F.; SCIENTIFIC REPORTS 11(1) Paper: 3497 (2021) https://www.nature.com/articles/s41598-021-83053-y

[Ref. 3.1] Zsolt Czigány and Viktória Kovács Kis, Calibration procedure to improve the accuracy of SAED in aberration corrected TEM, Microscopy and Microanalysis submitted

[Ref. 3.2] Nagy, P.; Rohbeck, N.; Hegedűs, Z.; Michler, J.; Pethö, L.; Lábár, J.L.; Gubicza, J. „Microstructure, Hardness, and Elastic Modulus of a Multibeam-Sputtered Nanocrystalline Co-Cr-Fe-Ni Compositional Complex Alloy Film.” Materials 2021, 14, 3357. https://doi.org/10.3390/ma14123357

[Ref. 3.3] Lábár. J.L., „Consistent indexing of a (set of) single crystal SAED pattern(s) with the ProcessDiffraction program”, Ultramicroscopy 2005, 103, 237–249 https://www.sciencedirect.com/science/article/pii/S0304399104002475

[Ref. 3.4] Lábár, J.L. “ Electron diffraction based analysis of phase fractions and texture in nanocrystalline thin films I-III.”, Microanal 2008, 14, 287–295; 2009, Microsc Microanal 15, 20–29; 2012, Microsc. Microanal. 18, 406–420 https://www.cambridge.org/core/journals/microscopy-and-microanalysis/article/abs/electron-diffraction-based-analysis-of-phase-fractions-and-texture-in-nanocrystalline-thin-films-part-i-principles/B5D7456CC66291441CF7BF1DAF4A5CA7

[Ref. 3.5] Nagy, K. H. & Misják, F. In-situ transmission electron microscopy study of thermal stability and carbide formation in amorphous Cu-Mn/C films for interconnect application. J. Phys. Chem. Solids 121, 312–318 (2018). https://www.sciencedirect.com/science/article/pii/S0022369718300787

[Ref. 3.6] Kovács Kis, V., Czigány, Z. & Németh, T. Nanostructural investigation of slightly altered rhyolitic volcanic glass. Mater. Charact. 127, 121–128 (2017). https://www.sciencedirect.com/science/article/pii/S104458031631021X

[Ref. 3.7] A.S. Racz, Z. Fogarassy, P. Panjan, M. Menyhard: Evaluation of AES depth profiles with serious artefacts in C/W multilayers, Applied Surface Science, 582 (2022) 152385. https://www.sciencedirect.com/science/article/pii/S0169433221034036

[Ref. 3.8] G. Sáfrán; Ultramicroscopy 187 (2018), 50-55 https://aip.scitation.org/doi/10.1063/1.5138106

[Ref. 3.9] J.L. Lábár; Microsc. Microanal. 14 (4) (2008), 287-295 https://www.cambridge.org/core/journals/microscopy-and-microanalysis/article/abs/electron-diffraction-based-analysis-of-phase-fractions-and-texture-in-nanocrystalline-thin-films-part-i-principles/B5D7456CC66291441CF7BF1DAF4A5CA7

[Ref. 3.10] S. H. Chen, C., Carter, Z. Elgat, L R, Zheng, and J. W. Mayer, The structure of Ni5Si2 formed in Ni-Si thin film lateral diffusion couples, J. Appl. Phys. 62 (4), (1987) 1189-1194. https://aip.scitation.org/doi/10.1063/1.339830

[Ref. 3.11] B. Bokhonov and M. Korchagin, In-situ investigation of the formation of nickel silicides during interaction of single-crystalline and amorphous silicon with nickel, Journal of Alloys and Compounds 319 (2001) 187–195. https://www.sciencedirect.com/science/article/pii/S0925838801009021

[Ref. 3.12] F. Nemouchi, D. Mangelinck, J.L. Lábár, M. Putero, C. Bergman and P. Gas, A comparative study of nickel silicides and nickel germanides: Phase formation and kinetics, Microelectronic Engineering 83, 2006, 2101–2106. https://www.sciencedirect.com/science/article/pii/S0167931706004825

[Ref. 3.13] E. Kretschmann and H. Raether. Zeitschrift für Naturforschung A 23.4 (1968), 615–617. issn: 1865-7109

[Ref. 3.14] G. Sáfrán: Hung. Patent No. P 15 00500 (2015)

[Ref. 3.15] G. Sáfrán, J. Szívós, M. Németh, A. Horváth, In: Ágnes, Kittel; Béla, Pécz (szerk.) 12th MCM 2015 Budapest, Magyarország : Akadémiai Kiadó, (2015) pp. 559-560. , 2 p.

[Ref. 3.16] Chinh, Nguyen Q. , Sáfrán, György, MRS COMMUNICATIONS, 4 p. (2019)

[Ref. 3.17] B. Kalas, Zs. Zolnai, G. Sáfrán, M. Serényi, E. Agocs,T . Lohner, A. Nemeth, N Q.Khánh, M. Fried, P.Petrik Scientific Reports | (2020) 10:19266 https://doi.org/10.1038/s41598-020-74881-5

[Ref. 3.18] Kalas György Benjamin, PhD Thesis

[Ref. 3.19] J. Károlyi, M. Németh, C. Evangelisti, G. Sáfrán, Z. Schay, A. Horváth and F. Somodi: Carbon dioxide reforming of methane over Ni-In/SiO2 catalyst without coke formation, Journal of Industrial and Engineering Chemistry, 58, 189 (2018)

[Ref. 3.20] M. Németh, G. Sáfrán, A. Horváth, F. Somodi: Hindered methane decomposition on a coke-resistant Ni-In/SiO2 dry reforming catalyst, Catalysis Communications, 118, 56 (2019)

[Ref. 3.21] M. Németh, F. Somodi and A. Horváth: Interaction between CO and a Coke-Resistant NiIn/SiO2 Methane Dry Reforming Catalyst: A DRIFTS and CO Pulse Study, Journal of Physical Chemistry C, https://pubs.acs.org/doi/10.1021/acs.jpcc.9b06839

[Ref. 3.22] G. Radnóczi, R. Dedoncker, G.Z. Radnóczi, Zs. Czigány, A. Sulyok, V. Kovács-Kis, D. Depla, The growth of a multi-principal element (CoCrFeMnNi) oxynitride film by direct current magnetron sputtering using air as reactive gas, Surface & Coatings Technology 421 (2021) 127433, https://doi.org/10.1016/j.surfcoat.2021.127433

[Ref. 3.23] D. Depla, High entropy alloy thin films deposited by magnetron sputtering of powder targets, Thin Solid Films 580 (2015) 71–76, https://doi.org/10.1016/j. tsf.2015.02.070 .

[Ref. 3.24] Varanasi, D.; Furkó, M.; Balázsi, K.; Balázsi, C. Processing of Al2O3-AlN Ceramics and Their Structural, Mechanical, and Tribological Characterization. Materials 2021, 14, 6055. https://doi.org/10.3390/ma14206055
[Ref. 3.25] Liao, Z.; Standke, Y.; Gluch, J.; Balázsi, K.; Pathak, O.; Höhn, S.; Herrmann, M.; Werner, S.; Dusza, J.; [Ref. 3.26] Balázsi, C.; et al. Microstructure and Fracture Mechanism Investigation of Porous Silicon Nitride-Zirconia-Graphene Composite Using Multi-Scale and In-Situ Microscopy. Nanomaterials 2021, 11, 285. https://doi.org/10.3390/ nano11020285

[Ref. 3.27] K. Balázsi, M. Furkó, Z. Liao, J. Gluch, D. Medved, R. Sedlák, J. Dusza, E. Zschech, C. Balázsi, Porous sandwich ceramic of layered silicon nitride-zirconia composite with various multilayered graphene content JOURNAL OF ALLOYS AND COMPOUNDS 2020, 832 Paper: 154984 . https://www.sciencedirect.com/science/article/pii/S0925838820313475

[Ref. 3.28] K. Balázsi, M. Furkó, Z. Liao, Z. Fogarassy, D. Medved, E. Zschech, J. Dusza, C. Balázsi, Graphene added multilayer ceramic sandwich (GMCS) composites: Structure, preparation and properties JOURNAL OF THE EUROPEAN CERAMIC SOCIETY 2020, 40 (4), 4792-4798.

[Ref. 4.1] Zs. Baji, Zs. Fogarassy, A. Sulyok, P. Petrik, Atomic layer deposition of HfS2 from tetrakis(dimethylamino)hafnium, submitted to JVSTA

[Ref. 4.2] B. Foerster et al., J. Phys. Chem. C 122: 19116−19123 (2018) https://pubs.acs.org/doi/10.1021/acs.jpcc.0c04629

[Ref. 4.3] Carsten Sönnichsen, PhD Thesis, Ludwig Maximilian University, Munich, 2001

[Ref. 4.4] A. Crut et al., Chem. Soc. Rev. 43: 3921 (2014) https://pubs.rsc.org/en/content/articlelanding/2014/cs/c3cs60367a

[Ref. 4.5] Ádám Dacher, Characterization of piezoelectric cantilevers, BSc Thesis

[Ref. 4.6] Zénó Pusztai, Középfülbe ültethető piezoelektormos MEMS spirálok minősítése (Characterization of piezoelectric MEMS spirals for implantation in the middle ear), MSc Thesis https://diplomaterv.vik.bme.hu/hu/Theses/Kozepfulbe-ultetheto-piezoelektromos-MEMS

[Ref. 4.7] Tamás Dózsa, János Radó, János Volk, Ádám Kisari, Alexandros Soumelidis, Péter Kovács, A novel force sensor based measurement system for abnormal road surface detection, submitted to Journal of IEEE Transactions on Instrumentation and Measurement

[Ref. 5.1] N. Samotaev, P. Dzhumaev, K. Oblov, A. Pisliakov, I. Obraztsov, Cs. Ducso and F. Biro, „Silicon MEMS Thermocatalytic Gas Sensor in Miniature Surface Mounted Device Form", Chemosensors 2021, 9(12), 340; https://www.mdpi.com/2227-9040/9/12/340 ,

[Ref. 5.2] Samotaev, N., Pisliakov, A., Filipchuk, D., Etrekova, M., Biro, F., Ducso, C., Bársony, I., „SOI Based Micro-Bead Catalytic Gas Sensor", International Youth Conference on Electronics, Telecommunications and Information Technologies, YETI 2020. (2021) Springer Proceedings in Physics, 255, pp. 105-111.

[Ref. 5.3] Ferenc Bíró, András Deák, Csaba Dücső, Zoltán Hajnal, "Microheater with uniform surface temperature", Utility model: U 20 001150, registration number 5279

[Ref. 5.4] Innováció a labordiagnosztikában, Innotéka, 2021. április,

https://www.innoteka.hu/cikk/innovacio_a_labordiagnosztikaban.2239.html

[Ref. 5.5] Petrovszki, Dániel; Valkai, Sándor ; Gora, Evelin ; Tanner, Martin ; Bányai, Anita ; Fürjes, Péter ; Dér, András, An integrated electro-optical biosensor system for rapid, low-cost detection of bacteria, MICROELECTRONIC ENGINEERING 239 Paper: 111523 , 9 p. (2021)

[Ref. 5.6] Rebeka Öcsi: Felületerősített Raman-spektroszkópiára alkalmas chipek fejlesztése sejtanalitikai célokra, Eötvös Loránd University, OTDK MATERIALS PHYSICS session I. place (supervisors: Zsolt Zolnai Zsolt, Péter Fürjes)

[Ref. 6.1.] T. Gerecsei, P. Chrenkó, N. Kanyo, B. Péter, A. Bonyár, I. Székács, B. Szabo, R. Horvath, „Dissociation constant of integrin-RGD binding in live cells from automated micropipette and label-free optical data", BIOSENSORS, vol. 11, 2021. https://www.ncbi.nlm.nih.gov/pmc/articles/PMC7911545/

[Ref. 6.2.] A. Saftics, S. Kurunczi, B. Peter, I. Szekacs, J. J. Ramsden, R. Horvath, „Data evaluation for surface-sensitive label-free methods to obtain real-time kinetic and structural information of thin films: A practical review with related software packages", ADVANCES IN COLLOID AND INTERFACE SCIENCE, vol. 294, 2021. https://www.sciencedirect.com/science/article/pii/S0001868621000725

[Ref. 6.3.] R. Ungai-Salánki, B. Csippa, T. Gerecsei, B. Péter, R. Horvath, B. Szabó, „Nanonewton scale adhesion force measurements on biotinylated microbeads with a robotic micropipette", JOURNAL OF COLLOID AND INTERFACE SCIENCE, vol. 602, 2021. https://www.sciencedirect.com/science/article/pii/S0021979721008687

[Ref. 6.4.] B. Péter, I. Boldizsár, G. M. Kovács, A. Erdei, Zs. Bajtay, A. Vörös, J. J. Ramsden, I. Szabó, Sz. Bősze, R. Horvath, „Natural compounds as target biomolecules in cellular adhesion and migration: from biomolecular stimulation to label-free discovery and bioactivity-based isolation", BIOMEDICINES, vol. 9, 2021 https://www.ncbi.nlm.nih.gov/pmc/articles/PMC8698624/

[Ref. 6.5.] H. S. Lawson, G. Holló, N. Német, S. Teraji, H. Nakanishi, R. Horvath, I. Lagzi, „Design of non-autonomous pH oscillators and the existence of chemical beat phenomenon in a neutralization reaction", SCIENTIFIC REPORTS, vol. 11, 2021. https://www.nature.com/articles/s41598-021-90301-8

[Ref. 6.6.] B. Kovacs, F. A. Kraft, Zs. Szabo, Y. Nazirizadeh, M. Gerken, R. Horvath, „Near cut-off wavelength operation of resonant waveguide grating biosensors", SCIENTIFIC REPORTS, vol. 11, 2021. https://www.nature.com/articles/s41598-021-92327-4

[Ref. 6.7.] R. Ungai-Salánki, E. Haty, T. Gerecsei, B. Francz, B. Béres, M. Sztilkovics, I. Székács, B. Szabó, R. Horvath, „Single-cell adhesion strength and contact density drops in the M phase of cancer cells", SCIENTIFIC REPORTS, vol. 11, 2021. https://pubmed.ncbi.nlm.nih.gov/34531409/

[Ref. 6.8.] K. D. Kovács, M. Novák, Z. Hajnal, Cs. Hős, B. Szabó, I. Székács, Y. Fang, A. Bonyár, R. Horvath, „Label-free tracking of whole-cell response on RGD functionalized surfaces to varied flow velocities generated by fluidic rotation", JOURNAL OF COLLOID AND INTERFACE SCIENCE, vol. 599, 2021.

[Ref. 6.9.] K. Kliment, I. Szekacs, B. Peter, A. Erdei, I. Kurucz, R Horvath, „Label-free real-time monitoring of the BCR-triggered activation of primary human B cells modulated by the simultaneous engagement of inhibitory receptors", BIOSENSORS AND BIOELECTRONICS, vol. 191, 2021. https://www.sciencedirect.com/science/article/pii/S0956566321005066

[Ref. 7.1]. A. Szolnoki, X, Chen, "Cooperation and competition between pair and multi-player social games in spatial populations" SCIENTIFIC REPORTS 11 (2021) 12101. https://www.nature.com/articles/s41598-021-91532-5

[Ref. 7.2.] György Szabó & Balázs Király General features of Nash equilibria in combinations of elementary interactions in symmetric two-person games, The European Physical Journal B volume 94, Article number: 102 (2021) https://link.springer.com/article/10.1140/epjb/s10051-021-00112-z

[Ref. 7.3] G Ódor, J Kelling, G Deco, Neurocomputing 461 (2021) 696-704,

https://www.sciencedirect.com/science/article/pii/S0925231221007712

[Ref. 7.4] G Ódor, J Kelling, M Gastner, G Deco Journal of Physics: Complexity 2 (2021) 045002.

https://iopscience.iop.org/article/10.1088/2632-072X/ac266c

[Ref. 7.5] G Ódor, G Deco, J Kelling Physical Review Research 4 (2022), 023057

https://journals.aps.org/prresearch/abstract/10.1103/PhysRevResearch.4.023057

[Ref. 7.6] G Ódor, Phys. Rev. E 103 (2021) 062112 https://journals.aps.org/pre/abstract/10.1103/PhysRevE.103.062112

FULL LIST OF MFA PUBLICATIONS IN 2021

[1] M. Arfaoui, V. Kovács-Kis, and G. Radnóczi, “Diffusionless FCC to BCC phase transformation in CoCrCuFeNi MPEA thin films,” *JOURNAL OF ALLOYS AND COMPOUNDS*, vol. 863, 2021. https://doi.org/10.1016%2Fj.jallcom.2021.158712

[2] A. Romanenko, E. Agócs, Z. Hózer, P. Petrik, M. Serényi, “In-situ Ellipsometry on the Oxidation of Zirconium at Medium Temperatures,” in *Optics, Photonics and Lasers*, 2021, pp. 138–139.

[3] Z. Baji, I. Cora, Z. E. Horvath, E. Agocs, and Z. Szabo, “Atomic layer deposition and characterization of Zn-doped Ga2O3 films,” *JOURNAL OF VACUUM SCIENCE AND TECHNOLOGY A-VACUUM SURFACES AND FILMS*, vol. 39, no. 3, 2021. https://doi.org/10.1116%2F6.0000838

[4] C. Balázsi, “Ceramics and graphene open up new possibilities for bone-like materials,” *AMERICAN CERAMIC SOCIETY BULLETIN*, vol. 100, no. 5, pp. 22–23, 2021.

[5] C. BALÁZSI, M. FURKO, and K. BALÁZSI, “Korszerű nitrid kerámiák előállítása és vizsgálata,” *Nemzetközi Gépészeti Találkozó*, vol. 29, pp. 93–96, 2021.

[6] K. Balázsi, M. Furkó, and C. Balázsi, “Ceramic Matrix Graphene and Carbon Nanotube Composites,” in *Module in Materials Science and Materials Engineering*, vol. 2, 2021, pp. 243–259. https://doi.org/10.1016%2FB978-0-12-818542-1.00070-9

[7] K. Bali, M. Bak, K. Szarka, G. Juhász, G. Sáfrán, B. Pécz, J. Mihály, and R. Mészáros, “Controlling the morphology of poly(ethyleneimine)/gold nanoassemblies through the variation of pH and electrolyte additives,” *JOURNAL OF MOLECULAR LIQUIDS*, vol. 322, 2021. https://doi.org/10.1016%2Fj.molliq.2020.114559

[8] Z. Balogh, G. Mezei, L. Pósa, B. Sánta, A. Magyarkuti, and A. Halbritter, “1/f noise spectroscopy and noise tailoring of nanoelectronic devices,” *NANO FUTURES*, vol. 5, no. 4, 2021. https://doi.org/10.1088%2F2399-1984%2Fac14c8

[9] I. Bányász, N. Q. Khanh, F. Pászti, G. U. L. Nagy, I. Rajta, S. Berneschi, G. Nunzi Conti, S. Pelli, G. C. Righini, M. Brenci, V. Havránek, V. Vosecek, E. Szilágyi, M. Fried, A. Watterich, N. Nagy, Z. Szabó, M. Veres, and A. Speghini, “Ion Beam Implanted Channel Waveguides in an Er-doped Tellurite Glass,” in *Optics, Photonics and Lasers*, 2021, pp. 80–83.

[10] I. Bársony, *Szilíciumtechnológia - és amit neki köszönhetünk*. Budapest: Magyar Tudományos Akadémia (MTA), 2021. https://doi.org/10.36820%2Fszekfoglalo.2021.barsony

[11] T. L. Ba, M. Bohus, I. E. Lukács, S. Wongwises, G. Gróf, K. Hernadi, and I. M. Szilágyi, “Comparative Study of Carbon Nanosphere and Carbon Nanopowder on Viscosity and Thermal Conductivity of Nanofluids,” *NANOMATERIALS*, vol. 11, no. 3, 2021. https://doi.org/10.3390%2Fnano11030608

[12] D. Bazeia, M. Bongestab, B. F. de Oliveira, and A. Szolnoki, “Effects of a pestilent species on the stability of cyclically dominant species,” *CHAOS SOLITONS & FRACTALS*, vol. 151, 2021. https://doi.org/10.1016%2Fj.chaos.2021.111255

[13] D. Beke, M. V. Nardi, G. Bortel, M. Timpel, Z. Czigány, L. Pasquali, A. Chiappini, G. Bais, M. Rudolf, D. Zalka, F. Bigi, F. Rossi, L. Bencs, A. Pekker, B. G. Márkus, G. Salviati, S. E. Saddow, K. Kamarás, F. Simon, and A. Gali, “Enhancement of X-ray-Excited Red Luminescence of Chromium-Doped Zinc Gallate via Ultrasmall Silicon Carbide Nanocrystals,” *CHEMISTRY OF MATERIALS*, vol. 33, no. 7, pp. 2457–2465, 2021. https://doi.org/10.1021%2Facs.chemmater.0c04671

[14] F. Bíró, A. Deák, C. Dücső, and Z. Hajnal, “Egyenletes felületi hőmérsékletet biztosító mikrofűtőtest,” 2021.

[15] L. P. Biró and B. Pécz, “Gyulai József, 1933–2021,” *FIZIKAI SZEMLE*, vol. 71, no. 3, pp. 90–91, 2021.

[16] B. Kalas, S., Soleimani, J. Volk, P. Petrik, “Optical Properties of CrxAl1-xN layers for Piezoelectric Applications,” in *Optics, Photonics and Lasers*, 2021, pp. 121–122.

[17] I. Borbáth, E. Tálas, Z. Pászti, K. Zelenka, I. Ayyubov, K. Salmanzade, I. Sajó, G. Sáfrán, and A. Tompos, “Investigation of Ti-Mo mixed oxide-carbon composite supported Pt electrocatalysts: Effect of the type of carbonaceous materials,” *APPLIED CATALYSIS A-GENERAL*, vol. 620, 2021. https://doi.org/10.1016%2Fj.apcata.2021.118155

[18] I. Borbáth, K. Zelenka, Á. Vass, Z. Pászti, G. P. Szijjártó, Z. Sebestyén, G. Sáfrán, and A. Tompos, “CO tolerant Pt electrocatalysts for PEM fuel cells with enhanced stability against electrocorrosion,” *INTERNATIONAL JOURNAL OF HYDROGEN ENERGY*, vol. 46, no. 25, pp. 13534–13547, 2021. https://doi.org/10.1016%2Fj.ijhydene.2020.08.002

[19] A. Bosio, A. Parisini, A. Lamperti, C. Borelli, L. Fornasini, M. Bosi, I. Cora, Z. Fogarassy, B. Pécz, Z. Zolnai, A. Németh, S. Vantaggio, and R. Fornari, “n-Type doping of ε-Ga2O3 epilayers by high-temperature tin diffusion,” *ACTA MATERIALIA*, vol. 210, 2021. https://doi.org/10.1016%2Fj.actamat.2021.116848

[20] K. Bukovinszky, M. Szalóki, I. Csarnovics, A. Bonyár, P. Petrik, B. Kalas, L. Daróczi, S. Kéki, S. Kökényesi, and C. Hegedűs, “Optimization of Plasmonic Gold Nanoparticle Concentration in Green LED Light Active Dental Photopolymer,” *POLYMERS*, vol. 13, no. 2, 2021. https://doi.org/10.3390%2Fpolym13020275

[21] B. Csernyus, Á. Szabó, R. Fiáth, A. Zátonyi, C. Lázár, A. Pongrácz, and Z. Fekete, “A multimodal, implantable sensor array and measurement system to investigate the suppression of focal epileptic seizure using hypothermia,” *JOURNAL OF NEURAL ENGINEERING*, vol. 18, no. 4, 2021. https://doi.org/10.1088%2F1741-2552%2Fac15e6

[22] B. D., B. F. M. J., de O. B. F., and S. A., “Environment driven oscillation in an off-lattice May–Leonard model,” *SCIENTIFIC REPORTS*, vol. 11, 2021. https://doi.org/10.1038%2Fs41598-021-91994-7

[23] B. F. de Oliveira and A. Szolnoki, “Social dilemmas in off-lattice populations,” *CHAOS SOLITONS & FRACTALS*, vol. 144, 2021. https://doi.org/10.1016%2Fj.chaos.2021.110743

[24] B. F. de Oliveira, M. V. de Moraes, D. Bazeia, and A. Szolnoki, “Mobility driven coexistence of living organisms,” *PHYSICA A - STATISTICAL MECHANICS AND ITS APPLICATIONS*, vol. 572, 2021. https://doi.org/10.1016%2Fj.physa.2021.125854

[25] A. Domán, J. Madarász, G. Sáfrán, Y. Wang, and K. László, “Copper benzene-1,3,5-tricarboxylate (HKUST-1) – Graphene oxide pellets for methane adsorption,” *MICROPOROUS AND MESOPOROUS MATERIALS*, vol. 316, 2021. https://doi.org/10.1016%2Fj.micromeso.2021.110948

[26] T. Elalaily, O. Kürtössy, Z. Scherübl, M. Berke, G. Fülöp, I. E. Lukács, T. Kanne, J. Nygård, K. Watanabe, T. Taniguchi, P. Makk, and S. Csonka, “Gate-Controlled Supercurrent in Epitaxial Al/InAs Nanowires,” *NANO LETTERS*, vol. 21, no. 22, pp. 9684–9690, 2021. https://doi.org/10.1021%2Facs.nanolett.1c03493

[27] S. Emanuela, G. Filippo, D. F. Salvatore, G. Giuseppe, F. Patrick, R. Fabrizio, P. Paweł, K. Piotr, L. Mike, C. Ildiko, P. Béla, F. Zsolt, and L. N. Raffaella, “Highly Homogeneous Current Transport in Ultra-Thin Aluminum Nitride (AlN) Epitaxial Films on Gallium Nitride (GaN) Deposited by Plasma Enhanced Atomic Layer Deposition,” *NANOMATERIALS*, vol. 11, no. 12, 2021. https://doi.org/10.3390%2Fnano11123316

[28] M. Fabian, I. Tolnai, A. Khanna, Z. Horvath, K. V. Kovacs, and Z. Kovacs, “Structural Characterization of Oxyhalide Materials for Solid-State Batteries,” *PHYSICA STATUS SOLIDI A-APPLICATIONS AND MATERIALS SCIENCE*, vol. 218, 2021. https://doi.org/10.1002%2Fpssa.202000682

[29] M. Furko, Z. E. Horváth, J. Mihály, K. Balázsi, and C. Balázsi, “Comparison of the Morphological and Structural Characteristic of Bioresorbable and Biocompatible Hydroxyapatite-Loaded Biopolymer Composites,” *NANOMATERIALS*, vol. 11, no. 12, 2021. https://doi.org/10.3390%2Fnano11123194

[30] Á. Gábor Nagy, N. Pap, R. Horvath, and A. Bonyár, “Determination of the Resonance Frequency and Spring Constant of FluidFM Cantilevers with Numerical Simulations,” in *2021 44th International Spring Seminar on Electronics Technology (ISSE)*, 2021. https://doi.org/10.1109%2FISSE51996.2021.9467594

[31] T. Gerecsei, P. Chrenkó, N. Kanyo, B. Péter, A. Bonyár, I. Székács, B. Szabo, and R. Horvath, “Dissociation Constant of Integrin-RGD Binding in Live Cells from Automated Micropipette and Label-Free Optical Data,” *BIOSENSORS*, vol. 11, no. 2, 2021. https://doi.org/10.3390%2Fbios11020032

[32] M. Gracheva, Z. Homonnay, K. Kovács, K. Béres, J. Biondi, Y. Wenchao, V. Kovács Kis, I. Gyollai, and M. Polgári, “Mössbauer characterization of microbially mediated iron and manganese ores of variable geological ages,” *ORE GEOLOGY REVIEWS*, vol. 134, 2021. https://doi.org/10.1016%2Fj.oregeorev.2021.104124

[33] S. Gurbán, A. Sulyok, M. Menyhárd, E. Baradács, B. Parditka, C. Cserháti, G. A. Langer, and Z. Erdélyi, “Interface induced diffusion,” *SCIENTIFIC REPORTS*, vol. 11, 2021. https://doi.org/10.1038%2Fs41598-021-88808-1

[34] J. Gyulai, “A Bay Zoltán Alkalmazott Kutatási Alapítvány születése,” in *A Bay Zoltán 120 Emlékkonferencia előadásainak ismertető kiadványa*, 2021, pp. 26–29.

[35] K. Hajagos-Nagy, “In-situ TEM Investigation of Solid Phase Transformations and Reactions,” *PERIODICA POLYTECHNICA-MECHANICAL ENGINEERING*, vol. 65, no. 3, pp. 252–260, 2021. https://doi.org/10.3311%2FPPme.17496

[36] V. Hanus, V. Csajbok, Z. Papa, J. Budai, Z. Marton, G. Z. Kiss, P. Sandor, P. Paul, A. Szeghalmi, Z. Wang, B. Bergues, M. F. Kling, G. Molnar, J. Volk, and P. Dombi, “Light-Field-Driven Current Control in Dielectrics with pJ-Level Laser Pulses at 80 MHz Repetition Rate,” in *2021 Conference on Lasers and Electro-Optics Europe & European Quantum Electronics Conference (CLEO/Europe-EQEC)*, 2021. https://doi.org/10.1109%2FCLEO%2FEurope-EQEC52157.2021.9541888

[37] V. Hanus, V. Csajbók, Z. Pápa, J. Budai, Z. Márton, G. Z. Kiss, P. Sándor, P. Paul, A. Szeghalmi, Z. Wang, B. Bergues, M. F. Kling, G. Molnár, J. Volk, and P. Dombi, “Light-field-driven current control in solids with pJ-level laser pulses at 80 MHz repetition rate,” *OPTICA*, vol. 8, no. 4, pp. 570–576, 2021. https://doi.org/10.1364%2FOPTICA.420360

[38] N. Hegedüs, K. Balázsi, and C. Balázsi, “Silicon Nitride and Hydrogenated Silicon Nitride Thin Films,” *MATERIALS*, vol. 14, no. 19, 2021. https://doi.org/10.3390%2Fma14195658

[39] N. Hegedüs, M. Furkó, K. Balázsi, and C. Balázsi, “Környezetbarát energiatermelés, energiahatékonyság és közlekedés szempontjából kritikus üvegek, kerámiák és fémek,” *ANYAGOK VILÁGA*, vol. XVI, no. 1, pp. 62–80, 2021.

[40] D. M. Holzapfel, Z. Czigány, A. O. Eriksson, M. Arndt, and J. M. Schneider, “Thermal stability of macroparticles in Ti0.27Al0.21N0.52 coatings,” *APPLIED SURFACE SCIENCE*, vol. 553, 2021. https://doi.org/10.1016%2Fj.apsusc.2021.149527

[41] A. Horváth, M. Németh, A. Beck, B. Maróti, G. Sáfrán, G. Pantaleo, L. Liotta, A. Venezia, and P. V. La, “Strong impact of indium promoter on Ni/Al2O3 and Ni/CeO2-Al2O3 catalysts used in dry reforming of methane,” *APPLIED CATALYSIS A-GENERAL*, vol. 621, 2021. https://doi.org/10.1016%2Fj.apcata.2021.118174

[42] P. T. Hung, M. Kawasaki, J.-K. Han, J. L. Lábár, and J. Gubicza, “Microstructure evolution in a nanocrystalline CoCrFeNi multi-principal element alloy during annealing,” *MATERIALS CHARACTERIZATION*, vol. 171, 2021. https://doi.org/10.1016%2Fj.matchar.2020.110807

[43] I.V. Alenkina, E. Kuzmann, I. Felner, V. Kovacs Kis, M.I. Oshtrakh, “Unusual temperature dependencies of Mössbauer parameters of the nanosized iron cores in ferritin and its pharmaceutical analogues,” *HYPERFINE INTERACTIONS*, vol. 242, 2021. https://doi.org/10.1007%2Fs10751-021-01737-3

[44] H. Jankovics, P. Szekér, É. Tóth, B. Kakasi, Z. Lábadi, A. Saftics, B. Kalas, M. Fried, P. Petrik, and F. Vonderviszt, “Flagellin-based electrochemical sensing layer for arsenic detection in water,” *SCIENTIFIC REPORTS*, vol. 11, no. 1, 2021. https://doi.org/10.1038%2Fs41598-021-83053-y

[45] G. Kádár, “A Bay Zoltán Tudomány- és Technikatörténeti Alapítvány,” in *A Bay Zoltán 120 Emlékkonferencia előadásainak ismertető kiadványa*, 2021, pp. 78–80.

[46] G. Kádár, “Bay Zoltán pályájának rövid összefoglalása,” in *A Bay Zoltán 120 Emlékkonferencia előadásainak ismertető kiadványa*, 2021, pp. 4–5.

[47] G. Kádár, *A Bay Zoltán 120 Emlékkonferencia előadásainak ismertető kiadványa*. Budapest: Bay Zoltán Tudomány- és Technikatörténeti Alapítvány, 2021.

[48] A. Kakanakova-Georgieva, F. Giannazzo, G. Nicotra, I. Cora, G. K. Gueorguiev, P. O. Å. Persson, and B. Pécz, “Material proposal for 2D indium oxide,” *APPLIED SURFACE SCIENCE*, vol. 548, 2021. https://doi.org/10.1016%2Fj.apsusc.2021.149275

[49] A. Kakanakova-Georgieva, I. G. Ivanov, N. Suwannaharn, C.-W. Hsu, I. Cora, B. Pécz, F. Giannazzo, D. G. Sangiovanni, and G. K. Gueorguiev, “MOCVD of AlN on epitaxial graphene at extreme temperatures,” *CRYSTENGCOMM*, vol. 23, no. 2, pp. 385–390, 2021. https://doi.org/10.1039%2FD0CE01426E

[50] B. Kalas, K. Ferencz, A. Saftics, Z. Czigany, M. Fried, and P. Petrik, “Bloch surface waves biosensing in the ultraviolet wavelength range - Bragg structure design for investigating protein adsorption by in situ Kretschmann-Raether ellipsometry,” *APPLIED SURFACE SCIENCE*, vol. 536, 2021. https://doi.org/10.1016%2Fj.apsusc.2020.147869

[51] K. Kertész, Z. Bálint, G. Piszter, Z. E. Horváth, and L. P. Biró, “Multi-instrumental techniques for evaluating butterfly structural colors: A case study on Polyommatus bellargus (Rottemburg, 1775) (Lepidoptera: Lycaenidae: Polyommatinae),” *ARTHROPOD STRUCTURE & DEVELOPMENT*, vol. 61, 2021. https://doi.org/10.1016%2Fj.asd.2020.101010

[52] K. Kertész, Z. Baji, A. Deák, G. Piszter, Z. Rázga, Z. Bálint, and L. P. Biró, “Additive and subtractive modification of butterfly wing structural colors,” *COLLOID AND INTERFACE SCIENCE COMMUNICATIONS*, vol. 40, 2021. https://doi.org/10.1016%2Fj.colcom.2020.100346

[53] V. Kis, A. Sulyok, M. Hegedűs, I. Kovács, N. Rózsa, and Z. Kovács, “Magnesium incorporation into primary dental enamel and its effect on mechanical properties,” *ACTA BIOMATERIALIA*, vol. 120, pp. 104–115, 2021. https://doi.org/10.1016%2Fj.actbio.2020.08.035

[54] K. Kliment, I. Székács, B. Peter, A. Erdei, I. Kurucz, and R. Horvath, “Label-free real-time monitoring of the BCR-triggered activation of primary human B cells modulated by the simultaneous engagement of inhibitory receptors,” *BIOSENSORS & BIOELECTRONICS*, vol. 191, 2021. https://doi.org/10.1016%2Fj.bios.2021.113469

[55] M. Kocsis, S. B. Ötvös, G. F. Samu, Z. Fogarassy, B. Pécz, Á. Kukovecz, Z. Kónya, P. Sipos, I. Pálinkó, and G. Varga, “Copper-Loaded Layered Bismuth Subcarbonate—Efficient Multifunctional Heterogeneous Catalyst for Concerted C–S/C–N Heterocyclization,” *ACS APPLIED MATERIALS & INTERFACES*, vol. 13, no. 36, pp. 42650–42661, 2021. https://doi.org/10.1021%2Facsami.1c09234

[56] M. Kocsis, O. Zheliuk, P. Makk, E. Tóvári, P. Kun, O. E. Tereshchenko, K. A. Kokh, T. Taniguchi, K. Watanabe, J. Ye, and S. Csonka, “In situ tuning of symmetry-breaking-induced nonreciprocity in the giant-Rashba semiconductor BiTeBr,” *PHYSICAL REVIEW RESEARCH*, vol. 3, no. 3, 2021. https://doi.org/10.1103%2FPhysRevResearch.3.033253

[57] L. Kócs, B. Tegze, E. Albert, C. Major, A. Szalai, B. Fodor, P. Basa, G. Sáfrán, and Z. Hórvölgyi, “Ammonia-vapour-induced two-layer transformation of mesoporous silica coatings on various substrates,” *VACUUM*, vol. 192, 2021. https://doi.org/10.1016%2Fj.vacuum.2021.110415

[58] B. Kovacs, F. A. Kraft, Z. Szabo, Y. Nazirizadeh, M. Gerken, and R. Horvath, “Near cut-off wavelength operation of resonant waveguide grating biosensors,” *SCIENTIFIC REPORTS*, vol. 11, no. 1, 2021. https://doi.org/10.1038%2Fs41598-021-92327-4

[59] K. D. Kovács, M. Novák, Z. Hajnal, C. Hős, B. Szabó, I. Székács, Y. Fang, A. Bonyár, and R. Horvath, “Label-free tracking of whole-cell response on RGD functionalized surfaces to varied flow velocities generated by fluidic rotation.,” *JOURNAL OF COLLOID AND INTERFACE SCIENCE*, vol. 599, pp. 620–630, 2021. https://doi.org/10.1016%2Fj.jcis.2021.04.091

[60] O. Kürtössy, Z. Scherübl, G. Fülöp, I. E. Lukács, T. Kanne, J. Nygård, P. Makk, and S. Csonka, “Andreev Molecule in Parallel InAs Nanowires,” *NANO LETTERS*, vol. 21, no. 19, pp. 7929–7937, 2021. https://doi.org/10.1021%2Facs.nanolett.1c01956

[61] T. Le Ba, Z. I. Várady, I. E. Lukács, J. Molnár, I. A. Balczár, S. Wongwises, and I. M. Szilágyi, “Experimental investigation of rheological properties and thermal conductivity of SiO2–P25 TiO2 hybrid nanofluids,” *JOURNAL OF THERMAL ANALYSIS AND CALORIMETRY*, vol. 146, no. 1, pp. 493–507, 2021. https://doi.org/10.1007%2Fs10973-020-10022-4

[62] H.-W. Lee, C. Cleveland, and A. Szolnoki, “Small fraction of selective cooperators can elevate general wellbeing significantly,” *PHYSICA A - STATISTICAL MECHANICS AND ITS APPLICATIONS*, vol. 582, 2021. https://doi.org/10.1016%2Fj.physa.2021.126222

[63] Z. Liao, Y. Standke, J. Gluch, K. Balázsi, O. Pathak, S. Höhn, M. Herrmann, S. Werner, J. Dusza, C. Balázsi, and E. Zschech, “Microstructure and Fracture Mechanism Investigation of Porous Silicon Nitride–Zirconia–Graphene Composite Using Multi-Scale and In-Situ Microscopy,” *NANOMATERIALS*, vol. 11, no. 2, 2021. https://doi.org/10.3390%2Fnano11020285

[64] R. Madalina, K. Melanie, G. Antal, V. Gábor, S. Ildikó, U. Inge, and S. Klaus, “Micromagnetic Characterization of Operation-Induced Damage in Charpy Specimens of RPV Steels,” *APPLIED SCIENCES-BASEL*, vol. 11, no. 7, 2021. https://doi.org/10.3390%2Fapp11072917

[65] M. H. Mahmood, L. Himics, T. Váczi, I. Rigó, R. Holomb, B. Beiler, and M. Veres, “Raman spectroscopic study of gamma radiation-initiated polymerization of diethylene glycol dimethacrylate in different solvents,” *JOURNAL OF RAMAN SPECTROSCOPY*, vol. 52, no. 10, pp. 1735–1743, 2021. https://doi.org/10.1002%2Fjrs.6207

[66] Á. G. Nagy, R. Horvath, A. Bonyár, and M. Sztilkovics, “A custom Software for the Evaluation of Single-Cell Force-Spectroscopy Data Acquired by FluidFM BOT,” in *2021 IEEE 27th International Symposium for Design and Technology in Electronic Packaging (SIITME)*, 2021, pp. 272–274. https://doi.org/10.1109%2FSIITME53254.2021.9663702

[67] P. Nagy, N. Rohbeck, Z. Hegedus, J. Michler, L. Pethoe, J. Lábár, and J. Gubicza, “Microstructure, Hardness, and Elastic Modulus of a Multibeam-Sputtered Nanocrystalline Co-Cr-Fe-Ni Compositional Complex Alloy Film,” *MATERIALS*, vol. 14, no. 12, 2021. https://doi.org/10.3390%2Fma14123357

[68] D. Nesheva, Z. Fogarassy, M. Fabian, T. Hristova-Vasileva, A. Sulyok, I. Bineva, E. Valcheva, K. Antonova, and P. Petrik, “Influence of fast neutron irradiation on the phase composition and optical properties of homogeneous SiOx and composite Si–SiOx thin films,” *JOURNAL OF MATERIALS SCIENCE*, vol. 56, no. 4, pp. 3197–3209, 2021. https://doi.org/10.1007%2Fs10853-020-05338-3

[69] H. Nikolett, L. Riku, S. Miklós, Z. Zsolt, P. Péter, M. Judit, F. Zsolt, B. Csaba, and B. Katalin, “Examination of the Hydrogen Incorporation into Radio Frequency-Sputtered Hydrogenated SiNx Thin Films,” *COATINGS*, vol. 11, no. 1, 2021. https://doi.org/10.3390%2Fcoatings11010054

[70] V. O. Odhiambo, C. R. M. Mustafa, L. B. Thong, Z. Kónya, C. Cserháti, Z. Erdélyi, I. E. Lukács, and I. M. Szilágyi, “Preparation of TiO2/WO3/C/N Composite Nanofibers by Electrospinning Using Precursors Soluble in Water and Their Photocatalytic Activity in Visible Light,” *NANOMATERIALS*, vol. 11, no. 2, 2021. https://doi.org/10.3390%2Fnano11020351

[71] G. Ódor, J. Kelling, and G. Deco, “The effect of noise on the synchronization dynamics of the Kuramoto model on a large human connectome graph,” *NEUROCOMPUTING*, vol. 461, pp. 696–704, 2021. https://doi.org/10.1016%2Fj.neucom.2020.04.161

[72] G. Ódor, M. T. Gastner, J. Kelling, and G. Deco, “Modelling on the very large-scale connectome,” *JOURNAL OF PHYSICS: COMPLEXITY*, vol. 2, no. 4, 2021. https://doi.org/10.1088%2F2632-072x%2Fac266c

[73] G. Ódor, “Nonuniversal power-law dynamics of susceptible infected recovered models on hierarchical modular networks,” *PHYSICAL REVIEW E: COVERING STATISTICAL NONLINEAR BIOLOGICAL AND SOFT MATTER PHYSICS (2016-)*, vol. 103, no. 6, 2021. https://doi.org/10.1103%2FPhysRevE.103.062112

[74] G. Ódor and S. B. de, “Heterogeneous excitable systems exhibit Griffiths phases below hybrid phase transitions,” *PHYSICAL REVIEW RESEARCH*, vol. 3, no. 1, 2021. https://doi.org/10.1103%2FPhysRevResearch.3.013106

[75] M. Oláh, E. Farkas, I. Székács, R. Horvath, and A. Székács, “A Roundup Classic és összetevőinek citotoxikus és genotoxikus hatásai NE-4C és MC3T3-E1 sejtvonalakon,” *Ökotoxikológia*, vol. 3, no. 2, pp. 18–19, 2021.

[76] V. S. Olsen, V. Øversjøen, D. Gogova, B. Pécz, A. Galeckas, J. Borgersen, K. Karlsen, L. Vines, and A. Kuznetsov, “ZnSnN 2 in Real Space and k-Space: Lattice Constants, Dislocation Density, and Optical Band Gap,” *ADVANCED OPTICAL MATERIALS*, vol. 9, no. 16, 2021. https://doi.org/10.1002%2Fadom.202100015

[77] Z. Osváth, “Special Issue: Synthesis and Characterization of Graphene-Based Hybrid Nanostructures,” *MATERIALS*, vol. 14, no. 24, 2021. https://doi.org/10.3390%2Fma14247770

[78] Z. Osváth, D. Zámbó, A. Sulyok, A. Pálinkás, and A. Deák, “Tuning the nanoscale rippling of graphene with PEGylated gold nanoparticles and ion irradiation,” *Carbon Trends*, vol. 5, 2021. https://doi.org/10.1016%2Fj.cartre.2021.100080

[79] A. Paudics, S. Farah, I. Bertóti, A. Farkas, K. László, M. Mohai, G. Sáfrán, A. Szilágyi, and M. Kubinyi, “Fluorescence probing of binding sites on graphene oxide nanosheets with Oxazine 1 dye,” *APPLIED SURFACE SCIENCE*, vol. 541, 2021. https://doi.org/10.1016%2Fj.apsusc.2020.148451

[80] B. Pécz, N. Vouroutzis, G. Z. Radnóczi, N. Frangis, and J. Stoemenos, “Structural Characteristics of the Si Whiskers Grown by Ni-Metal-Induced-Lateral-Crystallization,” *NANOMATERIALS*, vol. 11, no. 8, 2021. https://doi.org/10.3390%2Fnano11081878

[81] B. Pécz, G. Nicotra, F. Giannazzo, R. Yakimova, A. Koos, and A. Kakanakova-Georgieva, “Indium Nitride at the 2D Limit,” *ADVANCED MATERIALS*, vol. 33, no. 1, 2021. https://doi.org/10.1002%2Fadma.202006660

[82] C. Pei, S. Jin, P. Huang, A. Vymazalova, L. Gao, Y. Zhao, W. Cao, C. Li, P. Nemes-Incze, Y. Chen, H. Liu, G. Li, and Y. Qi, “Pressure-induced superconductivity and structure phase transition in Pt2HgSe3,” *NPJ QUANTUM MATERIALS*, vol. 6, no. 1, 2021. https://doi.org/10.1038%2Fs41535-021-00402-w

[83] B. Péter, I. Boldizsár, G. M. Kovács, A. Erdei, Z. Bajtay, A. Vörös, J. J. Ramsden, I. Szabó, S. Bősze, and R. Horvath, “Natural Compounds as Target Biomolecules in Cellular Adhesion and Migration: From Biomolecular Stimulation to Label-Free Discovery and Bioactivity-Based Isolation,” *BIOMEDICINES*, vol. 9, no. 12, 2021. https://doi.org/10.3390%2Fbiomedicines9121781

[84] D. Petrovszki, S. Valkai, E. Gora, M. Tanner, A. Bányai, P. Fürjes, and A. Dér, “An integrated electro-optical biosensor system for rapid, low-cost detection of bacteria,” *MICROELECTRONIC ENGINEERING*, vol. 239, 2021. https://doi.org/10.1016%2Fj.mee.2021.111523

[85] G. Piszter, K. Kertész, G. Sramkó, V. Krízsik, Z. Bálint, and L. P. Biró, “Concordance of the spectral properties of dorsal wing scales with the phylogeographic structure of European male Polyommatus icarus butterflies,” *SCIENTIFIC REPORTS*, vol. 11, no. 1, 2021. https://doi.org/10.1038%2Fs41598-021-95881-z

[86] A. Policicchio, A.-M. Putz, G. Conte, S. Stelitano, C. P. Bonaventura, C. Ianasi, L. Almásy, A. Wacha, Z. E. Horváth, and R. G. Agostino, “Hydrogen storage performance of methyl-substituted mesoporous silica with tailored textural characteristics,” *JOURNAL OF POROUS MATERIALS*, vol. 28, no. 4, pp. 1049–1058, 2021. https://doi.org/10.1007%2Fs10934-021-01058-4

[87] L. Pósa, Z. Balogh, D. Krisztián, P. Balázs, B. Sánta, R. Furrer, M. Csontos, and A. Halbritter, “Noise diagnostics of graphene interconnects for atomic-scale electronics,” *NPJ 2D MATERIALS AND APPLICATIONS*, vol. 5, no. 1, 2021. https://doi.org/10.1038%2Fs41699-021-00237-w

[88] L. Pósa, G. Molnár, B. Kalas, Z. Baji, Z. Czigány, P. Petrik, and J. Volk, “A Rational Fabrication Method for Low Switching-Temperature VO2,” *NANOMATERIALS*, vol. 11, no. 1, 2021. https://doi.org/10.3390%2Fnano11010212

[89] G. Radnóczi, R. Dedoncker, G. Z. Radnóczi, Z. Czigány, A. Sulyok, V. Kovács-Kis, and D. Depla, “The growth of a multi-principal element (CoCrFeMnNi) oxynitride film by direct current magnetron sputtering using air as reactive gas,” *SURFACE AND COATINGS TECHNOLOGY*, vol. 421, 2021. https://doi.org/10.1016%2Fj.surfcoat.2021.127433

[90] J. B. Renkó, A. Romanenko, P. J. Szabó, P. Petrik, and A. Bonyár, “Színesen mart ferrites acél vizsgálata spektroszkópiai ellipszometriával,” *BÁNYÁSZATI ÉS KOHÁSZATI LAPOK-KOHÁSZAT*, vol. 154., no. 3–4, pp. 32–36, 2021.

[91] A. Romanenko, B. Kalas, P. Hermann, O. Hakkel, L. Illés, M. Fried, P. Fürjes, G. Gyulai, and P. Petrik, “Membrane-Based In Situ Mid-Infrared Spectroscopic Ellipsometry: A Study on the Membrane Affinity of Polylactide-co-glycolide Nanoparticulate Systems,” *ANALYTICAL CHEMISTRY*, vol. 93, no. 2, pp. 981–991, 2021. https://doi.org/10.1021%2Facs.analchem.0c03763

[92] A. Saftics, S. Kurunczi, B. Peter, I. Szekacs, J. J. Ramsden, and R. Horvath, “Data evaluation for surface-sensitive label-free methods to obtain real-time kinetic and structural information of thin films: A practical review with related software packages,” *ADVANCES IN COLLOID AND INTERFACE SCIENCE*, vol. 294, 2021. https://doi.org/10.1016%2Fj.cis.2021.102431

[93] A. W. A. Salam, D. Mahmoud, P. László, M. János, and N. Péter, “Comparative multiphysics simulation of VO2 based lateral devices,” in *Proceedings of the 27th International Workshop on THERMal INvestigations of ICs and Systems (THERMINIC’21 online)*, 2021, pp. 178–181. https://doi.org/10.1109%2FTHERMINIC52472.2021.9626517

[94] N. Samotaev, A. Pisliakov, D. Filipchuk, M. Etrekova, F. Biro, C. Ducso, and I. Bársony, “SOI Based Micro-Bead Catalytic Gas Sensor,” *SPRINGER PROCEEDINGS IN PHYSICS*, vol. 255, pp. 105–111, 2021. https://doi.org/10.1007%2F978-3-030-58868-7_12

[95] . Samotaev, P. Dzhumaev, K. Oblov, A. Pisliakov, I. Obraztsov, C. Ducso, and F. Biro, “Silicon MEMS Thermocatalytic Gas Sensor in Miniature Surface Mounted Device Form,” *CHEMOSENSORS*, vol. 9, no. 12, 2021. https://doi.org/10.3390%2Fchemosensors9120340

[96] B. Sánta, Z. Balogh, L. Pósa, D. Krisztián, T. N. Török, D. Molnár, C. Sinkó, R. Hauert, M. Csontos, and A. Halbritter, “Noise Tailoring in Memristive Filaments,” *ACS APPLIED MATERIALS & INTERFACES*, vol. 13, no. 6, pp. 7453–7460, 2021. https://doi.org/10.1021%2Facsami.0c21156

[97] P. Sipos, V. Kovács Kis, R. Balázs, A. Tóth, and T. Németh, “Effect of pedogenic iron-oxyhydroxide removal on the metal sorption by soil clay minerals,” *JOURNAL OF SOILS AND SEDIMENTS*, vol. 21, no. 4, pp. 1785–1799, 2021. https://doi.org/10.1007%2Fs11368-021-02899-x

[98] W. Sun, L. Liu, X. Chen, A. Szolnoki, and V. V. Vasconcelos, “Combination of institutional incentives for cooperative governance of risky commons,” *ISCIENCE*, vol. 24, no. 8, 2021. https://doi.org/10.1016%2Fj.isci.2021.102844

[99] Á. Szabó, H. Liliom, Z. Fekete, K. Schlett, and A. Pongrácz, “SU-8 microstructures alter the attachment and growth of glial cells in vitro,” *MATERIALS TODAY COMMUNICATIONS*, vol. 27, 2021. https://doi.org/10.1016%2Fj.mtcomm.2021.102336

[100] G. Szabó and B. Király, “General features of Nash equilibria in combinations of elementary interactions in symmetric two-person games,” *EUROPEAN PHYSICAL JOURNAL B*, vol. 94, no. 5, 2021. https://doi.org/10.1140%2Fepjb%2Fs10051-021-00112-z

[101] I. Székács, N. Adányi, I. Szendrő, and A. Székács, “Direct and Competitive Optical Grating Immunosensors for Determination of Fusarium Mycotoxin Zearalenone,” *TOXINS*, vol. 13, no. 1, 2021. https://doi.org/10.3390%2Ftoxins13010043

[102] A. Szolnoki and M. Perc, “The self-organizing impact of averaged payoffs on the evolution of cooperation,” *NEW JOURNAL OF PHYSICS*, vol. 23, no. 6, 2021. https://doi.org/10.1088%2F1367-2630%2Fac0756

[103] A. Szolnoki and X. Chen, “Cooperation and competition between pair and multi-player social games in spatial populations,” *SCIENTIFIC REPORTS*, vol. 11, no. 1, 2021. https://doi.org/10.1038%2Fs41598-021-91532-5

[104] B. Tegze, E. Albert, B. Dikó, N. Nagy, A. Rácz, G. Sáfrán, A. Sulyok, and Z. Hórvölgyi, “Effect of Silver Modification on the Photoactivity of Titania Coatings with Different Pore Structures,” *NANOMATERIALS*, vol. 11, no. 9, 2021. https://doi.org/10.3390%2Fnano11092240

[105] R. Ungai-Salánki, E. Haty, T. Gerecsei, B. Francz, B. Béres, M. Sztilkovics, I. Székács, B. Szabó, and R. Horvath, “Single-cell adhesion strength and contact density drops in the M phase of cancer cells,” *SCIENTIFIC REPORTS*, vol. 11, no. 1, 2021. https://doi.org/10.1038%2Fs41598-021-97734-1

[106] R. Ungai-Salánki, B. Csippa, T. Gerecsei, B. Péter, R. Horvath, and B. Szabó, “Nanonewton scale adhesion force measurements on biotinylated microbeads with a robotic micropipette.,” *JOURNAL OF COLLOID AND INTERFACE SCIENCE*, vol. 602, pp. 291–299, 2021. https://doi.org/10.1016%2Fj.jcis.2021.05.180

[107] P. Vancsó, A. Mayer, P. Nemes-Incze, and G. I. Márk, “Wave packet dynamical simulation of quasiparticle interferences in 2d materials,” *APPLIED SCIENCES-BASEL*, vol. 11, no. 11, 2021. https://doi.org/10.3390%2Fapp11114730

[108] D. Varanasi, M. Furkó, K. Balázsi, and C. Balázsi, “Processing of Al2O3-AlN Ceramics and Their Structural, Mechanical, and Tribological Characterization,” *MATERIALS*, vol. 14, no. 20, 2021. https://doi.org/10.3390%2Fma14206055

[109] G. Vértesy, A. Gasparics, I. Szenthe, M. Rabung, M. Kopp, and J. M. Griffin, “Analysis of Magnetic Nondestructive Measurement Methods for Determination of the Degradation of Reactor Pressure Vessel Steel,” *MATERIALS*, vol. 14, no. 18, 2021. https://doi.org/10.3390%2Fma14185256

[110] G. Vértesy, A. Gasparics, I. Szenthe, and I. Uytdenhouwen, “Interpretation of Nondestructive Magnetic Measurements on Irradiated Reactor Steel Material,” *APPLIED SCIENCES-BASEL*, vol. 11, no. 8, 2021. https://doi.org/10.3390%2Fapp11083650

[111] Á. Vida, J. Lábár, Z. Dankházi, Z. Maksa, D. Molnár, L. K. Varga, S. Kalácska, M. Windisch, G. Huhn, and N. Q. Chinh, “A Sequence of Phase Transformations and Phases in NiCoFeCrGa High Entropy Alloy,” *MATERIALS*, vol. 14, no. 5, 2021. https://doi.org/10.3390%2Fma14051076

[112] R. Xie, S. Deng, W. Deng, and M. P. Pato, “Disordered beta thinned ensemble with applications,” *PHYSICAL REVIEW E: COVERING STATISTICAL NONLINEAR BIOLOGICAL AND SOFT MATTER PHYSICS (2016-)*, vol. 104, no. 5, 2021. https://doi.org/10.1103%2FPhysRevE.104.054144

[113] fang Yan, X. Chen, Z. Qiu, and A. Szolnoki, “Cooperator driven oscillation in a time-delayed feedback-evolving game,” *NEW JOURNAL OF PHYSICS*, vol. 23, no. 5, 2021. https://doi.org/10.1088%2F1367-2630%2Fabf205

[114] L. H. Yang, J. M. Gong, A. Sulyok, M. Menyhárd, G. Sáfrán, K. Tőkési, B. Da, and Z. J. Ding, “Optical properties of amorphous carbon determined by reflection electron energy loss spectroscopy spectra,” *PHYSICAL CHEMISTRY CHEMICAL PHYSICS*, vol. 23, no. 44, pp. 25335–25346, 2021. https://doi.org/10.1039%2Fd1cp02447g

[115] D. Zámbó, P. Rusch, F. Lübkemann, and N. C. Bigall, “Noble-Metal Nanorod Cryoaerogels with Electrocatalytically Active Surface Sites,” *ACS APPLIED MATERIALS & INTERFACES*, vol. 13, no. 48, pp. 57774–57785, 2021. https://doi.org/10.1021%2Facsami.1c16424

[116] Zs. Bálint, A. Parker, A. Ingram, K. Kertész, G. Piszter, Zs. E. Horváth, L. Illés, L. P. Biró “Scale granules and colours: Sexual dimorphism in Trichonis (Lepidoptera: Lycaenidae, Theclinae),” *ARTHROPOD STRUCTURE & DEVELOPMENT*, vol. 65, 2021. https://doi.org/10.1016%2Fj.asd.2021.101113